Challenging the Standard Model by high precision comparisons of the fundamental properties of antiprotons and protons

Von der QUEST-Leibniz-Forschungsschule
der Gottfried Wilhelm Leibniz Universität Hannover

zur Erlangung des akademischen Grades

Doktor der Naturwissenschaften
- Dr. rer. nat. -

genehmigte Dissertation von

M. Sc. Matthias Joachim Borchert

2021

1. Gutachter: Prof. Dr. Christian Ospelkaus
2. Gutachter: Prof. Dr. Fritz Riehle
3. Gutachter: Dr. Stefan Ulmer

Tag der Disputation: 28.01.2021

Für meine Eltern

Abstract

This thesis describes high precision measurements on the fundamental properties of the antiproton, namely the charge-to-mass ratio and the magnetic moment. This work is embedded in the experimental work of the BASE collaboration (Baryon Antibaryon Symmetry Experiment). BASE operates a sophisticated cryogenic Multi-Penning trap system in the Antiproton Decelerator facility at CERN. One main result of this thesis are significant technical improvements of the apparatus, which reduced the limitation of shot-to-shot cyclotron frequency scatter by a factor of more than five compared to earlier work. With this improved apparatus, a measurement campaign on the antiproton-to-proton charge-to-mass ratio with a statistical uncertainty of 20×10^{-12} and an overall uncertainty of about 35×10^{-12} was conducted. This campaign was part of a series of charge-to-mass ratio measurements on the antiproton with the overall goal to significantly improve the previous best measurement conducted by BASE in 2014, which yielded a fractional uncertainty of 69×10^{-12}. In this thesis, also the first dedicated heating rate measurement in a cryogenic Penning trap experiment is described. Here, the lowest heating rates ever reported for an ion trap were observed. As part of this thesis, phase sensitive methods for measuring the cyclotron frequency of a single trapped ion were implemented in the BASE experiment. These methods allowed to measure the cyclotron frequency with a shot-to-shot scatter improved by a factor of five compared to methods used in previous experiments. The significant improvements in cyclotron frequency scatter open up the possibility to measure the antiproton magnetic moment and the antiproton charge-to-mass ratio with much increased precision, and thereby enable more stringent tests of the fundamental CPT symmetry by direct comparisons of matter/antimatter conjugates.
Keywords: Penning trap, Antiproton, Charge-to-mass ratio

Contents

List of Figures

List of Tables

Abbreviations and acronyms

AC	alternating current
AD	antiproton decelerator
ADEV	Allan deviation
AEgIS	Antihydrogen experiment gravity interferometry spectroscopy
ALPHA	Antihydrogen Laser Physics Apparatus
ASACUSA	Atomic spectroscopy and collisions using slow antiprotons
AT	analysis trap
ATRAP	Antihydrogen trap
BASE	Baryon Antibaryon Symmetry Experiment
BASE-STEP	Baryon Antibaryon Symmetry Experiment - Symmetry Tests in Experiments with Portable Antiprotons
BMBF	Bundesministerium für Bildung und Forschung (German Federal Ministry of Education and Research)
bm	beam monitor
CERN	Conseil européen pour la recherche nucléaire (European Organization for Nuclear Research)
CL	Confidence level
CP	charge parity
CPT	charge parity time
CT	cooling trap
ELENA	Extra Low Energy Antiproton Ring
EMI	electromagnetic interference
es	electronics segment
FFT	Fast Fourier transform

FWHM	full width at half maximum
GBAR	Gravitational behavior of Anti-Hydrogen At Rest
GMR	giant magnetoresistance
LC	inductor capacitor
LHe	liquid helium
LIONTRAP	Light ION TRAP
LN2	liquid nitrogen
LS	long shutdown
LO	local oscillator
MACHO	massive astrophysical compact halo objects
MIT	Massachusetts Institute of Technology
NF	noise floor
NIST	National Institute of Standards and Technology
NMR	nuclear magnetic resonance
NT	top-noise level
OFHC	oxygen-free high thermal conductivity
PnA	Pulse and Amplify
PnP	Pulse and Probe
p.p.b.	parts per billion (10^{-9})
p.p.m.	parts per million (10^{-6})
p.p.t.	parts per trillion (10^{-12})
PT	precision trap
QED	quantum electrodynamics
RC	resistor capacitor
RF	radio frequency
RMS	root mean square
RRR	residual resistance ratio
RT	reservoir trap
SB	sideband
SM	Standard Model of particle physics
SME	Standard Model Extension
SMILETRAP	Stockholm-Mainz-Ion-LEvitation-TRAP
SNR	signal-to-noise ratio
SSB	single-sideband

SSC	self-shielding coil
TR	tuning ratio
WIMP	weakly interacting particle
XHV	extreme-high vacuum
YETS	year-end technical stop

1 | Introduction

The Standard Model of particle physics (SM) has been experimentally tested and verified many times. Prominent recent examples include the discovery of the top quark in 1995 at Fermilab [1, 2], and the discovery of the Higgs boson at CERN in 2012 [3, 4]. Another prediction already from quantum mechanics and special relativity is the existence of "anti-matter": For each type of matter particle, the existence of a corresponding antiparticle type is postulated, which exhibits identical fundamental properties (apart from the sign). The existence of antimatter was firstly proposed by Dirac [5] based on the Dirac equation formulated in 1928 [6], which predicted for each solution with positive energy a corresponding solution with negative energy. The positron, the anti-electron, was discovered in 1931 as the first antiparticle when Anderson investigated signals from cosmic rays [7]. In the Feynman-Stückelberg interpretation of quantum field theory [8, 9], the negative-energy solutions of the Dirac equation were interpreted as being distinct particles with positive energies, traveling backwards in time. Adopting the Feynman-Stückelberg interpretation, the CPT theorem was formulated implicitly by Schwinger in 1951 [10] and explicitly by Lüders and Pauli in 1954 [11, 12]. The CPT theorem states that any local, Lorentz invariant quantum field theory like the Standard Model must obey the combined symmetries of charge conjugation, parity and time reversal. Consequently, CPT symmetry is one of the most fundamental symmetries in the relativistic field theories of the Standard Model. One consequence of CPT symmetry is that matter/antimatter conjugates exhibit (apart from the sign) identical fundamental properties.

Despite its tremendous successes, the Standard Model remains incomplete. For example, no quantum mechanical description of gravity has been incorporated into the SM yet. According to cosmological findings [13], about 95 % of the universe's energy content is given by dark matter and dark energy, while the macroscopic nature of dark matter and

the origin of dark energy have yet to be understood. Another intriguing puzzle of the Standard Model is the existence of the non-zero neutrino mass [14].
The SM also fails to provide a compelling explanation for the fact that the observable universe is matter-dominated, and that, within our current knowledge, no clear indications for the existence of primordial antimatter in the universe could be found yet [15]. As a consequence of CPT symmetry, matter and antimatter should have been created at equal amounts during the big bang. In 1967, Sakharov proved that baryon asymmetry could have been generated in the framework of the Standard Model if three conditions were met [16]: Firstly, a violation of baryon number, secondly, a violation of C and CP symmetry, and thirdly, a deviation from thermal equilibrium. CP symmetry is indeed broken as firstly reported for the decay of neutral Kaons into two pions in 1964 [17], and subsequently observed also in other systems [18, 19, 20]. The observed baryon asymmetry in the universe is characterized by the ratio of baryon-to-photon number obtained from the cosmological background radiation [21]:

$$\eta_{\text{exp}} = \frac{N_B - N_{\bar{B}}}{N_\gamma} = 6.14(25)10^{-10}, \tag{1.1}$$

with the baryon number N_B, the antibaryon number $N_{\bar{B}}$ and the photon number N_γ. The CP violations observed so far however would only lead to asymmetry values η that are by about eight orders of magnitude lower than the observed asymmetry [22]. So far, the baryogenesis (the genesis of the observed baryon asymmetry) remains unexplained in the framework of the SM, and motivates theorists and experimentalists to provide compelling solutions. One alternative explanation for the baryogenesis for instance could potentially be provided by assuming an asymmetry in the leptonic sector (leptogenesis), which then leads to baryogenesis via hypothetical sphaleron processes that could convert groups of three antibaryons into three leptons [23]. Another approach for searching for a mechanism responsible for the baryogenesis is related to the search for certain hypothetical CPT symmetry violating processes, which would also violate the baryon number conservation [24]. Compared to the Sakharov criteria, the deviation from thermal equilibrium would not be needed any more for the baryogenesis in case of CPT violation and baryon number violation.

1.1. Tests of CPT symmetry

In the past decades, CPT symmetry has directly been tested by dedicated measurements on several matter-antimatter conjugates. For example, the mass difference of neutral kaons/antikaons $K_0/\bar{K}_0$ has been measured with a fractional precision[1] of 0.8×10^{-18} by comparing the decay channels to charged and neutral pions [25]. In the leptonic sector, the electron and positron g-factors have been compared in 1987 [26, 27], excluding a g-factor difference at a level of 2 p.p.t.[2], which still stands as one of the most stringent CPT tests in the leptonic sector. For the muon μ^-/μ^+, the $g-2$ values were compared with a fractional resolution of 3.7×10^{-9} in a storage ring experiment [30, 31].
For CPT tests incorporating baryonic antimatter, CERN's Antiproton Decelerator (AD) [32] is so far the only facility in the world at which low-energetic baryonic antimatter is made available to experimentalists such that it can be trapped and stored in designated particle traps [33]. In the AD, currently five collaborations are studying baryonic antimatter, focusing on antihydrogen (AEGIS, ALPHA, ASACUSA, GBAR), antiprotonic helium (ASACUSA) and single antiprotons (BASE). The results of some CPT tests in the baryonic sector are shown in Fig. 1.1.
After about ten years of development, rapid progress has been made in the field of antihydrogen physics during the past few years [34]. In 2017, ALPHA published a measurement on the antihydrogen ground state hyperfine splitting with a fractional resolution of 350 p.p.m. [35]. In 2018, the ALPHA collaboration measured the 1S-2S transition in antihydrogen with a fractional resolution of 2 p.p.t. [36].
The BASE collaboration has contributed to direct tests of CPT invariance by measuring the proton and antiproton g-factors at unprecedented precision on the p.p.b.-level and below [37, 38, 28, 29] and by comparing the antiproton-to-proton charge-to-mass ratios at unprecedented precisions on the 10^{-11} level [39]. BASE improved the precision of the antiproton magnetic moment by a factor of 3000 compared to the result of competing collaborations [40]. So far, no evidence for CPT violation has been found in the experiments listed above, while several million fold improved CPT invariance tests have been provided.

While experimental verifications of the CPT symmetry are of high relevance for physics

[1] For the use of the words "precision" and "accuracy" throughout this thesis, please refer to App. A.
[2] In this thesis, the terms p.p.b. and p.p.t. are used to denoted 10^{-9} and 10^{-12}, respectively, following the conventions used in the BASE publications [28, 29].

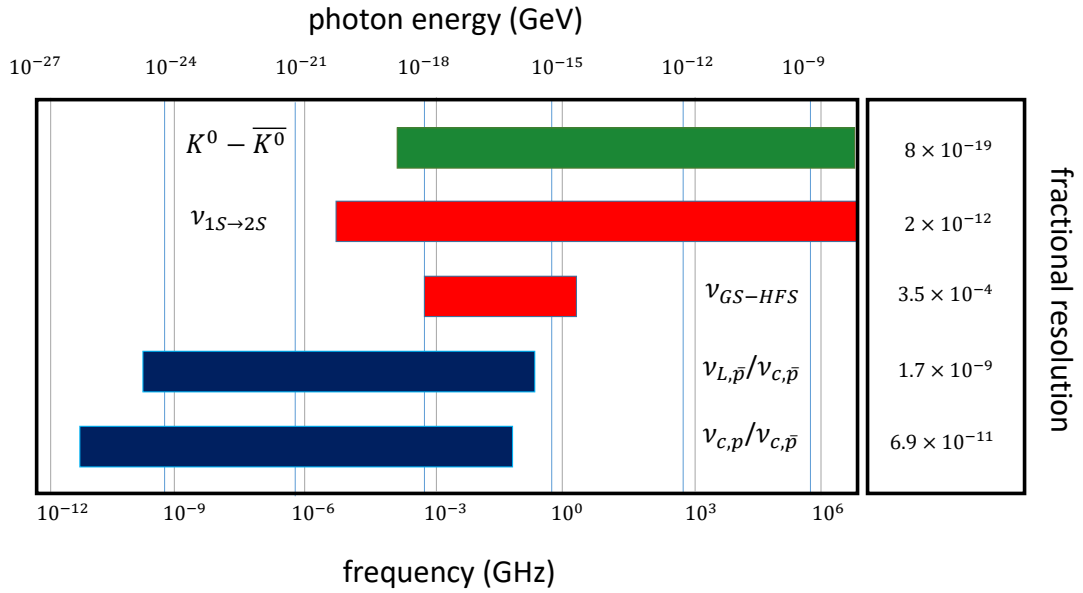

Figure 1.1.: Fractional and energy resolution of different CPT tests by comparing matter/antimatter conjugates in the baryonic sector. The green data depict the kaon mass comparison, which is the CPT test in the baryonic sector with the highest fractional precision. The red data denote antihydrogen measurements performed by the ALPHA collaboration [35, 36]. In blue, the measurement results on single antiprotons obtained by the BASE collaboration are shown [39, 28, 29]. While the kaon mass measurement and the 1S-2S measurement on antihydrogen have significantly lower fractional uncertainties, the BASE measurements yields the highest energy resolution and is more sensitive with respect to certain CPT odd SME coefficients [41]. Figure taken from [42].

due to the fundamental role the CPT symmetry plays in the Standard Model framework, no established fundamental physics theory proposes a CPT violation of a certain strength for a certain group of particles. However, general effective field theories which contain possible sources of Lorentz and CPT violation arising from some unknown fundamental physical processes have been proposed. It is possible to relate the coefficients multiplying new CPT-odd Lagrangian terms introduced by these theories to physical quantities measured in experiments. The most prominent framework in the antimatter community is the Standard Model Extension (SME), developed by Alan Kostelecky and co-workers [41]. The SME is an effective field theory that is based upon the standard model, which however involves minimal CPT violating interactions that contain symmetries which transform according to the general properties of the Poincare group. In the

SME, certain groups of hypothetical CPT odd coefficients can be constrained by performing measurements on a specific matter/antimatter conjugate, while other groups of coefficients can only be addressed from measurements on other systems. In order to test CPT symmetry in its entirety it is therefore important to investigate different systems. Here, the exotic interactions V_e perturb the energy levels E_k to $E_k + \Delta E_k$, with ΔE_k given by $\Delta E_k = \langle\psi| V_e |\psi\rangle$, and E_k being the energy of the unperturbed system with Hamiltonian H_0, $E_k = \langle\psi| H_0 |\psi\rangle$. H_0 might for instance describe a charged particle inside a Penning trap. The energy resolution of matter/antimatter comparisons can be used as one figure of merit for comparing CPT tests with different systems. The fractional resolution of different CPT tests and the related energy resolution for CPT-odd effects is shown in Fig. 1.1. The Kaon mass measurement with a fractional uncertainty of 0.8×10^{-18} GeV places constrains on the level of 10^{-18} GeV. Despite the significantly lower fractional resolution of the antiproton magnetic moment on the p.p.b.-level, an energy resolution of $< 2 \times 10^{-24}$ GeV is reached in this measurement. The high energy resolution of the BASE experiments is a consequence of the high frequency resolution on the mHz-level achieved by the BASE collaboration [42].

1.2. About this thesis

The author joined the BASE (Baryon Antibaryon Symmetry Experiment) collaboration [43] at CERN in February 2014 as part of his bachelor's project [44], which was to build single particle detection systems for the BASE Hannover/QLEDS project [45]. As an undergraduate student, the author spent in total about two years at the BASE experiment [46], before he started his PhD work in May 2017. The work described in this thesis was closely supervised and strongly supported by Stefan Ulmer, who is the founder and spokesperson of the BASE collaboration. While this thesis will mainly focus on the topics the author worked on independently or in close cooperation with another colleague, there are a few more topics that should be addressed briefly. The author joined the collaborative efforts of BASE that resulted in the following achievements:

- The first measurement of the antiproton magnetic moment $g_{\bar{p}}$ was performed by the BASE collaboration in 2016 [38], which improved on the previous best known value [40] by a factor of six in precision. While this measurement was performed in the BASE analysis trap exclusively,

- The most precise measurement of the antiproton magnetic moment [28] was performed in the BASE precision trap using the novel "triple trap method". The Larmor frequency ω_L and the cyclotron frequency ω_c were measured with two different particles, the analysis trap was used for spin state determination only. This measurement based on a method invented by BASE improved our previous measurement [38] by a factor of about 350 in precision, and the best measurement from the competing ATRAP collaboration by a factor of about 3000 [40]. This measurement is described in Chap. 4. One crucial prerequisite for this measurement was
- The first observation of individual spin transitions of a single antiproton [47]. During the 2015/2016 experimental run, the BASE collaboration realized
- A direct measurement on the lower antiproton lifetime limit [48] by storing a pure cloud of antiprotons in the BASE reservoir trap for 405 days and continuously recording the number of particles in the trap. Our result $\tau_{\bar{p}} > 10.2\,\mathrm{a}$ improved our previous best value [49] by a factor of 7. This work is discussed in Sec. 6.3. A more stringent limit $\tau_{\bar{p}} > 26.15\,\mathrm{a}$ on the antiproton lifetime is derived in Sec. 6.4, which includes the antiproton reservoir data acquired between 2017 and 2019.
- The world's first measurement on a possible CPT-odd interaction between antimatter and axion-like dark matter [50] enabled by a reanalysis of the 2016 data from [28], thereby combining two of the most intriguing puzzles of modern physics. This is described in Sec. 4.2.

While the author's contribution to the milestones mentioned above was of collaborative nature, this thesis will focus on three projects the author was either responsible or jointly responsible for:

- The world's first dedicated measurement of ion heating rates in a cryogenic Penning trap [51]. Employing the continuous Stern-Gerlach effect, we measured heating rates in the BASE analysis trap and obtained transition rates of 6(1) quanta/h and scaled electric field noises that were by two orders of magnitude lower than obtained in any other ion trap experiment. The heating rate measurement is described in Chap. 5 in detail.
- A comparison of the antiproton-to-proton charge-to-mass ratios with a statistical resolution of around 20 parts per trillion. Note that the systematic investigation of this measurement was ongoing when this thesis was submitted, and that the

final measurement uncertainty will be larger due to systematic uncertainties. The measurement campaign was carried out in April and May 2019 by means of sideband methods, and was part of a series of q/m measurements conducted from 2017 to 2019 with contributions from the entire BASE team at CERN. This series will improve the antiproton-to-proton charge to mass ratio precision significantly compared to the previous result of the BASE collaboration [39], that yielded a precision of 69 p.p.t. The campaigns before 2019 will be discussed in the PhD thesis of James Brydges-Harrington [52]. Aspects of these campaigns are also described in the PhD thesis of Takashi Higuchi [53]. The charge-to-mass ratio measurement from 2019 is discussed in Chap. 8, where a fractional precision of 34 p.p.t. has been reached.

- The implementation of phase sensitive methods for cyclotron frequency measurements. This involved the study of mode coupling in a Penning trap by characterizing so called classical Rabi oscillations [54], the demonstration of the pulse and phase [55, 54] technique and the pulse and amplify [56] technique. This work was carried out in close collaboration with Jack Devlin. The phase sensitive methods are described in Chap. 9.

2 | Penning trap physics

The ion trap technique allows to trap and store charged particles by employing electromagnetic fields, to isolate them for environmental effects and to study their fundamental properties with high precision. In this way, ion traps have enabled some of the greatest atomic physics achievements made in the 20th and 21th century, such as the first laser-cooling of trapped ions [57] and the g-2 comparison between electrons and positrons [26], which provides one of the most stringent test of CPT-symmetry in the leptonic sector since 1987 to the present day. Ion traps have also a wide range of application in quantum information and quantum computing, where they have been proposed as a candidate for implementing a quantum computer [58] in 1995, which started enormous efforts of physicist across the globe in order to construct quantum computers with large numbers of quantum bits (see for instance [59, 60]). In low energy physics, ion traps have enabled the most precise measurement of the electron g-factor and the at-that-time most precise measurement of the fine structure constant [61], and found important application in the formation of antihydrogen for high-precision tests of the CPT-symmetry [62, 36].

2.1. Principle of the Penning trap

As found out by Earnshaw in 1842 [63], it is impossible to generate a static electric potential minimum. In 1953, Wolfgang Paul proposed an ion trap based on oscillating electric potentials [64]. This type of particle trap later on became known as "Paul trap". The other main type of ion traps, the "Penning trap" consists of the superposition of a static quadrupolar electric field with a homogeneous magnetic field. Superposing a quadrupolar electric field and a homogeneous magnetic field was first proposed by Penning in 1936 [65] in order to slow down the diffusion of electrons to the walls of an

ionization gauge. Combining a homogeneous magnetic field and a quadrupolar electric field in order to yield a particle trap was proposed by Pierce in 1949 [66].
The Penning trap magnetic field is described by $\vec{B} = B_0\vec{e}_z$. Its electric quadrupole field is given by

$$\Phi(z,\rho) = C_2 V_r \left(z^2 - \rho^2/2\right), \tag{2.1}$$

with $\rho^2 = x^2 + y^2$. A particle with mass m and charge q experiences the Lorentz force $\vec{F}_L$,

$$\vec{F}_L = -q\nabla\Phi + q\left(\dot{\vec{x}} \times \vec{B}\right) \Rightarrow \begin{pmatrix} \ddot{x} - (\omega_z^2/2)x - \dot{y}\omega_c \\ \ddot{y} - (\omega_z^2/2)y + \dot{x}\omega_c \\ \ddot{z} + \omega_z^2 z \end{pmatrix} = \begin{pmatrix} 0 \\ 0 \\ 0 \end{pmatrix}, \tag{2.2}$$

with axial frequency ω_z and cyclotron frequency ω_c given by

$$\omega_z = \sqrt{\frac{2qV_rC_2}{m}}, \qquad \omega_c = \frac{qB_0}{m}. \tag{2.3}$$

C_2 is a characteristic trap parameter defined by the trap geometry and V_r denotes the trapping voltage. The axial motion z along the magnetic field lines is described by a harmonic oscillator with frequency ω_z. In order to determine the radial motion, Eq. 2.2 will be rewritten [67, 68]. We introduce $u = x + iy$ and obtain

$$\ddot{u} + i\omega_c\dot{u} - 1/2\omega_z^2 u = 0, \tag{2.4}$$

which is solved by the ansatz $u = \exp(-i\omega t)$,

$$\omega^2 - \omega_c\omega + 1/2\omega_z^2 = 0. \tag{2.5}$$

This leads to solutions at the characteristic frequencies

$$\omega_\pm = \frac{\omega_c}{2} \pm \sqrt{\left(\frac{\omega_c}{2}\right)^2 - \frac{1}{2}\omega_z^2}. \tag{2.6}$$

ω_+ is called the modified or reduced cyclotron frequency[1], ω_- is called the magnetron frequency. For non-imaginary trap frequencies $\omega_+, \omega_z, \omega_-$, the particle oscillates along the z-axis with the axial frequency ω_z and follows a superposition of two circular orbits

[1] From now on, the term "cyclotron frequency" will be used for ω_+, while ω_c will be referred to as "free cyclotron frequency", in order to be consistent with the literature.

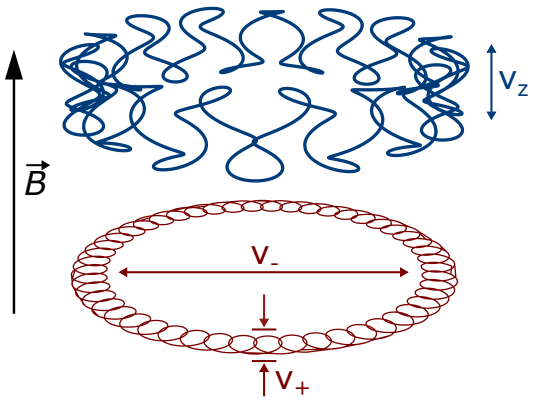

Figure 2.1.: Particle trajectory in a Penning trap. Axially, the particle oscillates with ν_z. The radial motion is a superposition of the cyclotron oscillation with frequency ν_+ and the magnetron oscillation ν_-. The oscillation amplitudes and frequencies depicted here are for illustrative purposes, but do not represent the actual frequencies and amplitudes in our Penning trap. The oscillation frequencies follow the hierarchy $\nu_+ \gg \nu_z \gg \nu_-$.

in the x-y plane, as visualized in Fig. 2.1. ω_+ can be understood as a slightly modified free cyclotron frequency ω_c that describes the circular motion of a charged particle in a homogeneous magnetic field in absence of an electric field. The magnetron motion ω_- results from an $\vec{E} \times \vec{B}$-drift: The particle is pulled radially by the trapping voltages, which generates a motion perpendicular to the magnetic field and guides the particle to another circular orbit. The principle of the Penning trap can be summarized by stating that the homogenous magnetic field confines the particle on a circular orbit perpendicular to the magnet field axis, while the electric potential prevents the particle from escaping the trap in the direction of the magnetic field axis. In BASE, the trap frequencies show the following hierarchy:

$$\omega_+ \gg \omega_z \gg \omega_-. \tag{2.7}$$

The free cyclotron frequency is obtained by quadratically summing up all frequencies, even with trap imperfections, by means of the Brown-Gabrielse invariance theorem [69]:

$$\omega_c^2 = \omega_+^2 + \omega_z^2 + \omega_-^2. \tag{2.8}$$

The invariance theorem is especially useful for traps with a slight misalignment between magnetic and electric field axis, and for traps with an ellipticity ϵ (Eq. 7.21) [69, 70].

The magnetron frequency is often estimated by [70]

$$\omega_- \approx \omega_z^2/(2\omega_+), \tag{2.9}$$

which is usually sufficiently accurate for computing ω_c by means of Eq. 2.8 as a consequence of the frequency hierarchy outlined in Eq. 2.7.
The axial energy E_z is given by

$$E_z = \frac{1}{2}m\omega_z^2 z^2 = m\omega_z^2 \bar{z}^2, \tag{2.10}$$

with z being the maximum axial excitation and $\bar{z}$ being the axial RMS amplitude. The magnetron energy E_- is predominantly given by its potential energy:

$$E_- = \frac{1}{2}m\omega_-^2\rho_-^2 - \frac{1}{4}m\omega_z^2\rho_-^2 \approx -\frac{1}{4}m\omega_z^2\rho_-^2. \tag{2.11}$$

The cyclotron energy E_+ is predominantly kinetic:

$$E_+ = \frac{1}{2}m\omega_+^2\rho_+^2 - \frac{1}{4}m\omega_z^2\rho_+^2 \approx \frac{1}{2}m\omega_+^2\rho_+^2. \tag{2.12}$$

Assuming coupling to a thermal reservoir, the expectation values for the energies are related to the respective reservoir temperatures by

$$\langle E_+ \rangle = k_B T_+, \qquad \langle E_z \rangle = k_B T_z, \qquad \langle E_- \rangle = k_B T_-. \tag{2.13}$$

2.2. The cylindrical Penning trap

Historically, the electric trapping potential of a Penning trap was firstly realized with a hyperbolic electrode geometry. Meanwhile, Penning traps are most commonly realized by means of a cylindrical electrode structure [71]. The cylindrical geometry is favorable as cylindrical electrodes can be fabricated with very small manufacturing uncertainties, and as multi-Penning trap systems can easily be realized in a cylindrical geometry with open endcaps. An example for a cylindrical geometry is shown in Fig. 2.2.
The trapping potential provided by a stack of cylindrical electrodes is calculated from electrostatic potential theory by employing the Laplace equation in free space, which is for instance described in [72]. Main aspect of this description will be recapitulated here,

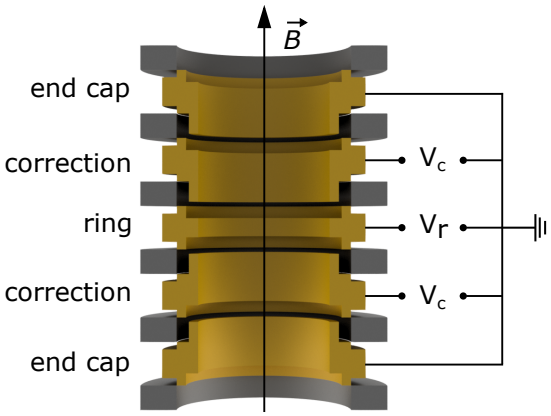

Figure 2.2.: Cylindrical Penning trap. The electrodes are designed in an orthogonal and compensated way [71], and provide a quadrupolar potential when the correct voltages are applied. The electrode end caps are grounded, the ring voltage V_r determines the axial frequency. The correction voltages V_c given by $V_c = \mathrm{TR} \times V_r$ with the tuning ratio TR ensuring the homogeneity of the potential for the matching tuning ratio. The electrodes are spatially separated by cylindrical sapphire spacers (gray). The electrode axes are aligned with the magnetic field $\vec{B}$.

but for the full description the reader is redirected to [72]. The on-axis potential can be expressed as a sum of powers of the C_j coefficients [71]:

$$\Phi(0, z) = V_r \sum_{j=0}^{n} C_j z^j. \tag{2.14}$$

For a five-pole trap, these coefficients are given by [72]

$$C_j = \frac{1}{j!\Lambda V_r} \sum_{n=1}^{\infty} \left[\frac{V_1 \cos(k_n z_0) - V_5 \cos(k_n \Lambda)}{k_n} + \sum_{i=2}^{5} \frac{V_i - V_{i-1}}{k_n^2 d} (\sin(k_n z_{2i}) - \sin(k_n z_{2i-1})) \right] \times \frac{(n\pi/\Lambda)^j}{I_0(k_n a)} \sin\left(\pi/2(n+j)\right). \tag{2.15}$$

Λ denotes the trap length, k_n is defined as $k_n = n\pi/\Lambda$, and d denotes the spacing between two electrodes. I_0 are the Bessel functions of the first kind. a is the inner radius of the cylindrical electrodes, z_{2i} the start coordinate of $(i+1)$th electrode in axial direction, and z_{2i-1} the end coordinate of the ith electrode. The ring electrode voltage is here

given by V_3, the correction electrode voltages are denoted by V_2 and V_4, and the end cap voltages are described by V_1 and V_5. Note that the end cap electrodes are grounded under normal experimental conditions. The correction electrode voltages are given by $V_2 = V_4 = \mathrm{TR} \times V_3$ for a symmetric trap, with TR denoting the tuning ratio. As the Penning trap is symmetric for $z \to -z$, all C_j with odd j vanish. We can then express the C_j-coefficients by [72]

$$C_j = E_j + D_j \times \mathrm{TR}, \tag{2.16}$$

with D_j and E_j given by the trap geometry. The trap diameter, the correction electrode length and the ring electrode length are three free parameters for the trap design, which are usually chosen such that the parameter D_2 vanishes and that the parameters C_4 and C_6 are simultaneously tuned to zero. $D_2 = 0$ is equivalent to state that the axial frequency does not change as a function of the tuning ratio. This behavior is called *orthogonality* and is of great advantage for trap optimization. Having C_4 and C_6 simultaneously tuned to zero is called *compensation* and is of particular interest as C_4 and C_6 induce undesirable energy-dependent trap frequency shifts (see Sec. 2.2.1). While the *compensation* can be theoretically achieved for a five-pole trap, in the experimental reality the trapping potential is distorted for instance due to manufacturing inaccuracies and due to parasitic voltage patches on electrode surfaces leading to offset potentials. Consequently, during the experimental operation usually only one of the two parameters C_4 and C_6 can be tuned to zero.

2.2.1. Trap anharmonicities and energy dependent shifts

Recalling the electric on-axis potential as outlined in Eq. 2.14, we obtain the equation of motion for the axial oscillation:

$$\ddot{z} = -\frac{qV_r}{m}\partial_z \sum_{j=0}^{n} C_j z^j = -\frac{qV_r}{m}\left(2C_2 z + 4C_4 z^3 + ...\right) = -\omega_z^2\left(z + \frac{2C_4}{C_2}z^3 + ...\right). \tag{2.17}$$

This is a generalized Duffing equation and can be solved accordingly [73]. The explicit frequency shifts arising for electric and magnetic inhomogeneities C_j, B_j are derived in

literature [70, 68, 74]. In [75, 68], these shifts are concisely summarized:

$$\begin{pmatrix} \Delta\omega_+/\omega_+ \\ \Delta\omega_z/\omega_z \\ \Delta\omega_-/\omega_- \\ \Delta\omega_L/\omega_L \end{pmatrix} = (\mathcal{M}_{C4} + \mathcal{M}_{B2}) \begin{pmatrix} E_+ \\ E_z \\ E_- \end{pmatrix} + \mathcal{M}_{C6} \begin{pmatrix} E_+^2 \\ E_z^2 \\ E_-^2 \\ E_+E_z \\ E_+E_- \\ E_zE_- \end{pmatrix} + \dots \,. \tag{2.18}$$

The matrices are given by

$$\mathcal{M}_{C4} = \frac{1}{qV_r}\frac{C_4}{C_2^2} \begin{pmatrix} 3/4\Omega^4 & -3/2\Omega^2 & -3\Omega^2 \\ -3/2\Omega^2 & 3/4 & 3 \\ -3\Omega^2 & 3 & 3 \\ 0 & 0 & 0 \end{pmatrix}, \qquad \mathcal{M}_{B2} = \frac{1}{m\omega_z^2}\frac{B_2}{B_0} \begin{pmatrix} -\Omega^2 & 1 & 2 \\ 1 & 0 & -1 \\ \Omega^2 & -1 & -2 \\ \Omega^4 & 2 & 4 \end{pmatrix},$$

$$\mathcal{M}_{C6} = \frac{1}{q^2V_r^2}\frac{C_6}{C_2^3} \begin{pmatrix} -15/16\Omega^6 & -45/16\Omega^2 & -45/4\Omega^2 & 45/8\Omega^4 & 45/4\Omega^4 & -45/2\Omega^2 \\ 45/16\Omega^4 & 15/16 & 45/4 & -45/8\Omega^2 & -45/2\Omega^2 & 45/4 \\ 45/8\Omega^4 & 45/8 & 15/2 & -45/2\Omega^2 & -45/2\Omega^2 & 45/2 \\ 0 & 0 & 0 & 0 & 0 & 0 \end{pmatrix}, \tag{2.19}$$

with $\Omega = \omega_z/\omega_+$, and assuming a negative magnetron energy $E_- < 0$.
The C_8-matrix and the matrices as a function of particle amplitudes are given in App. B.

2.3. Particle detection and frequency measurements

All frequency measurements performed in the BASE Penning traps rely on the detection of image currents by means of resonant high quality LC-circuits [57, 76]. The image current I generated through the axial oscillation is given by

$$I = q/D \times \dot{z} = q/D \times 2\pi\nu_z \cos(\omega_z t)z, \tag{2.20}$$

with z denoting the maximum oscillation amplitude, and D the effective electrode distance, which depends on the trap geometry and the electrode chosen for signal pick-up. The axial detector (see Fig. 2.3) consisting of a high-quality resonator and an ultra-low

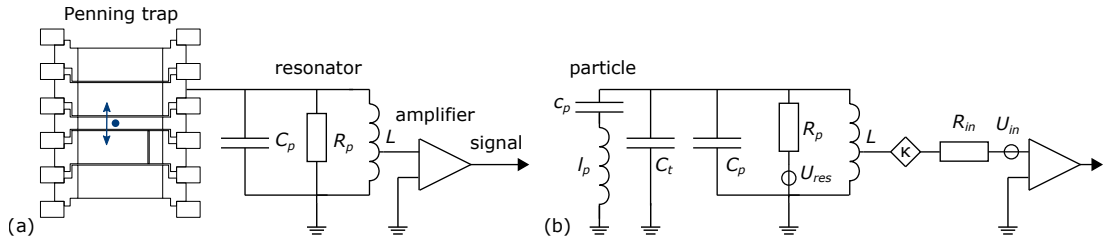

Figure 2.3.: Schematic of the axial detection system and the detector particle interaction. Left: The particle oscillates in axial direction inside the Penning trap, and thereby induces image currents in the trap electrodes. A superconducting resonator together with a cryogenic amplifier is used for particle detection. The resonator is depicted by the equivalent circuit diagram, consisting of a resistance R_p, inductance L and parasitic capacitance C_p. The resonator is inductively coupled to the cryogenic amplifier. Right: Once the particle is in thermal equilibrium with the detection system, its equivalent circuit diagram is given by a series LC-circuit as derived in Eq. 2.28. The inductive coupling factor between the resonator and the amplifier is given by κ. The particle shorts the thermal resonator noise u_{res}. The amplifier is described by the equivalent input noise u_{in} and the input resistance R_{in}.

noise cryogenic amplifier is connected to one correction electrode. The detector's resonance frequency ω_{res} is given by $\omega_{\mathrm{res}} = 1/\sqrt{LC}$ as for all parallel LC-circuits. Here, C is given by the parasitic resonator capacitance C_p, the parasitic trap capacitance C_t, and the parasitic capacitance arising from the remaining setup, for instance due to cabling. Usually, the axial oscillation frequency is tuned to the resonance frequency, $\nu_{\mathrm{res}} \approx \nu_z$. On resonance, the detector acts like a parallel resistance R_p given by

$$R_p = 2\pi\nu_{\mathrm{res}} \times QL, \tag{2.21}$$

where Q is the resonator quality factor. For an axially excited particle tuned to the resonator frequency, the voltage U_p generated by the particle's image current is given by

$$U_p = IR_p = q/D(2\pi\nu_z)z \times R_p. \tag{2.22}$$

The voltage signal scales linearly with R_p and thus with Q, which is why it is crucially important to have low parasitic losses in the detection resonators. At BASE, carefully designed toroidal superconducting resonators are used for this purpose [72, 76].

2.3.1. Particle detector interaction

We shall now consider the equation of motion for an axially excited particle damped by the detector:

$$m\ddot{z} = -m\gamma\dot{z} - m\omega_z^2 z, \tag{2.23}$$

with the damping constant γ. The equation above is rewritten to

$$\frac{1}{2}m\dot{z}^2 + \frac{1}{2}m\omega_z^2 z^2 = -\int \mathrm{d}t m\gamma_z \dot{z}^2, \tag{2.24}$$

by multiplying the equation with $\dot{z}$ and integrating over the time. The left side of this equation describes now the particle energy. We can then relate the damping constant to the loss in particle energy,

$$P = R_p I^2 \Rightarrow \gamma_z = \frac{R_p}{m}\frac{q^2}{D^2}, \tag{2.25}$$

to which end Eq. 2.20 is utilized. We may now rewrite Eq. 2.24 to

$$m\frac{D^2}{q^2}\dot{I} + R_p I + m\omega_z^2 \int \mathrm{d}t \frac{D^2}{q^2} I = 0. \tag{2.26}$$

By inserting the newly defined quantities l_p and c_p,

$$l_p = m\frac{D^2}{q^2}, \qquad c_p = \frac{1}{m\omega_z^2}\frac{q^2}{D^2}, \tag{2.27}$$

we yield the description of a series LC-circuit:

$$l_p \frac{\mathrm{d}}{\mathrm{d}t} I + R_p I + \frac{1}{c_p}\int \mathrm{d}t I = 0. \tag{2.28}$$

Consequently, the particle can be represented by a series LC-circuit as done in Fig. 2.3 (b). The particle impedance Z_p is then calculated from the equivalent circuit diagram in Fig. 2.3 (b),

$$Z_p = i\omega l_p + (i\omega c_p)^{-1}. \tag{2.29}$$

In the equations above, the resonator has been simplified by neglecting L and C and exclusively considering R_p. For a full treatment, the resonator impedance Z_0 has to be considered. Only its real part dissipates energy and has therefore to be considered for

the damping process and the particle-resonator interaction here. If the axial frequency exactly matches the resonator frequency, $\omega_z = \omega_{\mathrm{res}}$, the real part is indeed given by R_p, $\mathrm{Re}(Z_0(\omega_z)) = R_p$, which justifies the treatment above. The full resonator impedance Z_0 is given by

$$Z_0(\omega) = \left(\frac{1}{R_p} + i \left(\frac{\omega^2 - \omega_0^2}{\omega_0^2 \omega L} \right) \right)^{-1}, \tag{2.30}$$

with its real part $\mathrm{Re}(Z_0)$ following a Lorentzian lineshape given by

$$\mathrm{Re}\left(Z_0\right) = \frac{R_p \left(\omega_0^2 \omega L\right)^2}{\left(\omega_0^2 \omega L\right)^2 + R_p^2 \left(\omega^2 - \omega_0^2\right)^2}. \tag{2.31}$$

The overall impedance Z_{tot} is computed from the particle impedance Z_p (Eq. 2.29) and from the detector impedance Z_0:

$$Z_{\mathrm{tot}} = \left(\frac{1}{Z_0} + \frac{1}{Z_p} \right)^{-1} \Rightarrow \mathrm{Re}\left(Z_{\mathrm{tot}}\right) = \frac{R_p}{1 + \left(\frac{\gamma\omega}{(\omega_z^2 - \omega^2)} + R_p \frac{\omega^2 - \omega_0^2}{\omega_0^2 \omega L} \right)^2}. \tag{2.32}$$

Neglecting the frequency-dependency in Z_0 and assuming that the resonator is tuned to the particle frequency, $\mathrm{Re}\left(Z_{\mathrm{tot}}\right)$ can be rewritten to

$$\mathrm{Re}\left(Z_{\mathrm{tot}}\right) = \frac{R_p(\omega_z^2 - \omega^2)^2}{(\omega_z^2 - \omega^2)^2 + (\gamma\omega)^2}. \tag{2.33}$$

This simplified expression is frequently used for fitting and lineshape studies, as the resonator FWHM is usually significantly larger than the FWHM of the axial dip. $\mathrm{Re}(Z_{\mathrm{tot}})(\omega)$ vanishes for $\omega = \omega_z$, which can be interpreted as the particle shorting the resonator. The full width at half maximum $\delta\nu_z$ of this axial dip is given by

$$\delta\nu_z = \frac{1}{2\pi}\gamma = \frac{1}{2\pi}\frac{R_p}{m}\frac{q^2}{D^2} \tag{2.34}$$

for a single trapped particle. From here onwards, $\delta\nu_z$ will be referred to as "axial dip width". For a small cloud of N trapped particles, the dip width increases linearly [57]. This scaling can be used to determine the number of particles stored in a trap, and is used during our antiproton lifetime measurements (see Chap. 6 and [48]).
In order to model the SNR of an axial dip as depicted in Fig. 2.4, the equivalent circuit diagram from Fig. 2.3 (b) is re-examined. The resonator spectrum is amplified and

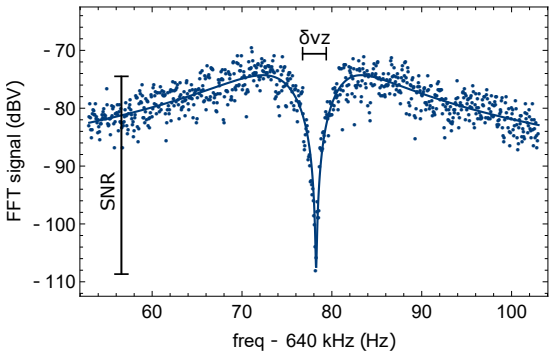

Figure 2.4.: Axial spectrum of a single trapped hydride ion. The particle shorts the thermal resonator voltage noise on resonance as described in the equivalent circuit diagram in Fig. 2.3 (b). The full width at half maximum of the axial dip is denoted $\delta\nu_z$, the SNR is given as the ratio of the resonator noise and the amplifier noise.

impedance-matched by means of an ultra-low noise cryogenic amplifier, and the voltage spectrum is read out by means of an FFT analyzer. The resonator Johnson noise u_{res} at temperature T and a spectral width $\Delta\nu$ is given by

$$u_{\mathrm{res}} = \sqrt{4k_B T R_p \Delta\nu}. \tag{2.35}$$

The equivalent input noise of the amplifier u_{in} is added quadratically. In addition, the coupling factor κ (as for instance introduced in [76]) has to be considered. As the particle only shorts the resonator, but not the amplifier noise, the minimum of the recorded voltage spectrum is given by u_{in}. The SNR is then given by

$$\mathrm{SNR} = \frac{\sqrt{(u_{\mathrm{res}}\kappa)^2 + u_{\mathrm{in}}^2}}{u_{\mathrm{in}}}. \tag{2.36}$$

2.3.2. Active electronic feedback

The effective detector temperature and thus also the particle temperature can be controlled by applying axial feedback [77, 78]. To this end, the detector signal is sent through a voltage controlled attenuator and an adjustable phase shifter, and afterwards coupled back into the trap (see Fig. 2.5 (a)). A single sideband down converter (SSB) is used in order to measure the axial frequency by means of an audio analyzer (*Stanford Research*

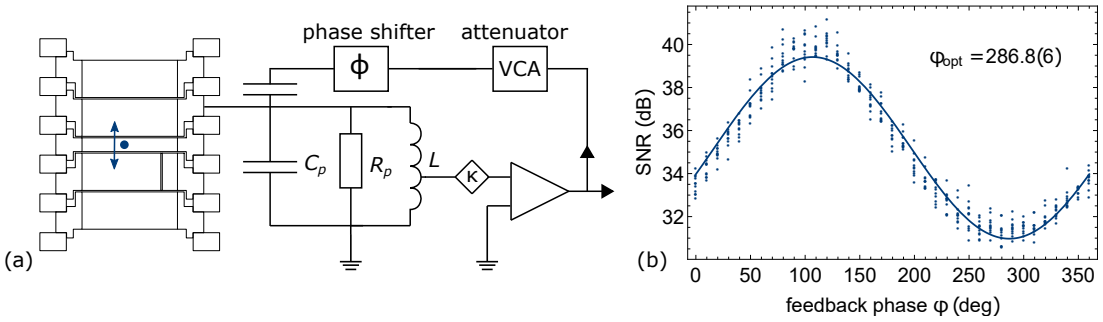

Figure 2.5.: Axial feedback system. Left: Schematic illustration. The detector signal is attenuated by means of voltage controlled attenuator, phase shifted, and fed back to the pick-up electrode. Right: Depending on the feedback gain G_{FB}, the effective detector resistance $R_{\mathrm{p,FB}}$ and thus the SNR and the dip width are modified. The feedback gain is controlled by the feedback phase ϕ. ϕ_{opt} denotes the feedback phase for the strongest negative feedback gain.

SR780). Depending on the phase shift applied, either negative or positive feedback is observed, as depicted in Fig. 2.5 (b). The feedback strength is adjusted by a voltage controlled attenuator. Application of the feedback changes the detector temperature T_z:

$$T_{z,\mathrm{FB}} = T_{z,0}\,(1 \pm G_{\mathrm{FB}}) \qquad R_{\mathrm{p,FB}} = R_p\,(1 \pm G_{\mathrm{FB}})\,. \tag{2.37}$$

As the effective detector resistance is a function of the feedback gain G_{FB}, the axial dip width $\delta\nu_z$ (Eq. 2.34), the axial dip SNR, and also the mean axial energy $\langle E_z \rangle$ change accordingly:

$$T_{z,\mathrm{eff}} = T_{z,0} \times \frac{\delta\nu_{z,\mathrm{FB}}}{\delta\nu_z} \qquad \langle E_z \rangle = k_B T_z. \tag{2.38}$$

Negative feedback is frequently used during the measurements performed by BASE, as a low particle amplitude is generally favorable, for instance when considering particle energy-dependent frequency shifts (Sec. 2.2.1). Eq. 2.38 starts to fail when strong negative axial feedback is applied, as noise on the feedback-loop is coupled back to the particle as well. Usually, it is possible to decrease the particle temperature by around a factor of six by the application of negative feedback.

2.4. Continuous Stern-Gerlach effect and magnetic bottle

For a particle with magnetic dipole moment, the spin precession in an applied external magnetic field $\vec{B}$ is described by the Larmor frequency ν_L. It is given by

$$\nu_L = \frac{1}{2\pi}\frac{g}{2}\frac{q}{m}|\vec{B}|. \tag{2.39}$$

The g-factor, which expresses the spin magnetic moment in units of the nuclear magneton, is given by twice the frequency ratio of cyclotron and Larmor frequency,

$$g = 2\frac{\nu_L}{\nu_c}. \tag{2.40}$$

This relation is used to determine the proton and antiproton magnetic moment at BASE. Unlike the cyclotron frequency ν_c, which can be calculated from the three trap eigenfrequencies (Eq. 2.8) that are measurable by means of image current detection, the Larmor frequency ν_L does not generate image currents and can thus not directly be measured by means of this method. Instead, the continuous Stern-Gerlach effect is utilized [79]. To this end, a so-called "magnetic bottle", which is a quadratic magnetic field inhomogeneity B_2, is deliberately implemented into the setup. The B_2-distortion couples the particle magnetic moment $\vec{\mu}$ to the axial motion and thus induces axial frequency shifts $\Delta\nu_z$ depending on $\vec{\mu}$ and thus also depending on the spin state. The Larmor frequency can now be measured by irradiating a radio-frequency drive with the drive frequency ν_{rf} being close to the Larmor frequency, and observing the spin transition probability as a function of drive frequency. From the resulting resonance spectrum, the Larmor frequency is determined [80, 37, 38, 28, 29].

The magnetic field in the presence of B_2 is given by

$$\vec{B}(\rho, z) = B_0\hat{e}_z + B_2\left(\left(z^2 - \rho^2/2\right)\hat{e}_z - \rho z\hat{e}_\rho\right). \tag{2.41}$$

The potential energy in the z-direction due to magnetic bottle is given by $E_B = -\left(\vec{\mu}\cdot\vec{B}(z)\right)$. The axial equation of motion is then given by

$$\ddot{z} = -\frac{q}{m}\frac{\partial\Phi_E(z,\rho)}{\partial z} - \frac{1}{m}\frac{\partial E_B(\rho,z)}{\partial z} = -\left(\frac{2qC_2V_r}{m} + \frac{2B_2\mu}{m}\right)z, \tag{2.42}$$

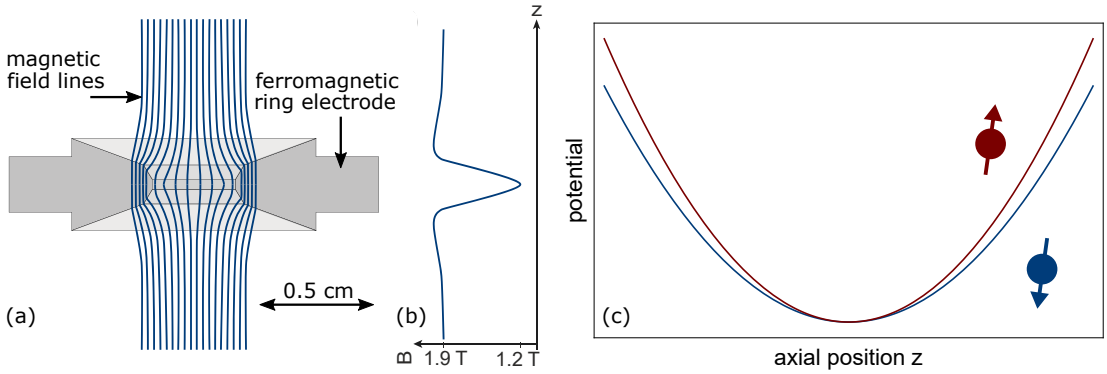

Figure 2.6.: Schematic of the magnetic bottle implemented in the BASE analysis trap. Left: Ferromagnetic ring electrode and corresponding magnetic field lines. Center: Axial magnetic field. Right: Axial potential. The magnetic inhomogeneity $B_2 = 271(15)\,\mathrm{kT/m^2}$ modifies the axial potential and thus the axial frequency depending on the spin state. The spin-state dependent axial frequency shift of $\Delta\nu_z = 172\,\mathrm{mHz}$ in the BASE analysis trap is used to resolve spin transitions and to record a resonance curve of the Larmor frequency during magnetic moment measurements. Figure adapted from [43].

with the electrical potential $\Phi_E(z,\rho)$ (Sec. 2.1). Consequently, the axial frequency ν_z is modified:

$$\nu_z = \nu_{z,0} \times \sqrt{1 + \frac{2\mu B_2}{4\pi^2 m_{\bar{p}} \nu_{z,0}^2}} \approx \nu_{z,0} + \frac{\mu B_2}{4\pi^2 m_{\bar{p}} \nu_{z,0}}, \tag{2.43}$$

with $\nu_{z,0}$ being the electrostatic axial frequency if no magnetic inhomogeneity B_2 were present. The magnetic moment $\vec{\mu}$ is given by the spin magnetic moment $\vec{\mu}_S$, and the magnetic moments $\vec{\mu}_+$, $\vec{\mu}_-$ arising from the radial motion:

$$\vec{\mu} = \vec{\mu}_S + \vec{\mu}_+ + \vec{\mu}_-. \tag{2.44}$$

The shift $\Delta\nu_z = \nu_z - \nu_{z,0}$ in Eq. 2.43 can be expressed in terms of the respective quantum numbers:

$$\Delta\nu_z \approx \frac{h\nu_+}{4\pi^2 m_{\bar{p}} \nu_{z,0}} \frac{B_2}{B_0} \left(\left(n_+ + \frac{1}{2} \right) + \frac{\nu_-}{\nu_+} \left(n_- + \frac{1}{2} \right) + \frac{g m_s}{2} \right), \tag{2.45}$$

with spin state quantum number $m_S = \pm\, 1/2$.

The continuous Stern-Gerlach effect has been applied to compare the electron/positron magnetic moments with high precision in 1987 [26], which constitutes one of the most stringent CPT tests in the leptonic sector until today. In 2011, the continuous Stern-Gerlach effect was firstly applied in order to resolve spin transitions of a single trapped

proton [80]. Subsequently, the ATRAP and the BASE collaboration performed measurements on the proton and antiproton magnetic moment [81, 82, 40, 37, 38, 28, 29]. The application of this method to protons/antiprotons is especially challenging as $\mu_{\bar{p}}/m_{\bar{p}}$ is a factor of approximately 10^{-6} smaller for protons compared to electrons. The most precise measurement of the antiproton magnetic moment [28] by means of the continuous Stern-Gerlach effect is described in Chap. 4. The magnetic bottle has also been used by the author for the first dedicated heating rate measurement in a cryogenic Penning trap [51], which is described in Chap. 5.

2.5. Modecoupling and sideband technique

The cyclotron and magnetron frequency can be measured by employing the so-called "sideband technique" [54]. To this end, the respective radial motion is coupled to the axial motion by applying a quadrupolar radio-frequency drive $\vec{E}_{\mathrm{rf}}(t)$ at the difference frequency $\omega_{\mathrm{rf}} = \pm\omega_{\pm} \mp \omega_z$,

$$\vec{E}_{\mathrm{rf}}(t) = \mathrm{Re}\left(\mathcal{E}_{\mathrm{rf}} \exp\left(i\omega_{\mathrm{rf}} t\right)\right)\left(x\vec{e}_z + z\vec{e}_x\right), \tag{2.46}$$

with the electric field amplitude $\mathcal{E}_{\mathrm{rf}}$. As discussed in Sec. 9.2.1 or in [83, 54], the sideband transfers energy between both modes at an energy exchange rate Ω/π, with the Rabi frequency Ω given by

$$\Omega = \frac{q\mathcal{E}_{\mathrm{rf}}}{2m\sqrt{\omega_{\pm}\omega_z}}. \tag{2.47}$$

In the Fourier transformed axial detector spectrum, instead of the single axial dip, a double dip can be seen as long as the coupling is applied (see Fig. 2.7). For a small detuning δ, $\delta = \omega_{\mathrm{rf}} \pm \omega_z \mp \omega_{\pm}$, the two frequencies of the double dip, ω_l and ω_r are given by

$$\omega_l = \omega_z \mp \frac{\delta}{2} - \frac{\Omega'}{2} \qquad \omega_r = \omega_z \mp \frac{\delta}{2} + \frac{\Omega'}{2}, \tag{2.48}$$

with the modified Rabi frequency Ω'

$$\Omega' = \sqrt{\Omega^2 + \delta^2}. \tag{2.49}$$

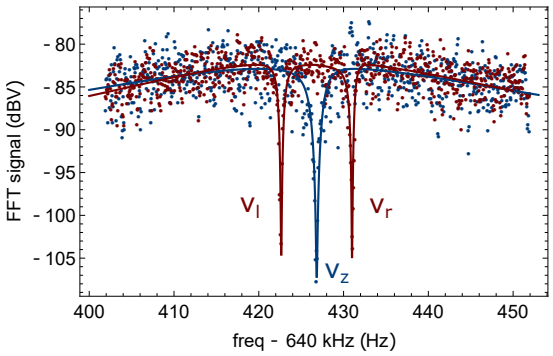

Figure 2.7.: Axial (blue) and double dip (red) spectrum of a single trapped antiproton.

Based on Eq. 2.48, the independently measured axial frequency ν_z and the known drive frequency, the cyclotron or magnetron frequency can be determined by

$$\omega_{\pm} = \omega_{\mathrm{rf}} \pm \omega_l \pm \omega_r \mp \omega_z. \tag{2.50}$$

Another important aspect lies in the energy exchange between both modes: During coupling, the axial mode is in thermal equilibrium with the axial detection system and continuously thermalizes while it also exchanges energy with the coupled radial mode. As a result, also the energy of the coupled motion is thermalized through the axial detector, and the relation

$$\langle E_{\pm} \rangle = \frac{\omega_{\pm}}{\omega_z} k_B T_z \tag{2.51}$$

is yielded for the mean energies. This process is referred to as "sideband cooling" throughout this thesis, and should not be mixed up with the "resolved sideband cooling" scheme known from laser cooling in ion traps. Aspects of sideband measurements are also discussed in Sec. 8.1. Mode coupling is discussed and derived in Sec. 9.2.

3 | Experimental apparatus

The BASE experiment is located in CERNs unique Antiproton Decelerator (AD) facility [32]. The AD is an oval-shaped storage and deceleration ring with a circumference of about 190 m. Currently, experiments of five collaborations (AEGIS, ALPHA, ASACUSA, BASE, GBAR) are located inside the decelerator ring, all equipped with dedicated transfer lines. The AD and the AD infrastructure are described in [32] in detail. After each antiproton deceleration cycle, which lasts about 120 s, a bunch of about 30×10^6 antiprotons is provided to the experiment that is on shift.
The BASE apparatus is described in detail in a dedicated publication [43]. It features a sophisticated Penning trap system, which consists of a superconducting high-precision magnet from Oxford instruments with a horizontal bore. In the homogeneous center of the magnet, the cylindrical trap electrodes are located, which are in orthogonal, compensated design [71]. The experiment is operated at temperatures of around 4 K enabled by two liquid helium and liquid nitrogen bath cryostats. Antiproton catching, the BASE beamline steering, and the related experimental setups and routines are described in detail for instance in [43]. BASE currently uses a four trap system consisting of the reservoir trap (RT), the precision trap (PT), the analysis trap (AT), and the cooling trap (CT). The reservoir trap is used for particle trapping and cleaning. Here, we will assume that a cold and clean reservoir of antiprotons[1] and hydride ions has been prepared inside the reservoir trap. Single ions can be extracted from the RT into the other traps by means of a potential tweezer scheme [49], as further discussed in Chap. 6. The apparatus is also described in the PhD theses of Hiroki Nagahama [84] and Takashi Higuchi [53] in detail. Additional upgrades will be described in the PhD thesis of James Brydges-Harrington, which is currently under preparation [52]. Therefore, this chapter

[1] Or of antiprotons and hydride ions, depending on the run.

will focus on recently implemented apparatus improvements to which the author contributed substantially during the course of his PhD work. The specific trap setups for each experimental campaign are individually described in the respective chapters, see Chap. 4, Sec. 5.1, Sec. 8.4 and Sec. 9.3.

3.1. Cryomechanical setup

The cryomechanical setup of the BASE apparatus is schematically depicted in Fig. 3.1. The core experiment consists of the trap can, the beam monitor (bm) and the electronics segment (es). It is located inside the horizontal bore of a superconducting magnet with an inner diameter of 150 mm. Two bath cryostats are located upstream and downstream of the experiment. With nitrogen volumes of 35 l each and helium volumes of 35 l each, the cryostats enable nitrogen standing times of more than 48 h, and helium standing times between 30 h and 135 h, depending on the run (Tab. 3.1). The different helium standing times will be discussed in detail in Sec. 3.3. An aluminum heat shield with an inner diameter of 127 mm and 3 mm wall thickness is locacted inside the magnet bore to reduce the radiative heat load onto the 4 K stage. The shield is thermally connected to the nitrogen stage of the cryostat by copper braids. It is mechanically mounted to the apparatus by means of two G10 disks that connect the heat shield to the vacuum chambers on both sides of the magnet. The G10 disks feature a labyrinth-like structure in order to increase the thermal path and thereby reducing the thermal flux. The 4 K stage of the experiment is thermally connected to the helium stage of both cryostats by means of two 16 mm diameter annealed copper rods. Until 2018, the 4 K stage was mechanically mounted to the 4 K finger of the helium cryostat. In 2018, a kelvar fiber structure was introduced that mounts the 4 K stage to the 77 K heat shield. This apparatus revision lead to significant improvement in apparatus performance, as will be discussed in Sec. 3.2.1. The kevlar structure is connected to cylindrical titanium elements (depicted in Fig. 3.3) that hold the experiment core. The experiment core consists of several cylindrical elements that contain the electronics segment, the beam monitor and most importantly the trap can. In the electronics segment, most of the image current detectors [76] are located, only the PT cyclotron detector is located inside the trap can since 2018 in order to reduce parasitic noise pick-up [52]. Also, the first filter stage is located inside the electronics segment [84]. The trap can is an indium-sealed dedicated vacuum chamber with a length of 234 mm and an inner diameter of 74 mm. Prior to

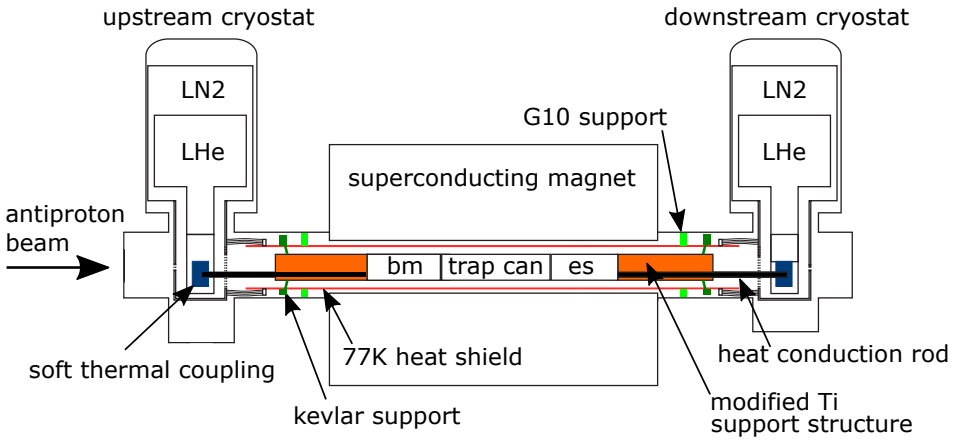

Figure 3.1.: Overview of the BASE setup. The main experiment is located inside the horizontal bore of a superconducting magnet. Two bath cryostats are located upstream and downstream of the magnet. The liquid nitrogen stages (LN2) of both cryostats are thermally connected to the 77 K heat shield located inside the magnet (red) by coupling braids. The 77 K heat shield is mounted to the vacuum chambers by means of two labyrinth G10-structures (light green). The 4 K stage of the experiment is mounted to the 77 K stage by means of two kevlar structures (dark green, see also Fig. 3.3). The kevlar structures are connected to titanium segments (orange). The 4 K stage is thermally connected to the liquid helium stage (LHe) of the cryostats by means of two heat-conduction rods made from annealed copper (black). These are thermally attached to the cryostats in a vibration-suppressing way by means of coupling braids (blue). The 4 K stage contains the beam monitor segment (bm), which is used for beam steering [43], the electronics segment (es) compromising the image current detection systems and cryogenic filters [84], and the indium-sealed trap in which the multi-Penning trap electrode system is located. The experiment side from which antiprotons are loaded is called "upstream" and shown on the left of this figure. This figure is adapted from [43]. In this drawing, the upgrades made during summer 2018 are already depicted, which will be discussed in detail in Sec. 3.2.

the experiment assembly, the trap can is pumped to pressures of order 10^{-7} mbar, and pinched-off afterwards [43]. In this way, residual background pressures below the level of 10^{-18} mbar are achieved after the experiment is pumped and cooled down to 4 K [48]. Inside the trap can, a stack of cylindrical gold-plated OFHC electrodes separated by sapphire spacers is placed, which realize the multi-Penning trap system shown in Fig. 4.1 and which is described for instance in Chap. 4.

3.2. Apparatus upgrades

We observed a strong scaling of the measured cyclotron frequency scatter as a function of time passed after the last filling of cryoliquids (see Fig. 3.2 (a)). When evaluating the pressure on the liquid helium recovery line connected to the experiment cryostat, a characteristic scaling of pressure fluctuations over time is observed (see Fig. 3.2 (b)). The pressure fluctuations are strongly increased shortly after filling and then relax over time, which is the same pattern as seen in the frequency fluctuation scaling over time. We interpret this being a result of the boiling liquid helium that generates pressure fluctuations, which are stronger if the cryostat gas volume is smaller. These pressure fluctuations likely induced vibrations that were directly translated onto the experimental 4 K stage as the 4 K stage was mounted directly onto the cryostat. Consequently, the support of the 4 K stage was revised in order to decouple the experiment from cryostat vibrations, and in addition much care was taken in reducing the heat load on the 4 K stage to reduce the evaporation rate. The apparatus revisions and upgrades discussed in the section were mostly developed and implemented in collaborative efforts of Stefan Ulmer and the author. After implementation of the discussed upgrades, no scaling in cyclotron frequency scatter over time was observed anymore.

3.2.1. Revisions on the cryogenic stage

The most important revision was the newly constructed kevlar support structure in order to mechanically mount the 4 K-stage to the vacuum chambers, which are mounted to the magnet. The revised cryo-mechanical setup incorporating the kevlar structure is schematically depicted in Fig. 3.1. Pictures of the kevlar structure are shown in Fig. 3.3. Three threaded rods are connected to each end of the cryogenic stage. These rods are connected to the 77 K heat shield by means of kevlar slings. Each sling is guided through the axial hole of a brass screw located on the outside of the heat shield. The slings are tensioned by pushing the screws outwards.
New titanium segments with reduced diameter and shorter length were constructed (right picture in Fig. 3.3). Three threaded rods are connected to the titanium support structure. We then used kevlar slings wound around a single rod each to mount the support structure inside the 77 K shield (left and central picture in Fig. 3.3). Tension in the kevlar structure was generated by drilling a hole along the screw axis into brass

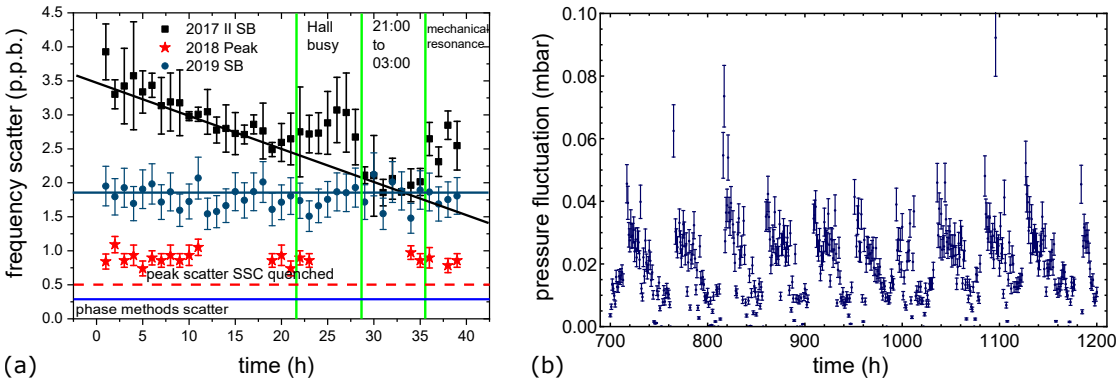

Figure 3.2.: Cyclotron frequency scatter for different experimental campaigns, and cryostat pressure fluctuation as a function of time. Left: The cyclotron frequency scatter measured in the 2017 sideband run (black), in 2018 peak run (red), and in the 2019 sideband run (blue). For comparison, the cyclotron frequency scatter during the first q/m measurement of the BASE collaboration in 2014 [39] was 5.6(2) p.p.b. In 2017, we observed a strong scaling of cyclotron frequency scatter as a function of the cryostat filling level/the time since the latest filling of cryoliquids. This was interpreted as being correlated to pressure fluctuations in the liquid helium vessels (right plot), which are strongly increased shortly after each filling cycle and subsequently relax, as is repeatedly observed during many filling cycles. These pressure fluctuation induced vibrations translated directly onto the experiment 4 K stage in the old setup. After the modifications described in Sec. 3.2.1, we did not observe a frequency scaling as a function of cryoliquid level any more. During the peak run (see Sec. 7.2.3) and the phase methods run (see Sec. 9.8.3), we observed shot-to-shot scatter values of around 800 p.p.t. (peak run, active self shielding coil system (SSC)), 500 p.p.t. (peak run, quenched SSCs), and 280(20) p.p.t. (phase run, quenched SSCs). The direct methods of measuring the cyclotron frequency are not limited by axial fit scatter unlike the sideband method and are therefor able to achieve much lower scatter values. However, under the experimental conditions of the 2017 sideband campaign, the quoted peak and phase scatter values are not achievable.

screws, guiding the fiber through the hole, and moving the screw away from the 77 K heat shield by means of nuts (left and central picture in Fig. 3.3). The 77 K shield is anchored against the vacuum chambers by means of the G10 structure schematically depicted in Fig. 3.1. Consequently, also the 4 K stage is mechanically anchored against the vacuum chambers, that are not exposed to cryostat vibrations. In order to decouple the 4 K stage from vibrations translated via the thermal coupling braids, we replaced the original stiff copper braids with much more flexible braids, which connect the heat conduction rod with the cryostat 4 K stage (see Fig. 3.1). A benefit of using kevlar fiber is the very low heat conductivity and the small related heat input onto the 4 K stage. In addition, the thermal expansion of kevlar is low, which is of benefit for the tension in

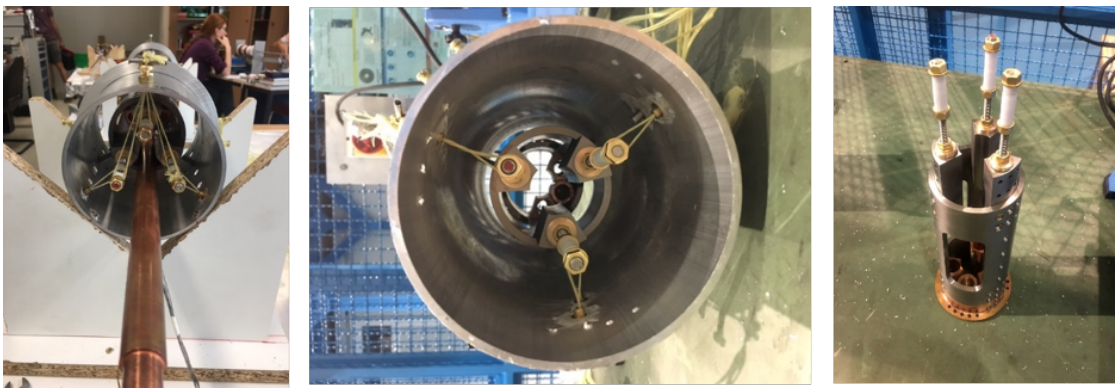

Figure 3.3.: Photographies of the novel kevlar support structure mounting the 4 K stage onto the 77 K heat shield. The newly designed titanium segments (right) at reduced diameter are held by kevlar strings (center and left). The kevlar strings are tensioned by pushing the brass screws outwards by adjusting the respective nuts (left).

the kevlar strings once cooled down to cryogenic temperatures.
We also revised the experiment in order to minimize the heat load. To this end, we closed any window from the 4 K stage to the 300 K stage by implementing additional small heat shields, and by constructing new filter boards at 77 K, where the input and output of the filters lay on opposite sides of the board, such that the filter boards itself act as heat shields. A slight improvement in heat load was gained by reducing the surface of the titanium support structure by decreasing the outer diameter from 940 mm to 820 mm in the new construction (Fig. 3.3). In the 2019 II run, we also closed the beam port window in the 77 K shield through which the antiprotons are injected into the apparatus, as the AD was in its long shutdown 2 (LS2), and measurements were exclusively performed with protons. The beam port closure reduced the heat load on the 4 K stage from 340 mW to 210 mW, while the other developed modifications decreased the heat load from 740 mW to 340 mW.

3.2.2. Experimental frame

The AD hall features an air conditioning system that manages to keep the hall temperature stable to about 1 K to 2 K peak-to-peak during the course of a day. Especially during times of the year when a strong temperature gradient between day time and night time is observed (spring and autumn), we observed strong temperature drifts in the experiment zone. In addition, temperature oscillations due to overshoots of the air

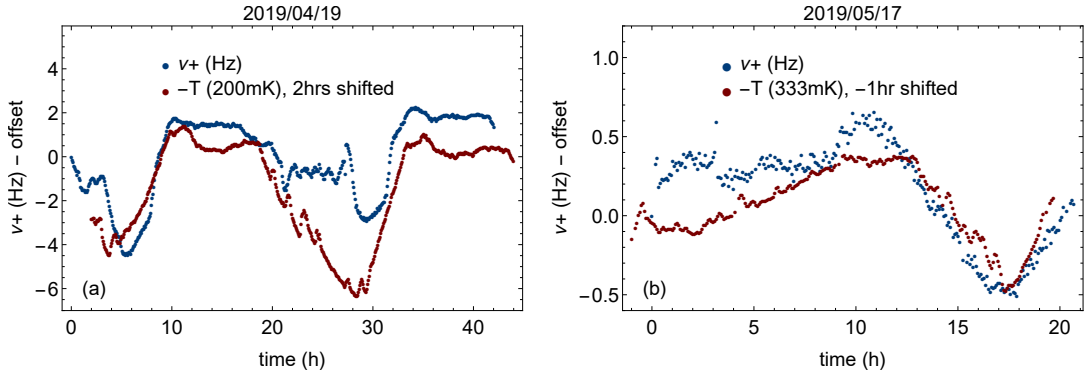

Figure 3.4.: Comparing the long-term cyclotron stability before and after the installation of passive thermal shielding of the experimental zone, which is denoted as "experimental frame". The cyclotron frequency is plotted in blue, the zone temperature is multiplied by -1 and an additional factor specified in the respective legends. An offset was added to the temperature data, and the temperature data were shifted in time (see legends) in order to match the cyclotron frequency pattern. A clear correlation between cyclotron frequency and temperature is observed prior and after the frame installation. The frame clearly smooths ambient changes. The peak-to-peak temperature fluctuation is decreased from 1.5 K to about 300 mK, in cyclotron peak-to-peak fluctuation we observe a similar decrease from 6.8 Hz to 1.2 Hz across the course of 24 hours.

conditioning control system are observed. As we observed clear correlations between changes in ambient temperature and long-term cyclotron frequency drifts, we implemented a thermal shielding of the entire experiment, which is herein referred to as "frame". In addition to suppressing temperature changes, the micro-climate generated by the experimental frame also smoothened external temperature changes experienced by the experiment. Note that no active stabilization has been implemented at BASE yet, but the existence of the experimental frame generally allows to do so. The BASE experimental zone top was covered by of a robust plastic tent already during the PhD work of James Harrington-Brydges [52]. In 2019, we then constructed a dedicated frame out of ITEM profiles inside the experimental zone, which also featured a platform for the LHe cryostat. Standard insulation plates made of polystyrene with a thickness about 40 mm purchased at a hardware store nearby were attached to the ITEM profiles. After the frame was implemented, we observed a significant decrease in cyclotron frequency peak-to-peak scatter and zone temperature over 24 hours as illustrated in Fig. 3.4.

3.3. Performance improvements

The revisions on the 4 K and the 77 K stage of the experiment resulted in significant improvements of the heat load on the 4 K stage, and in much higher cyclotron frequency stabilities. The results on the heat load are summarized in Tab. 3.1. After the major revision in 2018 outlined in Sec. 3.2.1,we observed a standing time of about 100 h, corresponding to a heat load of 500 mW on the 4 K stage, compared to 56 h and 900 mW in the setup used between 2015 and 2018. From independent measurements, the cryostats are known to consume about 80 mW each. The cryogenic amplifiers used in the image current detection systems consume in total about 40 mW, the experiment wiring is expected to contribute about 15 mW, which gives a residual heat load of 685 mW in 2018 and 285 mW in the 2019 I run. The experiment was warmed up during the summer 2019, and the beam port hole in the 77 K heat shield was closed. In the subsequent run, the residual heat load decreased to 155 mW, which emphases the importance of closing all windows between the 4 K stage and the 300 K stage. The residual heat load is attributed to thermal radiation. From the surface of the 4 K stage and the Stefan-Boltzmann law, an impact of 2.95 W would be expected if the surface emittance were $\varepsilon = 1$. Consequently, an emittance ε of about $\varepsilon = 0.05$ is obtained, which is within the range of emissivity values typically observed for multilayer insulation. After each cryoliquid filling, the experiment needs to re-thermalize for several hours, during which no meaningful measurements can be conducted. Therefore, an increased standing time allows for less frequent filling and therefore more data sampling.

Compared to the 2017/2018 run, the LHe standing time is increased by a factor of more than two. Compared to the first experimental run of BASE in 2014, the standing time is even increased by a factor of more than four. This 2014 run was conducted with the first experimental setup of BASE, featuring for instance a significantly longer magnet (1150 mm compared to 998.5 mm). The temperature of the 4 K stage in 2019 decreased significantly compared to the 2018 state prior to the experimental revision by about 700 mK, which is line with the linear relation between heat load and experiment temperature, $\mathrm{d}T_{4\mathrm{K}}/\mathrm{d}P_{\mathrm{HL}} = 1.38\,\mathrm{K/W}$, as obtained from Tab. 3.1.
Re-examining Fig. 3.2 (a), we note that the time dependency of the cyclotron frequency scatter is not present in the 2018 peak run (Sec. 7.2 and especially Sec. 7.2.3) and the 2019 sideband run (Chap. 8) anymore, compared to the 2017 sideband run. The 2019 sideband scatter is now constantly given by the minimum value of sideband scatter that

measured quantity	2014	2015/2018	2019 I	2019 II
standing time	30 h	56 h	100 h	135 h
power consumption	1680 mW	900 mW	500 mW	370 mW
cryo background (mW)	160 mW	160 mW	160 mW	160 mW
heat load on the 4 K stage	1520 mW	740 mW	340 mW	210 mW
radiation heat load	1465 mW	685 mW	285 mW	155 mW
experiment temperature	6.5 K	5.5 K	4.9 K	4.8 K

Table 3.1.: Cryogenic performance of different experimental campaigns. The 2014 and the 2015 data differ as the setup was revised by for instance implementing a shorter superconducting magnet. Between 2018 and 2019, the upgrades described in Sec. 3.2 were performed. These upgrades decreased the heat load on the 4 K stage by about 400 mW. Between the 2019 I run and the 2019 II run, the beam port hole in the 77 K heat shield was closed, which lead to an additional decrease in heat load of 130 mW. The cryo background specifies the power consumption of each cryostat without heat load, which was measured independently and is of order 80 mW per cryostat. The cryogenic amplifiers of the image current detection circuits contribute about 40 mW of heat load, the heat load of the experiment wiring is assumed to be around 15 mW. The remaining heat load is attributed to thermal radiation. The temperature of the 4 K stage decreased in accordance with the reduced heat load.

could be achieved in 2017. When examining the axial frequency scatter as done in Sec. 8.6, it can be shown that the sideband method in 2019 was entirely limited due to axial frequency scatter.

The direct methods of measuring the cyclotron frequency such as peak and phase methods are not limited by the axial frequency resolution, and thus enable significantly better frequency scatter values. During the peak methods run (Sec. 7.2), we obtain a cyclotron frequency scatter of around 800 p.p.t. for active self shielding coils (SSCs) [85], and around 500 p.p.t. for quenched SSCs (the effect of the SSC status onto the cyclotron frequency is discussed in Sec. 7.2.3 and Sec. 9.8.2 in detail). During the phase methods run in 2019 (Chap. 9), we even achieved a shot-to-shot frequency scatter of 280(20) p.p.t. (Sec. 9.8.3) at a longer measurement time of $t_{\mathrm{cyc}} = 265\,\mathrm{s}$.

It cannot be stressed enough that these significant improvements in frequency scatter by about a factor of 6 (if the longer cycle time is considered) could have not been achieved under the experimental conditions from 2017, as the frequency scatter was limited by the apparatus performance in 2017. Both, the improved short-term stability through the vibration-decoupling of the 4 K stage, and the improved long-term stability, which was facilitated by the experimental frame, enabled together the substantial progress made

during the implementation of phase methods, which is described in Chap. 9.

4 | Most precise measurement of the antiproton magnetic moment

In 2014, BASE conducted its first beamtime, during which the antiproton charge-to-mass ratio was measured with an unprecedented precision of 69 parts per trillion, constituting the most stringent test of CPT invariance in the baryonic sector at that time [39]. In the second operational beamtime in 2015, BASE performed spin state analysis for the first time using the analysis trap. Due to the excellent experimental progress, the experimental campaign was extended until December 21st 2016. During this campaign, several milestone measurements were conducted, such as the first measurement of the antiproton magnetic moment performed by the BASE collaboration with a fractional uncertainty of 0.8 p.p.b. [38], the first non-destructive resolution of individual antiproton spin transitions [47], the direct measurement of the antiproton lifetime [48], and the to-date most precise measurement of the antiproton magnetic moment with a fractional uncertainty of 1.5 p.p.b. [28], which improved the previous measurement by a factor of more than 300 in uncertainty [38]. Later on carried out analyses of this dataset also yielded the lowest heating rates ever measured in an ion trap [51] (see Chapter 5), and the first constraints on the interaction of antiprotons with axion-like dark matter [50]. Apart from [51], the author's contribution to the above mentioned achievements was of collaborative nature, as a member of the team maintaining the apparatus. Therefore, these research results shall only be briefly discussed here, but will not be part of the main focus of this thesis.

Essential parts of the experimental setup used during the 2015/2016 run are depicted

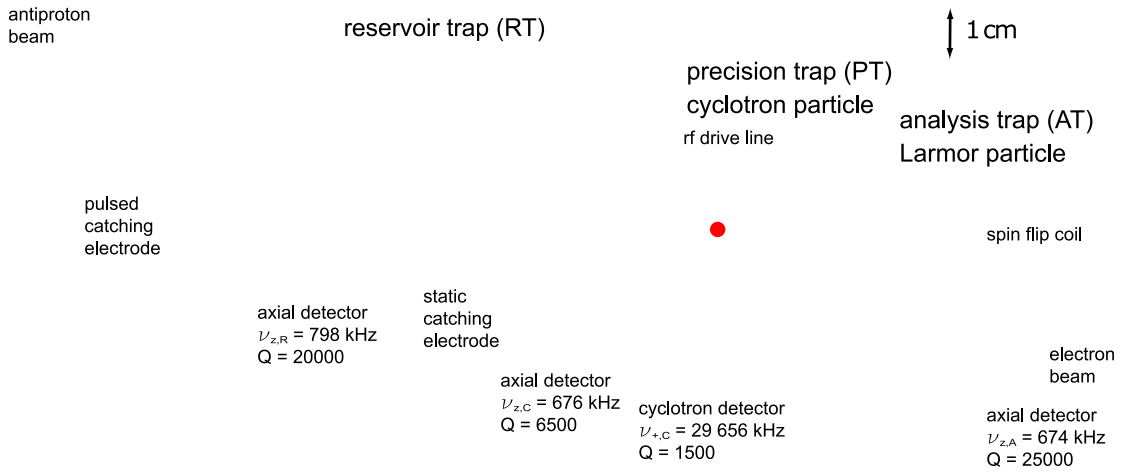

Figure 4.1.: Experimental setup used in the 2015/2016 measurement campaign. The Penning traps are mounted inside the horizontal bore of a superconducting magnet (not shown) at a magnetic field of $B_0 = 1.945\,\mathrm{T}$. The trap stack consists of gold plated OFHC electrodes (golden) separated by sapphire spacers (white). Antiprotons are injected into the trap stack coming from the Antiproton Decelerator [32] after having passed a degrader (not depicted) [43]. Electron cooling [86] is facilitated by means of an electron gun located downstream (not depicted). A clean cloud of cold antiprotons is prepared following the procedures explained in [43, 84, 33, 87, 86]. Single antiprotons are subsequently extracted from the reservoir trap (RT) [49] and individually shuttled to the precision trap (PT) and the analysis trap (AT). For the measurement of the antiproton magnetic moment $g_{\bar{p}}$ [28], one antiproton (red) is used for the cyclotron frequency determination, and a second antiproton (blue) is used for measuring the Larmor frequency. The analysis trap is equipped with a magnetic inhomogeneity $B_2 \approx 272(12)\,\mathrm{kTm}^{-2}$, often referred to as "magnetic bottle". The magnetic bottle allows to apply the continuous Stern-Gerlach effect to conduct spin state analysis [79, 80, 47]. All traps are connected to highly sensitive axial detection systems [76] used for multiple purposes, such as reservoir monitoring (RT), measurements of mode frequencies (PT, AT), and mode thermalization (all traps). All traps are equipped with radio frequency lines used for particle manipulation (not shown for the RT). Figure is taken from [38].

in Fig. 4.1. In total, three Penning traps were operated (reservoir trap, precision trap, analysis trap). All traps are equipped with superconducting detection systems used for measuring the axial motion [76]. In the precision trap, also a cyclotron detector is located [88]. The reservoir trap [49] is used for storage of a cold and clean reservoir of antiprotons that is continuously monitored. During the 2015/2016 experimental campaign, the reservoir was stored for in total 405 days (see section 6.3 and Fig. 6.1). The precision trap is used for particle manipulation and frequency measurements. In the analysis trap, a magnetic bottle $B_2 = 272(12)\,\mathrm{kTm}^{-2}$ is superimposed, which enables spin-state determination via application of the continuous Stern-Gerlach effect [79].
The Landé $g_{\bar{p}}$-factor for the antiproton expresses the antiproton magnetic moment in units of the nuclear magneton μ_N and can be expressed as the ratio of cyclotron frequency ω_c and Larmor frequency ω_L,

$$\frac{g_{\bar{p}}}{2} = \frac{\omega_L}{\omega_c} = -\frac{\mu_{\bar{p}}}{\mu_N}. \tag{4.1}$$

The cyclotron frequency is related to the three eigenfrequencies of a charged particle confined in a Penning trap following the Brown-Gabrielse invariance theorem [69], $\omega_c^2 = \omega_+^2 + \omega_z^2 + \omega_-^2$. It is obtained by measuring the three mode eigenfrequencies, which is routinely done in Penning trap experiments since many years. The experimental challenge for directly measuring $g_{\bar{p}}$ lies within the determination of ω_L. To this end, BASE employs the continuous Stern-Gerlach effect [79], which couples the particle magnetic moment to the axial motion ω_z and thus induces a frequency shift $\Delta\nu_z$ depending on the magnetic moment (see Fig. 4.3 (b))

$$\Delta\nu_z = |\vec{\mu}_+ + \vec{\mu}_- + \vec{\mu}_S| \times \frac{B_2}{4\pi^2 m_{\bar{p}} \nu_z}, \tag{4.2}$$

which is in case of a spin transition given by

$$\Delta\nu_{z,\mathrm{SF}} = \frac{\hbar\omega_L}{4\pi^2 m_{\bar{p}} \nu_z} \frac{B_2}{B_0} = 172(8)\,\mathrm{mHz}. \tag{4.3}$$

The Larmor frequency ω_L is then measured by irradiating an oscillating magnetic field at varying frequencies ω_{rf} via a spin-flip coil placed close to the trap electrodes and recording a resonance spectrum of the Larmor frequency, normalized by interleaved

cyclotron frequency measurements. The full expression of Eq. 4.2 reads

$$\Delta\nu_z = \frac{\hbar\omega_+}{2\pi m_{\bar{p}}\omega_z}\frac{B_2}{B_0}\left(\left(n_+ + \frac{1}{2}\right) + \frac{\omega_-}{\omega_z}\left(n_- + \frac{1}{2}\right) + \frac{g m_S}{2}\right), \tag{4.4}$$

as both radial modes are related to magnetic moments $\vec{\mu}_{+,-}$ that depend on their respective quantum numbers $n_{+,-}$. The related shifts are $\Delta\nu_{z,+} = 62(3)\,\mathrm{mHz}$ and $\Delta\nu_{z,-} = 40(2)\,\mu\mathrm{Hz}$. The radial modes are driven by electric field noise $S_E(\omega)$ present in the experimental apparatus, leading to nearly undirected random walks with transition rates $\zeta_{+,-}$ [51] (Eq. 5.12):

$$\zeta_{+,-} = n_{+,-} \times \frac{q^2}{2m\hbar\omega_{+,-}} S_E(\omega_{+,-}). \tag{4.5}$$

Note that the transition rates $\zeta_{+,-}$ are related to the overlap of the harmonic oscillator modes and thus scale proportional to the respective quantum numbers $n_{+,-}$. As the axial frequency shift corresponding to a change of three quanta in the cyclotron mode is already larger than the frequency shift caused by a spin transition, $3\Delta\nu_{z,+} > \Delta\nu_{z,\mathrm{SF}}$, spin transitions can only be resolved when the transition rates $\zeta_{+,-}$ are low. In order to obtain low transition rates, the electric field noise $S_E(\omega_{+,-})$ must be low and the particles need to be prepared with low radial quantum number $n_{+,-}$. The antiproton is prepared in such a state by means of subthermal cooling [89, 90]. A detailed analysis of the transition rates and the electric field noise $S_E(\omega_{+,-})$ in the BASE analysis trap is given in Chapter 5. For cooling of the magnetron motion, a radio-frequency drive $\omega_{\mathrm{rf}} = \omega_z - \omega_-$ is applied. The drive couples both modes and leads to an equipopulation of states, $n_z = n_-$, and thus a corresponding mode temperature $T_- = T_z \times \omega_-/\omega_z \approx 35\,\mathrm{mK}$. When the drive is turned off, the particle remains at a particular magnetron energy E_-, where the probability $p(E_-)$ for obtaining a particular energy E_- is given by a Boltzmann distribution, $p(E_-) \propto \exp\left(-E_-/\left(k_B T_-\right)\right)$. By recording $\Delta\nu_z$ for multiple cooling cycles, a threshold frequency ν_{tr} is determined, and a particle below the corresponding threshold energy $E_{-,\mathrm{tr}}/k_B = 0.7\,\mathrm{mK}$ is prepared. As applying the same technique to the cyclotron mode would heat it to $T_+ = T_z \times \omega_+/\omega_z \approx 360\,\mathrm{K}$, the cyclotron mode is instead thermalized by directly coupling the cyclotron motion to the cyclotron detector with an effective temperature of $T_+ \approx 12.8(8)\,\mathrm{K}$. The preparation of a cold particle with $E_+/k_B < 100\,\mathrm{mK}$ takes on average about ten hours employing this scheme.

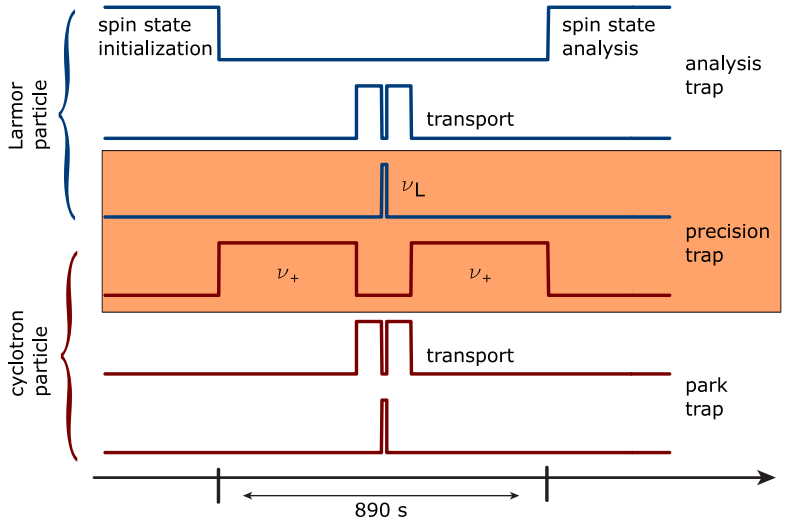

Figure 4.2.: Experimental procedure of the triple trap $g_{\bar{p}}$-factor measurement. The novel method uses a "cyclotron particle" for measuring the cyclotron frequency ω_c and a "Larmor particle" for obtaining ω_L. The spin state prior and after applying the spectroscopy drive is determined in the analysis trap, but all frequencies are measured in the precision trap. When one particle is brought to the precision trap for measuring either ω_c or ω_L, the other particle is transported to the analysis trap or an additional park trap. The sequence above takes about 900 s. Together with the spin state initialization (duration about 24 min), the full cycles takes on average about 40 min. Adapted from [28].

4.1. The triple trap scheme

When measuring the proton magnetic moment by means of the continuous Stern-Gerlach effect, two firstly counteracting objectives have to be considered: For measuring ω_L, a quadratic magnetic inhomogeneity B_2 is inevitably required. For measuring ω_c, a highly homogeneous magnetic field is desired as magnetic field inhomogeneities introduce mode-energy dependent frequency shifts. For the proton/antiproton magnetic moment, the attainable fractional uncertainty is limited to the ppm level when measuring ω_c in the presence of B_2 [38, 40, 81]. This principal limitation can be overcome by performing spin state analysis and frequency measurements in two separated traps, of which the "analysis trap" is equipped with a strong magnetic bottle B_2 for spin state detection, and the magnetically much more homogeneous "precision trap" is used for measuring ω_c

and ω_L.

The experimental cycle of our magnetic moment measurement is depicted in Fig. 4.2. In contrast to the commonly used "double trap technique" [91, 92], where a single particle is used both for the determination of ν_L and ν_c, our novel "triple trap method" or "two particle method" uses separate particles for the two frequency measurements [28]. This ingenious trick reduces the average experiment cycle duration from about 10 hours to about 40 minutes: When measuring the cyclotron frequency ω_+ by means of the sideband method [54], the cyclotron motion is thermalized to $T_+ = T_z \times \omega_+/\omega_z \approx 360\,\mathrm{K}$. If the same particle is used for measuring ω_+ and ω_L, its cyclotron motion has afterwards to be prepared at subthermal energies $E_+ < E_{+,\mathrm{tr}} = 100\,\mathrm{mK}$ at every experiment cycle in order to achieve spin state resolution. The average time needed for preparing a particle at such a low cyclotron energy is about 10 hours due to the comparable high effective temperature T_+ of our cyclotron detector, while the remaining measurement cycles consumes only about 40 minutes. With the "two particle method", the Larmor particle remains at subthermal energies for the full time while the cyclotron frequency is measured with the cyclotron particle, which results in an average cycle duration of about 40 minutes. Also compared to the recent proton measurement [29], where a cyclotron detector with a lower effective temperature T_+ and a higher threshold energy $E_{+,\mathrm{tr}}$ is used, the duration of one experiment cycle is about two times shorter.

At the beginning of each measurement cycle, the spin state of the Larmor particle is initialized in the analysis trap by inducing spin transitions and measuring differences in axial frequency, $\Delta_k = \nu_{z,k+1} - \nu_{z,k}$. Then, a threshold Δ_{TH} is defined. If $|\Delta_k| > \Delta_{\mathrm{TH}}$, a spin transition is assumed, and consequently the spin state is known from the sign of Δ_k. If a value for Δ_{TH} significantly larger than $\Delta\nu_{z,\mathrm{SF}}$ is chosen, the initialization error E_i for assuming a spin transition when no spin transition occurred, is low. On the contrary, many real spin transitions would be rejected, which leads to long preparation times. By assigning $\Delta_{\mathrm{TH}} = 190\,\mathrm{mHz}$, we achieve a fidelity of up to $1 - E_i > 99.9\%$ with an average preparation time of about 24 min [47].

After that, the Larmor particle is shuttled into the precision trap, where the spectroscopy drive is applied, and afterwards it is brought back to the analysis trap. Here, the spin state is determined again. If the final spin state $m_{s,f}$ is the same as the initial state $m_{s,i}$, $m_{s,f} = m_{s,i}$, no spin transition is observed and vice versa. In contrast to the initialization procedure, the final spin state cannot be determined by inducing multiple spin transitions and waiting until $\Delta_k > \Delta_{\mathrm{TH}}$ is met, as the information about $m_{s,f}$

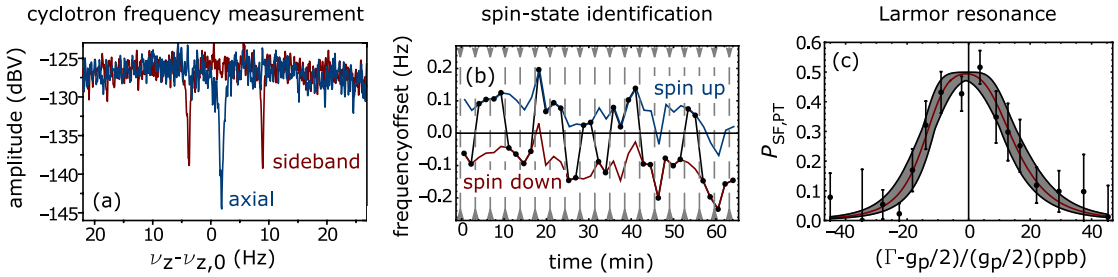

Figure 4.3.: Building blocks of the $g_{\bar{p}}$-measurement. Left: Cyclotron frequency measurement by means of the sideband method [54]. The axial (blue) and the sideband spectrum (red) are recorded successively. Center: Spin state identification sequence. The magnetic bottle induces an axial frequency shift depending on the spin state. After a spin state transition, a shift in axial frequency is observed and a spin state can be assigned. The usual initialization sequence takes about 24 min, but a longer sequence is depicted for illustrative purposes. Right: The final Larmor resonace normalized by the cyclotron frequency ω_c. Γ denotes the frequency ratio between the spectroscopy drive and the cyclotron frequency, $\omega_{\mathrm{rf}}/\omega_c$. Figure is adapted from [50].

would be lost in this way. Instead, a threshold $\Delta_{\mathrm{TH}} \approx 90 - 100\,\mathrm{mHz}$ is chosen, which identifies most of the real spin transitions without mistakenly assigning too many spin transitions. The error rate E_{TH} for identifying a wrong spin state is further reduced by inducing multiple spin transitions and considering the conditional probabilities [1]. In the $g_{\bar{p}}$-factor measurement, we obtained a fidelity $1 - E_{\mathrm{TH}}$ between 80 % and 90 % [28], while in the best cases, we even realized $1 - E_{\mathrm{TH}} = 94.2\,\%$ [47].

After the initial spin state $m_{s,i}$ is determined, the cyclotron frequency ν_c is measured with the cyclotron particle for in total three times by means of the "sideband method" [54]. To this end, the axial frequency ν_z is measured (Fig. 4.3 (a), blue). Afterwards, a coupling drive at $\omega_{\mathrm{rf}} \approx \omega_+ - \omega_z$ is applied and a double dip spectrum is obtained (Fig. 4.3 (a), red). The combined information of these two measurements yields ω_+ and ω_z and a sufficiently accurate estimation for ω_-, and thus ω_c following the invariance theorem [69]. The cyclotron particle is then shuttled into a park trap, and the Larmor particle is brought to the precision trap, where the Larmor spectroscopy drive is irradiated. Afterwards, both particles are brought back into their initial traps, and the cyclotron frequency is measured again for three times. This procedure allows to average over temporal drifts of the magnetic field, as the cyclotron frequency during the time of the

[1] E. g., if the spin flipped downwards in the first attempt, it cannot flip downwards again. Considering this, the rate of wrongly identified spin transitions is decreased, and thus the error rate is lowered. For a detailed description, see [47].

spectroscopy drive has to be obtained for determining the $g_{\bar{p}}$-factor.
The recorded $g_{\bar{p}}$-factor resonance is depicted in Fig. 4.3 (c). The fitted line shape is given by a convolution of the ideal line shape [83] with magnetic field fluctuations. We obtain

$$(g_{\bar{p}}/2)_{\mathrm{exp}} = 2.792\,847\,345\,3(30). \tag{4.6}$$

The linewidth of 13.3(1.0) p.p.b. is dominated by drive saturation (12.7(1.0) pbb), but also affected by magnetic field fluctuations (3.9(1) p.p.b.). While the two particle method profits from the higher sampling rate compared to a double trap measurement, the fact that two particles are used is a significant drawback, as the axial temperature of both particles during the spectroscopy drive is not necessarily identical. The dominant systematic uncertainty of 0.97 p.p.b. is given by this effect. The systematic corrections amount in total to $-0.4(1.0)$ p.p.b., which yields the final result:

$$g_{\bar{p}}/2 = 2.792\,847\,344\,1(42), \tag{4.7}$$

which gives an overall improvement of a factor of more than 300 compared to [38] and a factor of more than 3000 compared to [40] in uncertainty. The BASE sister experiment in Mainz [80] reported on measuring the proton g-factor g_p with an even smaller fractional uncertainty of 0.3 p.p.b. [29] shortly after the antiproton $g_{\bar{p}}$-factor was published[1]:

$$g_p/2 = 2.792\,847\,344\,62(82) \tag{4.8}$$

The combined result

$$(g_p - g_{\bar{p}})/2 = 5(74) \times 10^{-10} \tag{4.9}$$

is consistent with CPT invariance at a 95 % confidence level.

4.1.1. Limits on CPT-violating SME coefficients

The Standard Model Extension (SME) [93] is an effective field theory that discusses potential CPT-violating effects by introducing CPT-odd operators to the SM Lagrangian. The SME itself does not suggest certain CPT-violating mechanisms, but allows to derive limits on CPT-violating coefficients and to compare the sensitivity of different experi-

[1] To our knowledge, this was the first time that an antimatter quantity was known with lower fractional uncertainty than the corresponding matter counterpart

ments on antimatter for detecting possible CPT-odd phenomena [41]. The application of the SME to Penning trap based measurements is outlined in several dedicated publications, such as [94, 95].
Other collaboration located at the Antiproton Decelerator will place constraints on SME coefficients in the future. The ALPHA collaboration at CERN for instance performed the first measurement on the antihydrogen hyperfinestructur in 2017 [96]. Also at CERN, the ASACUSA collaboration is aiming for a high precision measurement on the antihydrogen hyperfinestructure that will allow to place limits on yet unconstrained SME coefficients [97, 41]. A significant improvement in measurement precision on the antihydrogen hyperfinestructur might in addition allow to improve upon the currently existing constrains on SME coefficients, depending on the measurement scheme [98].
The subsequent discussion of the SME constraints placed by the BASE collaboration follows the arguments presented in [95, 84, 75]. By applying Eq. (76) from [95], a difference between the proton and antiproton g-factors may arise by [38]

$$\left(\frac{g_p}{2}\right) - \left(\frac{g_{\bar{p}}}{2}\right) = \frac{2}{\omega_c^p \omega_c^{\bar{p}}} \left(\Sigma\omega_c^p \Delta\omega_a^p - \Delta\omega_c^p \Sigma\omega_a^p\right), \tag{4.10}$$

with

$$\begin{aligned} \Delta\omega_c^p &= \frac{1}{2}\left(\omega_c^p - \omega_c^{\bar{p}}\right) \\ \Sigma\omega_c^p &= \frac{1}{2}\left(\omega_c^p + \omega_c^{\bar{p}}\right) \\ \Delta\omega_a^p &= \frac{1}{2}\left(\delta\omega_a^p - \delta\omega_a^{\bar{p}}\right) \\ \Sigma\omega_a^p &= \frac{1}{2}\left(\delta\omega_a^p + \delta\omega_a^{\bar{p}}\right), \end{aligned} \tag{4.11}$$

with anomaly frequency $\omega_a = \omega_L - \omega_c$, and $\delta\omega_a$ denoting a shift in the anomaly frequency induced by hypothetical CPT-violating effects, while the cyclotron frequency is to first order not perturbed by CPT-odd coefficients. The anomaly frequency shifts are given by [95, 84]:

$$\begin{aligned} \delta\omega_z^p &= 2\tilde{b}_p^x - 2\tilde{b}_{F,p}^{xx} B \\ \delta\omega_z^{\bar{p}} &= -2\tilde{b}_p^{*x} + 2\tilde{b}_{F,p}^{*zz} B, \end{aligned} \tag{4.12}$$

SME coefficient	old constraints [38]	constraints from [28, 29]
$\lvert\tilde{b}_{F,p}^{Z}\rvert$	$< 2.1 \times 10^{-22}\,\mathrm{GeV}$	$< 6.9 \times 10^{-25}\,\mathrm{GeV}$
$\lvert\tilde{b}_{F,p}^{XX} + \tilde{b}_{F,p}^{YY}\rvert$	$< 1.2 \times 10^{-6}\,\mathrm{GeV}^{-1}$	$< 3.9 \times 10^{-9}\,\mathrm{GeV}^{-1}$
$\lvert\tilde{b}_{F,p}^{ZZ}\rvert$	$< 8.8 \times 10^{-7}\,\mathrm{GeV}^{-1}$	$< 3.3 \times 10^{-9}\,\mathrm{GeV}^{-1}$
$\lvert\tilde{b}_{F,p}^{*Z}\rvert$	$< 2.5 \times 10^{-22}\,\mathrm{GeV}$	$< 1.3 \times 10^{-24}\,\mathrm{GeV}$
$\lvert\tilde{b}_{F,p}^{*XX} + \tilde{b}_{F,p}^{*YY}\rvert$	$< 8.3 \times 10^{-7}\,\mathrm{GeV}^{-1}$	$< 2.8 \times 10^{-9}\,\mathrm{GeV}^{-1}$
$\lvert\tilde{b}_{F,p}^{*ZZ}\rvert$	$< 3.0 \times 10^{-6}\,\mathrm{GeV}^{-1}$	$< 1.0 \times 10^{-8}\mathrm{GeV}^{-1}$

Table 4.1.: SME constraints derived from the recent magnetic moment measurements [28, 29] in comparison to the old constraints derived based on the BASE single-trap antiproton g-factor measurement [38]. The respective limits were improved on by more than two orders of magnitude.

with B denoting the magnetic field strength. Explicit expressions for $\Delta\omega_a^p$ and $\Sigma\omega_a^p$ are given in [95], Eq. (65-69),

$$\begin{aligned}\Delta\omega_a^p, \Sigma\omega_a^p = &-\tilde{b}_p^Z \sin(\chi_M) - \frac{1}{2}\left(\tilde{b}_{F,P}^{XX} + \tilde{b}_{F,P}^{YY}\right) B \cos^2(\chi_M) - \tilde{b}_{F,P}^{ZZ} B \sin^2(\chi_M) \\ \mp &\left(\tilde{b}_p^{*Z} \sin(\chi_C)\cos(\gamma_C) + \frac{1}{2}\left(\tilde{b}_{F,P}^{*XX} + \tilde{b^*}_{F,P}^{YY}\right) B^* \left(\cos^2(\chi_C)\cos^2(\gamma_C) + \sin^2(\gamma_C)\right)\right) \\ &\mp \left(\tilde{b}_{F,P}^{*ZZ} B^* \sin^2(\chi_C)\cos^2(\gamma_C)\right).\end{aligned} \tag{4.13}$$

These coefficients dependent on the magnetic field orientation of both experiments with respect to the local x-axis[1] ($\gamma_C = 120°, \gamma_M = -162°$) and the respective co-latitudes ($\gamma_M = 40°$, $\gamma_C = 44°$). Limits on the SME coefficients are be determined by inserting Eq. 4.13 into Eq. 4.10, and assuming that all but the respective coefficients are vanishing. The improvements in measurement uncertainty allowed to constrain the respective CPT-violating SME coefficients more than two orders of magnitude more strictly. The energy-resolution reached with our experiments is similar to those performed with electron/positrons and those on the muon magnetic moment, which place limits on the order of $< 10^{-23}\,\mathrm{GeV}$ to $< 10^{-24}\,\mathrm{GeV}$ [30] and between $< 7 \times 10^{-24}\,\mathrm{GeV}$ and $< 6 \times 10^{-25}\,\mathrm{GeV}$ [99].

[1] With $\gamma = 0$ corresponding to a southward orientation.

4.2. Limits on the interaction of antiprotons with axion-like dark matter

While astrophysical and cosmological observations strongly suggest that about a quarter of the universe's total energy content consists of dark matter [13], the microscopic nature of dark matter remains yet unknown. Several candidates for dark matter have been proposed, such as weakly interacting particles (WIMPs), massive astrophysical compact halo objects (MACHOs), and axion-like particles [100]. Originally, the axion was proposed as a candidate for resolving the strong CP problem of quantum chromodynamics [101, 102]. While limits have been placed on the interaction between axion-like particles and matter particles such as nucleons, electrons, gluons, and photons [103, 104], the interaction between axion-like particles and antimatter has not been investigated prior to our research [50]. As CPT-even axion-proton interactions detectable within our measurement resolution would have been discovered in the matter studies already, our study searched for a CPT-odd effect, which could potentially link baryon asymmetry and dark matter. The underlying field theory then would necessarily be non-local [105].
According to the model presented in [106], where dark matter consists purely of axion-like particles, the axions form a coherently oscillating classical wave $a = a_0 \cos(\omega_a t)$ with angular frequency ω_a given by the axion mass m_a, $\omega_a \approx m_a c^2/\hbar$ [107]. Its derivative couples to spin polarized nucleons and thus induces an energy shift characterized by the Hamiltonian [50, 108, 107]

$$H_{\mathrm{int}}(t) = \frac{C_{\bar{p}} a_0}{2 f_a} \sin(\omega_a t) \boldsymbol{\sigma}_{\bar{p}} \cdot \boldsymbol{p}_a, \tag{4.14}$$

with Pauli spin-matrix vector $\boldsymbol{\sigma}_{\bar{p}}$, the momentum vector $\boldsymbol{p}_a$ of the axion field relative to an observer on earth, the axion decay constant f_a, and the model dependent dimensionless parameter $C_{\bar{p}}$. For the spin precession, this interaction is the same as one caused by a time-dependent oscillating (pseudo-)magnetic field, while the cyclotron motion remains unperturbed.
The time-dependent shift of ω_L described by Eq. 4.14 is given by:

$$\Delta\omega_L^{\bar{p}}(t) \approx \frac{C_{\bar{p}} m_a a_0 |\vec{v}_a|}{f_a} \left[A \cos(\Omega_{\mathrm{sid}} t + \alpha) + B\right] \sin(\omega_a t) \tag{4.15}$$

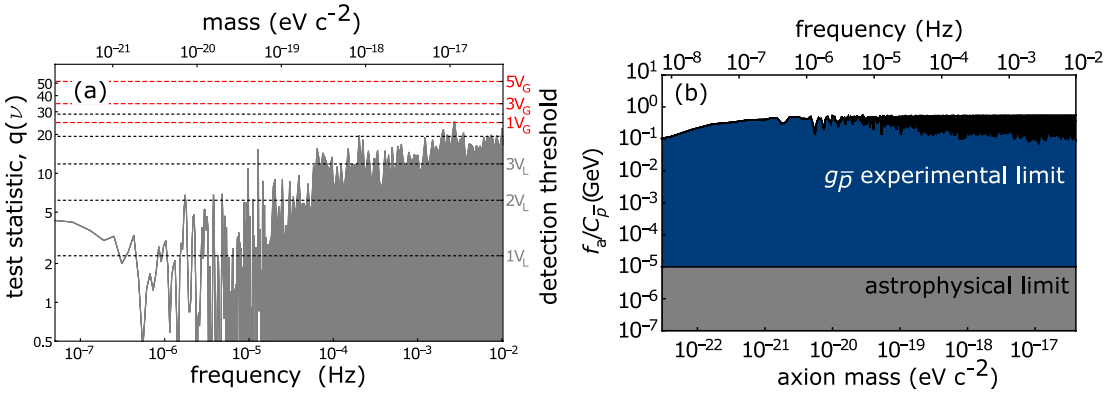

Figure 4.4.: Search for an interaction between antiprotons and axion-like dark matter. Left: Test statistic $q(\nu)$ of a multiple hypothesis-test. The red lines denote global confidence intervals for rejecting the zero-hypothesis, the black lines denote the local confidence intervals. Based on this data, the existence of an axion-antiproton coupling cannot be confirmed. Right: 95 % confidence exclusion limits on the interaction parameter $f_a/C_{\bar{p}}$ as a function of the axion mass. The supernovae data are depicted in gray, our limits are depicted in blue, with the black area denoting the peak-to-peak difference within one test frequency bin. Taken from [50].

with the average velocity $|\vec{v}_a|$ of the galactic axions respective to the sun, the sidereal frequency Ω_{sid}, and α, A, B describing the orientation of the experiment relative to the galactic axion dark-matter flux [109]. $\Delta\omega_L^{\bar{p}}(t)$ contains three frequencies, the axion frequency ω_a and the sidebands $|\omega_a \pm \Omega_{\text{sid}}|$. The Larmor frequency ω_L is instantaneously probed whenever an ω_L-spectroscopy drive is applied during the two-particle method [50].

In order to determine whether a periodic, time-dependent Larmor frequency shift $\Delta\omega_L^{\bar{p}}(t) \neq 0$ due to antiproton-axion interactions is observed, a multiple-hypothesis test with more than 150 000 test frequencies between 5 nHz and 10.49 mHz spaced each by 60 nHz is performed. Following Wilk's theorem [110], a global p-value $p_G = 0.254$ for rejecting the hypothesis $\Delta\omega_L^{\bar{p}}(t) = 0$ was obtained, which is why the zero-hypothesis of no antiproton-axion coupling cannot be rejected within this dataset (Fig. 4.4 (a)).
Applying the CL_s-method [22], the axion-antiproton coupling coefficient $f_a/C_{\bar{p}}$ was constrained (Fig. 4.4 (b)). As the axion field would produce nearly equal amplitudes at ω_a and both sidebands, all three modes can be used to constrain the interaction. In the mass range $2 \times 10^{-23}\,\text{eVc}^{-2} < 4 \times 10^{-17}\,\text{eVc}^{-2}$, limits between 0.1 GeV and 0.6 GeV were placed. The corresponding interaction on matter nucleons could be constrained several orders more strictly to $f_a/C_N \approx 10^4 - 10^6\,\text{GeV}$ for the same mass range, using experi-

ments on the neutron electric dipole moment [107] and with ultra-low field NMR [111]. However, comparing to the previous best limits on $C_{\bar{p}}$ that were based on astrophysical observations from supernovae1987A [112, 22], our limits are by up to five orders of magnitude more strict, and constitute the first direct measurement on the interaction between dark matter and antimatter.

5 | Measurement of motional heating

In the BASE experiment, the measurement of the Larmor frequency ω_L and thus the antiproton magnetic moment $g_{\bar{p}}$ relies on the unambiguous spin state determination[1] by means of the continuous Stern-Gerlach effect [79]. Due to the implementation of a quadratic magnetic inhomogeneity B_2, the particle's magnetic moment is coupled to the axial frequency ω_z and induces a small frequency shift $\Delta\omega_z$, as derived in Eq. 2.45:

$$\Delta\omega_z \approx \frac{\hbar\omega_+}{2\pi m_{\bar{p}}\omega_{z,0}}\frac{B_2}{B_0}\left(\left(n_+ + \frac{1}{2}\right) + \frac{\omega_-}{\omega_+}\left(n_- + \frac{1}{2}\right) + \frac{gm_s}{2}\right), \tag{5.1}$$

with spin quantum number $m_S = \pm\,1/2$ and radial quantum numbers $n_{+,-}$. The resolution of individual spin transitions with high fidelity is impeded by noise-driven quantum transitions in the radial modes as these also induce frequency shifts. For the BASE setup, the frequency shift due to one cyclotron quantum jumps is $g_{\bar{p}}/2$ times smaller than the frequency shift due to a spin transition, $g_{\bar{p}}/2 \times \Delta\omega_z(\Delta m_+ = \pm 1) \approx \Delta\omega_z(\Delta m_s = \pm 1)$. As each measurement of ω_z with sufficient resolution takes about 60 s, it is of crucial importance to obtain very low cyclotron transition rates ζ_+ of order $1\,\mathrm{min}^{-1}$ or better. In this chapter, the cyclotron mode stability that enabled the to-date most precise measurement of the antiproton magnetic moment $g_{\bar{p}}$ [28] is characterized and noise sources are discussed. The basic evaluation concept has already been presented in the author's master's thesis [46], but will be partly repeated here for reasons of completeness. The main analysis work has however been performed in the framework of this PhD thesis,

[1] In fact, $g_{\bar{p}}$ can also be measured by observing spin transitions in a statistical way without determining the spin state, but the achievable fractional precision is then limited to the ppm-level, see [40, 38].

which led to a publication in Phys. Rev. Lett. [51]. For self-consistency of this chapter, aspects already described in [46] will therefore be repeated. Here, an extensive description of the analysis is provided including several aspects which have not been described previously.

Besides its importance for Penning trap based g-factor measurements, quantum transitions driven by parasitic radio-frequency noise (i. e. heating rates) are a known and extensively studied challenge in RF trap experiments [113, 114], as they constitute one of the main sources of decoherence in such experiments and are among several aspects that hamper the scalability of multi-ion systems.

When heating rates were first studied in ion traps [115], [113], the observed electric field noise exceeded the one predicted from know noise sources like technical noise, thermal noise or blackbody radiation by orders of magnitude, a phenomenon that was then referred to as *anomalous heating* [115, 114]. Its origin remains under vivid discussion, but can for instance be investigated by comparing different experiments with various distances d between ion and the nearest electrode, and also by varying d directly in situ. Assuming for instance the presence of electrically oscillating potential patches scattered across the electrode surface: The electric-far-field of a dipole decreases with d^{-3} and its spectral noise density $S_E(f)$ with d^{-6}. As the effective area the ion is influenced by increases with d^2 in a planar surface trap, a d^{-4}-scaling would be observed [113]. Due to differences in the experimental setups, such as geometry, fabrication, used trap materials etcetera, it is difficult to extract a clear scaling $\propto d$ from comparison plots of different experiments, but a general scaling of the heating rate $\propto d^{-\beta}$ with $\beta > 0$ is suggested [114]. In traps with non-planar geometries, $\beta = 3.5(1)$ [116] and $\beta = 3.1$ [117] were measured, in planar traps, $\beta = 3.8(1)$ [118], $\beta = 3.9(2)$ [119] and $\beta = 2.6$ [120] were observed. The discrepancy in [120] from [118, 119] is explained by the authors by assuming that the electric field noise on the trap surface is locally correlated with correlation lengths being not negligible compared to d. This affects the noise scaling in the multipole expansion above.

In the center of the five-pole Penning trap in a compensated and orthogonal [71] design used in BASE, the electric field provided by the trap electrodes increases linearly with ρ, ρ being the distance to the trap axis, or the orbit radius for a trapped particle. Consequently, for typical particle amplitudes that are of relevance here, the electric field noise $S_E(\omega)$ caused by trapping voltage noise increases with ρ^2.

Using a single antiproton in the BASE analysis trap, we measured the long term stabil-

ity of the cyclotron mode by means of the continuous Stern-Gerlach effect and obtained transition rates $\zeta_+ = 6(1)\,\mathrm{h}^{-1}$ in the modified cyclotron oscillator [51], which is orders of magnitude lower than observed in any other ion trap experiment. Our investigations constitute the first explicit and detailed study of heating rates in a cryogenic Penning trap. By varying the particle's magnetron radius ρ_- and thus effectively its orbit radius ρ, we were able to identify electrode voltage noise as the dominant source of electric field fluctuations for $\rho > 6\,\mu\mathrm{m}$. For $\rho < 6\,\mu\mathrm{m}$, the scaled electric field noise spectral density $\omega S_E(\omega)$ is constrained to be at least a factor of 230 lower than reported on in room-temperature Penning traps [121] and at least a factor of 1800 lower than the lowest limits reported for Paul traps [122]. The observed transition rates can be related to residual voltage noise density of $S_V(\omega_+) = 225(54)\,\mathrm{pVHz}^{-1/2}$ present on each electrode. The experimental setup is examined in detail, and several sources of S_V are discussed.

5.1. Analysis trap setup

The measurements presented here have been performed in the analysis trap setup of the BASE experiment (see Fig. 5.1). It consists of a cylindrical five-pole Penning trap in an orthogonal and compensated design [71] located in the horizontal bore of a superconducting magnet. The central ring electrode is made out of a cobalt-iron alloy generating the strong magnetic inhomogeneity $B_2 \approx 300\,\mathrm{kT/m}^2$ required for spin state spectroscopy. A highly-sensitive superconducting image-current detector for the axial motion is connected to one of the endcap electrodes. Once the trapped antiproton is tuned into resonance with the detection circuit, the particle reaches a thermal equilibrium with the detector and appears as a dip with width $\delta\nu_z$ in the Fourier transformed voltage spectrum of the detector (see Fig. 5.1 (b)). The axial oscillation frequency ν_z is determined by performing a least squares fit to these spectra. Active electronic feedback (see Fig. 5.1 (a)) is applied [77, 78] in order to reduce the detector temperature down to $T_z = 1.92(10)\,\mathrm{K}$, thereby reducing the dip width to $\delta\nu_z = 2.3(1)\,\mathrm{Hz}$ and thus decreasing the fit uncertainty on ν_z. Accordingly, the quality factor is reduced to $Q = 8200(360)$ at a signal-to noise ratio $\mathrm{SNR} \approx 14.6(3)\,\mathrm{dB}$ and an effective parallel resistance of the detector is given by $R_p = 95(4)\,\mathrm{M\Omega}$. For the preparation of the cyclotron mode by means of subthermal cooling [89], the cyclotron motion is thermalized using the cyclotron detector located in the precision trap, with an effective parallel resistance of $R_{p,+,\mathrm{PT}} \approx 135\,\mathrm{k\Omega}$, and a cooling time constant of $t_{+,\mathrm{PT}} = 210\,\mathrm{s}$. The properties of the analysis trap and of

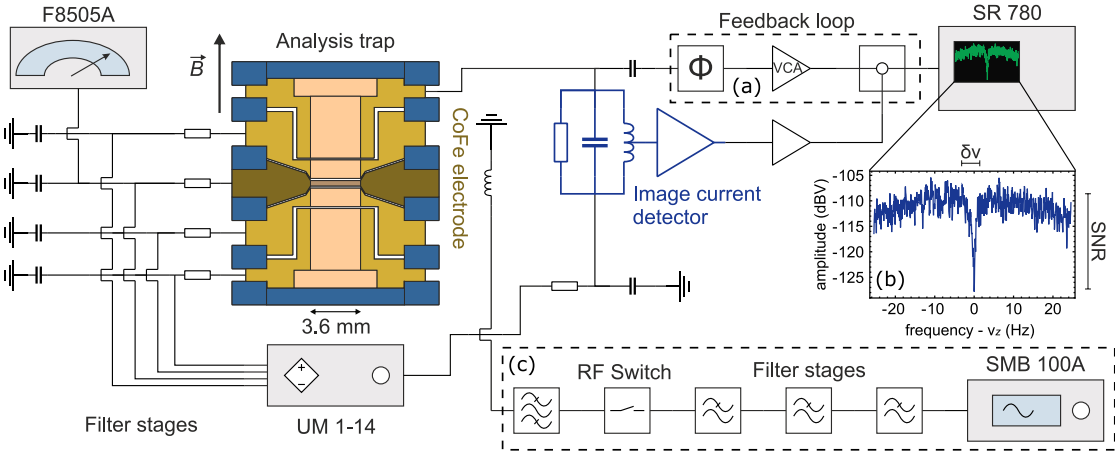

Figure 5.1.: Setup of the BASE analysis trap. The trap electrodes (golden/brown) with an inner diameter of 3.6 mm are displayed on the left, separated by sapphire spacers (blue). The central ring electrode, made out of cobalt-iron alloy, realizes the magnetic bottle $B_2 \approx 300\,\mathrm{kT/m^2}$ needed for the application of the continuous Stern-Gerlach effect [79]. The ultra-stable voltage source (Stahl electronics UM 1-14) provides the trap voltages that are filtered by multistage low-pass filters. The voltage applied to the central electrode is simultaneously recorded with a Fluke F8505A voltmeter in order to correct the measured axial frequency ν_z for voltage fluctuations. The axial frequency is measured by means of a feedback-cooled (a) [77, 78] image current detection system (blue) [57] connected to an endcap electrode. The axial frequency is obtained from the fast Fourier-transformed detector spectrum (b) measured by a Stanford Research SR780 signal analyzer. For particle manipulation, a Rohde&Schwarz SMB 100A frequency generator connected to high order low-pass and band-pass filters is used (c).

the precision trap cyclotron detector are summarized in Tab. 5.1

5.2. Perturbation theory

A theoretical model which discusses quantum transition rates induced by electrical field noise has been constructed [123] using perturbation theory in the interaction picture

ν_+	ν_z	$R_{p,z}$	$\delta\nu_z$	SNR	$R_{p,+,\mathrm{PT}}$	$t_{+,\mathrm{PT}}$
17.8 MHz	674 856 Hz	95(4) MΩ	2.3(1) Hz	14.6(3) dB	135 kΩ	210 s

Table 5.1.: Parameters of the BASE analysis trap and the precision trap cyclotron detector.

[124]. The Hamiltonian is described as

$$\hat{H} = \hat{H}_0 + \hat{V}(t), \tag{5.2}$$

where $\hat{H}_0$ is the time independent Penning trap Hamiltonian, the time-dependent perturbing potential $\langle \hat{V}(t) \rangle$ is small compared to $\langle \hat{H}_0 \rangle$ and $\langle \hat{V}(t) \rangle = 0$ for $t \leq t_0$. In the interaction picture, the Schrödinger equation is given by

$$i\hbar \frac{\partial}{\partial t} |\psi, t\rangle_I = -\hat{H}_0 |\psi, t\rangle_I + e^{i\hat{H}_0 t/\hbar} \left[\hat{H}_0 + \hat{V}(t)\right] |\psi, t\rangle \tag{5.3}$$

The time evolution of the initial state $|\psi, t\rangle = \exp(-iH_0 t/\hbar) |i\rangle = |i\rangle_I$ is derived using a recursive treatment. The index I denotes the vector in the interaction picture. For first order transitions, it is given by

$$|\psi, t\rangle = |i\rangle + \frac{1}{i\hbar} \int_{t_0}^{t} dt' \hat{V}_I(t') |i\rangle . \tag{5.4}$$

The transition probability $p_{i \to f}$ is calculated accordingly,

$$p_{i \to f} = |\langle f|\psi, t\rangle|^2 = \frac{1}{\hbar^2} \left| \int_{t_0}^{t} dt' e^{i(E_f - E_i)t'/\hbar} \langle f| \hat{V}(t') |i\rangle \right|^2 . \tag{5.5}$$

The perturbation operator $\hat{V}$ is expanded in a Taylor series as electric field noise might be present in terms of zero-th order field noise, gradient field noise, and higher order field noise,

$$\hat{V}(t, x) = q \left(E_0(t, x)\hat{x} + E_1(t, x)\hat{x}^2 + \mathcal{O}\left(\hat{x}^3\right) \right), \tag{5.6}$$

with particle charge q and position operator $\hat{x}$. The first order transition rate $\Gamma_{i \to i \pm 1}$ is calculated:

$$\begin{aligned} \Gamma_{i \to i \pm 1} &= \frac{1}{T} |\langle i \pm 1|\psi, t\rangle|^2 \\ &= \frac{1}{T} \left| \frac{1}{i\hbar} \int_0^T dt' \langle i \pm 1| qE_0(t', x)\hat{x} |f \pm 1\rangle e^{i\omega_m t'} \right|^2 , \end{aligned} \tag{5.7}$$

with ω_m denoting the frequency of the considered mode m. The averaging time T is short compared to the time scale over which the level population changes, but it is large compared to the correlation time of the electric field noise E_i. Therefore it is justified

to treat the transition matrix elements as constants, and to extend T to $+\infty$ [125]:

$$\begin{aligned}\Gamma_{i\to i\pm1} &= \frac{q^2}{\hbar^2}\left|\langle i\pm1|\,\hat{x}\,|i\rangle\right|^2 \times \frac{1}{T}\left|\int_0^T dt' E_0(t',x)e^{i\omega_m t'}\right|^2 \\ &= \frac{q^2}{\hbar^2}\left|\langle i\pm1|\,\hat{x}\,|i\rangle\right|^2 \times \lim_{T\to\infty}\frac{1}{T}\left|\int_0^T dt' E_0(t',x)e^{i\omega_m t'}\right|^2 \\ &= \frac{q^2}{2\hbar m\omega}\left(i+\frac{1}{2}\pm\frac{1}{2}\right)\int_0^\infty dt' e^{i\omega_m t'}\left\langle E_0(t)E_0(t+t')\right\rangle .\end{aligned} \tag{5.8}$$

A more detailed derivation of this equation is given in App. C. Following the convention from [125], we now introduce the power spectral density $S_E(\omega)$ given by the Fourier transform of the autocorrelation function,

$$\begin{aligned}S_E(\omega_m) &= 2\int_0^{+\infty} dt' e^{i\omega_m t'}\left\langle E_0(t)E_0(t+t')\right\rangle \\ &= 2\int_0^{+\infty} dt' e^{i\omega_m t'}\lim_{T\to\infty}\frac{1}{T}\int_0^T dt E_0(t)E_0(t+t'),\end{aligned} \tag{5.9}$$

which allows us to express the transition rates $\Gamma_{n\to\pm1}$ in the more convenient way:

$$\Gamma_{n\to n\pm1} = \left(n+\frac{1}{2}\pm\frac{1}{2}\right)\frac{q^2}{4m\hbar\omega_m}S_E(\omega_m). \tag{5.10}$$

As $\Gamma_{n\to n\pm1}$ scales proportional to n, it is of utmost importance to prepare a particle in a state with a low cyclotron quantum number in order to resolve spin transitions [72]. For particles in the ground state, $n = 0$, we obtain the standard heating rate formula [113, 114]:

$$\dot{\bar{n}} = \Gamma_{0\to1} = \frac{q^2}{4m\hbar\omega_m}S_E(\omega_m). \tag{5.11}$$

While most ion traps measuring heating rates operate with particles in the motional ground state, this regime is inaccessible without introducing laser cooling to the Penning trap. Instead, for $n \gg 0$, the rates for increase and decrease in n are nearly identical, $\Gamma_+ = \Gamma_{n\to n+1} \approx \Gamma_{n\to n-1} = \Gamma_-$, which results in a mostly undirected random walk with transition rate ζ, which can be interpreted as a diffusion constant. This behavior is shown in Fig. 5.2. ζ is given by the sum of the rates for increase Γ_+ and decrease Γ_-:

$$\zeta = \Gamma_+ + \Gamma_- \approx \frac{q^2 n}{2m\hbar\omega_m}S_E(\omega_m). \tag{5.12}$$

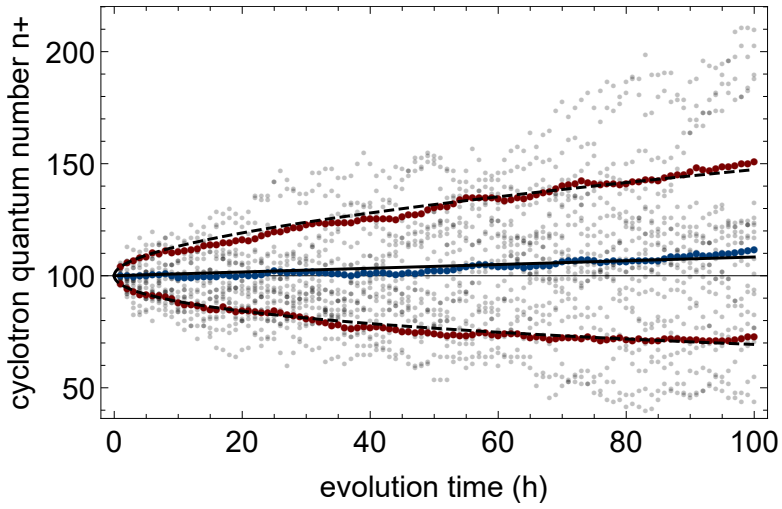

Figure 5.2.: Random walk simulation for an antiproton with an initial cyclotron quantum number $n_+(0) = 100$, and an electric field noise $S_E(\omega_+) = 7.5 \times 10^{-20}\,\mathrm{V^2 m^{-2} Hz^{-1}}$. The blue dots represent the mean quantum number $\bar{n}_+(t)$ after evolution time t, the red dots indicate the corresponding standard deviation $\sigma(n_+(t))$ denoted by the error bars. The solid black line shows the predicted heating rate $\dot{\bar{n}}$, while the dashed black lines denoted a $\propto \sqrt{t}$-fit to the standard deviations. The light dots indicate the random walks used for this simulation, with transition rate Γ_+ for the transitions $n_+ \to n_+ + 1$, and Γ_+ for $n_+ \to n_+ - 1$. The transition rate $\zeta_+ = \Gamma_+ + \Gamma_-$ can be interpreted as a diffusion constant.

The increase in average quantum number $\dot{\bar{n}}$ is again given by

$$\dot{\bar{n}} = \Gamma_+ - \Gamma_- = \frac{q^2}{4m\hbar\omega_m} S_E(\omega_m), \tag{5.13}$$

which agrees with Eq. 5.11. This brings us to the relation

$$\dot{\bar{n}} = \frac{\Gamma_+ - \Gamma_-}{\Gamma_+ + \Gamma_-}\zeta = \frac{(n+1) - (n)}{2n+1}\zeta \approx \frac{\zeta}{2n}. \tag{5.14}$$

One mechanism how electric field noise in the trap can be generated is due to trap voltage fluctuations. The trap voltages V_m relate linearly to radial and axial electric field components $E_{i,\rho}(\rho, z, t), E_{i,z}(\rho, z, t)$ of order i, which can be expressed [123] as follows :

$$E_{i,\rho}(\rho, z, t) = \sum_{m=1}^{5} \lambda_{i,\rho,m}(\rho, z) V_m(t) \tag{5.15}$$

n	ρ_-=10 μm $\lambda_{0,\rho,m}$
1	-0.580
2	-0.099
3	0.955
4	-0.099
5	-0.580

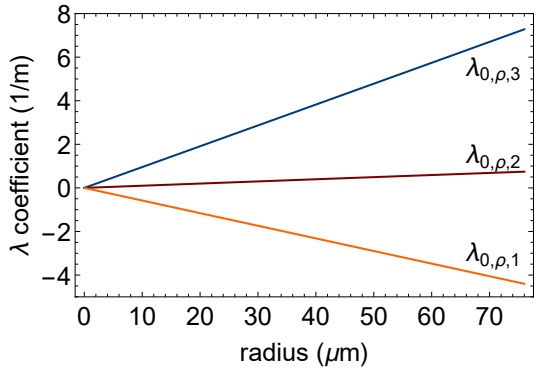

Figure 5.3.: λ coefficients for first order radial heating at different particle radii ρ. m is the electrode number, due to the symmetrical electrode design the λ coefficients for the correction electrodes and for the end caps are identical respectively. Due to the orthogonal design, the correction electrode noise $\lambda_{0,\rho,2}$ plays a minor role. The λ coefficients are calculated for z=0, at an axial temperature of 1.92 K the end cap contributions $\lambda_{0,\rho,1}$ and the ring electrode contributions $\lambda_{0,\rho,3}$ vary by less then 1 %, the correction electrode contribution $\lambda_{0,\rho,2}$ by less then 4 %. The nearly linear relation between particle radius and λ coefficients is displayed on the right.

The coefficients $\lambda_{i,\rho,m}(\rho_0, z_0, t)$ are defined by the electrostatic properties of the trap potential $\Phi(\rho, z)$, assuming a voltage of $V_m = 1\,\mathrm{V}$ is applied to the m-th electrode, while the remaining electrodes are set to 0 V:

$$\lambda_{i-1,\rho,m}(\rho_0, z_0) = -\frac{\partial^i \Phi(\rho, z)}{\partial \rho^i}\bigg|_{\substack{\rho=\rho_0, z=z_0 \\ V_n=1, \forall o\neq m: V_o=0}} \tag{5.16}$$

Thus, the electric field noise autocorrelation function is rewritten:

$$\langle E_{0,\rho}(\rho, z, t) E_{0,\rho}(\rho, z, t+t')\rangle = \langle \sum_{m=1}^{5} \lambda_{0,\rho,m}(\rho, z) V_m(t) \sum_{m=1}^{5} \lambda_{0,\rho,m}(\rho, z) V_m(t+t')\rangle \tag{5.17}$$

Now, the first order radial electric field noise $S_{E,0,\rho}(\omega, \rho, z)$ is expressed in terms of the voltage noise:

$$S_{E,0,\rho}(\omega, \rho, z) = \sum_{m=1}^{5} \left(\lambda_{0,\rho,m}(\rho, z)\right)^2 \langle V_m(t) V_m(t+t')\rangle \tag{5.18}$$

Discriminating between noise on different trap electrodes is experimentally very difficult. However, by assuming identical voltage noise on each electrode $\langle V_m(t) V_m(t+t')\rangle = S_V$,

we can compute an average voltage noise density:

$$S_{E,0,\rho}(\omega,\rho,z) = S_V(\omega)\sum_{m=1}^{5}\left(\lambda_{0,\rho,m}(\rho,z)\right)^2 = S_V(\omega)\Lambda^2, \tag{5.19}$$

where $1/\Lambda$ can be understood as a trap specific length. As a result of this discussion we eventually obtain the relation between the radial transition rates and voltage noise by referring back to Eq. 5.12

$$\zeta_{+,-} = \frac{q^2}{2m\hbar\omega_{+,-}} n_{+,-}\Lambda^2 S_V(\omega_{+,-}). \tag{5.20}$$

5.3. Differential Allan deviation as a measure of absolute transition rates

The Allan deviation [126] is a well-known quantity to describe frequency stability as a function of averaging time. It can be understood as the moving the standard deviation $\sigma_\nu(\tau)$ of frequency differences $\bar{\nu}_i - \bar{\nu}_{i+1}$, where $\bar{\nu}$ is averaged over time τ. At BASE, we use a quantity that is sligthly adapted to the Allan deviation [126], and will be referred to as "differential Allan deviation" following [51]. It is given by

$$\sigma_\nu^2(j) = \frac{1}{N-2j}\sum_{i}^{N-2j}\left(\bar{\nu}_{j,i} - \bar{\nu}_{j,i+1}\right)^2, \tag{5.21}$$

where $\nu_{j,i}$ describes the i-th average over a subset of j frequencies out of a set of N frequencies:

$$\bar{\nu}_{j,i} = \frac{1}{j}\sum_{k=i}^{i+j-1}\nu_k \tag{5.22}$$

Note that these averages are overlapping. Naturally, the averaging time of $\bar{\nu}_{j,i}$ is $j \times \tau$, where τ is the averaging time for each frequency measurement. From the time dependent scaling, dominant noise contributions and other information such as the most appropriate averaging time can be derived. For the differential axial frequency Allan deviation in the BASE analysis trap, the σ_{ν_z}-scaling is given by (compare Fig. 5.4)

$$\sigma_{\nu_z}(\tau) \propto \sqrt{\Xi^2_{\text{Back}} + \tau\left(\Delta_+^2\zeta_+ + \Delta_-^2\zeta_-\right)}. \tag{5.23}$$

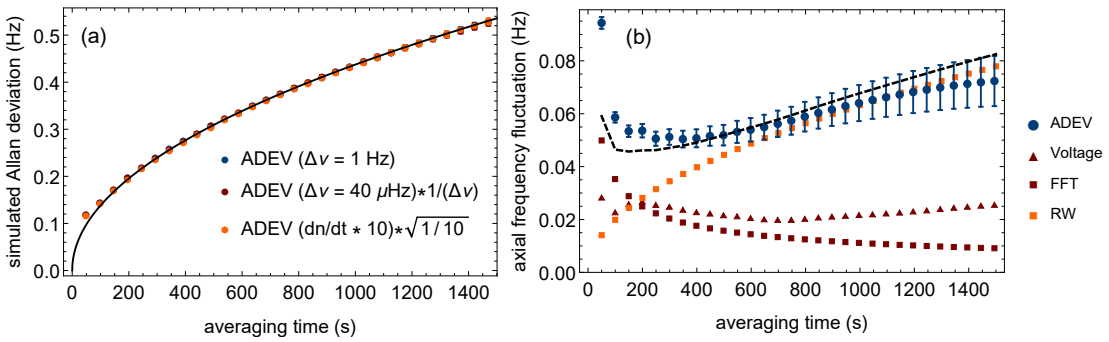

Figure 5.4.: Transition rate determination for simulated and measured data. (a) depicts differential Allan deviations from simulated frequency random walks scaled by the corresponding factors according to Eq. 5.23. The blue points represent the differential Allan deviation of a set of axial frequencies, where after 49 s a jump by $\Delta\nu_z = 1\,\mathrm{Hz}$ with a probability of $49/3600 \approx 1.3\,\%$ occurs. For the yellow points, $\Delta\nu = 40 \times 10^{-6}$, the ADEV is multiplied by $1/(\Delta\nu)$ in order to display the ADEVs in the same plot. Same for the green dots, where the transition rate is varied. Since the three simulations agree within their respective uncertainties, our model Eq. 5.23 is confirmed.
(b) Displays the axial frequency stability analysis for a particle at low cyclotron quantum number n_+ and low absolute transition rates ζ_+. To this end, 900 frequency measurements were conducted over 12 h. The differential Allan deviation $\sigma_{\nu_z}(\tau)$ is displayed in blue. Frequency measurement noise (FFT, dark red squares) and voltage fluctuations (dark red triangles) contribute to the observed frequency instability. Contributions from a simulated random walk of the cyclotron energy are displayed in orange. The dashed black line is given by the sum of random walk, FFT, and voltage contributions. For $\tau > 250\,\mathrm{s}$, the differential Allan deviation is dominated by random walks. Transition rate uncertainties are extracted from the differential Allan deviation uncertainty.

$\Delta_{+,-}$ denote the change in axial frequency $\Delta\nu_z$, when the respective quantum number changes by one. Ξ^2_{Back} denotes background noise contributions, such as voltage drifts $\sigma_V(\tau)$ leading to frequency drifts and the fit/readout noise denoted by $\sigma_{\mathrm{FFT}}(\tau)$. $\sigma_{\mathrm{FFT}}(\tau)$ is determined by simulations [127] and given by:

$$\sigma_{\mathrm{FFT}}(\tau) = \frac{8\pi}{\sqrt{2}}\sqrt{\frac{\delta\nu_z}{\tau}}\frac{1}{\mathrm{SNR}^{7/4}} \times (1.04). \tag{5.24}$$

σ_{FFT} depends on the signal-to-noise ratio SNR (dBV), the dip width $\delta\nu_z$ and the averaging time, but these parameters do not change over time and especially do not shift the measured frequency. Therefore, σ_{FFT} decreases as the averaging time increases and becomes negligible for reasonably short averaging times τ. $\sigma_V(\tau)$ is constrained by simultaneously recording the voltage V_r applied to the central ring electrode with an

independent high precision reference voltmeter (Fluke 8505a) (compare Fig. 5.1) and correcting the axial frequencies accordingly. However, it is observed that σ_{ν_z} is only decreased for some data sets when ν_z is corrected for voltage fluctuations, while for some other data sets, σ_{ν_z} is even very slightly increased. This means that the voltage fluctuations are at the same order of magnitude as the FLUKE readout precision, and it is not possible to entirely remove the impact of voltage fluctuations on σ_{ν_z}. When Ξ_{Back} becomes small, σ_{ν_z} is dominated by the transition rate effects and a $\sigma_{\nu_z} \propto \sqrt{\tau}$-scaling is observed for sufficiently long averaging times. Later on, it will be shown that the impact of the magnetron random walk ζ_- is negligible compared to the cyclotron random walk ζ_+. At low background noise Ξ_{Back}, Eq. 5.23 may be written as

$$\sigma_{\nu_z}(\tau) = A \times \sqrt{\tau \Delta_+^2 \zeta_+}, \tag{5.25}$$

By simulating a large number of random walks, $A \approx 0.013713$ is extracted. Consequently, $\Delta_+^2\zeta_+$ is obtained by performing $\sqrt{\tau}$-fits on the differential Allan deviations that are corrected by the effect of frequency readout noise and partly by the effect of voltage fluctuations.

5.4. Measurement procedure

Throughout the preparation and the measurement, the axial motion of the particle is in thermal equilibrium with the feedback cooled [77, 78] axial detector at $T_z \approx 1.92(10)\,\mathrm{K}$, which corresponds to an rms axial amplitude of $30(1)\,\mu\mathrm{m}$. In oder to obtain low absolute transition rates $\zeta_{+,-}$, a particle was prepared at low radial quantum number n_+, n_- by means of subthermal cooling [89, 90]. The magnetron motion is coupled to the axial motion by applying a radio frequency drive with $\omega_{\mathrm{rf}} \approx \omega_z - \omega_-$, which leads to equal population of both states, $n_z = n_-$, and thus $T_- = T_z \times \omega_-/\omega_z \approx 35\,\mathrm{mK}$. When the coupling drive is turned off, the magnetron energy E_- remains at one particular energy following the Boltzmann-statistics, $p(E_-) \propto \exp\left(-E_-/(k_B T_-)\right)$. In the magnetic bottle B_2, the magnetron energy E_- induces a shift $\Delta\nu_z = \nu_{z,E_-} - \nu_{z,0}$ of the axial frequency ν_z compared to the "cut frequeny" $\nu_{z,0}$ at vanishing magnetron energy:

$$\Delta\nu_z = \frac{E_-\nu_z}{m\omega_z^2}\frac{B_2}{B_0} = \rho_-^2\nu_z\frac{1}{4}\frac{B_2}{B_0}. \tag{5.26}$$

$\Delta\nu_z$ is measured for a certain number of times, usually about 50 times. Afterwards, the lowest measured frequency is defined to be the threshold frequency $\nu_{z,\mathrm{tr}}$. The threshold energy E_{tr} then is given by

$$\int_0^{E_{\mathrm{tr}}} dE_- \frac{1}{k_B T_-} \times \mathrm{e}^{-E_-/(k_B T_-)} \stackrel{!}{=} 1/50 \Rightarrow E_{\mathrm{tr}} = 0.7(7)\,\mathrm{mK}, \tag{5.27}$$

which corresponds to a frequency shift $\Delta\nu_z = 0.48(48)\,\mathrm{mHz}$. A particle is considered to be cold, when its axial frequency is less then $\nu_{\mathrm{acc}} = 500\,\mathrm{mHz}$ higher than ν_{min}, this leads to a magnetron radius ρ_-

$$\rho_- = \frac{1}{\nu_{\mathrm{acc}}} \int_{\nu_{min}}^{\nu_{min}+\nu_{\mathrm{acc}}} d\Delta\nu_z \sqrt{\frac{4\Delta\nu_z B_0}{\nu_z B_2}} = 2.7^{+1.3}_{-2.7}\,\mu\mathrm{m} \Rightarrow E_-/k_B = 4.0^{+4.7}_{-4.0}\,\mathrm{mK}, \tag{5.28}$$

where the lower bound is given by the lower bound of $\Delta\nu_z$, and the upper bound is given by the sum of ν_{acc} and the upper bound of $\Delta\nu_z$.

Subthermal cooling of the cyclotron motion is carried out in a similar way. However, if we would thermalize the cyclotron mode by irradiating the corresponding sideband $\omega_{\mathrm{rf}} = \omega_+ - \omega_z$, we would obtain a cyclotron temperature $T_+ = T_z \times \omega_+/\omega_z \approx 53\,\mathrm{K}$ in the analysis trap[1] and about 360 K in the precision trap. Instead, we use the cyclotron detector with $T_+ = 12.8\,\mathrm{K}$ located in the precision trap to thermalize the cyclotron motion, with an effective parallel resistance $R_p \approx 135\,\mathrm{k\Omega}$ and thermalization time constant $\tau_+ \approx 209\,\mathrm{s}$. After thermalization in the PT, the particle is then shuttled into the AT, where the axial frequency is measured, and afterwards shuttled back to the PT, where it again thermalizes. Repeating the procedure for many times allows to obtain the "cyclotron cut" $\nu_{z,E_+=0}$ sufficiently accurate to select a cold particle, similarly to the method described before for cooling the magnetron motion. Typically, we prepare a particle with a cyclotron energy $E_+/k_B \approx 50\,\mathrm{mK}$, corresponding to $\rho_+ = 0.25\,\mu\mathrm{m}$, within a preparation time of on average about 10 h.

When the data showing the first resolved single spin transitions on individual antiprotons [47] were recorded, pure axial frequency measurements were also carried out in the analysis trap for several days in order to characterize the background stability of our experiment (see Fig. 5.5). The particle was initially prepared with subthermal cyclotron and magnetron energies. Afterwards, we obtained very satisfying stabilities with

[1] In fact, due to the magnetic bottle B_2 and axial frequency shifts related to the cyclotron energy, it would be virtually impossible to cool the cyclotron motion in the analysis trap.

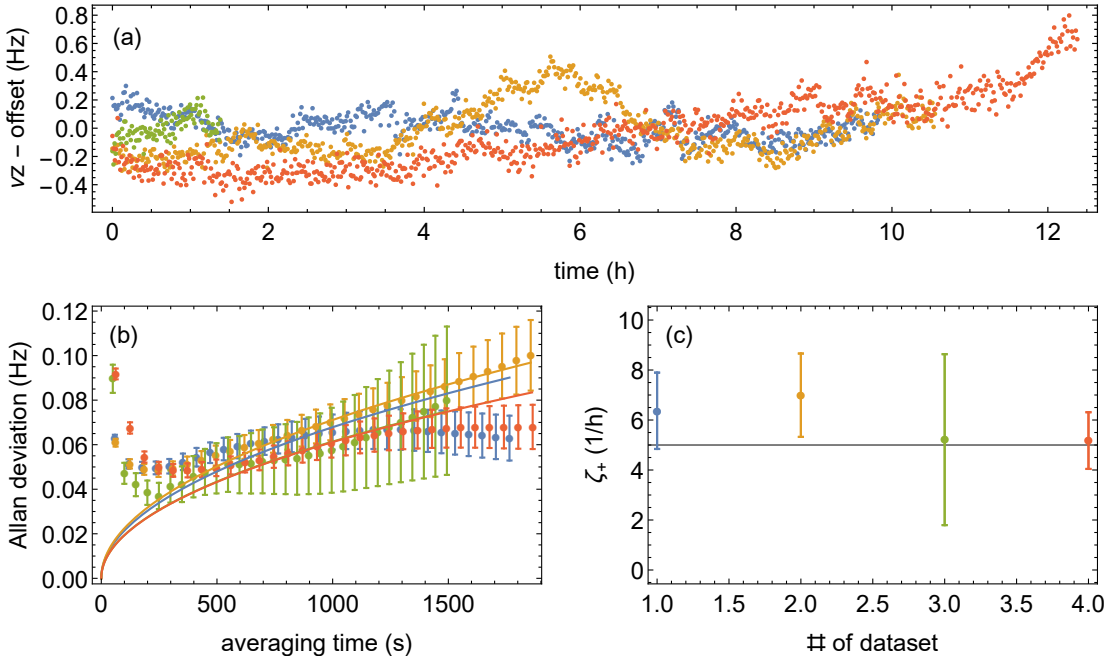

Figure 5.5.: Four different sets of axial frequency data showing ultra-low cyclotron transition rates. (a) depicts the axial frequencies corrected for voltage fluctuations. (b) shows the respective differential Allan deviations fitted with a function $\propto \sqrt{\tau}$, τ being the respective averaging time. (c) shows the cyclotron transition rates ζ_+ per hour, which are on the order 6(1) per hour. It should be kept in mind that the cyclotron quantum number is changing during the measurements and thus also ζ_+ is subject to change. The stability shown here is exceptional for ion trap experiments and will be discussed further below in the text.

transition rates $\zeta_+ < 10\,\mathrm{h}^{-1}$ for several days without the need to prepare n_+ again in a subthermal state. Occasionally, the magnetron motion was rethermalized. An upper bound for the cyclotron transition rate ζ_+ can be determined in an unambiguous way following the model described above (compare Fig. 5.5). It is naturally more difficult to estimate the cyclotron quantum number n_+ needed in order to compute the spectral field noise density $S_E(\omega_+)$, given that the particle experienced random walks in cyclotron for several days. Lacking a method to prepare the particle deterministically in a specific state or even in the ground state, we instead referred to the axial frequency evolution over several days. By comparing the average axial frequency during a heating rate measurement with the lowest axial frequency recorded closely before or after, the shift in

cyclotron quantum number between these two points in time is extracted:

$$\Delta\nu_z = \nu_{z,1} - \nu_{z,2} = \frac{\hbar\omega_+}{2\pi m_{\bar{p}}\omega_{z,0}}\frac{B_2}{B_0}\Delta n_+ \Leftrightarrow \Delta n_+ = \frac{2\pi m\omega_{z,0}}{\hbar\omega_+}\frac{B_0}{B_2}\Delta\nu_z. \tag{5.29}$$

Δn_+ now gives us a conservative lower bound for n_+, and thus allows to determine an upper bound for $S_E(\omega_+)$ following Eq. 5.12. For $n+ < 117$ and $n+ < 9$, we observed transition rates $\zeta_+ = 19.6(9)\mathrm{h}^{-1}$ and $\zeta_+ = 5.5(1)\mathrm{h}^{-1}$, leading to $\omega_+ S_E(\omega_+) \leq 8.8^{+4.0}_{-3.2} \times 10^{-12}\mathrm{V}^2\mathrm{m}^{-2}\mathrm{Hz}^{-1}$ and $\omega_+ S_E(\omega_+) \leq 3.1(6) \times 10^{-11}\mathrm{V}^2\mathrm{m}^{-2}\mathrm{Hz}^{-1}$.
In this context, it is important to note that n_+ is likely to be significantly larger than indicated by the lower bounds, which would result in lower upper bounds for $S_E(\omega_+)$. Also, in the model presented here, we account for axial frequency fluctuations arising from FFT averaging/fitting and from voltage noise, but not from other sources of long-term instability (see Eq. 5.23). The assumption that cyclotron transition rates can be accounted for most of differential axial frequency Allan deviation is supported by the $\propto \sqrt{\tau}$-behavior of $\sigma_{\nu_z}(\tau)$, but $\sigma_{\nu_z}(\tau)$ might also be affected by parameters like the change in ambient temperature (day/night fluctuations, operation of AD hall air conditioning system, change in cryoliquid levels, change in cryostat pressures, and many more). These processes often relate to frequency changes in a non-linear way, and are hard to be included in a reliable model. The neglection of these effects leads to a systematic overestimation of the upper limit on transition rates and electric field noise. We consider our method of extracting absolute transition rates ζ_+ and subsequently $\omega_+ \times S_E(\omega_+)$ to be conservative and to provide robust upper limits for the scaled electric field noise observed.

5.5. Magnetron-radius dependent heating rate measurement

In order to further investigate the origin of the electric field noise, we measured transition rates $\zeta_+(\rho_-)$ as a function of the magnetron radius. To this end, we excited the magnetron radius to by applying the subthermal cooling scheme, but selecting various states on the thermal distribution with $6\,\mu\mathrm{m} \leq \rho_- \leq 65\,\mu\mathrm{m}$ corresponding to magnetron energies $20\,\mathrm{mK} \leq E_-/k_B \leq 2.3\,\mathrm{K}$. The results of our measurement are depicted in Fig. 5.6. We observe a linear increase in the differential Allan deviation with magnetron radius ρ_-, $\sigma_{\nu_z} \propto \rho_-$ (b). Due to the low cyclotron quantum number n_+, the effective particle orbit at which the particle samples magnetic field noise is given by the mag-

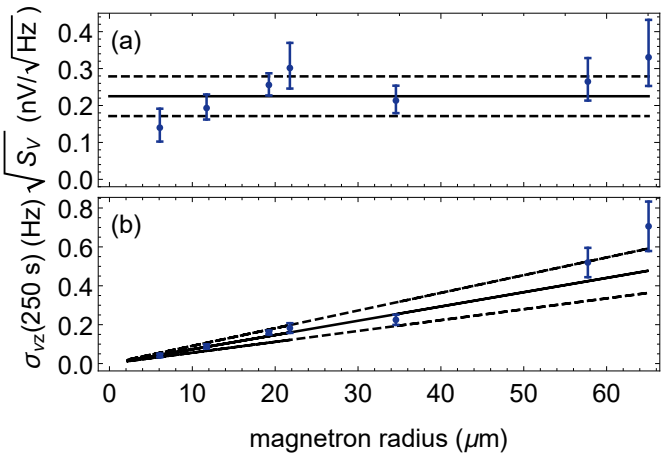

Figure 5.6.: Results of frequency stability measurements for particles at different magnetron radii ρ_-. (a) Square root of the calculated electrode voltage spectral noise density S_V. The extracted voltage fluctuation $S_V(\omega_+)$ (black lines) is constant for $6\,\mu\text{m} \leq \rho_- \leq 65\,\mu\text{m}$, confirming that this mechanism can be regarded as dominant source of electric-field fluctuations in the trap. (b) Measured differential Allan deviation $\sigma_{\nu_z}(\tau)$ of the axial frequency for an averaging time of $\tau = 250\,\text{s}$. The linear increase of $\sigma_{\nu_z}(\tau)$ is in good agreement with cyclotron transition rates driven by trapping voltage fluctuations. The black lines denotes calculated values for $\sigma_{\nu_z}(\tau)$ assuming the constant trap voltage density S_V extracted from (a).

netron radius, $\rho \approx \rho_-$. A linear increase in σ_{ν_z} corresponds to a quadratic increase in ζ_+, $\sigma_{\nu_z} \propto \zeta_+^2$ (see Eq. 5.23). Recalling Eq. 5.20, this can be explained by assuming electrode voltage noise as the dominant noise mechanism:

$$\zeta_+ = \frac{q^2}{2m\hbar\omega_+} n_+ \Lambda^2 S_V, \tag{5.30}$$

since $\Lambda \propto \rho$ (see Eq. 5.19). If the magnetron walk ζ_- would be dominant, however, we would in addition to the $S_E(\omega_-) \propto \rho^2$-scaling also observe an additional factor $n_- \propto \rho_-^2$, leading to $\zeta_- \propto \rho^4 \Rightarrow \sigma_{\nu_z} \propto \rho^2$. A dominant $\zeta_- \propto \rho^2$-scaling could also be explained by assuming that magnetron transition rates are generally dominant and in addition independent from electrode voltage fluctuations, but triggered by a different effect. This possibility is ruled out from our measurement campaign on the antiproton magnetic moment [28], where subthermal cooling of n_+ is an essential prerequisite for resolving individual spin transitions, which confirms that ζ_+ is dominant compared to ζ_- at the

typical low radial energies.
It has been reported that *anomalous heating* scales roughly $\propto d^{-\beta}$ with d being the electrode ion-distance, and β being in the range from $2.6 - 4$ [114], [116, 117, 118, 119, 120]. In this measurement, $d = r - \rho \approx 1.8\,\mathrm{mm}$ with inner electrode radius r remains roughly constant ($\Delta d/d = 1/60$) over the entire measurement, while the absolute transition rates ζ_+ vary by more than two orders of magnitude. Therefore, a $\propto d^{-\beta}$-scaling is ruled out as the dominant noise contribution for the considered magnetron radii, and can be constrained to $\omega_+ \times S_E(\omega_+) \leq 8.8^{+4.0}_{-3.2} \times 10^{-12}\mathrm{V}^2\mathrm{m}^{-2}$.
By referring back to Eq. 5.20, the voltage noise spectral density S_V is given by

$$S_V = \frac{2m\hbar\omega_+}{q^2}\frac{1}{n_+\Lambda^2}\zeta_+. \tag{5.31}$$

As discussed previously, we do not exactly know the cyclotron quantum number n_+. For the further discussion, we will assume $n_+ \approx 150$ which corresponds to $E_+ = 135\,\mathrm{mK}$, which is a reasonable value based on experimental experience and will be used in order to discuss the qualitative behavior. We then extract a trap voltage spectral noise density $(S_V)^{1/2} = 225(54)\,\mathrm{pVHz}^{1/2}$ (see Fig. 5.6 (b)).

5.6. Discussion of noise sources

The average voltage noise of $S_V = 225(54)\,\mathrm{pVHz}^{-1/2}$ corresponds to the Johnson noise of a resistance of $R = 143(69)\,\Omega$ at the experimental temperature $T \approx 6.4\,\mathrm{K}$. In order to examine noise sources present in our experiment, we refer to Fig. 5.1. The RC-filters connected to the trap electrodes are characterized by the transfer function $G(j\omega)$

$$G(j\omega) = \frac{1}{1 + j\omega RC}, \tag{5.32}$$

and consequently exhibit a spectral noise density S_{RC}

$$S_{\mathrm{RC}}(\omega) = \frac{1}{1 + \omega RC} \times \sqrt{4k_BTR}. \tag{5.33}$$

We obtain noise densities of about or below $1\,\mathrm{pVHz}^{-1/2}$ for the various filters with $(R, C) = (500\,\mathrm{k}\Omega, 8.2\,n\mathrm{F}), (1\,\mathrm{M}\Omega, 22\,\mathrm{nF}), (1\,\mathrm{M}\Omega, 180\,\mathrm{nF})$. The trap wiring is made out of approximately 10 cm long OFHC cables with a diameter of $0.25\,\mu\mathrm{m}$, leading to $S_{\mathrm{c}} \approx$

$0.3\,\mathrm{pVHz}^{-1/2}$. The amplifier noise $u_n = 600\,\mathrm{pVHz}^{-1/2}$ is filtered by an effective LC-filter consisting of the combined trap/resonator capacitance $C \approx 22\,\mathrm{pF}$, and the decoupled inductance $L = (1-\kappa)^2 L_r \approx 3/4 L_r$, $L_r = 2.47\,\mathrm{mH}$:

$$S_{\mathrm{amp}}(\omega) = \frac{1}{1+\omega^2 LC} u_n \tag{5.34}$$

The corresponding voltage noise is $S_{\mathrm{amp}}(\omega) = 1.4\,\mathrm{pVHz}^{-1/2}$. In order to compute the noise at cyclotron frequency ω_+ generated by the resonator, we consider the real part of the impedance derived in Eq. 2.31:

$$\mathrm{Re}(Z_0(\omega)) = \frac{1/R_p}{(1/R_p)^2 + (\omega^2-\omega_0^2)^2 \times \left(\omega_0^2 \omega L\right)^{-2}}, \tag{5.35}$$

and obtain $\mathrm{Re}(Z_0(\omega)) = 0.5\,\mathrm{m\Omega}$, corresponding to $S_{V,\mathrm{res}} = 0.4 \times 10^{-12}\,\mathrm{pVHz}^{-1/2}$. Electromagnetic losses in the trap electrodes related to the non-vanishing resistance of the material can enhance the blackbody radiation significantly following the dissipation-fluctuation theorem. This effect is approximated by [128, 114]

$$S_E^{\mathrm{BB}} = \frac{k_B T \rho_e}{2\pi d^3}\left(s_\eta + \frac{d}{\delta_s}\right), \tag{5.36}$$

with skin depth $\delta_s(\omega) = \sqrt{2\epsilon_0 c^2 \rho_e/\omega}$, resistivity ρ_e and $s_\perp = 1/2$ for electric field noise perpendicular to the surface. With $\rho_e = 2.2 \times 10^{-10}\,\Omega\mathrm{m}$ for gold at $T \approx 6\,\mathrm{K}$ [129], we obtain $\omega_+ \times S_E(\omega_+) \sim 5 \times 10^{-14}\,\mathrm{V^2 m^{-2}}$, which is orders of magnitude too low to account for the observed heating rates.

Another heating mechanism that is even independent from the electrode-ion distance d is given by collisions with residual background gas. In our direct measurement of the antiproton lifetime [48], we did not observe any loss of trapped particles over the time of 405 days. This allowed us to derive upper limits on the partial pressure of hydrogen $p_{\mathrm{upper,H}} < 1.2 \times 10^{-18}\,\mathrm{mbar}$ and helium $p_{\mathrm{upper,He}} < 2.7 \times 10^{-18}\,\mathrm{mbar}$. Elastic collisions can lead to mode heating. Their rate can be estimated by [130, 131, 132]

$$\gamma_e = n_d \langle \sigma v \rangle \approx 1.23 \times 10^5 n_d \tilde{v}^{1/3} \alpha^{2/3}, \tag{5.37}$$

with polarizability α [133, 134], cross section σ, relative velocity $\tilde{v} = \sqrt{2k_B T/\mu}$, reduced mass μ, and local density $n_d = p/(k_B T)$. We obtain $\gamma_{e,\mathrm{H}} < 5 \times 10^{-7}\,\mathrm{s}^{-1}$ and $\gamma_{e,\mathrm{He}} <$

Observed $\sqrt{S_V}$	$225(54)\,\mathrm{pV\,Hz^{-1/2}}$
Axial detection system	$1.5\,\mathrm{pV\,Hz^{-1/2}}$
RC filter stages	$< 1\,\mathrm{pV\,Hz^{-1/2}}$
Electrode Johnson noise	$3 \times 10^{-3}\,\mathrm{pV\,Hz^{-1/2}}$
Blackbody radiation	$\omega_+ \times S_E(\omega_+) \approx 5 \times 10^{-14}\,\mathrm{V^2 m^{-2}}$
Background pressure	$\zeta_+ < 4 \times 10^{-9}\,\mathrm{s^{-1}}$
Grounded but unfiltered RF line	unknown
external EMI noise	$\omega_+ \times S_E^{\mathrm{EMI}} \approx 2 \times 10^{-6}\,\mathrm{V^2 m^{-2}}$

Table 5.2.: Parasitic voltage fluctuation and heating rate contributions. None of the components inside the experimental apparatus can be accounted for the observed voltage fluctuation on the trap electrodes. The observed electric field noise might be related to coupling of the external EMI noise to the experiment through the grounded but unfiltered radio frequency line depicted in Fig. 5.1. For details, see text.

$5 \times 10^{-7}\,\mathrm{s^{-1}}$, which is by 4 orders of magnitude lower than the observed transition rates ζ_+. Note that we apply the ideal gas equation to obtain n_d, and that the derivation of γ_e includes an average over a thermal distribution. Both is not necessarily justified in the XHV-range of the BASE apparatus, which is why the extracted rates should be understood as a rough estimate.
We might also calculate the rate of inelastic scatter γ_i, which is related to particle loss. Here, the ion polarizes neutral background gas atoms and thus induces collisions, for which an upper limit is given by the Langevin rate [130, 131]:

$$\gamma_i = n_d \sigma v = n_d q \sqrt{\frac{\pi\alpha}{\epsilon_0 \mu}}, \tag{5.38}$$

we obtain $\gamma_{i,\mathrm{H}} \approx \gamma_{i,\mathrm{He}} < 4 \times 10^9\,\mathrm{s^{-1}}$.

Johnson noise due to the non-vanishing resistance of the electrode materials induces voltage fluctuations on the electrode surface. We estimate this effect by modeling the electrodes as rings with inner diameter r, outer diameter R, and depth d. We then divide the electrode into n slices width length 2π times the intermediate radius, width d, and height $(R-r)/n$. The electrode resistance R_e is then given by

$$R = \rho \frac{l}{A} = \rho \sum_i \frac{(R-r)/n}{2\pi\,(R-(i-1)(R-r)/n)\,d}, \tag{5.39}$$

with cross-sectional area A, and length l. With $\rho = 1.68 \times 10^{-10}\,\Omega\mathrm{m}$ (residual resistance ratio RRR=100), $r = 1.8\,\mathrm{mm}$, $R = 7.5\,\mathrm{mm}$, $d = 2\,\mathrm{mm}$, we obtain $S_V(\omega) = \sqrt{4k_BTR} \approx 3 \times 10^{-3}\,\mathrm{pVHz}^{-1/2}$. The noise sources present in the experimental apparatus are summarized in Tab. 5.2.

In order to roughly estimate the ambient noise in the AD hall, we follow the approach given in [114]. The spectral noise density of electromagnetic interference (EMI) is given as a multiple of the blackbody radiation, $S_E^{\mathrm{EMI}} = F_a \times S_E^{\mathrm{BB}}$. F_a is the pickup of a perfect antenna. Inside commercial buildings, a noise of 120 dB at 1 MHz that declines with ω^{-5} has been reported [135]. This translates to an electric field noise density $S_E^{\mathrm{EMI}}(\omega) \approx 10^{-10} \times (\omega/(1\,\mathrm{MHz}))^{-3}\,\mathrm{V^2m^{-2}Hz^{-1}}$ [114]. At ω_+, we would then expect a scaled noise density of $\omega_+ \times S_E^{\mathrm{EMI}} \approx 2 \times 10^{-6}\,\mathrm{V^2m^{-2}}$. The ambient noise in an accelerator hall is likely to exceed the ambient noise level of commercial buildings, and will depend on the operation of electronic equipment that are only occasionally operated. However, this allows to estimate that the external noise in the experiment is at least suppressed by roughly five orders of magnitude. The residual noise might be coupled into the experiment through the grounded but unfiltered spin flip line depicted in Fig. 5.1.

5.7. Comparison to other ion trap experiments

We have measured and characterized the heating rates in the BASE analysis trap. Our study [51] is the first detailed investigation of heating rates in a cryogenic Penning trap. By employing the continuous Stern-Gerlach effect [79] and observing the differential axial frequency Allan deviation, we have measured transition as low as 6(1) quanta per hour and heating rates below $0.1\,\mathrm{h}^{-1}$. Our average mode energy increase is on the order of peV/s (see Fig. 5.7), demonstrating a to-date unique stability in experiments with trapped ions.

By conducting magnetron dependent transition rate measurements, we were able to identify electrode voltage noise driven electric field fluctuations to be the dominant noise mechanism for magnetron radii $6\,\mu\mathrm{m} \leq \rho_- \leq 65\,\mu\mathrm{m}$. We were able to constrain the effect of anomalous heating to $\omega_+ \times S_E(\omega_+) \leq 8.8^{+4.0}_{-3.2} \times 10^{-12}\mathrm{V^2m^{-2}Hz^{-1}}$, which is a factor of 1800 lower than observed in the Paul trap showing the lowest noise [122] and by a factor of 230 lower than the lowest values measured in a Penning trap [121]. Unlike the referenced experiments in Fig. 5.7, our transition rates were measured with particles that were not laser cooled and energetically far above their ground state.

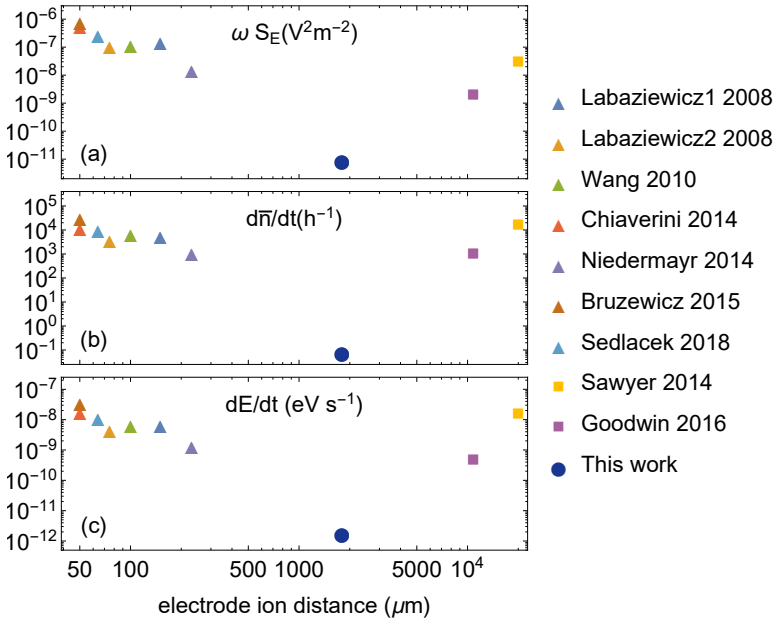

Figure 5.7.: This plot compares mode stabilities measured in different ion trap experiments as a function of the respective electrode-ion distance d. (a) shows the electric-field noise spectral density $S_E(\omega)$ scaled by the angular trap frequency ω. The scaling with ω is done following the literature convention in order to account for the typical $1/f$-characteristic of electromagnetic noise. (b) depicts the respective heating rates $\dot{\bar{n}}$. (c) highlights the energy increase dE/dt. The triangles represent measurements carried out in cryogenic 2D-Paul traps [136, 137, 138, 130, 122, 139, 119]; squares denote measurements in Penning traps on single ions [121] and ion crystals [140, 141] conducted at room temperature. Our work [51] constitutes the first detailed heating rate study in a cryogenic Penning trap and is plotted as a blue circle.

The fact that our heating rates are much lower than in cryogenic Paul traps might be partially explained by the different electrode-ion distance d, which is for BASE 1.8 mm, but for most cryogenic Paul traps between 50 μm and 200 μm. It is not surprising that heating rates in a cryogenic Penning trap are much lower than in room-temperature Penning traps [140, 121, 141], as it has been reported that the operation of Paul traps at cryogenic temperatures decreased the observed electric field noises by orders of magnitude [136]. With the observation of much lower heating rates and electric field noise, we contribute to the ongoing discussion about the origin of *anomalous heating*.
While the data analysis presented here was mainly carried out in the framework of this thesis, the unique stabilities presented here are the result of about 15 years of experimen-

tal development carried out in the framework of the Mainz proton experiment [80] and the BASE experiment at CERN [43]. This mode stability is the necessary prerequisite for conducting a multi-trap measurement of the antiproton/proton magnetic moment like [28, 29].

6 | Improved direct limits on the antiproton lifetime

The unique reservoir trap technology [49] was developed at the BASE experiment at CERN. It allows to store a clean cloud of particles in the reservoir trap and to extract individual particles whenever needed for the experimental operation. To this end, a voltage configuration is applied to the electrode stack such that the stored reservoir experiences a double well potential, which divides the reservoir cloud into two clouds. The fraction of particles in both clouds can be tuned by adjusting the voltage configuration. Subsequently, the cloud contents can be studied by analyzing the particle signal on the axial detector, and a particle number can be extracted. Both clouds can be re-merged, and another separation procedure can be carried out until a single ion is separated. The described scheme is referred to as "potential tweezer".
In this way, the reservoir trap allows for continuous operation regardless of the Antiproton Decelerator beam times that are restricted by CERNs year-end technical stops (YETS) and CERNs long shutdowns (LS). For a high-precision experiment on trapped particles, these time windows are especially interesting as the experiment is then not hampered by ambient temperature fluctuations and electro-magnetic background fields present in the AD hall related to the operation of the AD and the experiments within, such as high voltage ramps, magnetic field ramps, radio frequency signals, and more. As the reservoir trap allows for in principle arbitrarily long experimental operation times [48], it gives the experimental operators the opportunity to study the experimental apparatus in great detail and to reach the most favorable experimental conditions achievable with the current setup - this is especially of advantage as a warm-up and cool-down cycle requires at least one month of time plus additional time for the implementation

of hardware upgrades and time required to commission and optimize the apparatus, which usually takes several months. Beyond these valuable experimental advantages, the study of the antiproton reservoir also yields an attractive physics perspective, as these data allow to place the to-date most stringent directly measured limits on the antiproton lifetime [48]. As the antiproton reservoir is an essential prerequisite for performing experiments on antiprotons in the BASE apparatus, the entire experimental team contributes to the reservoir maintenance. The data presented in this thesis are thus the results of collaborative efforts, to which the author contributed during his time as a master student (2016 campaign) and as a PhD student (2017-2019). Similar results will also be discussed in the PhD thesis of James Brydges-Harrington [52].

6.1. Motivation

As the CPT invariance requires particles and their antimatter counterparts to exhibit (apart from the sign) identical fundamental properties, such as charge, mass, magnetic moment or lifetime, a comparison of τ_p and $\tau_{\bar{p}}$ yields a test of CPT invariance. The proton lifetime τ_p has been experimentally constrained up to 3.6×10^{29} a [142]. To this end, the decay channel $^{16}\mathrm{O} \rightarrow {}^{15}\mathrm{N}^*$ has been considered, and gamma ray signals produced by de-excitation of $^{15}\mathrm{N}^*$ have been searched for. For the antiproton lifetime, a lower limit $\tau_{\bar{p}} > 800\,000$ a was derived by comparing the cosmic-ray background flux with theoretical predictions [143]. However, it should be noted that this limit is only valid assuming that the models applied for antiproton production, propagation and interaction in the framework of the Standard Model of particle physics are accurate. Direct limits have been obtained by studies performed at Fermilab's Antiproton Accumulator, where about 10^{12} antiprotons were circulated. The APEX collaboration placed a detector around this storage ring and established limits on 13 different decay channels, ranging from $\tau\left(B(\bar{p} - e^-\omega)\right) > 2 \times 10^2$ a to $\tau\left(B(\bar{p} - e^-\gamma)\right) > 7 \times 10^5$ a [144, 145]. Some antiproton decay channels which have been favored by Grand Unified Theories, such as for example $\bar{p} \rightarrow \nu_{e,\mu}K^-$ [146], have not been studied by the above experiments. Ultimately, both measurement methods, the cosmic flux analysis and the detector search, rely on certain model assumptions and constrain the antiproton lifetime indirectly.

In the BASE apparatus on the other side, the antiprotons stored in the reservoir trap are continuously monitored. This enables a direct measurement of a lower limit for the antiproton lifetime that is also sensitive to any yet unexpected antiproton decay channel,

without relying on model assumptions.

6.2. Measurement principle

The reservoir trap is a five-pole Penning trap equipped with a resonant LC detection circuit for the axial motion. It is located upstream of the precision trap and features the same geometry (see Fig. 4.1). The reservoir trap is controlled using a dedicated computer disentangled from the rest of the experiment. Experimental operations are only performed for magnetron cooling before and after each cryogenic filling cycle, for occasional contaminants cleaning and for extracting single particles whenever needed for the experimental operation. Trap contaminations are related to secondary electrons generated from beta-decays of the partially activated degrader foil and trap stack. They are detected by decreasing signal-to-noise ratios and drifting axial frequencies and are afterwards removed by means of the methods described in [43, 84, 86]. Contaminants are removed from the trap by firstly applying either broadband or frequency specific radio-frequency pulses, and subsequently lowering the trapping potential for a short period of time. The excited contaminants will then leave the shallow potential, while the reservoir cloud remains trapped, as their oscillation modes were in thermal equilibrium with the axial detection system prior to lowering the potential (axial) or purposely cooled by sideband cooling prior to the voltage ramp. Electrons can also be removed by performing an "electron kick-out", where a fast voltage ramp is applied to a kick-out electrode, whose biasing line is not filtered and thus allows for rapid voltage changes. Due to the lower mass of the electron and the resulting 40 times higher axial oscillation frequency, the electrons leave the trap during the kick-out, while the reservoir remains trapped [84]. For most of the experimental time, axial spectra are continuously recorded at a rate of about once per minute without further experimental action.
A single trapped ion with axial motion being in thermal equilibrium with a dedicated LC detection circuit leads to a voltage dip in the Fourier transformed noise spectrum with a FWHM dip width given by [57]

$$\delta\nu_z = 1/(2\pi) \times 1/\tau_z = 1/(2\pi)(R_p/m_{\bar{p}})(q_{\bar{p}}/D_{\text{eff}})^2, \tag{6.1}$$

with cooling time constant τ_z, effective electrode distance D_{eff} and effective detector parallel resistance $R_p = \omega_z QL$. The axial detector in the reservoir trap has a resonance

frequency $\omega_{\mathrm{res}}/(2\pi) \approx 790\,\mathrm{kHz}$ and an inductance $L = 1.675(25)\,\mathrm{mH}$. Its quality factor Q varies from run to run due to different parasitic losses. In 2017/2018, the quality factor was $Q \approx 28\,500$ resulting in an effective parallel resistance $R_p = 237(4)\,\mathrm{M\Omega}$. The effective electrode distance $D_{\mathrm{eff}} = 10.03\,\mathrm{mm}$ is computed by potential theory and does not vary significantly within the manufacturing accuracy.
For a clean cloud of N trapped ions, the dip width as a function of particle number increases linearly with $\delta\nu_z(N) = N \times \delta\nu_z(1)$ [57], which means that N can be determined by comparing the single ion dip width and the multi-ion dip width,

$$N = \delta\nu_z(N)/\delta\nu_z(1) = \delta\nu_z(N)/ \times \left(\frac{1}{2\pi}\frac{R_p}{m}\frac{q^2}{D^2}\right)^{-1}. \tag{6.2}$$

Another way of determining N is by extracting single particles and evaluating the discrete changes in $\delta\nu_z(N)$. Both particle number calibration agree well for the numbers of trapped particles N at which the BASE reservoir has been operated so far.
In order to estimate a lower lifetime limit, the exposure time is obtained by integrating $N(t)\mathrm{d}t$. The total exposure is then given by $T_{\mathrm{exp,tot}} = \sum T_{\mathrm{exp},i}$, which allows to combine the data from different measurement campaigns. As antiproton decays can be described by Poisson statistics, the probability for obtaining n decays during the exposure time T_{exp} is given by

$$p(n;\lambda) = \lambda^n \exp(-\lambda)/n!, \tag{6.3}$$

with $\lambda = T_{\mathrm{exp}}/\tau_{\bar{p}}$ depending on the antiproton lifetime $\tau_{\bar{p}}$. The confidence level $\mathrm{CL}(\lambda)$ for obtaining 0 events at a given rate λ is then given by $1 - p(0;\lambda)$,

$$\mathrm{CL} = 1 - p(0;\lambda). \tag{6.4}$$

Antiproton lifetime limits $\tau_{\bar{p}}$ are then given by equating Eq. 6.4 with the desired confidence level.

6.3. Antiproton lifetime limits measured in 2016

During the successful 2015/2016 beam time, we trapped a reservoir of initially 18 antiprotons for the course of 405 days, which enabled the first dedicated measurement on limits on the antiprotons lifetime performed in the BASE apparatus [48]. The cor-

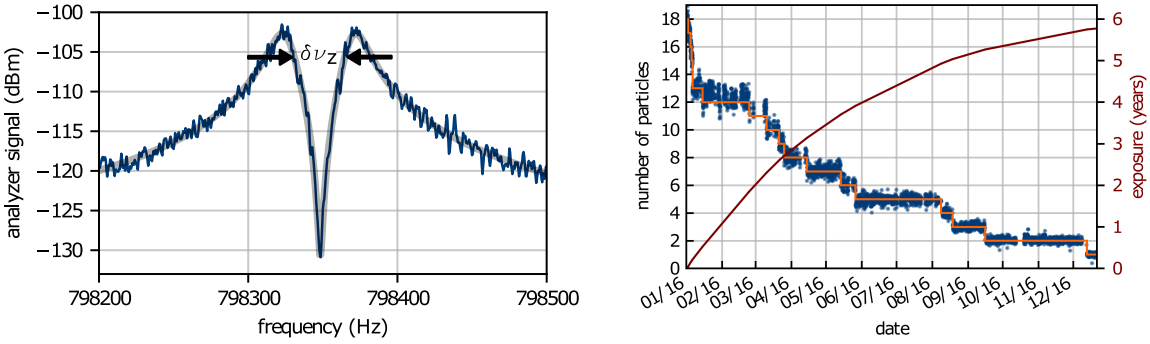

Figure 6.1.: Direct measurement on constraining the antiproton lifetime $\tau_{\bar{p}}$ performed in 2016. Left: Fast Fourier transformed signal of the axial detector in the reservoir trap (blue) fitted with the theoretical lineshape (black). A clean cloud of cold antiprotons shorts the Lorentzian-shaped Johnson noise of the detector. From the dip width $\Delta\nu_z$, the number of trapped particles is extracted. Right: Determination of the exposure in the reservoir trap. In blue, the number of trapped particles derived from the dip width is displayed, the orange line denotes the corresponding integer numbers of trapped particles. The total exposure is plotted in red. The particle number is only reduced when a single antiproton is extracted from the reservoir trap into the measurement traps, which becomes necessary when a particle gets lost during experimental routines. All particle losses in the measurements traps are related to experimental operations or distinct events such as occurrence of contaminants. No antiproton decay or annihilation is observed. Antiprotons were trapped for in total 405 days. Figure adapted from [48].

responding data are depicted in Fig. 6.1. From the reservoir data, an exposure time $T_{\mathrm{exp,res}} = 5.77\,\mathrm{a}$ is obtained (red line, Fig. 6.1) by integrating $N(t)\mathrm{d}t$. Two antiprotons trapped in the analysis trap and the precision trap yielded $T_{\mathrm{exp},2} = 1.72\,\mathrm{a}$. In 2015, we obtained $T_{\mathrm{exp},3} = 2.61\,\mathrm{a}$. In the 2014 beam time, we obtained $T_{\mathrm{exp},4} = 1.56\,\mathrm{a}$ [49], resulting in a total exposure time of $T_{\mathrm{exp,tot}} = 11.66\,\mathrm{a}$.

At a confidence level of 90 %, we obtain a lower lifetime limit of $\tau_{\mathrm{lower},\bar{p}} = 5.06\,\mathrm{a}$, and $\tau_{\mathrm{lower},\bar{p}} = 10.2\,\mathrm{a}$ at a confidence level of 68 %. Following the treatment given in [147], upper limits on the partial pressures of residual helium and hydrogen atoms $p_{\mathrm{upper,H}} < 1.2 \times 10^{-18}\,\mathrm{mbar}$ and $p_{\mathrm{upper,He}} < 2.7 \times 10^{-18}\,\mathrm{mbar}$ were derived.

This measurement constituted the at-this-time best direct measurement on $\tau_{\mathrm{lower},\bar{p}}$, improving on the previous best limit of $\tau_{\mathrm{lower},\bar{p}} = 1.56\,\mathrm{a}$ [49] by a factor of more than seven.

6.4. Antiproton limits measured in 2017 - 2019

During the 2017/2018 run and the 2018/2019 run, reservoir spectra have been continuously recorded, which enables a significant improvement upon our 2016 lifetime constraints [48].
In both cases an antiproton bunch was injected into the trap close to the end of CERN's annual shutdown, and the reservoir was kept and continuously monitored while precision measurements were conducted in the homogeneous precision trap. More than 80 % of the presented results were recorded during accelerator shutdown. For the data-set sampled during the 2017/2018 run, a time span of 201.5 days is considered in which 239 892 reservoir spectra were recorded, for the 2018/2019 run 170 789 spectra were evaluated, covering a time span of 230 days. A reservoir screenshot featuring 72 trapped antiprotons

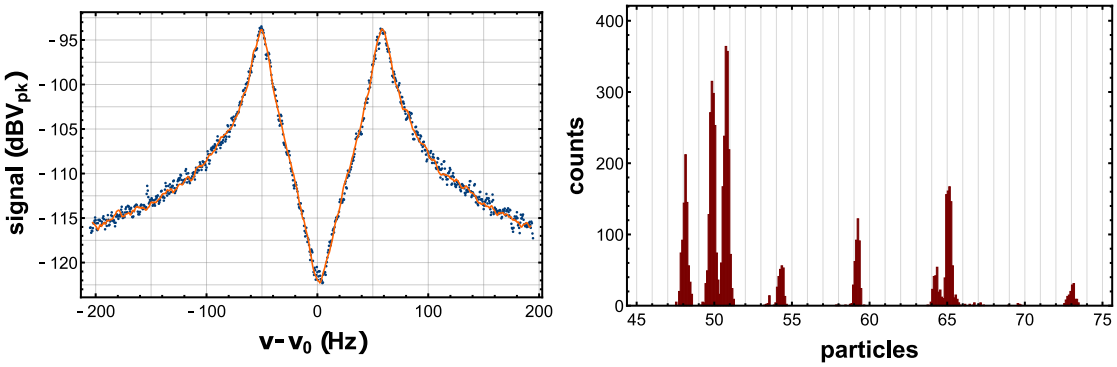

Figure 6.2.: On the left, the Fourier transformed spectrum of a mixed cloud 72 antiprotons and hydride ions is shown, which short the noise spectrum of the axial detector. The dip width corresponds to 72 particles. The blue data points show the raw data, which are fitted by the solid orange line. On the right, histograms of the calibrated particle numbers are plotted. The particle number calibration is done by discriminating the sub-distributions and performing a likelihood evaluation on the respective particle numbers. By considering the discrete differences in each sub-distribution, a single-ion dip width is calibrated which agrees well with the theoretical prediction.

and hydride ions (H^-) is depicted in Fig. 6.2 (left), with the reservoir cloud shortening the Fourier transformed voltage spectrum of the axial resonator. A histogram showing different reservoir contents for 2018/2019 run is depicted on the right side. This histogram is obtained by applying Eq. 6.2, where $\delta\nu_z$ is determined by independent least-squares fits. The uncertainty on the resonator inductance L leads to an uncertainty of 85 mHz in the single particle dip width. Compared to the 2016 reservoir, in the

2017/2018 run and the 2018/2019 run a much larger reservoir has been trapped, which is why the resulting calibration has to be tested using likelihood ratio tests [148]. To this end, sub-distributions of the measured line-widths were discriminated (see Fig. 6.2, right), and individual Gaussian distribution parameters were determined, p-values for the corresponding Kolmogorov-tests on the order of 0.67 justify the assumption that the subdistributions are distributed according to Gaussian distributions. The number of trapped particles N is determined from likelihood tests by comparing the hypothesis N with the hypotheses $(N+1, N-1)$ with a fidelity of above 95 %, being in consistency with the single-ion dip width $\delta\nu_z = 5.77(9)$ derived following Eq. 6.1 from independent detector inductance measurements.

The number of particles in the reservoir and the calculated exposure times for the

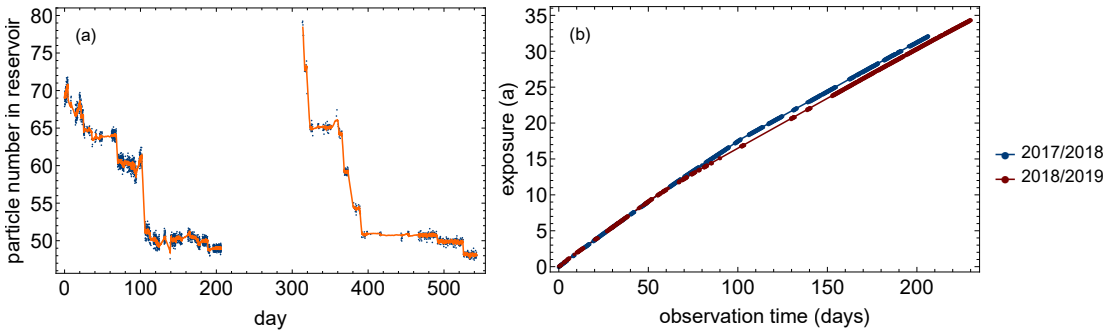

Figure 6.3.: Antiproton reservoir data recorded during the 2017/2018 and 2018/2019 campaign. (a) shows the number of particles in the reservoir, which were computed following the approach outlined in the text by fitting individual detector spectra. Afterwards the number of particles is calibrated both by comparing the measured dip width to the theoretical single-ion dip width and by monitoring discrete jumps in the fitted dip width. The blue points depict the individual data while the orange line shows a moving average. Only every tenth extracted particle number is plotted. Every step in particle number is related to documented experimental interventions like particle extractions or contaminants cleaning. The exposure (b) is obtained by integrating the data depicted in (a). For the 2017/2018 data set, an exposure time of 31.3 a is obtained, for 2018/2019, the exposure time is 34.1 a.

2017/2018 run and the 2018/2019 run are depicted in Fig. 6.3. (a) depicts the number of trapped particles in the reservoir, where the blue data points shows the individual particle numbers extracted from each spectrum fit, and the orange line indicates a moving average. Dip width fluctuations are related to uncertainties in the fitting routine due to the finite acquisition time of each spectrum. In addition to that, secondary electrons generated by beta-decays in the partially activated degrader foil and the trap stack lead

to rare contamination events. The electrons accumulate over time and modify the effective trapping potential experienced by the reservoir such that the axial frequency is slightly reduced and the signal-to-noise ratio is decreased. This can eventually lead to a slight overestimation of the dip width, which is considered in the life time evaluation.
Every reduction in particle number is related to explicit experimental actions performed on the antiproton reservoir, such as the extraction of particles from the reservoir into the measurement traps. During the first weeks of experimental operation the experimental setup is commissioned, which leads to an increased particle consumption. The discrete jump after 65 days for 2017/2018 is related to an unscheduled power-cut that caused the loss of a particle in the measurement traps. Afterwards, three particles were extracted of which two were dumbed in the precision trap when the particle number was reduced to one. After about 100 days, the first measurement campaign was completed, and an extensive contaminants cleaning has been performed, during which nine trapped particles were lost. It is suspected that these losses were caused by parasitic noise in the particle's frequency range on the strong radio frequency drives used for trap cleaning. In the subsequent months, systematic measurements and an additional precision measurement campaign took place, during which only three additional particles had to be extracted from the reservoir. The 2017/2018 campaign was completed after in total 201 days. During this time, we extracted 21 particles from the reservoir, all discrete jumps in the reservoir trap content depicted in Fig. 6.3 (a) were related to these extractions. No change in the particle number uncorrelated to experimental operations has been observed, which could indicate an "antiproton decay".
During the 2018/2019 campaign, we recorded a slightly more stable antiproton reservoir likely being related to the exchange of the antiproton degrader, which was then only activated by the few antiproton capturing shots in this specific campaign. After the initial commissioning period, we consumed only a single particle during the course of 3.5 months, and only four additional during a second period of 5.5 months. Three discrete jumps in the number of trapped particles are observed in the time between day #350 and day #400. All of these events are related to the extraction of single particles for performing measurements in the precision trap. We assume that these particle-losses occur during the re-merging, which is performed when a small cloud of particles instead of a single particle is extracted, as the number of particles lost during the extraction is correlated to the number of extraction attempts during this run. This behavior was not observed during other experimental campaigns. No particle loss in the reservoir is

Run	Run-Time	Spectra	Particles Consumed	Exposure
2017/2018	201.5 days	239 892	21	31.28 a
2018/2019	231.0 days	170 789	29	34.12 a
Total	432.5 days	410 581	50	64.40 a

Table 6.1.: Summary on the reservoir data recorded from 2017 - 2019.

observed during times when no experimental actions apart from spectrum sampling are performed on the reservoir. Particle losses in the precision trap can be clearly correlated to experimental actions such as shuttling the content of a contaminated trap. The particle loss in the precision trap around day # 390 for instance was related to the fact the connection between the BASE experiment and the electrical ground of the AD hall was cut during construction works related to CERNs long shutdown 2 (LS2). Afterwards, the reference grounds of the BASE voltage sources started drifting in a uncontrollable way, which lead to a loss of the particles trapped in the precision trap. The exposure time for both campaigns (Fig. 6.3 (b)) is evaluated by projecting the trap content to integer numbers and integrating these over time. During the 2017/2018 campaign, an exposure of $T_{\mathrm{exp}} = 31.3\,\mathrm{a}$ has been obtained, for the 2018/2019 campaign, an exposure of $T_{\mathrm{exp}} = 34.1\,\mathrm{a}$ is measured.
Combining the results from both experimental campaigns, we stored two mixed clouds consisting of antiproton and hydride ions with an exposure time of $T_{\mathrm{exp}} = 65.4\,\mathrm{a}$. During the over 400 days of experimental operation, in total 50 particles were lost, of which 18 particles were lost during experimental operations (miscommunicating devices, powercuts, ...), 16 particle losses were related to human error during experimental operation and 26 particle losses occurred during particle extractions and reservoir cleaning procedures.

6.4.1. Antiproton content of the reservoir

Unlike in the 2016 run, when a pure reservoir of antiprotons was trapped, from 2017 - 2019, a mixed cloud consisting of antiprotons and hydride ions was trapped in the campaigns that took place from 2017 - 2019. In order to compute a lower limit for the antiproton lifetime, the ratio of antiprotons and hydride ions in the reservoir has to be estimated first. To this end, we consider the history of extraction attempts and use the ratio of single extracted antiprotons to single extracted hydride ions in order to estimate

the ratio of both ion species in the reservoir[1]. For extracting single antiprotons, the potential tweezer scheme outlined in [49] is used. The species of the single extracted ion is determined by shuttling the ion to the precision trap and measuring its axial oscillation frequency ν_z, which differs by about 350 Hz in the BASE precision trap due to the different masses of antiprotons and hydride ions.
The probability of extracting a specific number of antiprotons ions from a reservoir consisting of N particles is given by

$$P_S(N_{\bar{p}}) = \prod_{k,1}^{N} P_k(N_k, N_{\bar{p},k}), \tag{6.5}$$

with the estimator $N_{\bar{p},k}$ denoting the number of antiprotons in the reservoir. The probability $P_S(N_{\bar{p}})$ is maximized, and initial numbers of antiprotons $N_{\bar{p},2018} = 36(7)$, $N_{\bar{p},2019} = 19(8)$ are obtained for the 2017/2018 and 2018/2019 campaigns, with uncertainties given at the one-sigma confidence level.

6.5. Improved antiproton lifetime limit

In addition to the particles stored in the reservoir trap, a single antiproton was stored for the full period of both measurement campaigns in the BASE precision trap (denoted by other in Tab. 6.2). We also add the exposure times obtained in the 2016 measurement [48] and in the 2014 antiproton run [49], see Tab. 6.2. The total exposure time $T_{\mathrm{exp,tot}}$ is then given by $T_{\mathrm{exp,tot}} = \sum_i T_{\mathrm{exp},i} = 33.03\,\mathrm{a}$, with a lower limit of 29.80 a (CL = 0.68). Applying the Poisson model, this results in a mean limit on the directly measured antiproton lifetime of $\tau_{\mathrm{lower},\bar{p}} = 29.03\,\mathrm{a}$, with a lower limit ($T_{\mathrm{exp,tot}} > 29.8\,\mathrm{a}$) given by $\tau_{\mathrm{lower},\bar{p}} = 26.15\,\mathrm{a}$ at confidence level CL = 68 %, which is an improvement of a factor of about 2.6 compared to our previous results [48].
Following the arguments presented in [147, 48], these results can be interpreted in order to constrain the background gas pressure in the 1.2 l volume trap can (assuming that antiprotons are stable within experimental observation periods). We obtain lower limits in the partial pressures for hydrogen $p_{\mathrm{H}} < 0.46 \times 10^{-19}\,\mathrm{mbar}$ and helium $p_{\mathrm{He}} < 1.04 \times 10^{-19}\,\mathrm{mbar}$. Naively using ideal gas laws to translate these pressures to

[1] As both experimental campaigns were terminated by unforeseen events, we did not have the chance to selectively remove one ion species and to count the remaining particles in order to determine the exact reservoir trap content.

Run	Exposure Time	Lower Limit
2017/2018 RT	16.08 a	12.09 a
2017/2018 other	0.55 a	0.55 a
2018/2019 RT	8.42 a	4.87 a
2018/2019 other	0.63 a	0.63 a
2016	10.10 a	10.10 a
2014	1.56 a	1.56 a
Total	33.03 a	29.80 a

Table 6.2.: Summary on all antiproton exposure times recorded in BASE from 2014 - 2019.

particle numbers, and assuming the "gas" is thermalized to the environmental experiment temperature of $\approx 5\,\mathrm{K}$, these pressures would correspond to about 800 residual hydrogen atoms and 1700 helium atoms in our trap can.

6.6. Discussion

An improved lower limit on the antiproton lifetime $\tau_{\mathrm{lower},\bar{p}} = 26.15\,\mathrm{a}$ is derived by evaluating the ion reservoir trapped in the BASE reservoir trap and the BASE precision trap during the measurement campaigns performed from 2017 to 2019, which is an improvement of a factor of 2.6 compared to our previous best measurement [48], and more than 100 compared to the best direct values obtained by other experiments [149]. Our direct measurement is model-insensitive and complimentary to indirect measurements [144], which are able to place much higher limits but are only sensitive to certain types of possible antiproton decays.

The exposure is determined by integrating the number of trapped particles over time, which itself is determined by analyzing the continuously recorded axial detector spectra and computing the number of trapped particles from the well-known lineshape [57]. The fraction of antiprotons trapped in the mixed reservoir cloud consisting of antiprotons and hydride ions is estimated based on the statistics of non-destructively extracted single ions [49]. While a total exposure time $T_{\mathrm{exp,tot}} = 64.4\,\mathrm{a}$ is obtained, only $T_{\mathrm{exp,tot},\bar{p}} > 29.8\,\mathrm{a}$ can be attributed to antiprotons. In the future, BASE is considering to setup a dedicated antiproton lifetime experiment. As discussed in [48], we consider it feasible to reach trap-based lifetime limits of order $10^3\,\mathrm{a}$ to $10^4\,\mathrm{a}$, with such a dedicated experiment.

7 | Optimization of a Penning trap

A Penning trap offers a well-isolated environment for studying individual charged particles and isolating them from the environmental influences. In order to serve this purpose best, inhomogeneity parameters of the trap have to be well-characterized. Some of these parameters can be tuned such that they have negligible influence on cyclotron frequency measurements at the targeted level of precision. Some others can even be used for specific purposes, such as the quadratic inhomogeneity generated by the magnetic bottle in the BASE analysis trap [79, 80, 82], which is essentially needed for the g-factor measurements. The inhomogeneities can either be studied by means of dip methods - methods, where the eigenfrequencies are mostly determined with the particle's axial motion being in thermal equilibrium with the axial detection system, or by means of peak methods, where peak signals generated on the cyclotron detector by the excited cyclotron motion of the ion are studied. This chapter will review how trap inhomogeneities can be determined, characterized, tuned and used for systematic studies and frequency measurements.

7.1. Dip methods

This section reviews some of the essential methods for optimizing and characterizing a high-precision Penning trap by means of dip methods. Since most of the methods outlined here have been described in previous theses (for instance [72, 150, 84, 75]), they will only be explained briefly and the reader is redirected to the respective literature for further information.

7.1.1. Tuning ratio scans

Tuning ratio scans are one of the most essential methods for optimizing a Penning trap. Here, the ratio between the voltage V_r applied to the central ring electrode and the voltage V_{corr} applied to the corrections electrodes, which is known as the tuning ratio $\mathrm{TR} = V_{\mathrm{corr}}/V_r$, is varied and the properties of the axial frequency dip such as the signal-to-noise ratio (SNR) as a function of the tuning ratio are investigated. The first anharmonic term in the electrostatic potential C_4 can be tuned to zero by adjusting the tuning ratio, since $C_4 = D_4 \times \mathrm{TR} + E_4$ (Eq. 2.16). $D_4 = 1.28(4) \times 10^9\,1/\mathrm{m}^4$ is given by the trap geometry. Its uncertainty of about three percent arises from inserting the typical manufacturing tolerances of order $10\,\mu$m and the typical uncertainties on the trap voltages arising from offset potentials. Tuning ratio scans allow to determine the temperature of the axial mode. To this end, we first consider the axial frequency shift, which arises in the presence of the C_4 coefficient:

$$\nu_z\left(Z_0, C_4\right) = \nu_{z,0}\left(1 + \frac{3}{4}\frac{C_4}{C_2}Z_0^2\right), \tag{7.1}$$

with the RMS amplitude given by $z_{\mathrm{rms}} = Z_0/\sqrt{2}$. During the axial frequency measurement, the particle is in thermal equilibrium with the detection system at temperature T_z. The rms amplitude is then given by $z_{\mathrm{rms}} = \left(k_B T_z / \left(m\left(2\pi\nu_{z,0}\right)^2\right)\right)$. We may rewrite the equation above to

$$\nu_z = \nu_{z,0}\left(1 + \frac{3}{4}\frac{C_4}{C_2}\frac{2E_z}{m\left(2\pi\nu_{z,0}\right)^2}\right) = \nu_{z,0}\left(1 + \frac{3}{4}\frac{C_4}{C_2^2}\frac{E_z}{qV_r}\right) = \nu_{z,0}\left(1 + \frac{3}{4}\frac{C_4}{C_2^2}\frac{k_B T_z}{qV_r}\right). \tag{7.2}$$

The latest conversion is also explicitly confirmed by solving the equations of motion numerically. For the BASE precision trap, we obtain $\Delta\nu_z = \nu_z - \nu_{z,0} = 33.9\,\mathrm{Hz/mU/K}$, with the unit milliunit (mU), $1\,\mathrm{mU} = 10^{-3}$.

When the trapped particle is tuned into resonance with the axial detection system and reaches a thermal equilibrium with the detector, its axial motion acts like a series LC circuit that shorts the thermal voltage noise of the detector at the particle oscillation frequency, which results in a dip in the Fourier transformed voltage spectrum. The particle-detector interaction and the dip detection is discussed in Sec. 2.3.1 in detail. The unperturbed dip lineshape χ is given by the real part of the impedance of the equivalent circuit of the particle-detector interaction. Here, we neglect the Lorentzian

lineshape of the axial detector as its FWHM is much higher compared to the axial dip width (compare Eq. 2.33). The dip lineshape $\chi(\nu)$ is given by

$$\chi\left(\nu\right) = R_p \frac{\left(\nu - \nu_{z,0}\right)^2}{\left(\nu - \nu_{z,0}\right)^2 + \left(\gamma/\left(4\pi\right)\right)^2}, \tag{7.3}$$

with γ given by the inverse cooling time constant τ, $\gamma = 1/\tau$, and the dip width $\delta\nu_z$ given by $\delta\nu_z = \gamma/\left(2\pi\right)$. The energy of the axial mode is described by the Boltzmann distribution, with a probability density function $f(E_k)$ of the energy E_k:

$$f(E_k) = \frac{1}{k_B T_{z,0}} \exp\left(\frac{-E_k}{k_B T_{z,0}}\right). \tag{7.4}$$

Since the cooling time constant $\tau \approx 30\,\mathrm{ms}$ given by the inverse damping constant γ is small compared to the FFT averaging time of about 1 min, $t_{\mathrm{avg}} \gg \tau$, the Boltzmann distribution of E_z is convolved into the lineshape, resulting in a modified lineshape $\tilde{\chi}$

$$\begin{aligned}\tilde{\chi}\left(\nu, T_z\right) &= \frac{1}{T_z}\int \mathrm{d}T\, \chi(\nu, T_z) \exp\left(-T/T_z\right) \\ &= \frac{R_p}{T_{z,0}} \int_0^\infty \mathrm{d}T \frac{\left(\nu - \nu_{z,0}\left(1 + \frac{3}{4}\frac{C_4}{C_2^2}\frac{k_B T}{q V_r}\right)\right)^2}{\left(\nu - \nu_{z,0}\left(1 + \frac{3}{4}\frac{C_4}{C_2^2}\frac{k_B T}{q V_r}\right)\right)^2 + \left(\delta\nu_z/2\right)^2} \exp\left(-\frac{T}{T_{z,0}}\right).\end{aligned} \tag{7.5}$$

The modification of the lineshape due to the axial energy E_z depends on the C_4 parameter, which linearly depends on the tuning ratio (see Eq. 2.16). This behavior is depicted in Fig. 7.1 (left), where a dip at an unperturbed dip width of 1 Hz and an unperturbed SNR of 25 dB is simulated for different axial temperatures ranging from $T_z = 1\,\mathrm{K}$ to $T_z = 30\,\mathrm{K}$. Both, the fitted axial frequency, and the fitted SNR are modified. By introducing the coefficients α and δ,

$$\delta = \nu - \nu_{z,0} \qquad \alpha = \nu_{z,0}\left(\frac{3}{4}\frac{C_4}{C_2^2} \times \frac{k_B T}{q V_r}\right), \tag{7.6}$$

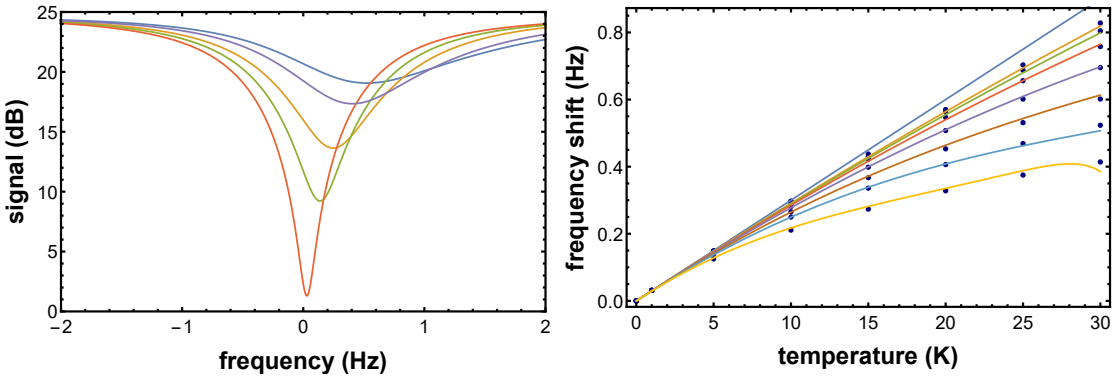

Figure 7.1.: Results of the numerical calculation of the axial motion as a function of temperature and C_4. Left: Theoretical axial dip lineshape $\tilde{\chi}(\nu, T_z)$ for $\alpha = 30\,\mathrm{mHz/K}$ for temperature values ranging from $T_z = 1\,\mathrm{K}$ (red) to $T_z = 30\,\mathrm{K}$ (blue). Right: Frequency of the dip minimum as a function of temperature computed for different values of the dip width $\delta\nu_z$, ranging from $\delta\nu_z = 1\,\mathrm{Hz}$ (dark yellow) to $\delta\nu_z = 10\,\mathrm{Hz}$ (light yellow), the axial frequency itself is plotted in blue. The minimum of the modified lineshape is closer to the axial frequency for low values of $\delta\nu_z$.

we may rewrite the lineshape

$$\begin{aligned}\tilde{\chi}(\delta, \alpha, T_z) &= \frac{R_p}{T_{z,0}} \int_0^\infty \mathrm{d}T \frac{(\delta + \alpha T)^2}{(\delta + \alpha T)^2 + (\delta\nu_z/2)^2} \exp\left(-\frac{T}{T_{z,0}}\right) \\ &= \frac{R_p}{T_{z,0}} \left(\frac{2}{\delta\nu_z}\right)^2 \int_0^\infty \mathrm{d}T\, (\delta + \alpha T)^2 \left(1 + \sum_k (-1)^k \left(\frac{(\delta + \alpha T)^{2k}}{(\delta\nu_z/2)^{2k}}\right)\right) \exp\left(-\frac{T}{T_{z,0}}\right).\end{aligned} \tag{7.7}$$

The minimum is then close to $\delta = -\alpha T$, but gets modified due to the asymptotic series below the integral. In the regime $\delta\nu_z/2 > |\alpha| T$, this effect is marginal, and a resonance frequency $\nu_{\mathrm{th}} = \nu_{z,0} + \alpha \langle T_{z,0} \rangle$ is obtained. Since the BASE traps are usually operated in this regime, we approximate the lineshape by

$$\begin{aligned}\tilde{\chi}(\delta, \alpha, T_z) &= \frac{R_p}{T_{z,0}} \left(\frac{2}{\delta\nu_z}\right)^2 \int_0^\infty \mathrm{d}T\, (\delta + \alpha T)^2 \exp\left(-\frac{T}{T_{z,0}}\right) \\ &= R_p \left(\frac{2}{\delta\nu_z}\right)^2 \left(\delta^2 + 2\delta\alpha T_0 + \alpha^2 T_0^2\right) \\ &= R_p \left(\frac{2\alpha T_0}{\delta\nu_z}\right)^2,\end{aligned} \tag{7.8}$$

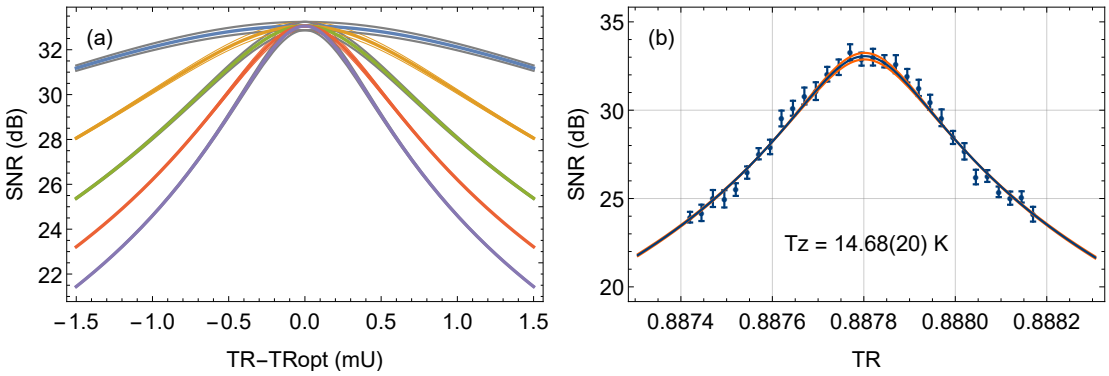

Figure 7.2.: Axial temperature determination by performing tuning ratio scans. Left: Simulated SNR for various axial temperatures T_z ranging from $T_z = 1\,\mathrm{K}$ (blue) to $T_z = 5\,\mathrm{K}$ (purple) and the BASE precision trap parameters. Right: Tuning ratio scan and axial temperature determination performing with a single hydride ion in the BASE precision trap. The determined temperature is $T_z = 14.68(20)\,\mathrm{K}$. This measurement was performed on 2019/01/07, after the peak ratio run was completed. The gray lines on the left/the orange lines on the right denote the fit uncertainty due to an assumed measurement uncertainty in SNR/the measurement uncertainty.

where we used the approximation $\delta \approx \alpha T_0$. This approximation leads to an uncertainty of about 3 %-5 %, which is of the same order as the usual statistical uncertainty of our measurements. With Eq. 7.8, we obtain an SNR of

$$\begin{aligned} \mathrm{SNR} &= 10\log_{10}\left(A^2+B^2\right) - 10\log_{10}\left(A^2\left(\frac{2\alpha T_z}{\delta\nu_z}\right)^2 + B^2\right) \\ &= 10\log_{10}\left(\frac{A^2+B^2}{A^2\left(\frac{2\alpha T_z}{\delta\nu_z}\right)^2 + B^2}\right), \end{aligned} \tag{7.9}$$

with B being defined by the noise floor NF, $B^2 = 10^{\mathrm{NF}/10}$, and $A^2 + B^2$ given by the top-noise level NT, $10^{\mathrm{NT}/10} = A^2 + B^2$, with NF and NT measured in logarithmic units. The temperature is then determined by recording axial spectra at different tuning ratios. Several axial feedback settings can be used in addition, as the different feedback settings allowing to conduct a reasonability check since a linear increase of temperature with increasing dip width is expected (compare Fig. 7.2 (left)). It is important to chose the FFT range $\Delta\nu_{\mathrm{FFT}}$ small enough such the effect of spectral leakage and the effect of the averaging inside each FFT bin is negligible. For the spectra used in Fig. 7.2, that

were recorded at $\Delta\nu_{\mathrm{FFT}} = 25\,\mathrm{Hz}$, at least 30 frequency bins are located inside the 3 dB-width of the axial dip, which allows to resolve the dip sufficiently well. In addition, the trap parameter $D_2 = \mathrm{d}C_2/\mathrm{dTR}$, which shifts the axial frequency as a function of the tuning ratio, is compensated for in a way that the particle's axial frequency is always centered close to the axial detector frequency. The result of such a temperature evaluation is depicted in Fig. 7.2 (right) that shows the measured SNR as a function of the tuning ratio, with a result of $T_z = 14.68(20)\,\mathrm{K}$. It is important to note that the so determined axial temperature T_z is not necessarily identical to the physical temperature of the detection circuit, which is about 4.8 K, measured by a thermometer attached to the detection resonator. Instead, T_z is the electronic noise temperature of the detector, which is depends on the physical temperature, the current noise of the low-noise cryogenic amplifier, the amplifier feedback and regeneration, and external noise sources. As the particle is in thermal equilibrium with the detector, the temperature measured with the particle is used both to quantify the particle temperature and the effective detector temperature. Unless otherwise stated, the term "axial temperature" always refers to the effective detector temperature/the temperature measured with the particle, since this effective axial temperature determines the axial rms amplitude of the particle, which is the corresponding quantity of interest for systematic studies. The value of $T_z = 14.68(20)\,\mathrm{K}$ is consistent with axial temperatures determined by different methods, that are described in Sec. 7.2.1 and Sec. 7.2.5.

Tuning ratio as a function of time

Multiple tuning ratio scans have been conducted in the context of the 2019 systematic measurements for the peak method. The first tuning ratio scan in this series is depicted in Fig. 7.2 (a), which yielded an optimal tuning ratio $\mathrm{TR}_{\mathrm{opt}} = 0.887\,802(3)$ and an axial temperature $T_z = 14.68(20)\,\mathrm{K}$. Over the course of about two months, we conducted four additional high resolution tuning ratio scans, the results of which are depicted in Fig. 7.3. By combing all results on the optimal tuning ratio, we obtain $\mathrm{TR}_{\mathrm{opt}} = 0.887\,800(7)$ (a), which is for the peak campaign used as the reference tuning ratio that tunes C_4 to zero. The temperature varies over time in the range between $T_z = 14\,\mathrm{K}$ and $T_z = 15.5\,\mathrm{K}$ (b). This is related to parasitic noise pickup on the axial detector, which affects the effective detector temperature and thus the particle temperature. While the median temperature of the experiment is stable to about 10 % over time, we occasionally observe peak to

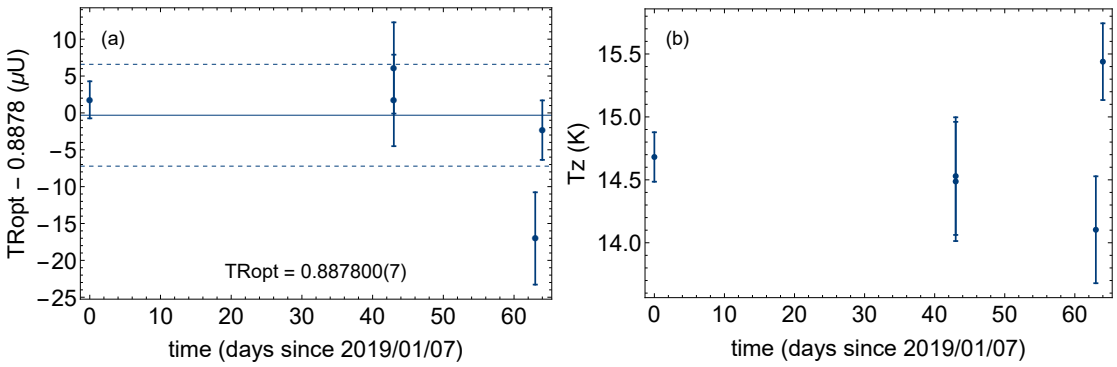

Figure 7.3.: Results of several tuning ratio scans conducted over the time of about two months. The first scan ($t = 0\,\mathrm{d}$) is depicted in Fig. 7.2 in detail. The weighted mean of the tuning ratio scans yields $\mathrm{TR}_{\mathrm{opt}} = 0.887\,800(7)$ (a). The axial temperature T_z when no feedback is applied fluctuates in the range between $T_z = 14\,\mathrm{K}$ and $T_z = 15.5\,\mathrm{K}$ (b), which is likely due to parasitic pickup of the axial detector that affects the effective detector temperature. The effective temperature T_z is not identical to the physical temperature of the detector, which is about 5 K.

peak temperature variations of up to 15 K. For the next experimental campaign, an improvement in axial temperature stability is targeted. To this end, additional RF switches that ground RF lines for grounding temporarily not-needed radio frequency lines will be implemented, and the noise-suppressing feedback loops will be operated continuously.

Effect of the axial temperature onto the cyclotron frequency

The axial temperature T_z leads to cyclotron frequency shifts, as it couples the axial motion to the residual magnetic inhomogeneity B_2, and thus modifies the magnetic field experienced by the particle. The shift is given by (see Sec. 2.2.1)

$$\frac{\Delta\nu_+}{\nu_+} = -\frac{1}{m\,(2\pi\nu_z)^2}\frac{B_2}{B_0}k_B T_z \Rightarrow \frac{\mathrm{d}\Delta\nu_+/\nu_+}{\mathrm{d}T_z} \approx -23.4(2)\,\mathrm{p.p.t./K}. \tag{7.10}$$

While the temperature scan resolution of 200 mK above corresponds to a cyclotron frequency resolution of 4.7 p.p.t., the important figure of merit for q/m ratio measurements is the temperature difference between both ion species. At a temporal temperature variation of about 1 K as seen in Fig. 7.3 (b), additional measures have to be undertaken in order to sufficiently constrain the temperature difference between two different ions

in a q/m campaign. Here, usually the difference ΔS in the top level of the Fourier transformed resonator voltage spectrum is used in order to determine the axial temperature difference of the detector in both ion configurations and thus also the temperature difference between both ions (Sec. 8.11.1). The temperature determination above then allows to benchmark the relation between axial resonator level and absolute temperature. ΔS relates to the resonator levels as follows, when the resonator top noise level S is measured in dBV:

$$\Delta S = 10 \times \log_{10} \left(\frac{R_{p1}}{R_{p2}} \left(1 - \frac{\Delta T_z}{T_{z,0}} \right) \right), \tag{7.11}$$

with R_{p1} and R_{p2} describing the effective parallel resistance of the detector for both ion species, which is affected by the different states of the varactor diode (see Fig. 8.5 and Sec. 8.11.1). ΔT_z denotes the temperature difference, and $T_{z,0}$ the absolute temperature. A scaling of $\mathrm{d}S/\mathrm{d}T_z = 0.22\,\mathrm{dB/K}$ is observed, which allows to constrain the temperature difference during the campaign with an uncertainty of $u\left(T_z\right) = 52\,\mathrm{mK}$, which corresponds to a cyclotron frequency uncertainty $u\left(\Delta\nu_+\right) = \mathrm{d}\nu_+/\mathrm{d}T_z \times 52\,\mathrm{mK} = 1.22(1)\,\mathrm{p.p.t.}$, which is well below the targeted precision of 20 p.p.t.

7.1.2. Asymmetry compensation

Even though the Penning traps used at BASE are designed in a symmetrical, compensated and orthogonal way [71], asymmetries in the electric trapping field that shift the particle position away from the center are easily generated by contact potentials in the trap wiring and by small leakage currents. The resulting trap asymmetry is typically on the order of 100 mV and can thus not be neglected. The general concept of the asymmetry compensation has been laid out in [72] and will briefly be recapitulated.
While the correction electrode voltage is given by $V_{\mathrm{corr}} = \mathrm{TR} \times V_r$, for the asymmetry compensation a small offset is added to one of the correction electrodes, in our case to the P5 electrode located downstream from the ring electrode, $V_{\mathrm{P5}} = \mathrm{TR} \times V_r + V_{\mathrm{offs}}$. Due to the symmetric setup of the trap, it does not matter whether the upstream or the downstream electrode is chosen. For each offset voltage V_{offs}, the tuning ratio is adjusted in order to meet the highest SNR, and the ring voltage V_r that centers the particle onto the axial resonator is determined. A quadratic scaling of the ring voltage V_r as a function of the applied offset V_{offs} is observed as an effect of second order, with its minimum

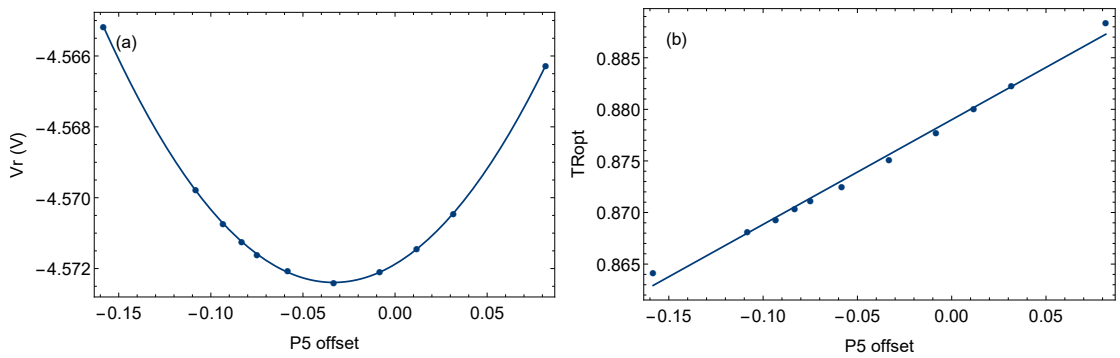

Figure 7.4.: Asymmetry compensation by adjusting the downstream correction electrode voltage to $V_{\mathrm{P5}} = \mathrm{TR} \times V_r + V_{\mathrm{offs}}$. The ring voltage V_r that centers the particles axial frequency onto the axial resonator follows a quadratic scaling as a function of the offset (a), since an axial displacement of the ion from the trap center leads to an increased C_2 . From the minimum of the scaling, the symmetric configuration of the trap is determined [72]. (b) depicts the scaling of the optimal tuning ratio, which yields the highest SNR, with the offset voltage V_{offs}. The scaling is linear, as a higher absolute voltage applied to one correction electrodes requires a lower tuning ratio to achieve the most homogeneous configuration.

denoting the symmetrical trap configuration (see Fig. 7.4 (a)). In this case, the trap is symmetrized for an offset voltage $V_{\mathrm{offs}} = -33\,\mathrm{mV}$ applied to the P5 correction electrode. The optimal tuning ratio $\mathrm{TR}_{\mathrm{opt}}$ scales linearly with the offset, as lower correction voltages are needed if a higher absolute voltage is applied to one of the correction electrodes. If the ion is displaced from the trap center, this effectively leads to an increased C_2 coefficient and thus a higher resonance frequency [72]. The benefit from operating in an asymmetry-compensated configuration is for instance seen in Fig. 7.4 (a), as the scaling $\mathrm{d}V_r/\mathrm{d}V_{\mathrm{offs}}$ is minimal in the symmetric configuration, which is equivalent to the scaling $\mathrm{d}\nu_z/\mathrm{d}V_{\mathrm{offs}}$ being minimal. If for instance drifts in the correction electrode voltages would occur after shuttling a particle into the precision trap, such effects would be naturally suppressed. Since both particles are trapped in the same trapping potential (unlike in the 2015 measurement, where the ring voltage had to be modified in order to match the particle's oscillation frequency with the axial detector frequency [39]), the effect of trap asymmetries unto the measured cyclotron frequency ratio is strongly suppressed. The asymmetry compensation is still carried out routinely.

7.1.3. Magnetron burst measurements

The magnetron burst scheme for measuring higher order trap parameter such as C_6 and C_8 has first been introduced in [72] and relies on exciting the magnetron motion with a defined radio frequency drive and measuring the change in axial difference related to the increase in magnetron energy E_-. Subsequently, the particle is cooled back into thermal equilibrium, $\langle E_- \rangle = \nu_-/\nu_z \times E_z$. This procedure is performed for radio frequency drives with different burst cycle numbers, and for different tuning ratios. The magnetron radius after excitation is given by (compare Sec. 7.2.1)

$$\rho_- = \alpha \times N_i \times \sqrt{P}, \tag{7.12}$$

with N_i being the number of cycles in the frequency burst (the pulse length t_{rf} is given by $t_{\mathrm{rf}} = N_i/\nu_{\mathrm{rf}}$), drive power P and the proportionality factor α, which depends on the trap geometry. With increasing magnetron radius, an axial frequency shift $\Delta\nu_z$ is observed due to the C_4 coefficient:

$$\begin{aligned} \frac{\Delta\nu_z}{\nu_z} &= \frac{1}{qV_r}\frac{C_4}{C_2^2} \times 3E_- \\ &= -\frac{1}{qV_r}\frac{C_4}{C_2^2} \times \frac{3}{4} m \left(2\pi\nu_z\right)^2 \rho_-^2 = -\frac{1}{qV_r}\frac{C_4}{C_2^2} \times \frac{3}{4} m \left(2\pi\nu_z\right)^2 \left(\alpha N\right)^2 \end{aligned} \tag{7.13}$$

C_4 depends linearly on the tuning ratio, $C_4 = D_4 \times \mathrm{TR} + E_4$ (see Eq. 2.16), which can be proven by trap theory. Recorded axial frequency shifts can then be fitted with a function $C\left(\mathrm{TR}\right) = \eta(\mathrm{TR}) \times N^2$. The derivative of $\eta\left(\mathrm{TR}\right)$ is given by

$$\frac{\mathrm{d}\eta}{\mathrm{dTR}} = -\frac{1}{qV_r}\frac{2\pi\nu_z}{C_2^2} \times \frac{3}{4} m \left(2\pi\nu_z\right)^2 \alpha^2 D_4. \tag{7.14}$$

A scaling of 474(2) nm/cycle is observed for a drive power of -45 dBm, which corresponds to

$$\alpha = 83.9(4)\, \frac{\mu\mathrm{m}}{\left(\mathrm{cycle} \times \sqrt{\mathrm{mW}}\right)}. \tag{7.15}$$

$C_8 = 4 \times 10^{17}\, 1/\mathrm{m}^8$ is known to be a robust parameter, both from trap theory and from measurements taken during different runs. We therefore deduct the C_8 effect specified

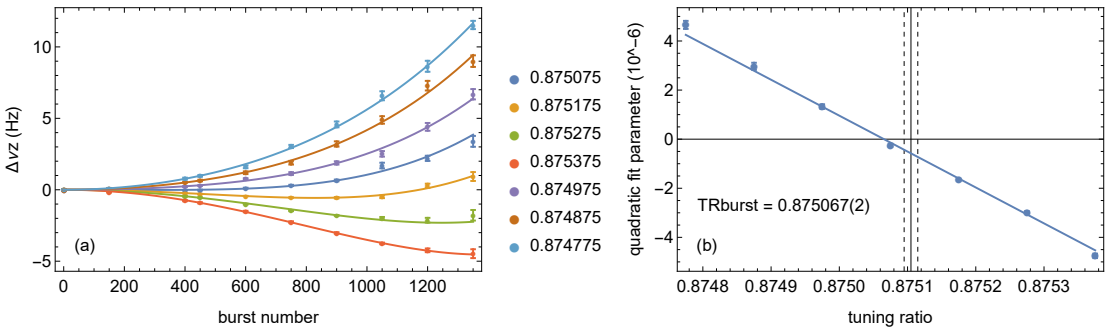

Figure 7.5.: Magnetron burst measurement performed during the phase methods campaign with both parking electrodes set to 0 V, ($V_{\mathrm{T4}} = V_{\mathrm{T6}} = 0\,\mathrm{V}$). On the left side, the axial frequency shift as a function of burst number for different tuning ratios is depicted. From the scaling of quadratic component (right), an optimal tuning ratio $\mathrm{TR}_{\mathrm{burst}}$ is obtained. $\mathrm{TR}_{\mathrm{burst}} = 0.875\,067(2)$ is close the optimal tuning ratio determined by tuning ratio scans $\mathrm{TR}_{\mathrm{opt}} = 0.875\,105(10)$, indicated by the vertical grid lines (for the phase run data, see Fig. 9.1).

by (see Sec. 2.2.1)

$$\frac{\Delta\nu_z}{\nu_z} = -\frac{35}{32}\frac{C_8}{C_2}4\rho_-^6 \tag{7.16}$$

from the measured axial frequency changes. Fig. 7.5 (a) already shows the axial frequency shifts corrected for the effect of C_8. By inserting $\rho_- = \alpha \times N$, the C_6 coefficient is determined from the following relations (see also Fig. 9.5):

$$\frac{\Delta\nu_z}{\nu_z} = \frac{15}{16}\frac{C_6}{C_2}3\rho_-^4 \Rightarrow C_6 = -24(3) \times 10^{10}\,1/\mathrm{m}^6. \tag{7.17}$$

The magnetron burst method and the tuning ratio scans differ only by about $\mathrm{TR}_{\mathrm{opt}} - \mathrm{TR}_{\mathrm{burst}} = 38(11)\,\mu\mathrm{U}$ when the park electrodes T4 and T6 are set to 0 V, which is not of great concern at our trap geometry. In the shuttling configuration characterized by $V_{\mathrm{T4}} = V_{\mathrm{T6}} = \pm 13.5\,\mathrm{V}$[1] however, tuning ratio offsets of order $150\,\mu\mathrm{U}$ are observed for a similar magnetron energy range. The reason for this deviation is yet to be understood, but might be related to a higher order coefficient. This explanation is supported by the fact that the offset between both methods decreases to about $50\,\mu\mathrm{U}$ when the fit area is constrained to lower burst numbers. The tuning ratio scan method is considered to be especially robust with regards to C_4 and is therefore used as the reference measurement

[1] During shuttling measurements, the parking voltages are applied both to the empty electrode and to respective storage electrode.

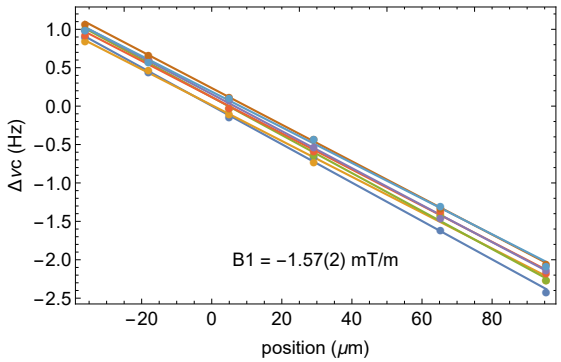

Figure 7.6.: Measurement of B_1 by means of the sideband method. To this end, various offset voltages ranging from $-160\,\mathrm{mV}$ to $60\,\mathrm{mV}$ are applied to the P5-electrode, which cause a shift of the ion position along the trap axis from about $-30\,\mu\mathrm{m}$ to $90\,\mu\mathrm{m}$ compared to the position at $0\,\mathrm{mV}$. Each color represents a single measurement cycle, which consists of applying all voltage offsets once. From potential theory, the respective ion positions are calculated. The cyclotron frequency is measured at each position. From the gradient $\mathrm{d}\nu_c/\mathrm{d}z_0$, $B_1 = -1.57(2)\,\mathrm{mT/m}$ is computed.

for determining C_4 and the tuning ratio that tunes C_4 to 0.

7.1.4. B_1 measurement

The linear magnetic field gradient B_1 is easily determined by performing cyclotron frequency measurements at different ion positions. In order to shift the ion along the trap axis, various offset voltages are applied to one of the correction electrodes. The ion position is then determined from potential theory. A value of $B_1 = -1.57(2)\,\mathrm{mT/m}$ is obtained (see Fig. 7.6), which is a factor of six smaller than in the last q/m measurement [39], and by factor of three better compared to the state prior to the last dedicated magnet shimming [53].

The particle position $\langle z \rangle$ is shifted as the particle magnetic moment couples to the magnetic gradient $\partial B/\partial z = B_1$. The particle magnetic moment is dominantly given by its cyclotron motion,

$$|\vec{\mu}_+| = \frac{q}{m}\frac{E_+}{2\pi\nu_+} \approx \frac{E_+}{B_0}. \tag{7.18}$$

The equilibrium position $\langle z \rangle$ is determined by

$$\begin{aligned} -\frac{\partial \Phi_V(z)}{\partial z} &\stackrel{!}{=} -\frac{\partial \Phi_M(z)}{\partial z} \Leftrightarrow -|\vec{\mu}_+|B_1 \stackrel{!}{=} -2\,\langle z \rangle\, C_2 V_r q \\ \Rightarrow \langle z \rangle &= -\frac{1}{4\pi^2 m \nu_z^2} \times E_+ \frac{B_1}{B_0}. \end{aligned} \tag{7.19}$$

With the approximation $\nu_+ \approx \nu_c = 1/(2\pi) \times q/m \times B$ and $B = B_0 + B_1 \langle z \rangle$, the cyclotron frequency shift $\Delta\nu_+$ is given by

$$\frac{\Delta\nu_+}{\nu_+} = \frac{B_1}{B_0}\langle z \rangle = -\frac{1}{4\pi^2 m \nu_z^2} \times E_+ \left(\frac{B_1}{B_0}\right)^2 = -3.9(1)\,\text{p.p.t./eV} \tag{7.20}$$

Considering sideband measurements, where the cyclotron energy is given by $E_+ = k_B \times \nu_+/\nu_z$, the cyclotron frequency shift is given by $\Delta\nu_+/\nu_+ = -15.4(4)\,\text{p.p.q./K}$, or $\Delta\nu_+ = -0.215(5)\,\text{p.p.t.}$ for $T_z = 14\,\text{K}$. For cyclotron frequency measurements using the sideband method, this effect is orders of magnitude lower than the targeted precision, and can thus be neglected in cyclotron. For peak based frequency measurements, the shift due to anharmonicities is given by $\Delta\nu_+ = -129\,\text{p.p.t./eV}$, which is mainly attributed to B_2 (see Tab. 7.1), while the relativistic shift contributes to $\Delta\nu_+ = 1066\,\text{p.p.t./eV}$. The B_1-effect thus leads to very small modification in the effective B_2-value, which can be neglected at the targeted measurement precision.
If a q/m ratio measurement is performed where the trap potential is adjusted for each ion species [39], additional frequency shifts depending on the respective ion position have to considered. Due to the tunable axial detection system, which is implemented into the BASE apparatus since the 2017 measurement campaign, this effect is removed as measurements on both ions are performed in identical potentials.

7.1.5. Trap angle measurement

While the electric and magnetic field are perfectly aligned in the ideal Penning trap, the tilt between both axes is characterized by the angles θ, ϕ for the real Penning trap. In addition, a small ellipticity ϵ might be present [69], which modifies the trapping field to

$$\Phi\,(x, y, z) = C_2 V_r \left(z^2 - \frac{1}{2}(x^2 + y^2) - \epsilon(x^2 - y^2)\right). \tag{7.21}$$

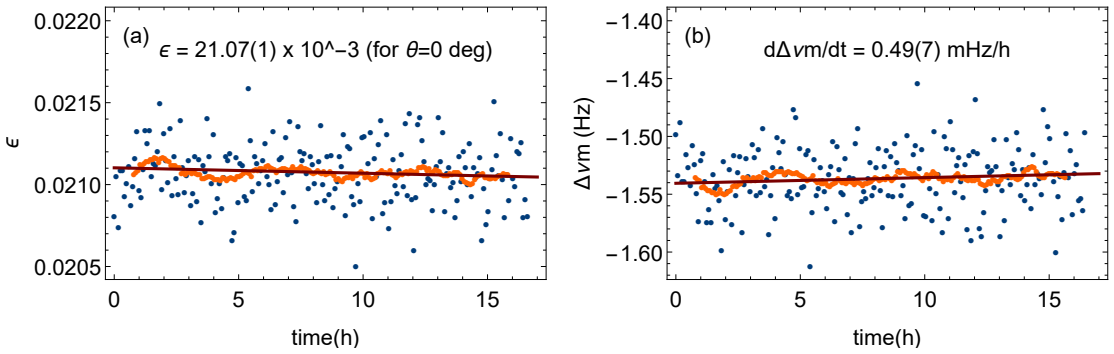

Figure 7.7.: Measurement of trap ellipticity and trap angle. On the left, the ellipticity calculated from the difference in approximated and measured magnetron frequency, $\Delta\nu_- = \nu_- - \tilde{\nu_-}$ is depicted. Assuming an angle $\theta = 0$, an ellipticity $\epsilon = 21.07(1) \times 10^{-3}$ is obtained. If we assume that the magnet axis and the electric field axis are misaligned by 1 mm across the magnet length of 1 m, the measured $\Delta\nu_-$ would correspond to $\epsilon = 123.356(2) \times 10^{-3}$. On the right, the $\Delta\nu_-$ is depicted. We observe a shift of 0.49(7) mHz/h in $\Delta\nu_-$, indicating a small tilt of the experiment axes by about 0.01 deg/h. This tilt might be related to the effect of changing cryoliquid levels.

While the invariance theorem [69], $\nu_c^2 = \nu_+^2 + \nu_z^2 + \nu_-^2$ is still valid in traps with non-zero values for ϵ, θ, ϕ, the oscillation frequencies ν_+, ν_z, and ν_- get modified. The usual estimation $\nu_- \approx \tilde{\nu}_- = \nu_z^2/(2\nu_+)$ is reformulated to

$$\nu_- = \frac{\nu_z^2}{2\nu_+} \frac{\sqrt{1-\epsilon^2}}{\left(1 - \frac{3}{2}\sin^2(\theta)\left(1 + \frac{1}{3}\epsilon\cos(2\phi)\right)\right)^{3/2}}. \tag{7.22}$$

Using a few approximations, Eq. 7.22 is approximated by

$$\frac{\nu_-}{\tilde{\nu}_-} \approx 1 + \frac{9}{4}\theta^2 - \epsilon^2/2. \tag{7.23}$$

From Eq. 7.23, we may then calculate the ellipticity from the ratio $\nu_-/\tilde{\nu}_-$:

$$\epsilon \approx \frac{9}{2}\theta^2 - 2\frac{\tilde{\nu}_-}{\nu_-} + 2 \tag{7.24}$$

In order to study the trap angles and the ellipticity, we measured the cyclotron and the magnetron frequency subsequently by means of the sideband method (Fig. 7.7). From $\mu(\nu_-) = 6916.66\,\text{Hz}$ and $\mu(\tilde{\nu}_-) = 6918.19\,\text{Hz}$, we compute $\epsilon = 21.07(1) \times 10^{-3}$ assuming $\theta = 0$ (see Fig. 7.7 (a)). If both axis were misaligned by 1 mm across a magnet length of

1 m, we would obtain $\epsilon = 123.356(2) \times 10^{-3}$.
When evaluating $\Delta\nu_- = \nu_- - \tilde{\nu}_-$, the difference between the approximated and the measured magnetron frequency, we observe a shift of $\Delta\nu_- = 0.49(7)$ mHz/h (see Fig. 7.7 (b)), which corresponds to an angle change of 0.01 deg/h. This tilt might be related to the effect of changing cryoliquid levels.
Since the invariance theorem also holds for Penning traps where θ, ϕ, and ϵ are non-vanishing, the only way that these imperfections enter into measured cyclotron frequencies is due to that usually $\tilde{\nu}_-$ is used as an estimation for ν_- in order to increase the sampling rate. With $\Delta\nu_- = -1.54$ Hz, this shifts the determined cyclotron frequency by about 0.36 mHz or about 12 p.p.t. In the charge-to-mass ratio, this effect is suppressed down to about 13 p.p.q. and can therefore safely be neglected, which justifies to use the approximation above.

7.2. Peak methods

The so-called "peak method" (see Fig. 7.8) relies on exciting the cyclotron motion of a trapped ion and subsequently observing the signal of the excited cyclotron motion, which appears as a peak on top of the Fourier-transformed voltage spectrum of the dedicated cyclotron detector connected to a segmented electrode of the trap. This method enabled for instance several at-this-time most precise measurements of the proton-to-antiproton charge-to-mass ratio performed by the TRAP collaboration, which finally reached a fractional uncertainty of 90 p.p.t. in 1999 [151, 152, 153]. Unlike the "sideband method" [54], where the cyclotron motion is coupled to the axial mode, the cyclotron frequency is measured directly. As the magnetic field of a superconducting magnet can be stabilized much better than the best high-precision voltage sources, the peak method has the potential to measure cyclotron frequencies with much increased precision. A significant disadvantage of the peak method however is given by the fact that the cyclotron and axial frequencies at excited cyclotron motion, $\nu^*_{+,z}$ are to first order linearly shifted with respect to $\nu_{+,z}$ at negligible cyclotron energy depending on the cyclotron energy E_+:

$$\Delta\nu_{+,z} = \nu^*_{+,z} - \nu_{+,z} = \mathcal{M}_{+,z}(B_2, C_4, \mathrm{SR}) \times E_+ \tag{7.25}$$

$\mathcal{M}_{+,z}$ relates to magnetic and electric field inhomogeneities such as B_2 and C_4 as well as relativistic effects, which have to be carefully corrected for. Note here that the cyclotron

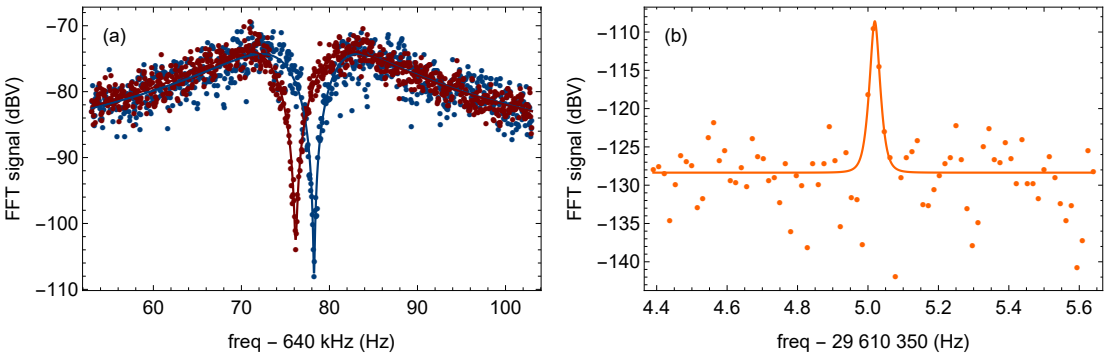

Figure 7.8.: Principle of the peak method. A particle is cyclotron-wise excited to a non-negligible cyclotron energy E_+ by means of a radio-frequency drive. The corresponding image current generates a peak signal observed on the Fourier transformed cyclotron detector spectrum (displayed on the right), a least-squares fit yields the excited cyclotron frequency ν_+^*. As the spectra are recorded during an FFT averaging time t_{avg} of usually $t_{\mathrm{avg}} \approx 64\,\mathrm{s}$, the obtained spectra represent integrals over time. Relativistic corrections and electro-magnetic inhomogeneities such as B_2 and C_4 lead to linear frequency shifts in the axial and cyclotron mode. The energy is calibrated my measuring the axial frequency ν_z at negligible cyclotron energy (left side, blue) and the axial frequency ν_z^* at excited cyclotron motion (red), with $\Delta\nu_z = \nu_z - \nu_z^* \propto E_+$. For an excitation energy of 12 eV, the axial frequency is shifted by $\Delta\nu_z = 2.094(54)\,\mathrm{Hz}$. The corresponding cyclotron shift is given by $\Delta\nu_+ = 334.0(3.0)\,\mathrm{mHz}$, for the typical inhomogeneity values during this run ($B_2 = -89.4(0.6)\,\mathrm{mT/m^2}$ and $C_4 = 0$). The spectra presented here were measured using a single hydride ion.

frequencies are measured at an averaging time t_{avg}, which is usually 64 s for the q/m ratio measurement, and about 42 s for the cooling curves. During t_{avg}, the particle dissipates energy and its mode frequencies is shifted accordingly. As the shifts in both frequencies are to first order linear, this effect is negligible to first order, but should be kept in mind. The measured spectra represent integrals of the cyclotron and axial frequency over the FFT acquisition time t_{avg}.

The shifts corresponding to Eq. 7.25 are displayed in Tab. 7.1. This makes a highly precise and accurate determination of inhomogeneity coefficients and particle energies crucial for being the application of the peak method. When all relevant trap coefficients are known, the axial frequency difference $\Delta\nu_z = \nu_z^* - \nu_z$ is used in order to calibrate the cyclotron energy E_+ and subsequently correcting the ν_+^* for the energy-dependent shift and obtaining ν_+. The excited cyclotron peak offers several approaches for studying the relevant trap coefficients, which are discussed in this section.

	scaling	for $E_+ = 5\,\mathrm{eV}$
$\Delta\nu_+$	-27.8 mHz/eV	-139.2 mHz
$\Delta\nu_+$ (rel)	-31.6 mHz/eV	-158.0 mHz
$\Delta\nu_+$ (anharmonicities)	3.8 mHz/eV	18.8 mHz
$\Delta\nu_z$	-174.5 mHz/eV	-872.4 mHz
$\Delta\nu_z$ (rel)	-0.3 mHz/eV	-1.7 mHz
$\Delta\nu_z$ (anharmonicities)	-174.1 mHz/eV	-870.7 mHz
$\Delta\nu_+/\Delta\nu_z$	1/6.27	1/6.27
targeted resolution (20 p.p.t.)	0.6 mHz	0.6 mHz

Table 7.1.: Frequency shifts occurring in the peak method, scaling and explicit shifts for a typical excitation energy of $E_+ = 5\,\mathrm{eV}$. The relativistic shift in cyclotron is about 1 p.p.b./eV, which means that the energy resolution should be at a few meV, if a frequency accuracy on the 10 p.p.t. level shall be reached. To this end, the axial frequency difference $\Delta\nu_z$ is evaluated, which is dominated by the effect of anharmonicities, while the relativistic effects are much weaker.

7.2.1. Driven harmonic oscillator

The following sections describe measurements related to the cyclotron peak method. In order to introduce the basic theoretical framework, we discuss the basic properties of the resonantly excited harmonic oscillator. The harmonic oscillator with angular frequency ω, amplitude z, charge q, driven by the electric field E_{drive} is described by

$$\ddot{z} + \omega^2 z = \frac{qE_{\mathrm{drive}}}{m} \cos(\omega t)\,. \tag{7.26}$$

The ansatz $z(t) = Z(t)\cos(\omega t + \phi)$ is used:

$$\ddot{z}(t) = \ddot{Z}\cos(\omega t - \phi) + 2\dot{Z}(t)\sin(\omega t + \phi)\,\omega - Z(t)\cos(\omega t + \phi)\,\omega^2. \tag{7.27}$$

This can be rewritten to

$$\ddot{z} + \omega^2 z = \ddot{Z}(t)\cos(\omega t + \phi) - 2\dot{Z}(t)\sin(\omega t + \phi)\,\omega. \tag{7.28}$$

Inserting the equation of motion, one obtains

$$\ddot{Z}(t)\cos(\omega t + \phi) - 2\dot{Z}\sin(\omega t + \phi)\,\omega = \frac{qE_{\mathrm{drive}}}{m}\cos(\omega t)\,. \tag{7.29}$$

By decoupling fast and slow components, this reduces to

$$\Rightarrow \frac{qE_{\mathrm{drive}}}{m\omega}\cos(\omega t) = -2\dot{Z}(t)\sin(\omega t+\phi) = 2\dot{Z}(t)\sin(\omega t+\pi/2)\,. \tag{7.30}$$

We obtain

$$\dot{Z}(t) = \frac{qE_{\mathrm{drive}}}{2m\omega} \Rightarrow z(t) = \left(z(t_0)\cos(\phi_0) + \frac{qE_{\mathrm{drive}}}{2m\omega}t\right)\cos(\omega t) \tag{7.31}$$

The same relation applies to the radial modes $\rho_{+,-}$:

$$\rho_{+,-}(t) = \left(\rho_{+,-}(t_0)\cos(\phi_0) + \frac{qE_{\mathrm{drive}}}{2m\omega_{+,-}}t\right)\cos(\omega_{+,-}t) \tag{7.32}$$

Given a resonant excitation, the radius increases linearly with excitation time. In order to cyclotron-wise excite a particle to $E_+ = 5\,\mathrm{eV}$, we usually irradiate a resonant radio-frequency drive at a power of -25 dBm for about 675 μs, which increases the cyclotron radius from $\rho_+ \approx 12\,\mu\mathrm{m}$ to $\rho_+ \approx 166\,\mu\mathrm{m}$.
Examining Eq. 7.32, it is noted that the initial orbit radius $\rho_{+,-}$ adds incoherently to the excitation period. Its contribution to the radius after excitation remains invariant. As the energy is proportional to the squared particle radius, the contribution of the initial radius will contribute $\propto \sqrt{E_{\mathrm{th}}E_{\mathrm{exc}}}$ to the energy uncertainty, with E_{th} being the initial energy, and E_{exc} being the amount of energy transferred into the oscillation mode during the excitation.
In order to derive the standard deviation of the cyclotron energy after excitation (what is called the "excitation scatter" from here onwards), a formalism for instance introduced in [75] is used. Additional aspects of this formalism are also discussed in context of the phase methods in Sec. 9.6.1. Here, the particle motion is described by the vector $\vec{\rho} = (x, -v/\omega)$, with the length given by the mode energy, $|\vec{\rho}| = \left(2E/\left(m\omega^2\right)\right)^{1/2}$. In polar coordinates, the vector is described by (ρ, ϕ). While the phase ϕ is initially uniformly distributed in [0,2π), the radius ρ is distributed according to a Rayleigh distribution, as the energy is Boltzmann distributed:

$$\begin{aligned} f(\rho) &= \frac{m\omega^2}{E_0}\rho\exp\left(-\frac{m\omega^2\rho^2}{2E_0}\right)\mathrm{d}\rho\mathrm{d}\phi/\left(2\pi\right) = \frac{\rho}{2\pi\sigma^2}\exp\left(-\frac{\rho^2}{2\sigma^2}\right)\mathrm{d}\rho\mathrm{d}\phi \\ &= -\frac{\mathrm{d}}{\mathrm{d}\rho}\frac{1}{2\pi}\exp\left(-\frac{\rho^2}{2\sigma^2}\right)d\rho\mathrm{d}\phi, \end{aligned} \tag{7.33}$$

with $\sigma^2 = E_0/(m\omega^2)$. Since the particle's cyclotron motion is cooled by coupling it to the axial motion using a sideband drive [54] prior to each measurement, the initial cyclotron energy is given by

$$E_0 = E_{+,\mathrm{th}} = \frac{\nu_+}{\nu_z} E_z \Leftrightarrow \frac{1}{2} m\omega_+^2 \langle \rho_+^2 \rangle = \frac{\nu_+}{\nu_z} k_B T_z. \tag{7.34}$$

After excitation described by $\vec{\rho}_{\mathrm{exc}} = (x_{\mathrm{exc}}, y_{\mathrm{exc}})$, the distribution is given by (see Eq. 9.35)

$$f(\sigma, \vec{\rho}_{\mathrm{exc}}, \rho, \phi) = \frac{\rho}{2\pi\sigma^2} \exp\left(-\left((\rho\cos(\phi) - x_{\mathrm{exc}})^2 + (\rho\sin(\phi) - y_{\mathrm{exc}})^2\right)/\sigma^2\right) \mathrm{d}\rho. \tag{7.35}$$

The standard deviation of the excited particles energies $\sigma(E)_+$ is computed from the variance, $\sigma(E_+)^2 = \langle E_+^2 \rangle - \langle E_+ \rangle^2$,

$$\langle E_+^2 \rangle = \left(\frac{1}{2} m\omega_+^2\right)^2 \int_\Omega \mathrm{d}A \rho^4 f(\sigma, \vec{\rho}_{\mathrm{exc}}, \rho, \phi) = E_{\mathrm{exc}}^2 + 2E_{\mathrm{th}}^2 + 4E_{\mathrm{th}}E_{\mathrm{exc}} \tag{7.36}$$

and

$$\langle E_+ \rangle^2 = \left(\frac{1}{2} m\omega_+^2\right)^2 \left(\int_\Omega \mathrm{d}A \rho^2 f(\rho, \phi, \rho_+, \vec{\rho}_{\mathrm{exc}})\right)^2 = E_{\mathrm{exc}}^2 + E_{\mathrm{th}}^2 + 2E_{\mathrm{th}}E_{\mathrm{exc}}. \tag{7.37}$$

The variance $\sigma(E_+)^2$ is then

$$\sigma(E_+)^2 = \langle E_+^2 \rangle - \langle E_+ \rangle^2 = 2E_{\mathrm{th}}E_{\mathrm{exc}} \left(1 + \frac{1}{2}\frac{E_{\mathrm{th}}}{E_{\mathrm{exc}}}\right), \tag{7.38}$$

and the standard deviation $\sigma(E_+)$ accordingly:

$$\sigma(E_+) = \sqrt{2E_{\mathrm{th}}E_{\mathrm{exc}}} \times \sqrt{1 + \frac{1}{2}\frac{E_{\mathrm{th}}}{E_{\mathrm{exc}}}} \approx \sqrt{2E_{\mathrm{th}}E_{\mathrm{exc}}} \left(1 + \frac{1}{4}\frac{E_{\mathrm{th}}}{E_{\mathrm{exc}}}\right) \tag{7.39}$$

This relation agrees with our principal considerations based upon Eq. 7.32 and is experimentally well verified in Fig. 7.9. (a) depicts the energy scatter $\sigma(E_+)$ as a function of excitation energy E_{exc}, obtained when no axial feedback was applied ($\delta\nu_z = 6.1\,\mathrm{Hz}$, blue data points) and when axial feedback was applied ($\delta\nu_z = 2.1\,\mathrm{Hz}$, red data points). Since the axial temperature is linearly related to the axial dip width, $\delta\nu_z \propto T_z$, and the initial energy E_{th} is given by $E_z \times \nu_+/\nu_z$ (Eq. 7.34), the two dip widths correspond to different initial energies E_{th}. We obtain $T_z(\delta\nu_z = 6.1\,\mathrm{Hz}) = 12.4(2)\,\mathrm{K}$ and

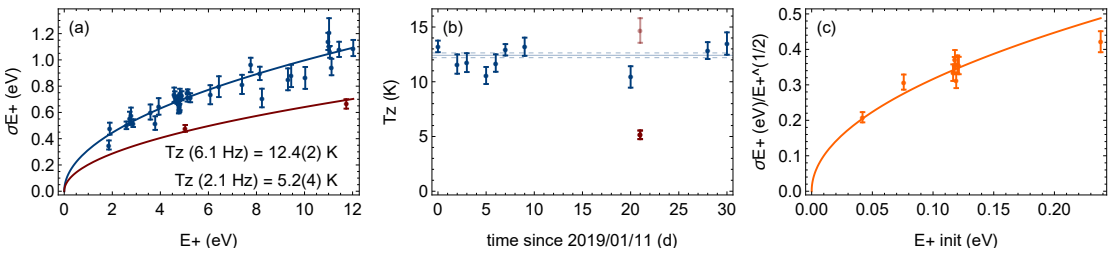

Figure 7.9.: Excitation scatter investigation. On the left side, the excitation scatter as a function of excitation energy is depicted. The blue data were taken across multiple days at a dip width $\delta\nu_z = 6.117(5)\,\mathrm{Hz}$. The red data correspond to a single data set that was recorded at a dip width $\delta\nu_z = 2.147(11)\,\mathrm{Hz}$, when negative feedback was applied. Applying Eq. 7.39 and Eq. 7.34, axial temperatures $T_z(6.1\,\mathrm{Hz}) = 12.4(2)\,\mathrm{K}$ and $T_z(2.1\,\mathrm{Hz}) = 5.2(4)\,\mathrm{K}$ are computed. In (b), the axial temperature determined from each subset of the data presented in (a) is depicted, with the blue grid lines denoting the combined value $T_z(6.1\,\mathrm{Hz}) = 12.4(2)\,\mathrm{K}$. The red data point represents the same data as depicted in (a), with the shaded red point denoting the corresponding feedback-free temperature $T_z(2.1\,\mathrm{Hz}) \times 6.1/2.1 = 14.7(1.2)\,\mathrm{K}$, which is in agreement with the feedback-free individual temperature measurements, taking into account the temporal temperature variation. The feedback-free temperature measurements indicate a temperature variation during individual dates, that is not reflected in a changing dip width. In (c), the excitation scatter normalized by the excitation energy as a function of initial particle energy is depicted. The solid line is not a fit to the data but represents the $\sqrt{E_{+,\mathrm{init}}}$-behavior predicted from Eq. 7.39 and agrees very well the observed scaling.

$T_z(\delta\nu_z = 2.1\,\mathrm{Hz}) = 5.2(4)\,\mathrm{K}$. In Fig. 7.9 (b), the axial temperature determined from the individual scatter measurements is denoted. The feedback-free temperature (blue) scatters between $T_z = 10.6(8)\,\mathrm{K}$ and $T_z = 13.5(1.0)\,\mathrm{K}$, while at $\delta\nu_z = 2.1\,\mathrm{Hz}$, an axial temperature $T_z = 5.2(4)\,\mathrm{K}$ is obtained, which corresponds to a feedback-free temperature $T_z(2.1\,\mathrm{Hz}) \times 6.1\,\mathrm{Hz}/\,(2.1\,\mathrm{Hz}) = 14.7(1.2)\,\mathrm{K}$ (light red point). This is slightly higher than the temperatures measured without the application of feedback, but still consistent considering the temporal variation of the axial temperature. In Fig. 7.9 (c), the normalized energy scatter $\sigma(E_+)/\sqrt{E_+}$ is plotted against the intial energy E_{th}. The data follows a $\sqrt{E_{\mathrm{th}}}$-function, that is depicted as the solid orange line depicts and is not a fit to the data. Excellent agreement between Eq. 7.39 and the data depicted in Fig. 7.9 is demonstrated.

The analysis of energy scatter data yields a fast and precise way for determining the axial temperature, which has to the authors knowledge not been used previously. Especially, this method allows to monitor changes in axial temperature between individual days or even during specific measurements, which was practically not possible beforehand with-

out performing dedicated measurements as for instance described in Sec. 7.1.1, which require a lot of additional time. This method was proposed by Stefan Ulmer. As this method was only developed during data analysis after the corresponding measurement run was completed, the full potential of this method could not be exploited, but will be studied in future measurement campaigns. In addition, following this model, the cyclotron excitation scatter can be reduced by pre-cooling the cyclotron motion to lower initial energies E_{th}, which is of great use for the further application of the peak method.

7.2.2. B_2 determination via cooling curves

A cyclotron-wise excited particle coupled to an LC-detection circuit is resistively damped with a cooling time constant τ_+. The cyclotron energy as a function of time is then given by

$$E_+(t) = E_{+,0} \times \mathrm{Exp}(-t/\tau_+), \tag{7.40}$$

with the initial excitation energy given by $E_{+,0}$. The cyclotron frequency is linearly shifted as a function of cyclotron energy due to relativistic effects and the B_2 and C_4 inhomogeneities:

$$\frac{\Delta\nu_+}{\nu_+}(E_+) = \left(-\frac{1}{mc^2} - \frac{1}{m\omega_+^2}\frac{B_2}{B_0} + \frac{3}{4}\frac{1}{qV_r}\frac{C_4}{C_2^2}\left(\frac{\omega_z}{\omega_+}\right)^4\right) E_+ \tag{7.41}$$

Similarly, the axial frequency experiences a linear shift $\Delta\nu_z(E_+)$ described by

$$\frac{\Delta\nu_z}{\nu_z}(E_+) = \left(-\frac{1}{2mc^2} - \frac{3}{2qV_r}\frac{C_4}{C_2^2}\left(\frac{\omega_z}{\omega_+}\right)^2 + \frac{1}{m\omega_z^2}\frac{B_2}{B_0}\right) E_+. \tag{7.42}$$

For the peak campaign, it can be assumed the parameter C_4 is tuned to zero with the resolution demonstrated in the tuning ratio scans ($u(C_4) = u(\mathrm{TR_{opt}}) \times D_4 = 7700(9000)\,1/\mathrm{m}^4$). If all measurements are conducted at the same tuning ratio and thus at the same (small or vanishing) value of C_4, it is justified to include the C_4-effect into B_2 and quote an effective B_2 instead of the real B_2, which is done in this thesis unless otherwise stated. Higher order electric field inhomogeneities such as C_6 and C_8 contribute to linear and higher-order frequency shifts depending on the cyclotron energy E_+ and their respective values, but are insignificant for excitation energies of a few eV usually applied at BASE.

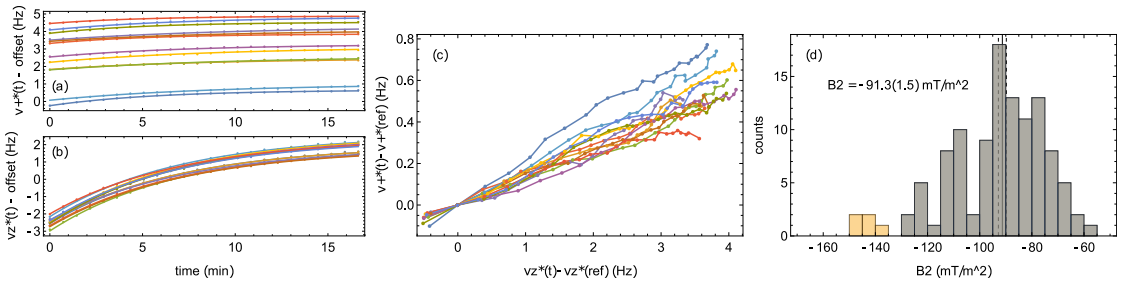

Figure 7.10.: B_2 determination via cooling curves. The cyclotron motion ν_+^* (b) is damped by dissipating energy in the cyclotron detector. (a) depicts the axial frequency $\nu_z^*(t)$, the asterisk $*$ donates that the cyclotron motion is excited. The axial and cyclotron motion vary as a function of time due to energy related frequency shifts. These shifts are due to relativistic effects and due to the magnetic inhomogeneity B_2 that can be measured by comparing (a) and (b) as described in the text. When (a) and (b) are plotted against each other, the linear relation between both frequency shifts becomes apparent (c). B_2 is determined from the fits in (a) and (b). These results are scattered as the cyclotron cooling curves are affected by magnetic field fluctuations that are not observed in the axial curves. Therefore, the obtained B_2 values (yellow) are Grubbs filtered [154] (blue), and 108 of the in total 120 cooling curves are used for determining $B_2 = -91.3(1.5)\,\mathrm{mT/m^2}$. The respective initial excitation energies are given by $E_{+,0,\mathrm{H}^-} = 25.7(3)\,\mathrm{eV}$ and $E_{+,0,\bar{p}} = 27.7(3)\,\mathrm{eV}$. The cooling curves were recorded in 14 different measurements that took place between 2018/11/14 and 2019/01/06, the total measurement time for the cooling curves presented here is about 35 hours.

For a cyclotron-wise excited particle, the cyclotron frequency and the axial frequency as a function of time can then be described by the sum of a constant frequency and an exponentially decaying shift following Eq. 7.40 (see Fig. 7.10 (a,b)),

$$\begin{aligned}\nu_{+,z}^*(t) &= \nu_{+,z,\mathrm{ref}} + \mathcal{M}_{+,z}(B_2, \mathrm{SR}) \times E_{+,0} \times \mathrm{Exp}(-t/\tau_+) \\ &= \nu_{+,z,\mathrm{ref}} + A_{+,z} \times \mathrm{Exp}(-t/\tau_+),\end{aligned} \tag{7.43}$$

with $\mathcal{M}_{+,z}(B_2, \mathrm{SR})$ given by Eq. 7.41 and Eq. 7.42. Here, it is assumed that both reference frequencies $\nu_{+,z,\mathrm{ref}}$, which denote the respective oscillation frequencies at no cyclotron energy, remain constant during the cooling curve acquisition time. The asterisks $*$ denotes cyclotron-wise excited particles.

In order to determine the B_2 coefficient, we regularly recorded cooling curves as depicted in Fig. 7.10 (a,b) for both ion species each time when the q/m ratio was measured by means of peak methods. Here, we firstly excite the cyclotron energy to $E_{+,0} \approx 25\,\mathrm{eV}$, and afterwards record axial and cyclotron spectra simultaneously with an averaging time of usually 42 s per spectra for about 17 minutes. During this time, the particle's

cyclotron motion continuously dissipates energy due to the interaction with the cyclotron detector, that damps the cyclotron motion with $\tau_+ \approx 450\,\mathrm{s}$. The set of cyclotron and axial frequencies over time then resembles an exponential cooling curve, as outlined in Eq. 7.43, see Fig. 7.10 (a,b). If the cyclotron frequency shift during the acquisition of the cooling curve is plotted against the corresponding axial frequency shift, the linear relation between both shifts is seen (Fig. 7.10 (c)). From the coefficients $A_{+,-}$ in the exponential fits, the B_2 coefficient is extracted by inserting the relations from Eq. 7.41, 7.42, see Fig. 7.10 (d). A few distinct outliers are observed among the determined B_2 values, which are likely related to background magnetic field drifts, that bias the cyclotron cooling curve, while leaving the axial curve unaffected. Such field drifts are likely related to apparatus thermalization after filling of cryoliquids or ambient temperature drifts and are observed on a regular basis. The corresponding outliers are removed by Grubbs filtering [154], and a final value of $B_2 = -91.3(1.5)\,\mathrm{mT/m^2}$ is observed.
While these methods offer an accessible way for determining B_2, there are several drawbacks that need to be considered. Firstly, the acquisition of cooling curves such as depicted in Fig. 7.10 (a,b) requires a time span of at least 10 min, usually rather 15-20 min. During this time, the ambient magnetic field might change due to changes in internal and external conditions, such as magnet ramps in the experiment surroundings or changes in the ambient temperature, pressure inside the cryogenic vessels and cryoliquid level. Changes in the magnetic field will impact on the measured cyclotron frequency, but not on the axial frequency, which can shift A_+ only and thus affects the determined B_2. As a consequence, the obtained B_2 values were Grubbs filtered [154] (see Fig. 7.10). For the low-energy shots of the cooling curve, the particle energy is sometimes too low to generate a significantly prominent peak on the cyclotron detector, which requires to introduce threshold criteria in the data analysis for rejecting these fits that misidentified noise peaks for particle signals. On the other side, the cooling curve approach allows to determine the cyclotron cooling time constant τ_+ explicitly.
Comparably large excitation energies $E_{+,0}$ of about 25 eV are required in order to record long cooling curves, energies at which the effect of non-linear shifts due to C_6, C_8 and higher order coefficients become stronger. The combined effect of C_6 and C_8 onto the axial frequency is given by $\Delta\nu_z(E_+, C_6, C_8) = -327\,\mu\mathrm{Hz/eV^2} + 9.9\,\mu\mathrm{Hz/eV^3}$, which corresponds to a axial frequency shifts of at maximum 1.5 % compared to the linear term $\Delta\nu_z(E_+, B_2, \mathrm{SR}) = -174(4)\,\mathrm{mHz/eV}$ arising from B_2 and special relativity for the energy range of up to 35 eV. The non-linear scaling in cyclotron is suppressed even further,

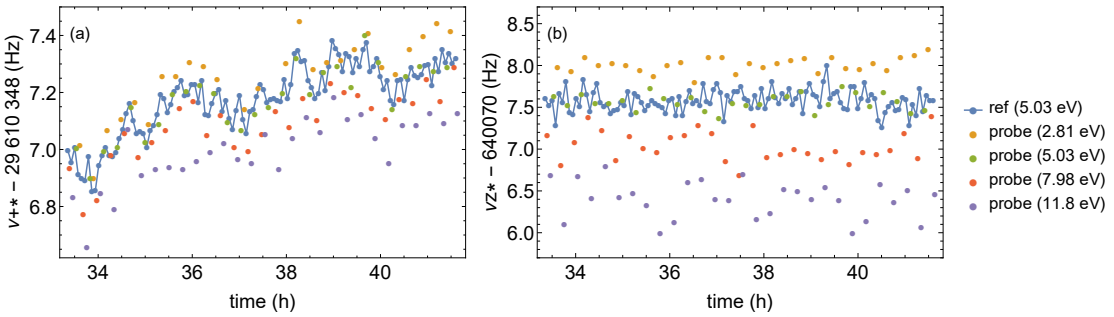

Figure 7.11.: Principle of B_2 determination via variation of excitation energies. On the left, the excited cyclotron frequencies are depicted. Reference frequencies (blue) and probe frequencies (remaining colours) are measured alternatingly, one of the probe frequency has the same mean energy as the reference frequency. Here, four different probe energies are used by adjusting the number of burst cycles used in the excitation drive. Corresponding axial frequencies at excited cyclotron motion are depicted on the right side. The data presented in the plot represent about seven hours of data taking out of a weekend-long measurement. A scaling of both frequency shifts proportional to the excitation energy is observed. From this scaling, B_2 can be determined as discussed in the text and depicted in Fig. 7.12.

where the linear scaling of $\Delta\nu_+(E_+)$ is dominated by special relativity and not by B_2. For these reasons, the effect of C_6 and C_8 is neglected here, while in the next section another method for determining B_2 is presented, which operates at lower cyclotron energies of 12 eV and less, which is used to determine the reference B_2 value for the peak campaign.

7.2.3. B_2 determination via variation of excitation energy

Another way of determining B_2 has been developed in the context of this thesis. In this method, a particle is cyclotron-wise excited alternating between a reference energy $E_{+,\mathrm{ref}}$ and a probe energy $E_{+,\mathrm{probe}}$, by adjusting the cycle number in the excitation drive. Simultaneously, the corresponding frequencies $\nu^*_{+,z}$ are measured, with the asterisk * denoting an excited cyclotron motion, see Fig. 7.11. After each measurement of the excited cyclotron frequency, the particle is sideband cooled to the thermal temperature $T_+ = T_z \times \nu_+/\nu_z$.

Linear shifts in both frequencies $\nu^*_{+,z}$ scaling proportionally to the cyclotron energy are observed. In contrast to the B_2 determination by means of recording cyclotron cooling curves (Sec. 7.2.2), now frequency shifts between excited particles at two different energies are considered, $\Delta\nu^*_{+,z} = \nu^*_{+,z,\mathrm{ref}} - \nu^*_{+,z,\mathrm{probe}}$, and the corresponding slope $\Delta\nu^*_+/\Delta\nu^*_z$ is

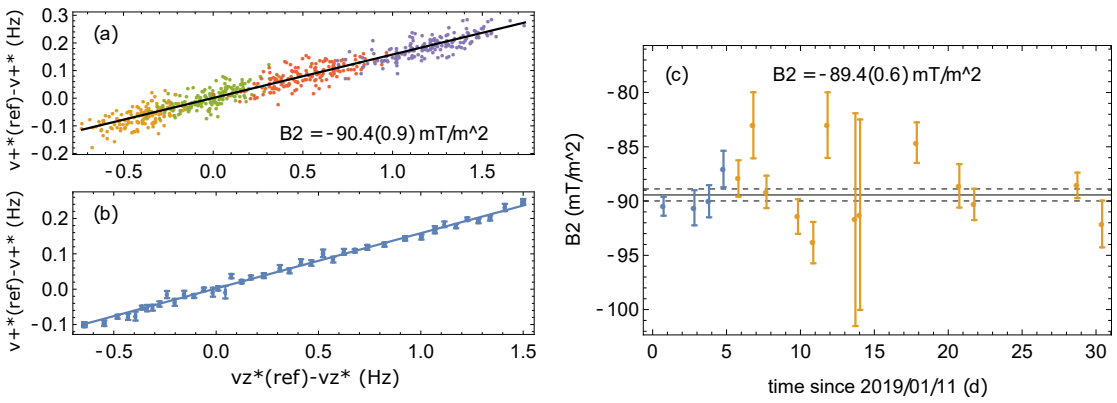

Figure 7.12.: B_2 measured via variation of burst energy. (a) and (b) depict the results from a weekend measurement of B_2. The different colors in (a) correspond to the various burst numbers and respective energies already presented in Fig. 7.11, while the results from (a) are binned up and plotted in (b). The determined B_2 of this 46 h long measurement campaign is $B_2 = -90.4(0.9)\,\mathrm{mT/m^2}$. In total, 17 measurements of B_2 have been conducted between January 11th and February 10th, 2019, all depicted in (c). The blue data points represent measurements carried out with the hydride ion, the yellow data points were measured with an antiproton. The combined B_2 is $-89.4(0.6)\,\mathrm{mT/m^2}$. The uncertainty was slightly corrected upwards by considering the reduced $\chi^2 = 1.9$, which points to a slight variation of B_2 over time. This might be explained by varying ambient conditions, for instance by magnet ramps in the experiment surroundings, or also changes in the cryoliquid pressures, ambient temperature, or cryoliquid levels. A similar measurement conducted from March 15th-24th, 2019, yielded $B_2 = -88.6(7)\,\mathrm{mT/m^2}$, demonstrating the long-term stability of B_2.

examined. Similarly to the cooling curve determination, B_2 is determined by comparing these shifts (see Fig. 7.12 and Eq. 7.41 and 7.42),

$$\begin{aligned} \frac{\Delta\nu_+^*/\nu_+}{\Delta\nu_z^*/\nu_z} &= \frac{-\left(\frac{1}{mc^2}+\frac{1}{4\pi^2 m\nu_+^2}\frac{B_2}{B_0}\right)}{\left(-\frac{1}{2mc^2}+\frac{1}{4\pi^2 m\nu_z^2}\frac{B_2}{B_0}\right)} \\ \Leftrightarrow B_2 &= \frac{-2B_0\left(2\pi\nu_+\right)^2\left(2\pi\nu_z\right)+B_0\left(2\pi\nu_+\right)\left(2\pi\nu_z\right)^2\Delta\nu_+^*/\Delta\nu_z^*}{2c^2\left(2\pi\nu_z+2\pi\nu_+\Delta\nu_+^*/\Delta\nu_z^*\right)}. \end{aligned} \tag{7.44}$$

The results of a weekend-long measurement ($t_{\mathrm{meas}} = 46\,\mathrm{h}$) are depicted in Fig. 7.12 (a,b). In (a), the individual shifts are plotted, with four colors representing the four different excitation settings, corresponding to the mean excitation energies $E_{\mathrm{exc}} = 2.81\,\mathrm{eV}$, 5.03 eV, 7.98 eV, and 11.8 eV. A least squares fit in (a) yields $B_2 = -90.4(0.9)\,\mathrm{mT/m^2}$, the B_2 precision achieved in this measurement is better than the obtainable resolution

in similar cooling curve measurements (compare Fig. 7.10). In (b), the data from (a) were binned together in sets of 15 individual data points. In (c), the results of in total 17 measurements of B_2 by means of this method are depicted. They were conducted over the course of 30 days. The data depicted in (a,b) are represented by the first data point in (c). The B_2 measurements were conducted using a single hydride ion (blue) and a single antiproton (yellow). When computing the weighted mean, a combined value of $B_2 = -89.4(0.6)\,\mathrm{mT/m^2}$ is obtained. This value is used as the reference B_2-value throughout this thesis, when the peak run is discussed. Its uncertainty was slightly corrected upwards taking into account the reduced $\chi^2 = 1.9$, which might indicate a slight temporal variation of B_2. This variation could be related to changes in external conditions, such as the ambient temperature, and magnet ramps of other experiments/the accelerator facility. The B_2 value determined here, $B_2 = -89.4(0.6)\,\mathrm{mT/m^2}$, is in good agreement with the B_2 value determined from cooling curve measurements ($B_{2,\text{cooling curves}} = -91.3(1.5)\,\mathrm{mT/m^2}$). The reference frequency measurements are performed interleaved with probe frequency measurements, which allows the removal of the effect of linear magnetic and electric field drifts from the data by performing linear interpolations, which constitutes a significant advantage compared to the cooling curve method. Also the about five times faster sampling time significantly suppresses the effect of ambient field changes during the measurement. This method allows measurements of B_2 at lower energies compared to the cooling curve method, which further suppresses the small effect of potential anharmonicities of higher order, such as C_6, C_8. It can be shown that the attenuation bias/the reliability ratio [155, 156] affects the determined B_2 by much less than 1 %, which is why this effect is neglected here.

Effect of the B_2 uncertainty onto the measured cyclotron frequency

When computing the cyclotron frequency ν_+ with vanishing cyclotron energy E_+, the axial frequency shift $\Delta\nu_z$ and the correction slope $\Delta\nu_+/(\Delta\nu_z)$ are considered:

$$\nu_+ = \nu_+^* - \Delta\nu_+ = \nu_+^* - \Delta\nu_z \times \frac{\mathrm{d}\Delta\nu_+}{\mathrm{d}\Delta\nu_z} \tag{7.45}$$

The uncertainty of $\Delta\nu_+$ and thus the uncertainty of ν_+ arising from the slope uncertainty is given by $u(\nu_+) = u(\Delta\nu_+) = 11.9\,\mathrm{p.p.t.}/\left(\left(\mathrm{mT/m^2}\right) \times \mathrm{eV}\right)$. With the above determined B_2 value of $B_2 = -89.4(0.6)\,\mathrm{mT/m^2}$, this results in $u(\nu_+) \approx 36\,\mathrm{p.p.t.}$ for the

typically used excitation energy of $E_{+,\mathrm{exc}} = 5\,\mathrm{eV}$. In the context of measurements of the ratio R of the q/m ratios of antiprotons and hydride ions, the more important figure of merit is the scaling $\mathrm{d}R/\mathrm{d}B_2$, which is theoretically given by $0.065\,\mathrm{p.p.t./}\left(\mathrm{mT/m^2}\right)$ for a typical excitation energy of $E_{+,\mathrm{exc}} = 5\,\mathrm{eV}$, assuming the mean energies of both ion species are identical. When evaluating an example data set of 350 frequency ratio measurements as a function of inputted B_2, for this specific dataset a value of $1.39\,\mathrm{p.p.t./}\left(\mathrm{mT/m^2}\right)$ is obtained. This scaling is currently under investigation by other members of the BASE collaboration, who analyze the peak charge-to-mass ratio measurement campaign, but is likely related to an interplay of non-identical energies and residual non-linearities. Our B_2 uncertainty $u(B_2) = 0.6\,\mathrm{mT/m^2}$ then gives rise to a systematic uncertainty of $u(R) = 0.8\,\mathrm{p.p.t.}$ (experimental data) or $u(R) = 0.15\,\mathrm{p.p.t.}$ (theoretical value), both values being far below the targeted precision of $u(R) = 20\,\mathrm{p.p.t.}$

Comparing the sideband and the peak method

The peak method for measuring the cyclotron frequency largely depends on the ability to correct precisely and accurately for the energy dependent shifts. In order to verify the consistency between the peak method and the well-characterized sideband method [54, 39], interleaved measurements of the cyclotron frequency by both methods have been performed (see Fig. 7.13). In (a), the cyclotron frequency difference $\nu_+ - \nu_+^*$ is plotted against the axial frequency difference $\nu_z - \nu_z^*$, where ν_+^* and ν_z^* were determined by means of the peak method, while ν_z and ν_+ at thermal cyclotron energies were measured by means of the dip and the double dip method. In addition, the excitation energy used in the peak measurement was alternated between two values to provide additional input for the B_2 determination described in Sec. 7.2.3. The four different colors represent measurements carried out on four different days. The slope of the solid lines is defined by the B_2 coefficient, with $B_2 = -89.4\,\mathrm{mT/m^2}$, and their abscissa given by the offset determined in each measurement by

$$\nu_+(\mathrm{SB}) - \nu_+(\mathrm{PK}) = \nu_+(\mathrm{SB}) - \left(\nu_+^* - (\nu_z^* - \nu_z) \times \frac{\mathrm{d}\nu_+}{\mathrm{d}\nu_z}\right). \tag{7.46}$$

The result of each of the four individual measurements is depicted in Fig. 7.13 (b), with the combined result yielding $\nu_+(\mathrm{SB}) - \nu_+(\mathrm{PK}) = 5.3(2.0)(1.7)\,\mathrm{mHz}$, with the first uncertainty indicating the statistical uncertainty, and the seconding indicating the systematic

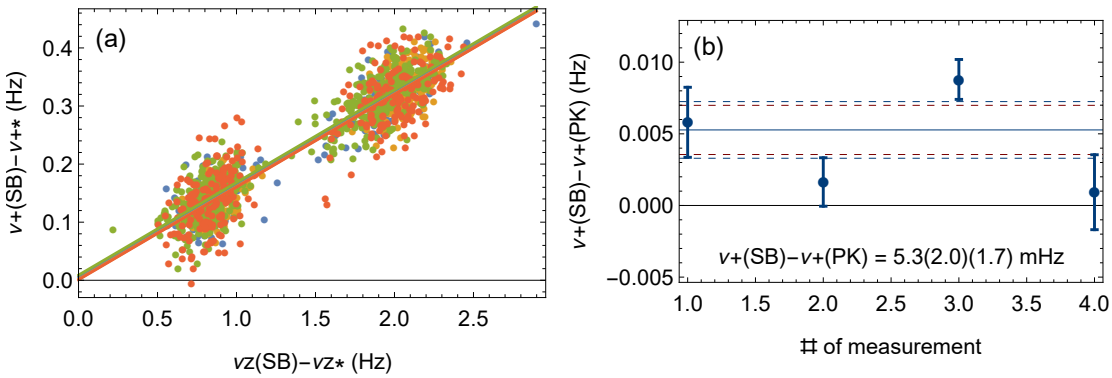

Figure 7.13.: Comparison of peak and sideband method. Left: Raw data from four different measurements. From each individual data point, a cyclotron frequency with vanishing cyclotron energy is computed. The data were Grubbs filtered [154] based on their fit residuals from a least-squares linear fit, which gives the results as first computing the offset and subsequently Grubbs filtering the offsets. In this way, a few outliers were excluded. The solid lines do not represent fits to the data. Instead, the slopes show the scaling of $\Delta\nu_+^*/\Delta\nu_z^*$ expected from theory assuming assuming $B_2 = -89.4\,\mathrm{mT/m^2}$, and their abscissa are given by the mean offset between both measurement types for each set of measurements. The corresponding offsets are depicted on the right, with a weighted mean indicated by the solid blue line and the statistical uncertainty indicated by the dashed blue lines. The dashed red lines indicate the systematic uncertainty due to the uncertainty on B_2. The combined offset between both methods is $\nu_+(\mathrm{PK}) - \nu_+(\mathrm{SB}) = 5.3(2.0)(1.7)\,\mathrm{mHz}$. Here, the well characterized FFT effect [52] is already subtracted, which shifts $\nu_+(\mathrm{PK}) - \nu_+(\mathrm{SB})$ down by 3.9 mHz. The reduced χ^2 for the blue data points is 4.6. This is already considered in the statistical uncertainty. This statistical inconsistency could be explained by assuming a slight variation of B_2 over time.

uncertainty arising from the B_2 uncertainty, with $B_2 = -89.4(0.6)\,\mathrm{mT/m^2}$. During the systematic studies on the peak method, the behavior of the Stanford Research SR780 audio analyzer[1] as a function of the frequency range was investigated. To this end, frequencies across the frequency range off the FFT (10 kHz - 100 kHz) have been irradiated by a dedicated frequency generator, and the corresponding frequency spectra were evaluated. During these investigations, a systematic offset scaling linearly with the FFT frequency was discovered, which was studied in detail and carefully characterized in the PhD thesis of James Brydges-Harrington [52]. The scaling is given by:

$$\nu_{\mathrm{true}}^{\mathrm{corr}} = \nu_{\mathrm{SR780}}^{\mathrm{meas}} + 0.2576(32) \times 10^{-6} \nu_{\mathrm{SR780}}^{\mathrm{meas}} + 50(190) \times 10^{-6}, \tag{7.47}$$

[1] This analyzer was manually equipped with an interface for a 10 MHz reference clock, which improved both the stability and accuracy much compared to the factory state that does not have such an interface by default.

with $\nu_{\mathrm{SR780}}^{\mathrm{meas}}$ denoting the frequency measured by the FFT, and $\nu_{\mathrm{true}}^{\mathrm{corr}}$ being the real frequency, which is identical to the frequency irradiated by the frequency generator in this measurement. Since the measurements presented in Fig. 7.13 were conducted at an FFT center frequency of about 66 kHz, while the sideband measurements were recorded at a center frequency of 50.427 kHz, $\nu_+(\mathrm{SB}) - \nu_+(\mathrm{PK})$ needs to be corrected downwards by 3.9 mHz, which is already considered in the offset $\nu_+(\mathrm{SB}) - \nu_+(\mathrm{PK}) = 5.3(2.0)(1.7)\,\mathrm{mHz}$. Examining the statistical distribution of the four measured points, a reduced $\chi^2 = 4.6$ is observed. Even though the sample size of four is low, the statistical uncertainty quoted here was increased accordingly. The combined uncertainty from statistics and systematics is 2.6 mHz, which yields an offset that is only within 2.1 standard errors in agreement with no offset. This slight discrepancy was only observed during the data evaluation after this experimental run was concluded. No significant offset scaling as a function of cyclotron energy could be found in the data taken. Consequently, it was concluded that non-linear terms did not gave rise to this tension. Another explanation for this tension would be given by assuming a slight variation of B_2 over time. Such a variation could also lead to an increased reduced χ^2. Considering that the mean cyclotron frequency shift of the data sample was 235(3) mHz, the observed offset corresponds to 2.3(1.1) %. A deviation of B_2 of similar order would be sufficient to entirely explain the offset. The offset of 5.3(2.6) mHz corresponds to 180(90) p.p.t. Taking the interval of 2 standard errors, the offset between both methods is constrained here to be below 360 p.p.t.

While in this measurement, the peak method was compared against the sideband method, for charge-to-mass ratio measurements one peak measurement is compared against the other. For particles at identical mean energies, effectively no energy correction would have to be applied to first order[1], as the frequency shift scales linearly with energy, and the different individual particle energies would thus average out. For particles at different mean energies $\Delta E_+ \neq 0$, an offset resulting from an incorrect energy correction (for instance due to a wrong B_2 assignment) would be suppressed by $\Delta E_+/\mu(E_+)$, with $\mu(E_+)$ denoting the energy mean value. The combined corrected offset between the peak and the sideband method is $\Delta\nu_{+,\mathrm{SB,PK,\ corr}} = 5.3(2.6)\,\mathrm{mHz}$. At an energy difference of 2 % ($\Delta E_+ = \mu(E_+)/50$), which is routinely achieved during peak ratio measurements, this would lead to an offset of $\Delta\nu_{+,1,2} = 0.11(0.06)\,\mathrm{mHz}$, corresponding to 4(2) p.p.t., which is well below the targeted uncertainty of 20 p.p.t.

[1] The different masses of the antiproton and the hydride ion would still lead to a small correction.

Frequency stability achieved with the peak method

The sideband method [54, 39] relies on coupling the cyclotron motion to the axial motion, which is why the attainable resolution in the determination of the cyclotron frequency is dominantly limited by the uncertainty with which the axial frequency can be determined within a defined time window. The axial frequency uncertainty is dominantly limited by the uncertainty of the least-squares fit to the axial dip lineshape. By employing the peak method, the excited cyclotron frequency ν_+^* is measured directly. Its achievable stability is to first order solely constrained by the magnet stability and not limited by the axial frequency resolution any more, but a good axial frequency resolution is still required in order to correct for the cyclotron energy dependent shift $\Delta\nu_+$ as described in Eq. 7.25. Consequently, the peak method principally enables a higher cyclotron frequency resolution to be achieved.

In order to investigate the limits of the current peak-ratio measurement, a 46 hour long measurement of cyclotron frequencies is investigated, see Fig. 7.14 (a). The displayed frequencies are already energy corrected. Three frequency jumps are observed, and the corresponding differential Allan deviation [126] for all four subsets is computed, see Fig. 7.14 (b). Notably, the frequency stability changes after each frequency jump, with the best frequency scatter in terms of the differential Allan deviation given by 960(40) p.p.t and the worst given by 2080(110) p.p.t. While this behavior remained unexplained at the time of the observation, a possible mechanism for generating these frequency jumps and changes in frequency stability was provided later on when the multilayer self-shielding coil (SSC) wound around the BASE trap can was characterized in detail [85]. For the measurement presented here, the 75 mm and the 85 mm coil were active, while the 65 mm coil was quenched. If the SSC axis and the magnet axis are slightly misaligned by an misalignment angle θ, the SSC shielding factor S is reduced accordingly [85]. If vibrations, for instance imposed by boiling cryo-liquids are present in the experimental apparatus, the temporal variation of θ can also induce excess magnetic field noise (see Eq. 5 in [85]). Jumps in the magnetic field might arise from abrupt changes in θ, that could be related to the relief of stress that had built up due to changes in cryoliquid levels or changes in ambient temperature or ambient pressure. While the SSC is absolutely crucial for performing high-precision cyclotron frequency measurements in an accelerator hall when either other experiments or the accelerator are operated, it also limits the achievable stability during times when no or little ambient magnetic field noise

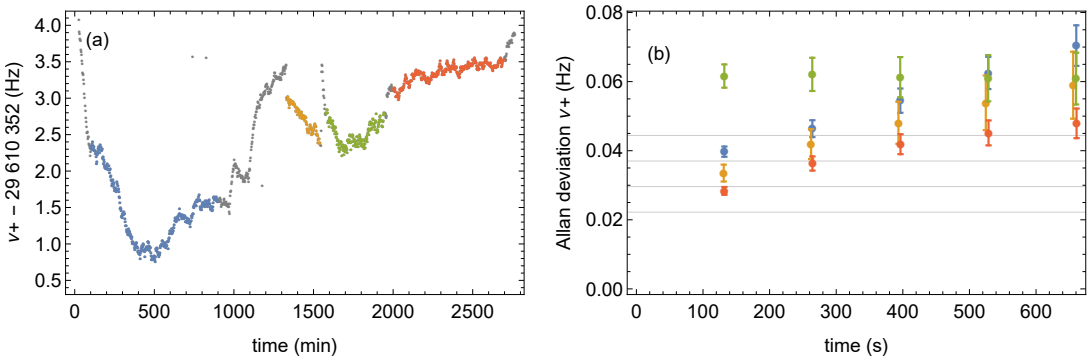

Figure 7.14.: Investigation of the cyclotron frequency stability across a 46 hour long measurement. The excited cyclotron frequencies ν_+^* were measured by means of the peak method, and energy-corrected by simultaneously recorded axial frequency differences $\Delta\nu_z = \nu_z^* - \nu_z$ (as discussed in Fig. 7.8 and Eq. 7.25). The corrected cyclotron frequencies ν_+ are displayed either in gray or in colors on the left side. Three frequency jumps are observed at $t \approx 1330\,\text{min}, 1540\,\text{min}$, and 1960 min. These jumps are supposedly related to the multi-layer self shielding coil (SSC) wound around the trap can [85], which adds magnetic field noise due to vibrations present in the apparatus and a slight misalignment between the SSC axis and the magnet axis, when the coil is active. The frequency stability of each of the four subsets is investigated, and the corresponding differential Allan deviations are plotted on the right side, with the grid lines denoting 0.75 p.p.t., 1.0 p.p.t., 1.25 p.p.t., 1.5 p.p.t. For the first point of the differential Allan deviation, we observed values of 960(40) p.p.t. (red), 1130(80) p.p.t. (yellow), 1320(50) p.p.t. (blue), 2080(110) p.p.t. (green). For the q/m campaign conducted during the year-end technical stop (yets) of CERN with active SSCs, we observed a median frequency scatter of about 900 p.p.t when the scatter of 1 h long sets of frequencies is evaluated individually. These frequency fluctuations demonstrate an improvement in stability of about a factor of two compared to the sideband method, where a scatter of about 1.7 p.p.b. was achieved in the best cases. When there is no magnetic field background noise, and all SSCs are quenched, even scatter values around 400 p.p.t. to 500 p.p.t. can be reached.

is present.

Once this SSC related behavior was observed, cyclotron frequency stabilities at a calm magnetic background were investigated for different SSCs being active or quenched. During these investigations, a frequency scatter of order 400-500 p.p.t. was achieved reproducibly when all coils were quenched. The typical scatter in axial frequency at the usual 42 s of averaging time is $\sigma(\nu_z) \approx 38\,\text{mHz}$, which leads to an axial scatter of about $\sigma(\Delta\nu_z) \approx 54\,\text{mHz}$, neglecting the effect of the cyclotron cooling, which might induce a few mHz of additional scatter in $\sigma(\Delta\nu_z)$. Due to $\Delta\nu_+/\Delta\nu_z(B_2) \approx 1/6.3$, this leads to a cyclotron scatter of about $\sigma(\nu_+(\sigma(\Delta\nu_z))) \approx 290\,\text{p.p.t.}$ The cyclotron frequency scatter

related to magnetic field scatter $\sigma_B(\nu_+)$ is then estimated by

$$\sigma_B(\nu_+) \leq \left(\sigma(\nu_+)^2 - \sigma(\nu_+(\sigma(\Delta\nu_z)))^2\right)^{1/2} \approx 280\,\text{p.p.t. to } 410\,\text{p.p.t.}, \tag{7.48}$$

with this value indicating a principal limitation, probably due to magnetic field scatter. It should be noted here that the described peak run was the first experimental run during which BASE was operating at such high cyclotron frequency resolution. While the changes in frequency stability described in Fig. 7.14 seem to be dominantly related to the SSC status, this behavior was only discovered approaching the end of the run. The interplay between the SSC status, ambient experimental conditions such as external magnetic field ramps, ambient temperature variations and pressure inside cryo-liquid vessels remains to be studied in greater detail in further experimental campaigns. In addition to that, ambient experimental conditions contribute to the changes in magnetic field stability that are not related to active SSC coils, and offer a wide field of study for experimental stabilization and isolation.
With the sideband method, a lowest frequency scatter of 1.7 p.p.b. is achieved for optimal ambient conditions, which is then mostly limited by the axial frequency stability. Compared to the sideband method, the best observed peak method stability of 400-500 p.p.t. constitutes an improvement of a factor of about four in frequency scatter, or of about sixteen in frequency resolution. Of course, during normal operation of the Antiproton Decelerator or when other experiments are being operated, the SSC has to be active. For these conditions, the values depicted in Fig. 7.14 represent more realistic stabilities. Under such conditions, the peak method is dominantly limited by other environmental fluctuations which affect the magnetic field stability, not by the method itself.

7.2.4. Disentangling B_2 and C_4

So far, the effect of C_4 has been neglected and instead of the "real" $B_{2,\text{real}}$ purely resulting from the quadratic magnetic inhomogeneity, an "effective" $B_{2,\text{eff}}$ was calculated that includes all linear shifts except from the relativistic shift. This treatment is especially justified in the case where C_4 is close to zero, in which case $B_{2,\text{eff}} \approx B_{2,\text{real}}$. However, if one performs peak measurements at a tuning ratio $\text{TR} \neq \text{TR}_{\text{opt}}$, the effect of B_2 and C_4 can be disentangled. We recapitulate Eq. 2.16, and describe C_4 as a function of the

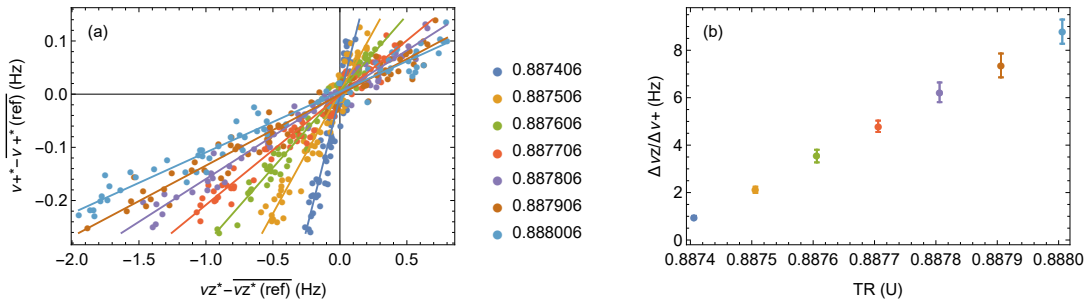

Figure 7.15.: Cyclotron frequency measurement by means of the peak method at different energies and different tuning ratios. To this end, measurement cyclotron and axial frequencies $\nu_{+,z}^*$ at varying cyclotron energies are subtracted from reference frequencies $\nu_{+,z,\text{ref}}^*$ measured at a reference energy $E_{+,\text{ref}}$. All cyclotron frequencies were measured using the peak method. The raw data are depicted on the left, the inverse slopes $\left(\Delta\nu_+^*/\Delta\nu_z^*\right)^{-1}$ for each tuning ratio is given on the right.

tuning ratio and the D_4 trap parameter calculated from potential theory:

$$C_4 = D_4\,(\text{TR} - \text{TR}_{\text{opt}}) \tag{7.49}$$

Now, the effect of C_4 is included in Eq. 7.44 and the following relation is obtained:

$$\frac{\Delta\nu_+^*/\nu_+}{\Delta\nu_z^*/\nu_z} = \frac{\left(-\frac{1}{mc^2} + \frac{3}{4}\frac{1}{qV_r}\frac{C_4}{C_2^2}\left(\frac{\nu_z}{\nu_+}\right)^4 - \frac{1}{m(2\pi\nu_+)^2}\frac{B_2}{B_0}\right)E_+}{\left(-\frac{1}{2mc^2} - \frac{3}{2}\frac{1}{qV_r}\frac{C_4}{C_2^2}\left(\frac{\nu_z}{\nu_+}\right)^2 + \frac{1}{m(2\pi\nu_z)^2}\frac{B_2}{B_0}\right)E_+} \tag{7.50}$$

By choosing different values for TR, we are able to tune the slope $\Delta\nu_z^*/\Delta\nu_+^*$ as depicted in Fig. 7.15, where the cyclotron frequency was measured by means of the peak method for four different excitation energies and seven different tuning ratios. The raw data are shown in (a), while the fitted inverse slope $\left(\Delta\nu_+^*/\Delta\nu_z^*\right)^{-1}$ is plotted in (b). The C_4 values for each tuning ratio are determined from inserting TR_{opt} measured in Sec. 7.1.1 into Eq. 7.49, and values for $B_{2,\text{real}}$ are computed for each tuning ratio (see Fig. 7.16 (a)). Since the obtained values for $B_{2,\text{real}}$ do not vary across the considered tuning ratio range within their individual uncertainties, our understanding of the trap parameters is confirmed. The weighted mean yields $B_{2,\text{real}} = -88.8(2.5)\,\text{mT/m}^2$, which is in good agreement with our independently determined effective $B_{2,\text{eff}} = -89.4(0.6)\,\text{mT/m}^2$ (7.12). The uncertainty on $B_{2,\text{real}}$ is given by the C_4 uncertainty $u(C_4)$ and the slope un-

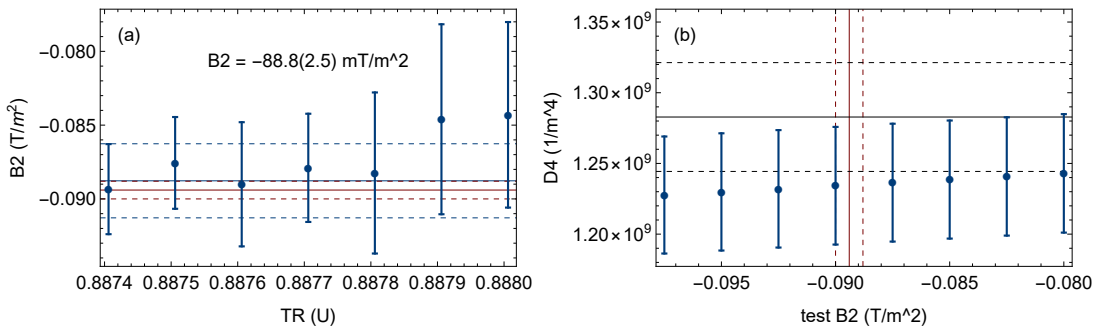

Figure 7.16.: Determination of $B_{2,\mathrm{real}}$ (left) and D_4 (right). $B_{2,\mathrm{real}}$ is determined by applying Eq. 7.50 and inserting the relation $C_4 = E_4 + D_4 \times \mathrm{TR}$. The calculated values for $B_{2,\mathrm{real}}$ are constant within their respective uncertainties across the considered tuning ratio range, which confirms our understanding of the dominant trap inhomogeneity parameters. The weighted mean $B_{2,\mathrm{real}} = 88.5(2.5)\,\mathrm{mT/m^2}$ indicated by the blue grid lines agrees well with the effective B_2 determined in Sec. 7.12 (red grid lines). On the right, the data from Fig. 7.15 are used for determining D_4. To this end, values for $B_{2,\mathrm{test}}$ ranging from $-100\,\mathrm{mT/m^2}$ to $-80\,\mathrm{mT/m^2}$ are inserted into Eq. 7.50. The calculated values for D_4 are in agreement with the theoretical $D_4 \approx 1.28(4) \times 10^9\,1/\mathrm{m^4}$ (horizontal grid lines) derived from potential theory.

certainty $u(\Delta\nu_z/\Delta\nu_+)$. The contribution of $u(C_4)$ to $u(B_{2,\mathrm{real}})$ ranges from $2.9\,\mathrm{mT/m^2}$ to $1.8\,\mathrm{mT/m^2}$ and increases for larger absolute values of C_4 due to $u(D_4)$. The contribution arising from the slope uncertainty $u(\Delta\nu_z/\Delta\nu_+)$ on the other side decreases for steeper slopes and reaches a lowest contribution of $0.9\,\mathrm{mT/m^2}$ for $\mathrm{TR} = 0.887\,406$. In this way, our measurement demonstrates that in principle a higher resolution on B_2 can be reached when measuring at non-vanishing C_4. However, this would require a more precise knowledge of C_4 than available for this dataset.

On the other side, this measurement can also be used to determine D_4 for a given "test" value $B_{2,\mathrm{test}}$ (see Fig. 7.16 (b)). To this end, C_4 parameters are extracted by applying Eq. 7.50, computing individual C_4 values for each tuning ratio and inserting the relation $D_4 = \mathrm{d}C_4/\mathrm{dTR}$. Within a 3 % uncertainty on D_4 arising from the manufacturing tolerances, the determined values for D_4 are in good agreement with the theoretical prediction for $-100\,\mathrm{mT/m^2} \leq B_{2,\mathrm{test}} \leq -80\,\mathrm{mT/m^2}$.
Both interpretations outlined here provide important independent confirmation measurements for our understanding of the trap parameters, which are most relevant for systematic studies, and our accurate control of the related systematic effects (at the level of the aimed fractional uncertainty of 20 p.p.t.).

7.2.5. Cyclotron frequency as a function of axial temperature

When performing a measurement on the antiproton-to-proton charge-to-mass ratio, the scaling of cyclotron frequency with axial temperature, $\Delta\nu_+(T_z)/\nu_+ = -23.4(6)\,\mathrm{p.p.t./K}$ discussed in Sec. 7.1.1 is one of the dominant effects that have to be considered in the ratio evaluation. The axial temperatures of both particles are not necessarily identical, but can differ on the level of several 100 mK, which can lead to frequency ratio shifts of order 10 p.p.t. As long as the temperature difference is constrained, this effect can be corrected for and only the uncertainty of the temperature difference affects the ratio uncertainty. The high frequency resolution of the peak method allows to explicitly measure this scaling for the first time in the BASE apparatus. The full expression for $\Delta\nu_+(T_z)/\nu_+$ from Eq. 2.38 (multiplied by the inverse dip width $1/\delta\nu_z$) is given by

$$\frac{\Delta\nu_+}{\nu_+} \times \frac{1}{\delta\nu_z} = \frac{1}{m\omega_z^2}\frac{B_2}{B_0}\,(k_B T_z) \times \frac{1}{\delta\nu_z}. \tag{7.51}$$

The axial temperature is varied by the application of active electronic feedback [78]. The axial temperature T_z and the dip width are related linearly, $\delta\nu_{z,1}/\delta\nu_{z,2} = T_{z,1}/T_{z,2}$ (see also Sec. 2.3.2). By measuring the cyclotron frequency as a function of axial temperature, the coefficient $B_2 \times (k_B T_z)$ is measured explicitly:

$$B_2 \times (k_B T_z) = \frac{\Delta\nu_+}{\delta\nu_z}\left(\frac{\nu_+}{m\omega_z^2} \times \frac{1}{B_0}\frac{1}{\delta\nu_z}\right)^{-1}, \tag{7.52}$$

where the coefficients in the bracket are known and not subject to this measurement. In order to characterize $\Delta\nu_+(T_z)/\nu_+$, we adjust the strength and the feedback phase of the axial feedback loop, which controls the axial temperature, and determine the cyclotron frequency by means of the peak method. The feedback is alternatingly switched on and off. When feedback is applied, axial dip widths between 2.1 Hz and 12.5 Hz are obtained, while the feedback-free dip width is $\delta\nu_z = 6.1\,\mathrm{Hz}$. This corresponds to an axial temperature variation of a factor of six. As shown in Fig. 7.17 (a), a clear scaling of the cyclotron frequency as function of the axial dip width is observed. By inserting $B_2 = -89.4(0.6)\,\mathrm{mT/m^2}$ into Eq. 7.52 and performing a least-squares fit to the data, a temperature scaling $T_z/(\delta\nu_z) = 2.37(39)\,\mathrm{Hz/K}$ is obtained. For the typical dip width $\delta\nu_z = 6.1\,\mathrm{Hz}$, this yields an axial temperature $T_z = 14.5\,(2.4)\,\mathrm{K}$, which is in excellent agreement with the axial temperature determined by means of tuning ratio

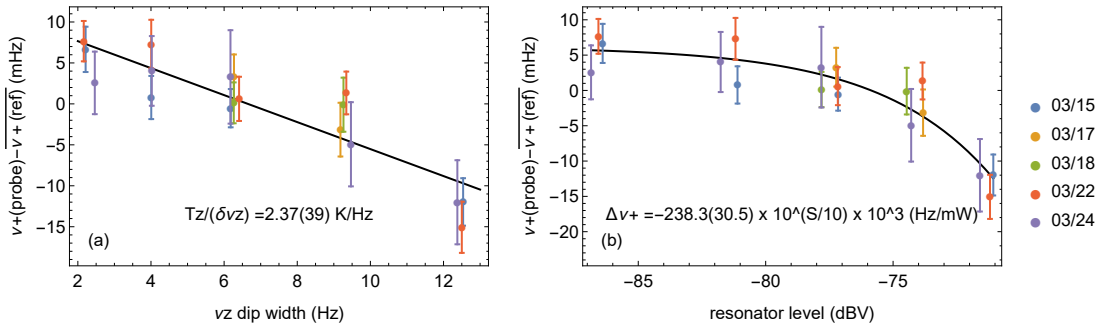

Figure 7.17.: Cyclotron frequency as a function of axial temperature. On the left, the cyclotron frequency as a function of axial dip width $\delta\nu_z$ is depicted. The axial dip width is varied by applying active feedback, with the feedback-free dip width given by $\delta\nu_z = 6.1\,\mathrm{Hz}$. As $\delta\nu_z$ is a linear function of the axial temperature T_z (see Eq. 2.38), this measurements allows to extract $B_2 \times T_z(\delta\nu_z)$ following the procedure outlined in the text. Inserting the known $B_2 = -89.4(0.6)\,\mathrm{mT/m^2}$, a temperature $T_z(\delta\nu_z) = 2.37(39)\,\mathrm{K/Hz}$ is obtained. This corresponds to an axial temperature $T_z = 14.5\,(2.4)\,\mathrm{K}$ for $\delta\nu_z = 6.1\,\mathrm{Hz}$, which is in good agreement with the axial temperature $T_z = 14.68(20)$ determined by tuning ratio scans in Fig. 7.2, and roughly in agreement with the axial temperatures determined by excitation scatter measurements (Fig. 7.9), which vary over time between $T_z = 10.6(8)\,\mathrm{K}$ and $T_z = 13.5(1.0)\,\mathrm{K}$. On the right side, the cyclotron frequency as a function of the resonator level is plotted. From this curve, the contribution of differences in axial temperature onto the q/m ratio determined by means of the peak method is constrained down to $\Delta\nu_+ = 0.8(3)\,\mathrm{p.p.t.}$ (see Eq. 7.55).

scans ($T_z = 14.68(20)\,\mathrm{K}$, see Fig. 7.1) and the axial temperature determined by means of the above described energy scatter analysis ($T_z = 12.4(2)\,\mathrm{K}$, see Fig. 7.9). This measurement provides an independent value for the axial temperature explicitly utilizing the potentially dominant systematic frequency ratio shift and is an important independent check, which probes at the same time our understanding of this shift.

While the data depicted in Fig. 7.17 (a) are used to determine the axial temperature T_z by comparing the scaling $\mathrm{d}\nu_+/\mathrm{d}\delta\nu_z$, the data depicted in Fig. 7.17 (b) allow to study the scaling of the resonator noise level S with temperature, and the relation $\mathrm{d}\nu_+/\mathrm{d}S$ explicitly. As it was outlined in Sec. 7.1.1, the comparison of resonator levels is one of the main methods for constraining the temperature difference in a q/m measurement campaign. The resonator noise level S is derived from the Johnson noise of the resonator,

$$S = 10\log_{10}\left(\left(4k_B R_p T_z \kappa^2 + e_n^2\right)\gamma\right), \tag{7.53}$$

with the effective parallel resistance R_p, the coupling constant κ, the amplifier noise e_n^2 and the parameter γ, which incorporates amplifier gain and FFT settings. From Eq. 7.52 and Eq. 7.53, we perform a least-squares fit on $\Delta\nu_+(S)$, and obtain

$$\Delta\nu_+(S) = A + B \times 10^{S/10} \qquad \text{with } A = 6.2(1.1) \qquad B = -2.4(3) \times 10^8 \tag{7.54}$$

During the q/m-campaign performed with peak methods, the signal level difference is constrained to $\Delta S = -0.089(9)\,\mathrm{dB}$ (uncorrected). When correcting for the changed detector impedance in the two different working points, $\Delta S = 0.025(9)\,\mathrm{dB}$ is obtained, which yields the following cyclotron frequency shift:

$$\Delta\nu_+(\Delta S = 0.025(9)\,\mathrm{dB}) = 0.8(3)\,\mathrm{p.p.t.} \tag{7.55}$$

Note that relation 7.55 is obtained without making assumptions about the interplay between dip width and resonator level, and without inserting a value for the axial temperature, but purely by inserting the resonator levels measured during the campaign. In this way, it provides an important independent measurement, which tests and benchmarks our understanding of one of the dominant systematic frequency ratio shifts. The uncertainty on the constrained cyclotron frequency shift is well below the targeted precision of 20 p.p.t.

7.2.6. Cyclotron frequency as a function of varactor voltages

When measuring the antiproton-to-proton charge-to-mass ratio, it is of crucial importance to measure both particles under identical conditions, as for instance any ion displacement could leed to significant cyclotron frequency shift due to residual magnetic field gradients. However, due to the different masses of both ions, the axial detector has to be detuned by $\Delta\nu_{\mathrm{res,ax}} = 348.5\,\mathrm{Hz}$ in order to match the axial resonator frequency and the axial oscillation frequency. In some measurements, also the cyclotron detector frequency was tuned by means of another varactor diode for the same reason. Due to the low Q-factor of the cyclotron detector/the high FWHM $\approx 150\,\mathrm{kHz}$, this detector tuning is optional, as the cyclotron frequencies only differ by about $\Delta\nu_{\mathrm{res,cyc}} \approx 32\,\mathrm{kHz}$. The resonators are tuned using dedicated varactor diodes, whose capacities are adjusted by applying appropriate varactor voltages $V_{\mathrm{cyc,vac}}, V_{\mathrm{ax,vac}}$. Due to potential ground loops and potential voltage leakage, the applied varactor voltage could slightly affect the elec-

trostatic potential depending on the ion species and in this way cause significant undesired shifts in the cyclotron frequency ratio. While a potential effect of the axial varator voltage has been studied in detail and consequently excluded during the course of the sideband based q/m-campaign, potential ratio shifts imposed by the cyclotron varactor voltage $V_{\mathrm{vac,cyc}}$ remain to be investigated. To this end, measurements with both the peak and the sideband method were performed.

As the cyclotron detector itself is not used for frequency measurements in the sideband scheme, we operate alternatingly at cyclotron varactor voltages of $V_{\mathrm{cycvac}} = 0\,\mathrm{V}, 10\,\mathrm{V}$, which is the entire specified voltage range in order to maximize the impact of any possible ion displacement related for instance to ground loops and voltage leakage. We obtain frequency shifts $\Delta\nu_+(0\,\mathrm{V},10\,\mathrm{V}) = 0.04(3.17)\,\mathrm{mHz}$ and $\Delta\nu_+(10\,\mathrm{V},0\,\mathrm{V}) = 4.14(3.31)\,\mathrm{mHz}$ (see Fig. 7.18 (a)). In order to tune the resonator between the antiproton and the Hminus cyclotron frequency, $\Delta\nu_{\mathrm{res,cyc}} \approx 32\,\mathrm{kHz}$, the varactor voltage is varied by 144 mV when the peak method is applied. We constrained the shift across the full 10 V voltage range of the cyclotron varactor diode to $\Delta\nu_+ = 4.1(3.3)\,\mathrm{mHz}$ (see Fig. 7.18, the higher of both consistent values is taken here in order to set an upper limit). Considering the 0.144 V range, this would result in a measured frequency offset of

$$\frac{\Delta\nu_+}{\nu_+} = \frac{4.1(3.3)\,\mathrm{mHz}}{29.6\,\mathrm{MHz}} \times \frac{0.144\,\mathrm{V}}{10\,\mathrm{V}} \approx 2.0(1.6) \times 10^{-12} \tag{7.56}$$

between both ions. Consequently, potential cyclotron frequency related to the different cyclotron varactor voltages can be disregarded at the desired measurement resolution.

When performing this measurement by employing the peak method, the cyclotron detector used for the cyclotron frequency measurement is detuned from the particle's oscillation frequency, thereby effectively increasing the cooling time constant of the detector. Consequently, not only a potential ion displacement, but also the varied ion-detector interaction is investigated in this scheme. To this end, we recorded cyclotron peak measurements with two different probe detector frequencies $\nu_{\mathrm{res}} = 29.57\,\mathrm{MHz}, 29.69\,\mathrm{MHz}$ and a reference frequency $\nu_{\mathrm{res}} = 29.63\,\mathrm{MHz}$, while the particle cyclotron frequency is given by $\nu_{+,\bar{\mathrm{p}}} = 29.64\,\mathrm{MHz}$. We obtain $\nu_+(0.428\,\mathrm{V},0.733\,\mathrm{V}) = 0.33(77)(68)\,\mathrm{mHz}$ and $\nu_+(1.038\,\mathrm{V},0.733\,\mathrm{V}) = 1.78(81)(72)\,\mathrm{mHz}$, with the first bracket denoting the statistical uncertainty and the second bracket denoting the systematic uncertainty due to $B_2 = -89.4(0.6)\,\mathrm{mT/m^2}$. The results are displayed in Fig. 7.18 (b) and indicate no scaling of the measured cyclotron frequency as a function of the cyclotron varactor volt-

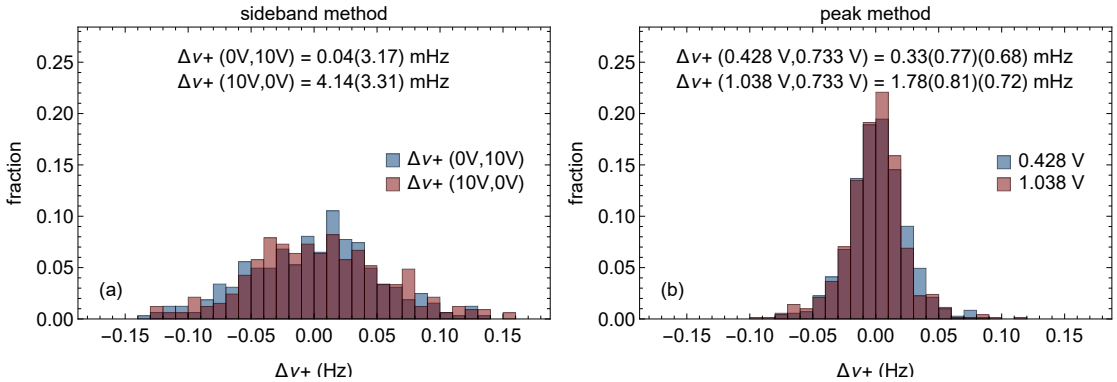

Figure 7.18.: Cyclotron frequencies as a function of the cyclotron varactor voltage. Left: Measurement by means of the sideband method. The cyclotron frequency is measured alternating at the cyclotron varactor voltages $V_{\mathrm{cycvac}} = 0\,\mathrm{V}, 10\,\mathrm{V}$. For $\Delta\nu_+(0\,\mathrm{V},10\,\mathrm{V})$, $\nu_+(0\,\mathrm{V}) - \mathrm{Mean}(\nu_+(10\,\mathrm{V}))$ is computed, and vice versa for $\Delta\nu_+(10\,\mathrm{V},0\,\mathrm{V})$. The results are subsequently Grubbs filtered [154] in order to exclude a few outliers. Both results are consistent with each other within their uncertainties and indicate no scaling as a function of the cyclotron frequency with the cyclotron varactor voltage. Right: Measurement of cyclotron frequency shift as a function of particle detector detuning. The voltages $V_{\mathrm{cycvac}} = 0.438\,\mathrm{V}, 0.733\,\mathrm{V}, 1.038\,\mathrm{V}$ corresponded to resonator frequencies $\nu_{\mathrm{res}} = 29.57\,\mathrm{MHz}, 29.63\,\mathrm{MHz}, 29.69\,\mathrm{MHz}$, while the individual cyclotron frequencies are $\nu_{+,\bar{\mathrm{p}}} = 29.64\,\mathrm{MHz}$ and $\nu_{+,\mathrm{H}^-} = 29.61\,\mathrm{MHz}$. The measurements presented here were conducted using a single antiproton. Outliers were removed from the data presented here by using a conservative threshold. The first bracket indicates the statistical uncertainty, while the second bracket denotes the systematic uncertainty due to $B_2 = -89.4(0.6)\,\mathrm{mT/m^2}$. The particle was excited to $E_+ = 5.30(4)\,\mathrm{eV}$ (0.428 V) and $E_+ = 5.89(4)\,\mathrm{eV}$ (1.038 V), for the reference points, the excitation was alternated between $5.36(4)\,\mathrm{eV}$ and $12.67(5)\,\mathrm{eV}$ in order to provide input for the B_2 measurement in Sec. 7.2.3. At our measurement resolution, we do not see an indication for a shift of the cyclotron frequency with the detector frequency or the resonator varactor voltage.

age/the particle detector detuning, which is consistent with the results obtained from sideband measurements.

7.3. Summary on cyclotron frequency measurements and trap coefficients

The effect of the coefficients determined in the sections above onto the measured cyclotron frequency are summarized in Tab. 7.2.

coefficient	effect size	used quantity	discussion
$\Delta\nu_+(B_2, \mathrm{SR})$	-939 p.p.t./eV	$B_2 = -89.4(0.6)\,\mathrm{mT/m^2}$	Sec. 7.2.3
$\mathrm{d}\nu_+/\mathrm{d}B_2 \times u(B_2)$	8.5 p.p.t./eV	$B_2 = -89.4(0.6)\,\mathrm{mT/m^2}$	Sec. 7.2.3
$\Delta\nu_+(T_z)$	-344 p.p.t.	$T_z = 14.68(20)\,\mathrm{K}$	Sec. 7.1.1
$\mathrm{d}\Delta\nu_+/\mathrm{d}T_z \times u(T_z)$	4.7 p.p.t.	$T_z = 14.68(20)\,\mathrm{K}$	Sec. 7.1.1
$\Delta\nu_+(B_1)$	3.9 p.p.t./eV	$B_1 = -1.57(2)\,\mathrm{mT/m}$	Sec. 7.1.4
$\mathrm{d}\Delta\nu_+/\mathrm{d}B_1 \times u(B_1)$	98.2 p.p.q./eV	$B_1 = -1.57(2)\,\mathrm{mT/m}$	Sec. 7.1.4

Table 7.2.: Summary on the effect of trap coefficients onto the measured cyclotron frequency for the trap configuration from the peak methods run. The upper row denotes the well-characterized frequency shift, and the lower row the corresponding uncertainty.

8 | Antiproton to proton charge-to-mass ratio measurement in 2019

After the successful high-precision measurement of the antiproton magnetic moment performed during the 2015/2016 experimental campaign [28], the BASE collaboration targeted a high-precision measurement of the antiproton charge-to-mass ratio with a considerable improved precision compared to the measurement performed in 2015, which yielded a fractional resolution of 69 p.p.t [39]. To this end, the experimental apparatus was carefully revised and improved, which is discussed in the PhD theses of Takashi Higuchi [53] and James Brydges-Harrington [52]. In the 2017/2018 antiproton run, a high-precision q/m measurement was conducted, which is subject of the PhD thesis of James Brydges-Harrington [52]. Afterwards, the experimental apparatus was again revised by implementing a vibration-decoupled cryogenic support structure and by reducing the heat load on the 4 K stage significantly (see Sec. 3.2). As a result, the measured cyclotron-frequency scatter was improved and did not exhibit a scaling with the cryoliquid levels anymore. Instead, the experiment is now entirely limited by the principal limitations of the sideband method throughout the entire operation cycle (compare Fig. 3.2). With this apparatus, we conducted another measurement campaign on the antiproton-to-proton charge-to-mass ratio in April and May 2019, which is described in this chapter. The content presented in this chapter is the result of collaborative efforts, to which the author for instance contributed as the responsible experimental operator during this measurement campaign, and by contributing the apparatus improvements outlined in Sec. 3.2.

8.1. Sideband method consistency checks - avoided crossing - power scaling - dip width

For the high precision measurement on the antiproton-to-proton charge-to-mass ratio described in this chapter, the so-called "sideband technique" was used [54], which has been introduced in Sec. 2.5 and is also discussed in Sec. 9.2. This methods relies on coupling the cyclotron motion to the axial motion by irradiating a quadrupolar radiofrequency drive ν_{rf} close to the difference frequency of cyclotron and axial frequency, $\nu_{\mathrm{rf}} = \nu_+ - \nu_z + \delta$, with the drive detuning δ being small.
On the axial detector spectrum, a so-called "double-dip" spectrum with dip frequencies ν_l, ν_r is observed (Fig. 8.3). The double-dip frequencies ν_r, ν_l can be understood as representing classical "dressed states" [54]. They are given by

$$\nu_{z,r} = \nu_z + \frac{1}{2}\left(-\delta + \sqrt{\Omega_0^2 + \delta^2}\right) \tag{8.1}$$

$$\nu_{z,l} = \nu_z + \frac{1}{2}\left(-\delta - \sqrt{\Omega_0^2 + \delta^2}\right), \tag{8.2}$$

with an effective Rabi frequency $\Omega(\delta) = \sqrt{\Omega_0^2 + \delta^2}$. The cyclotron frequency ν_+ is then given by

$$\nu_+ = \nu_{\mathrm{rf}} + \nu_l + \nu_r - \nu_z,$$

as already shown in Eq. 2.50.
The dressed states $\nu_{l,r}$ are investigated by varying the drive detuning δ and also varying the field-strength of the coupling drive. Results of this study are shown in Fig. 8.1. Fig. 8.1 (a) shows "classical avoided crossings", here the red points represent measured frequencies ν_r while the blue points are the measured frequencies ν_r. The solid lines are single parameter fits of Eq. 8.1 and Eq. 8.2 to the data. The green line represents the mean of the two frequencies, the slope of this line is called the crossing-skew $\delta/2$. Fig. 8.1 (b) shows the measured effective Rabi frequency $\nu_r - \nu_l$ (blue scatter points) as a function of detuning $\Omega(\delta) = \sqrt{\Omega_0^2 + \delta^2}$ for different drive strengths E_0, the red lines show fits based on this model. From those fits, we obtain the scaling $\Omega_0(V_{\mathrm{RMS}}) = \alpha \times V_{\mathrm{RMS}}$ with the important experiment parameter $\alpha = 1.511(3)\,\mathrm{kHz/V}$.
As a last aspect to test the applied sideband measurement method, we discuss the dip widths of ν_r and ν_l as a function of detuning and for different drive powers. The explicit

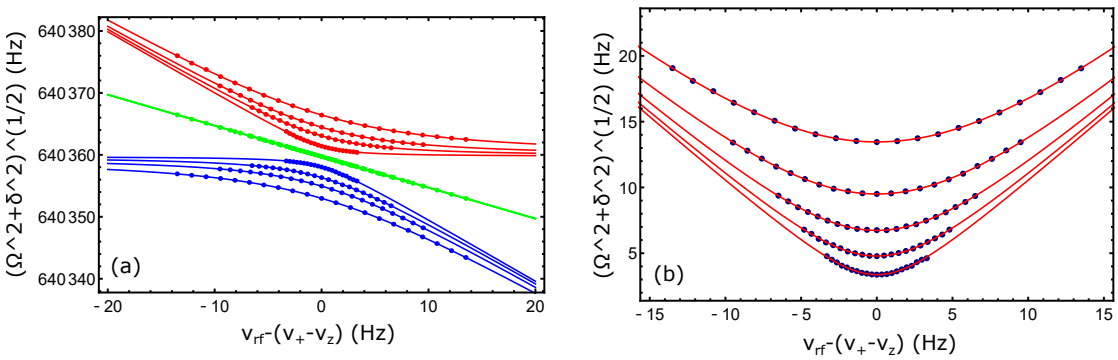

Figure 8.1.: Avoided Crossing. Left: The lower double dip frequency ν_l is plotted in blue, the upper double dip frequency ν_r is shown is plotted in red. In green, the mean $(\nu_l + \nu_r)/2 = \delta/2$ is shown. The solid lines represent fits to the data. Right: Measured Rabi frequency as a function of detuning δ. The blue dots indicate data points including error bars, the solid line is a single parameter fit. These data were taken as part of the PhD work of James Brydges-Harrington [52].

solution for the time dependent axial signal is [54]

$$z(t) = \sqrt{\omega_z}\exp\left(-i\omega_z t\right)\left(\left(\cos\left(\frac{1}{2}\sqrt{\Omega_0^2+\delta^2}t\right) - \frac{\delta}{\sqrt{\Omega_0^2+\delta^2}}\sin\left(\frac{1}{2}\sqrt{\Omega_0^2+\delta^2}t\right)\right)\right). \quad (8.3)$$

This can be rewritten as a linear combination of the normal mode oscillations at frequencies

$$\omega_r = \omega_z + \frac{1}{2}\left(-\delta + \sqrt{\Omega_0^2+\delta^2}\right), \quad (8.4)$$

$$\omega_l = \omega_z + \frac{1}{2}\left(-\delta - \sqrt{\Omega_0^2+\delta^2}\right), \quad (8.5)$$

and sub-modes with amplitudes $Z_1(\delta,\Omega_0)$ and $Z_2(\delta,\Omega_0)$ where

$$Z_1(\delta,\Omega_0) = \frac{Z_0}{2}\left(1 + \frac{\delta}{\sqrt{(\Omega_0^2+\delta^2])}}\right), \quad (8.6)$$

$$Z_2(\delta,\Omega_0) = \frac{Z_0}{2}\left(1 - \frac{\delta}{\sqrt{(\Omega_0^2+\delta^2])}}\right), \quad (8.7)$$

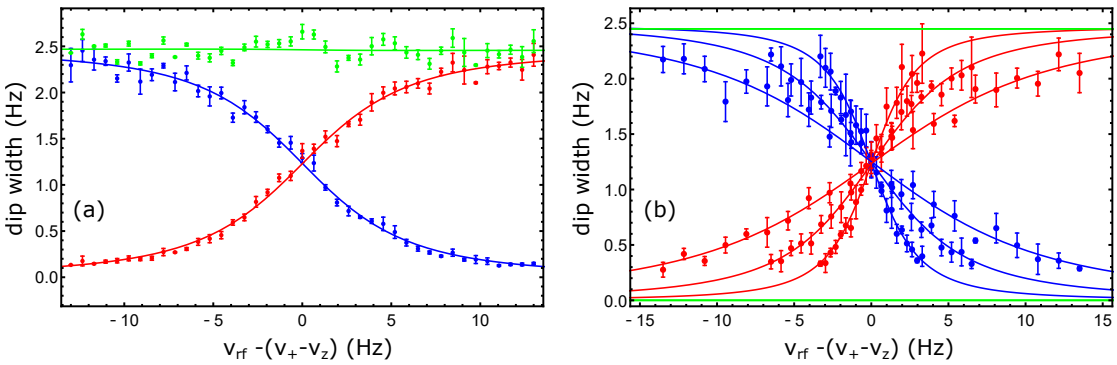

Figure 8.2.: Dip width in avoided crossing. Widths of the left (blue) and the right (red) frequency dips as a function of detuning. Left: Result of a broad band scan at a power of −34 dBm. Right: Results of scans at different drive power. These data were taken as part of the PhD work of James Brydges-Harrington [52].

These expressions actually describe the width of ν_l and ν_r, as illustrated experimentally in Fig. 8.2.

8.2. Cyclotron frequency measurements based on the sideband method

In the "fast shuttling" measurement scheme developed by BASE [39], the cyclotron frequencies of the antiproton and the hydride ion are measured alternatingly by means of sideband methods at a sampling rate of about $1/(4\,\mathrm{min})$ for a full measurement cycle. As the cyclotron frequency ν_c is given by $\nu_c = q/m \times B_0/(2\pi)$ with the magnetic field strength B_0, we consider the cyclotron frequency ratio R between both ions,

$$R_{\mathrm{exp}} \quad = \quad \frac{\nu_{\mathrm{c},\bar{p}}}{\nu_{\mathrm{c,H^-}}} = \frac{(q/m)_{\bar{p}}}{(q/m)_{\mathrm{H^-}}}, \tag{8.8}$$

and consequently obtain the ratio of both charge-to-mass ratios. The sideband method for measuring the cyclotron frequency of a single trapped ion [54] has been introduced in Sec. 2.5 and in the section above (Sec. 8.1). In our measurement procedure, firstly, the axial frequency is measured by means of image current detection and obtained from fitting the well-known lineshape to the Fourier transformed detector voltage spectrum (see Fig. 8.3, red data), as described in Sec. 2.3.1. Afterwards, the cyclotron motion ν_+

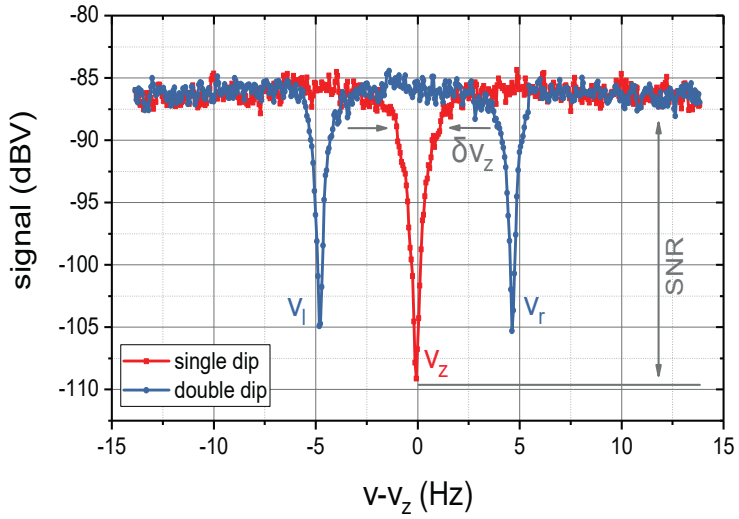

Figure 8.3.: Dip signals recorded with the axial detector in the precision trap. Red: Single particle dip. Blue: Double dip spectrum recorded while a coupling radio-frequency drive is irradiated to the particle.

is coupled to the axial motion ν_z by means of a quadrupole radio frequency pulse with frequency $\nu_{\mathrm{rf}} = \nu_+ - \nu_z$. We then observe a "double dip" structure on the detector spectrum resulting from mode coupling (blue data in Fig. 8.3). The cyclotron frequency ν_+ is related to the double dip frequencies ν_l, ν_r, the drive frequency ν_{rf}, and the axial frequency ν_z by $\nu_+ = \nu_{\mathrm{rf}} + \nu_l + \nu_r - \nu_z$ as specified in Eq. 2.50. The magnetron frequency is typically estimated from the relation $\nu_- \approx \nu_z^2/(2\nu_+)$ [70] (Eq. 2.9), which is sufficiently accurate for our purposes. The free cyclotron frequency ν_c is then computed from using the invariance theorem [69],

$$\nu_c \quad = \quad \sqrt{\nu_+^2 + \nu_z^2 + \nu_-^2}. \tag{8.9}$$

All frequency measurements are conducted with the axial and cyclotron mode being in thermal equilibrium with the detection system. The associated mode energies are low and the energy-dependent shifts consequently small, which is of advantage for measurement systematics. Other methods for measuring the cyclotron frequency of single trapped ions, such as the peak detection [152] and phase methods [55], rely on purposely exciting the cyclotron motion (see Sec. 7.2 and Chap. 9). The sideband method allows for continuous

uninterrupted frequency sampling, and is rather insensitive to background magnetic field drifts and fluctuations, which are common in an accelerator hall [85]. One principal resolution limitation of the sideband method is given by the achievable axial frequency resolution, which depends on the averaging time t_{avg}, the SNR of the axial detector, and the particle dip width $\delta\nu_z$. At the magnetic field homogeneity in the center of the BASE precision trap, the principal magnetic field scatter is usually much lower than the measurement scatter σ imposed by the axial frequency determination.

8.3. Experiment upgrades since the 2014 charge-to-mass ratio campaign

Since the last dedicated q/m measurement conducted in 2014 [39], several substantial upgrades to the experimental apparatus have been implemented by the collaboration, which are summarized in this section:

- The installation of a new high precision superconducting magnet. The state-of-the-art device, manufactured by Oxford Instruments according BASE-custom specifications, incorporates 12 shim coils in order to ensure an ultra-homogeneous magnetic field in the trap center. The magnet was installed by Stefan Ulmer and Christian Smorra, and was already used for the high precision measurement of the antiproton magnetic moment in 2015/2016 [28].
- In order to suppress external magnetic field fluctuations, a novel multi-layer self-shielding coil system has been implemented. The design was proposed by Stefan Ulmer, firstly realized within the PhD thesis of Takashi Higuchi [53], and later upgraded and carefully characterized by Jack Devlin and Elise Wursten [85]. The concept of a magnetically self shielding coil was developed by Gabrielse [157]. It consists of a closed coil of superconducting wire that suppresses ambient magnetic field changes. In the BASE system, several coils of different length are used, which is novel [85]. With this system, a shielding factor of $S = 225(15)$ is achieved, which is a significant improvement compared to the shielding factor $S \approx 10$ used during the 2014 campaign [39].
- Passive shieldings of external temperature changes were implemented, including thermal shielding of the sensitive cryostat tops, covering the previously open experiment zone by a robust plastic tent, and thermally insulating the experiment

boil-off lines connected to CERN's helium recovery by means of several layers of standard insulation foam. These actions improved the temperature drifts experienced by the experiment by up to a factor of 11. This work is described in the PhD thesis of James Brydges-Harrington [52].

- Implementing varactor diodes for frequency tuning of the axial detection systems. This addresses the main systematic contribution of the 2014 measurement [39], which arose due to a slight potential mismatch relating to the uncertainty in asymmetry compensation, the different ion masses, and the residual B_1 term. With axial detection systems tunable to the axial frequency difference $\nu_{z,\bar{p}} - \nu_{z,\mathrm{H}^-} \approx 350\,\mathrm{Hz}$, both ions can be measured in identical potentials. The tunable detection systems were developed and characterized within the master's thesis of Toya Tanaka [158], and are inspired by [159].
- The implementation of the new high-precision custom-made Penning trap voltage supply UM1-14-LN-25 from Stahl electronics, which has a five-fold reduced output relaxation time constant (4 s) compared to the previous generation.
- The implementation of a single sideband downconverter (SSB) developed by Stefan Ulmer and Mustafa Besirli [160]. This suppresses parasitic noise occurring during down conversion and improves the SNR by 3 dB, thereby enabling a higher axial frequency resolution at constant averaging time.
- The replacement of the internal reference clock of the FFT analyzer with an external 10 MHz rubidium clock. The corresponding electronic modifications were developed by Georg Schneider [75] from the BASE Mainz team, and were implemented at CERN by Mustafa Besirli.
- An upgraded sensor logging system was installed. It consists of multiple temperature sensors distributed in the experiment zone and inside the experiment's room temperature and cryogenic stages. It also features pressure sensors that monitor the ambient pressure, the pressure inside the cryogenic LHe vessels and the Helium recovery system. In addition, Hall sensors, GMR sensors and flux-gate sensors are placed in the experiment zone for monitoring the ambient magnetic field. The logger system was developed within the PhD work of Takashi Higuchi [53], and later considerably upgraded by Jack Devlin, Jan Schaper and Axel Ponten.
- The implementation of a Labview experimental control code, herein referred to as "sequencer". The code was developed by Christian Smorra and Stefan Ulmer for

the magnetic moment measurement [28], and afterwards adapted for charge-to-mass ratio measurements. The sequencer enables flexible operation of individual experiment routines and has outstanding long-term performance. The sequencer for the charge-to-mass ratio measurement has been developed within the PhD work of James Brydges-Harrington [52], to which Elise Wursten, Jack Devlin and the author contributed in addition.

- The implementation of a revised cryomechanical setup that entirely suppresses cyclotron frequency scatter induced by cryostat vibrations related to boiling cryoliquids. This apparatus revision was developed within the framework of this thesis and is described in Sec. 3.2.1.
- The implementation of full passive thermal shielding of the apparatus, which is referred to as "experiment frame" in this thesis, and discussed in Sec. 3.2.2.

As a result of all the revisions listed above, a significant improvement in experiment stability was achieved, which is depicted in Fig. 8.4. The red data show the antiproton-to-

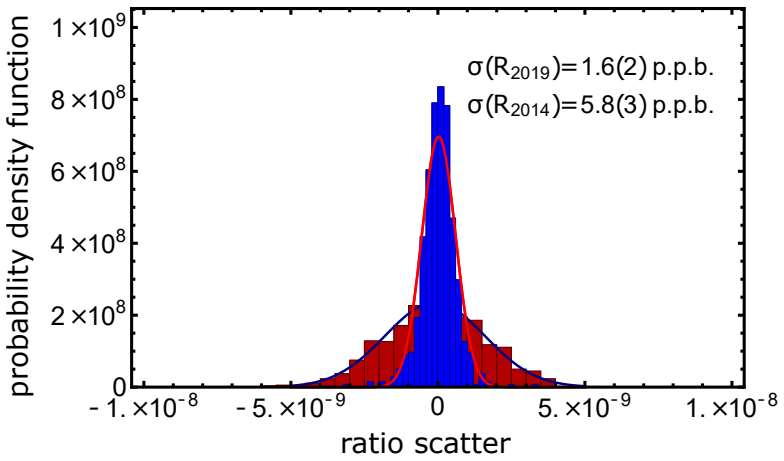

Figure 8.4.: Comparison of experiment stability. The red histogram represents the stability of the frequency ratio achieved during the 2014 antiproton-to-proton charge-to-mass ratio measurement campaign, the blue histogram shows the stability reached in 2019 with the technical improvements described in this section. The ratio stability now reflects the principal limit of the sideband measurement method. Compared to 2014, the stability is improved by about a factor of 3.6.

hydride cyclotron frequency scatter $\sigma(\nu_{c,\bar{p}}/\nu_{c,\mathrm{H}^-})$ obtained during the 2014 measurement campaign, while the blue data show the scatter obtained during the 2019 campaign

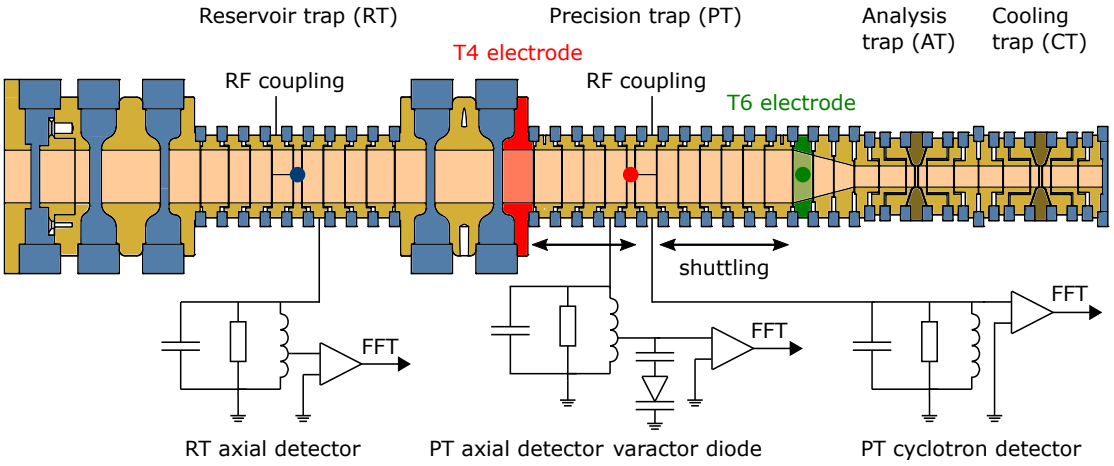

Figure 8.5.: Schematic drawing of the trap setup used during the 2019 charge-to-mass ratio campaign. The reservoir trap (RT) is located left (most upstream) and contains a mixed reservoir of antiprotons and hydride ions (indicated by the blue filled circle). Two particles, an antiproton and a hydride ion, are used for the charge-to-mass ratio (denoted by the red and the green filled circle). The trap electrodes are made of oxygen-free high thermal conductivity copper (OFHC) and are gold plated. The are separated by sapphire spacers (blue). While the cyclotron frequency of one particle is measured in the precision trap (PT), the other particle is located in the respective parking electrode (T_4 and T_6 electrode). The ions are simultaneously shuttled in and out of the trap by means of adiabatic shuttling [39]. The RT and the PT are equipped with superconducting image current detection circuits [76] for measuring the axial oscillation frequency. The precision trap is also equipped with a cyclotron detector employed for peak-based cyclotron frequency measurements (Sec. 7.2). The resonance frequency of the axial detection system can be shifted by means of a varactor diode, which enables to measure the cyclotron frequency of both ions in identical trap potentials. This addresses the main systematic uncertainty in the last high precision q/m-measurement [39]. The analysis trap and the cooling trap are not used during this measurement campaign.

presented in this chapter. The 2019 scatter is more than a factor of 3 smaller compared to the 2014 data. This significant improvement is mainly attributed to the revised cryomechnical support, the experiment frame, and the multi-layer self shielding coil system [85].

8.4. Experimental implementation and measurement scheme

The cyclotron frequency is measured in the precision trap, which is depicted in Fig. 8.5. The BASE trap system is located inside the horizontal bore of a superconducting magnet

operated at a magnetic field strength $B_0 = 1.944\,846\,\mathrm{T}$. The magnet axis is oriented at a 60 degree angle with respect to the earth rotation axis. The cylindrical trap electrodes are carefully designed in a compensated and orthogonal way [71], all electrodes are made out of OFHC copper and are gold plated. The inner trap diameter is 9 mm. Two park electrodes, T_4 and T_6, are located upstream and downstream from the trap, and are used for storage of one ion when the other is located in the precision trap. Frequency measurements are conducted alternatingly, the particles in the precision trap are exchanged by means of fast adiabatic transport ramps. The trap stack is located inside a dedicated in-situ vacuum chamber, which is called trap can. The trap can is indium-sealed, of cylindrical shape and contains a volume of about 1 liter. Before cooling and pumping of the apparatus, it is pumped to pressures of order 10^{-7} mbar at room temperature. Prior to experiment assembly, the pumping port is pinched off and the trap can is mounted inside the experimental apparatus. Once the experiment is cooled down to 4 K, pressures below 10^{-18} mbar are achieved, which allows to store antiprotons for years without particle loss (see [49, 48] and Chap. 6).
Highly-sensitive image current detection systems [76] are used for frequency measurements. The axial detector frequency can be tuned via varactor diodes [158], which resolves the dominant systematic uncertainty from [39]: Here, the axial potential had to be adjusted by 5 mV depending on the ion species in order to match axial and detector frequency. A systematic uncertainty arose then from the an uncertainty in the trap asymmetry compensation and the residual magnetic field gradient B_1. With the tunable detection circuits, both ions can be measured in identical electrostatic potentials. The detector properties are summarized in Tab. 8.1.

Monitoring the detector quality factor over time, we obtain the differential Allan deviation:

$$\sigma(Q) = \frac{18\,800(1100)}{\sqrt{t_{\mathrm{avg}}}} + 5.5(2). \tag{8.10}$$

We therefore consider the quality factor to be stable. The resonance frequency is dominated by $1/\sqrt{t_{\mathrm{avg}}}$-scaling, but also shows a slow drift

$$\sigma(\nu_{\mathrm{res}}) = \frac{14.9(1)\,\mathrm{Hz}}{\sqrt{t_{\mathrm{avg}}}} + 16(6)\,\mu\mathrm{Hz} t_{\mathrm{avg}}^{0.91(4)}. \tag{8.11}$$

Parameter	Antiproton	H^--ion
resonance frequency (Hz)	640 427(1)	640 077(1)
quality-factor	12 652(11)	12 886(11)
signal-to-noise ratio (dB)	25.01 (4)	25.20 (4)
single dip-width (Hz)	2.467 (2)	2.515(2)
double dip-width (Hz)	1.234(4)	1.251(4)
Pickup-Length D_{eff} (mm)	10.03	10.03

Table 8.1.: Axial detector parameters for both working points during the 2019 sideband campaign.

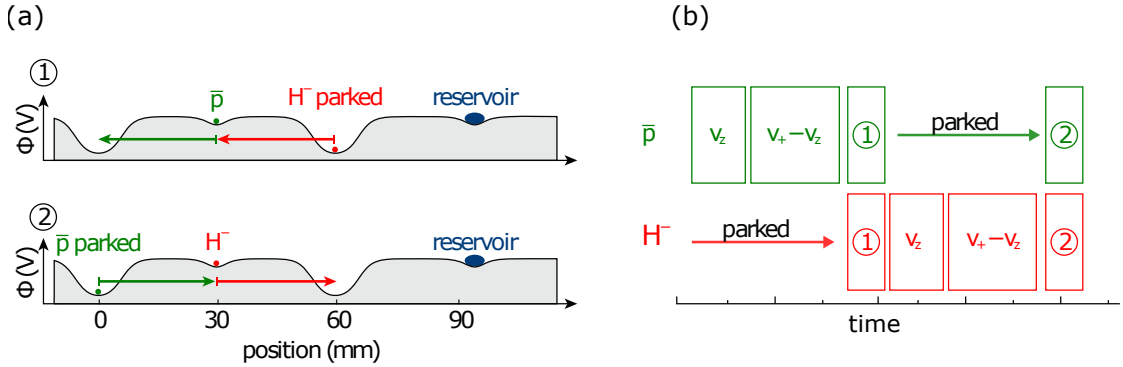

Figure 8.6.: Left: Illustration of the measurement scheme. The antiproton and the hydride ion are moved to the measurement trap by applying potential ramps. Right: Timing scheme of the experiment sequence, the determination of one antiproton-to-hydride cyclotron frequency ratio takes about 4 minutes. This figure is adapted from [75].

The noise on the axial detection systems varies as a function of time, and is discussed separately in Sec. 8.11.1, where the related systematic uncertainties are examined. The measurement procedure is schematically depicted in Fig. 8.6, with the electric potential configuration in (a) and the temporal sequence (b). Prior to data taking, possible contaminations (electrons and negative ions) are removed by applying rf and kick-out pulses in the precision trap and the magnetron mode is cooled. The same procedure is repeated for the other ion. The measurement routine is initialized by shuttling the particles back and forth. When the antiproton is located in the precision trap, the hydride ion is located inside the T_6 electrode, when the hydride ion is located inside the precision trap, the antiproton is stored in T_4. The measurement time applied in the

2019 campaign is $t_{\mathrm{meas}} = 136.6\,\mathrm{s}$, which are divided into

- 56 s of an axial frequency measurement,
- 64 s of double-dip measurement,
- and 16.6 s for particle shuttling (4 s) and waiting times for voltage relaxation (12.6 s).

The axial detector is tuned to match the particle's oscillation frequency by means of the varactor diode, which leaves the trapping potential unaffected. One experiment cycle consisting of a cyclotron frequency measurement for each particle takes in total 273 s, which is about 40 times faster compared to the measurement sequence applied in [152]. After 32 frequency measurements on each particle (every 2.5 hours), a contaminant cleaning sequence is performed for both ions. These sequences are important, as the degrader becomes activated during antiproton injection from the AD, and thus emits β-decay electrons. Even though the precision trap is about 5 cm away from the degrader, electron contamination is experienced from time to time, during the 2019 campaign about once per week. The cleaning routine consists of electron kick-out pulses, rf-cleaning ramps, and magnetron cooling. The cleaning routine takes about 9 min of time, we thus acquire about 13 frequency ratios per hour and 302 ratio during 24 hours.

8.5. Data distribution and experiment stability

During the measurement campaign presented here, CERN and the Antiproton Decelerator were not operated due to CERN's long shutdown 2 (LS2, 2019-2020). The reservoir trap was loaded on October 17th, 2018, with one of the last shots delivered from the AD. After LS2, the ELENA upgrade [161] will provide antiprotons to the experiments, after having slowed the AD antiprotons further down. The measurement campaign started on April 17th, 2019, and ended on May 25th, 2019. In total, 8837 frequency ratios were accumulated. Even though the Antiproton Decelerator itself was not being operated during that time window, multiply other activities were carried out in the AD hall during that time, which partially involved ambient magnetic field noise. For instance, the ELENA upgrade was being commissioned. In addition, construction works were carried out that involved frequent usage of the overhead crane, which generates a strong magnetic signal of up to 2.2 μT in the BASE zone. Also the neighboring collaborations were operating their experiments without antiprotons. In addition to these actions that

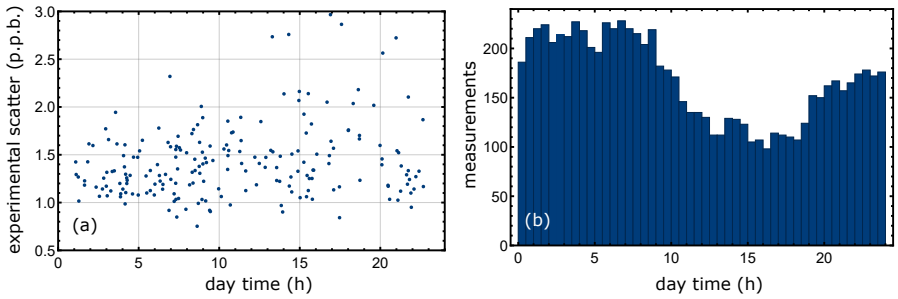

Figure 8.7.: Left: Experiment scatter as a function of daytime. In the time window from 10:00 to 22:00, the experiment scatter increases. This is related to increased temperature and magnetic field fluctuation imposed by other users and installation works. Right: Number of accumulated measurements as a function of daytime. Apparatus maintenance and re-thermalization is performed synchronously to the main activity windows of others users and the installation service.

usually happen during daytime, temperature fluctuations in the hall are larger during daytime, for instance due to opening and closing of the hall doors. Consequently, the cyclotron frequency stability is much better during night and morning times (10 pm and 10 am) compared to day and evening times (10 am to 10 pm), as shown in Fig. 8.7 (a). We therefore conducted the experiment maintenance cycles usually around midday. The maintenance cycle consists of about 2 h of filling of cryogenic liquids, and 4 h of experiment relaxation, and is conducted twice a week. Overall, the data taking rate is about 45 % higher during night and morning times compared to day and evening times.

8.6. Axial frequency fluctuations

In the sideband method, the cyclotron frequency is determined by reading out the axial frequency spectrum during mode coupling and without mode coupling (see Eq. 2.50). Consequently, one fundamental limitation of the method is given by the axial frequency stability. A set of 4.5 h long axial frequency sequences is shown in Fig. 8.8 (a), with the corresponding differential Allan deviations shown on right (Fig. 8.8 (b)).

The red solid line in Fig. 8.8 (b) denotes the median values given by

$$\sigma(\nu_z) = \frac{0.443(18)}{\sqrt{t_{\mathrm{avg}}}} + 3.7(5.2) \times 10^{-6} t_{\mathrm{avg}}\ [\mathrm{Hz}], \tag{8.12}$$

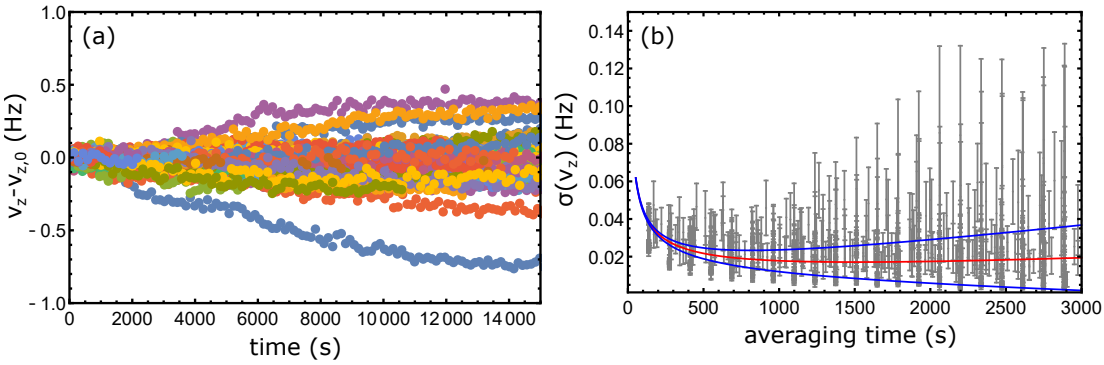

Figure 8.8.: Axial frequency data of the 2019 q/m campaign. Left: About 10 days of axial frequency measurements as a function of time. Right: Differential Allan deviations of the sequences shown in (a). The red solid line is a fit to the median of the differential Allan deviation data, the blue solid lines indicate the uncertainty of the fit.

and the blue line denotes the related uncertainty.

The axial frequency scatter $\Xi_z = \sigma(\nu_{z,\bar{p},k} - \nu_{z,\mathrm{H}^-,k})$ corresponding to Fig. 8.8 (a) is $\Xi_z = 32.81(3)\,\mathrm{mHz}$. Based upon these values, we expect a ratio stability of

$$\sigma(R) \approx \sqrt{\Xi_z^2 + 2\left(\sqrt{\frac{\delta\nu_{z,\mathrm{SB}}}{\delta\nu_z}}\frac{\mathrm{SNR}_z}{\mathrm{SNR}_{z,\mathrm{SB}}}\Xi_z\right)^2} = 1.67(2)\,\mathrm{p.p.b.} \tag{8.13}$$

$\delta\nu_z$ and $\delta\nu_{z,\mathrm{SB}}$ depict the dip widths of the single dip and the double dips respectively, the related SNRs are denoted accordingly. In the equation above, the power-supply common noise is neglected, which contributes noise at a level of about 14 mHz. Our estimation in Eq. 8.13 is consistent with the measured cyclotron frequency scatter in Fig. 8.4, which indicates that the experiment is operated at the principal limitation of the sideband method arising from the axial frequency noise. When direct cyclotron frequency methods are employed for cyclotron frequency measurements, such as the peak method (Sec. 7.2.3) or phase methods (Chap. 9), significantly lower frequency scatter values of order 500 p.p.t. (peak) and 280(20) p.p.t. (phase methods) can be obtained. These stabilities can only be achieved since 2018 due to the improved cryomechanical setup (compare Fig. 3.2 and Sec. 3.2.1), as the frequency scatter induced by the apparatus was above 1 p.p.b. before the 2018 upgrades were implemented.

8.7. Axial frequency drifts

A deviation in axial frequency ν_z translates to shifts of the cyclotron frequency ratio by $\mathrm{d}R/\mathrm{d}\Delta\nu_z = 3.38 \times 10^{-8}/\mathrm{Hz}$. Consequently, axial frequency drifts have to be carefully characterized. The scaling of axial frequency with trap voltage is given by

$$\frac{\mathrm{d}\nu_z}{\mathrm{d}V_r} = 69.24(24)\,\mathrm{Hz/mV}. \tag{8.14}$$

An effective voltage difference of 14 nV between both particles would consequently already induce a frequency ratio shift of about 30 p.p.t.
The axial frequency stability is characterized by investigating the sequence of axial frequency measurements $\nu_{z,2k-1}$ that contain all axial frequencies measured for one ion species, and predict the set of axial frequencies $\nu_{z,2k}$ of the other ion. From linear interpolations, we obtain

$$\langle \nu_{z,2k} - \nu_{z,2k-1,\mathrm{int}} \rangle = -73(327)\,\mu\mathrm{Hz}, \tag{8.15}$$

which is consistent with no offset between prediction and measured data. The corresponding residual ratio shift is 2(11) p.p.t, which is implicitly considered in the lineshape correction.

8.8. Magnetic field

The global magnetic field stability is characterized by comparing the cyclotron frequency over time to the initial cyclotron frequency, as shown in Fig. 8.9. In the upper row, the cyclotron frequency stability prior to the frame installation at the start of the 2019 campaign is shown. At this time, concrete blocks at the upstream side of the experimental zone were removed in order to install the electrostatic transfer lines, which will be used after LS2 when antiprotons are delivered from ELENA. This action caused an unusual high temperature fluctuation inside the experiment zone. In order to improve the long-term frequency stability and passively shield external temperature fluctuations, we constructed the frame further described in Sec. 3.2.2. After the frame installation was completed, a significantly improved experimental long-term stability was yielded, as shown in the lower row of Fig. 8.9. The corresponding linear magnetic field drifts (red

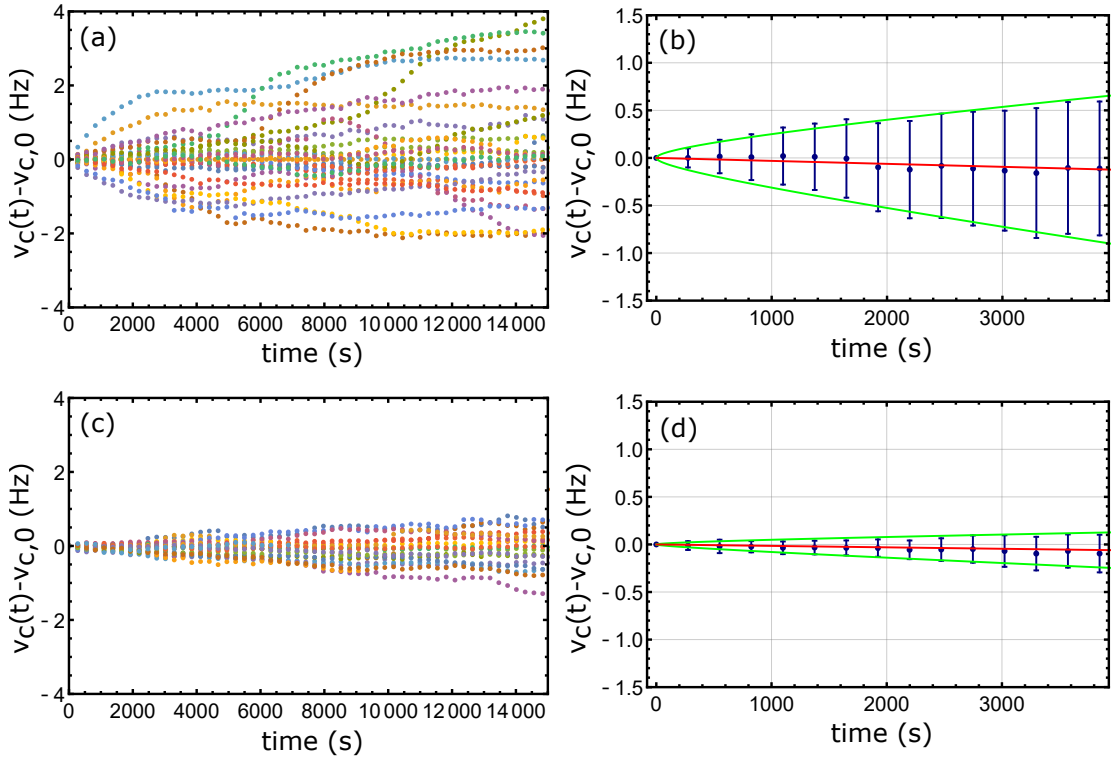

Figure 8.9.: Cyclotron frequency stability before and after frame installation. The upper row shows the stability before the installation of the experiment frame when the upstream part of the experiment zone was open. The lower row shows the stability after the installation of the frame (Sec. 3.2.2). On the left, cyclotron frequencies over time are plotted. The right plots show the corresponding mean values, with the error bars denoting one standard deviation.

lines) are given by

$$\left(\frac{1}{B_0}\frac{\mathrm{d}B_0}{\mathrm{d}t}\right)_1 = -5.63(51)\,\mathrm{p.p.b./h}, \tag{8.16}$$

$$\left(\frac{1}{B_0}\frac{\mathrm{d}B_0}{\mathrm{d}t}\right)_2 = -2.64(26)\,\mathrm{p.p.b./h}. \tag{8.17}$$

The random walks corresponding to the solid green lines in Fig. 8.9 are characterized the effective diffusion constants D_K, for which we obtain

$$D_{B,1} = 21(2)\,\mathrm{p.p.b./h^{1/2}}, \tag{8.18}$$

$$D_{B,2} = 5.2(1.1)\,\mathrm{p.p.b./h^{1/2}}. \tag{8.19}$$

for the upper an the lower case, respectively. Consequently, a drift reduction by a factor of about 2.2 and a random walk suppression of a factor of 4 is achieved due to the frame installation.

We may also investigate the corresponding differential Allan deviations, again for

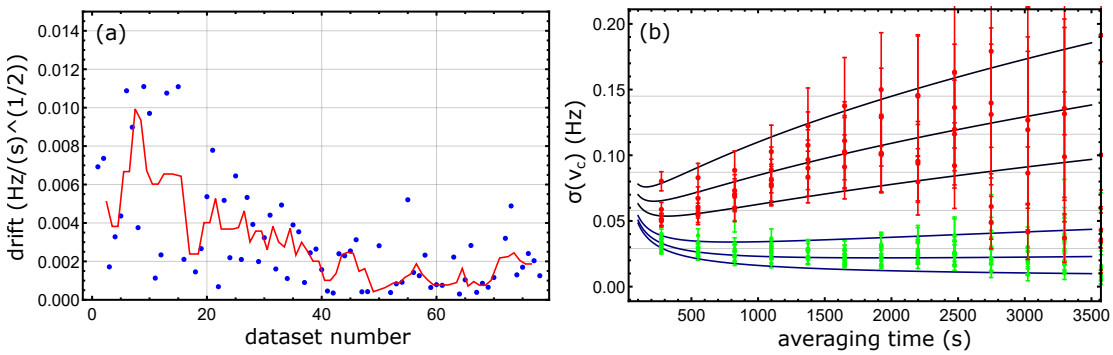

Figure 8.10.: Cyclotron frequency drift prior and after installation of the experimental frame. Left: Observed frequency drift coefficient of different data sets, each data-set contains an equivalent measurement time of 4-5 h. Right: Differential Allan deviations of the magnetic field after installation of the new experiment frame. Green is for night measurements, red for measurements taking during the day.

frequency subsets of a length of 4.5 h each. Each differential Allan deviation is then fitted with a function $\xi_k(t) = A_k/\sqrt{t} + B_k\sqrt{t}$, with B_k describing the frequency diffusion. The results on B_k are plotted in Fig. 8.11 (left). The frame was installed sequentially in the window when the data points 20 to 40 were installed. From point 40 onwards, we reached the highest magnetic field stability achieved at BASE until that date. Across the data set in Fig. 8.10 (left), we observe two levels of stability, which can be attributed to data taking during day/data taking during night. As other users and the AD group are active during day times, the magnetic field tends to be less stable during these times compared to night times. This is visualized on the right side of Fig. 8.11, where the differential Allan deviations after frame installation are plotted. The red data correspond to measurements performed during day time, the green data correspond to night data. For the night data, the diffusion cannot be reasonably quantified any more, but can be constrained by $D_{B_{\mathrm{night}}} < 1.5\,\mathrm{p.p.b.}/\mathrm{h}^{1/2}$. In the best cases, a magnetic field scatter of 300 p.p.t. is reached after one hour of averaging time.

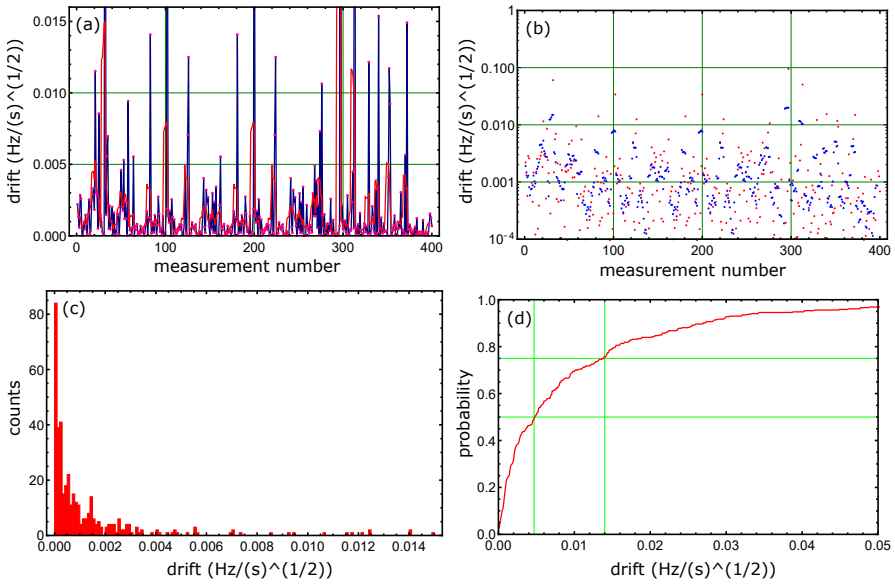

Figure 8.11.: Analysis of magnetic field drift. Upper row left: Drift coefficient as a function of measurement number, where each point represents data acquired for an equivalent of about one hour. Right: Log-plot of the data shown on the left. Lower left: Histogram of the drift coefficients shown in the upper row. Lower right: Cumulative density function of the data shown on the left. About 50 % of the data are in a drift coefficient range below $4.7\,\mathrm{mHz}/\sqrt{s}$ and about 75 % of the data below $12.2\,\mathrm{mHz}/\sqrt{s}$.

8.9. Frequency evaluation by linear interpolation and cleaning filters

Considering the axial frequency stability and the magnetic field behavior outlined in the previous sections, an interpolating approach was chosen for the frequency ratio evaluation. To this end, the axial frequency sets ν_{z,k,H^-} and $\nu_{z,k,\bar{p}}$ are interpolated using linear splines. The axial frequency $\nu_z(t)$ during the acquisition of the sideband spectrum is obtained from the interpolation, and the cyclotron frequency is calculated (Eq. 2.50). The magnetron frequency is then estimated (Eq. 2.9) and the free cyclotron frequency ν_c is calculated using the invariance theorem (Eq. 8.9). From the resulting sets of free cyclotron frequencies $(t_{\mathrm{H}^-,k}, \nu_{c,\mathrm{H}^-,k})$ and $(t_{\bar{p},k}, \nu_{c,\bar{p},k})$, the naive linearly interpolated cy-

clotron frequency ratios are computed,

$$R_{\text{upper}} = \frac{\nu_{c,\bar{p},k}}{1/2\left(\nu_{c,\text{H}^-,k} + \nu_{c,\text{H}^-,k+1}\right)}, \tag{8.20}$$

$$R_{\text{lower}} = \frac{1/2\left(\nu_{c,\bar{p},k} + \nu_{c,\bar{p},k+1}\right)}{\nu_{c,\text{H}^-,k+1}}. \tag{8.21}$$

These ratio data are for instance affected by external magnetic field disturbances (confirmed by the flux gate sensors). We therefore apply a 5σ trim filter and a χ^2 filter, and remove all cyclotron frequencies measured in between the trap cleaning routines. Ratio data affected by occasional trap contaminations (electrons and negative ions) are addressed by a specific contamination filter. To explain the filter, we recall that the axial frequency is given by

$$\nu_z = \frac{1}{2\pi}\sqrt{\frac{2C_2qV_r}{m}}, \tag{8.22}$$

with the characteristic trap parameter C_2. Since the trap voltage V_r is identical for both particles, the axial frequency difference is a function of fundamental ion properties. It is given by

$$\Delta\nu_z = \frac{1}{2\pi}\sqrt{2C_2q\Delta V_r}\sqrt{\left(\frac{1}{m_{\bar{p}}} - \frac{1}{m_{\text{H}^-}}\right)} = \frac{1}{2\pi}\sqrt{2C_2q\Delta V_r}\sqrt{\left(\frac{m_{\text{H}^-} - m_{\bar{p}}}{m_{\bar{p}}m_{\text{H}^-}}\right)}. \tag{8.23}$$

If a change in axial frequency difference is observed, this clearly indicates either a malfunctioning voltage source, strong external voltage drifts, or co-trapped contaminating particles. The voltage source is continuously monitored in order to detect voltage drifts or malfunction of the device, which have not been observed during the 2019 sideband campaign. Consequently, changes in the axial frequency difference that are larger than expected from the independently measured voltage background scatter indicate contaminating particles. In the presence of these co-trapped particles, the contamination repels the measurement ion, and effectively lowers the axial trapping potential thereby. The axial frequency of the measurement ion decreases consequently. The differential Allan deviation of the axial frequency difference $\Delta\nu_{z,\bar{p},\text{H}^-} = \nu_{z,\text{H}^-} - \nu_{z,\bar{p}}$ is shown in Fig. 8.12. During the eight days of measurement for which the data were evaluated, a $1/\sqrt{t}$-scaling

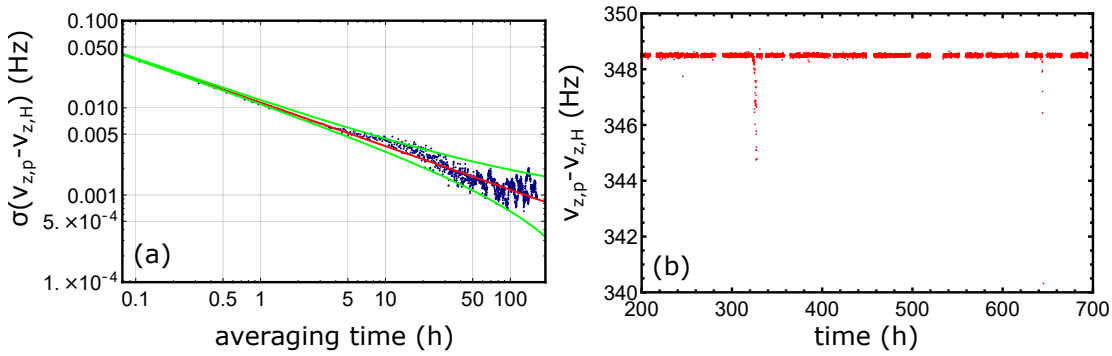

Figure 8.12.: Axial frequency difference stability and detection of contaminant particles. Left: Differential Allan deviation of the axial frequency difference between both particles. For the evaluated range of about eight days of axial frequency measurements, the measured frequency difference shows a stable $1/\sqrt{t}$-scaling. Right: Uncleaned axial frequency difference as a function of time. The frequency difference is constant, as indicated by the figure on the left, however, two events are observed where the axial frequency instability is induced by contaminating electrons in the antiproton trap potential.

is observed in the differential Allan deviation,

$$\xi(t) = \frac{0.01163(4)}{\sqrt{(t)}}, \tag{8.24}$$

with t denoting the averaging time in hours. In Fig. 8.12 (b), the raw axial frequency difference $\Delta\nu_{z,\bar{p},\mathrm{H}^-}$ as a function of time is shown. Generally, $\Delta\nu_{z,\bar{p},\mathrm{H}^-}$ is stable over time as seen from the differential Allan deviation. However, two contaminating events are detected in Fig. 8.12 (b), were the axial frequency is affected due to electron contamination. After careful trap cleaning by means of electron kick-out and by means of selectively exciting oscillation modes of negative ions, the initial axial frequency difference is preserved again. The contamination events are detected from a moving median filter, and consequently the data since last cleaning cycle before are removed from the evaluation.

From the 8837 measured frequency ratios, 8106 ratios are left after application of the filters listed above. The initial trim filter rejects 70 measured ratios, 76 ratios are rejected due to contamination, and 535 ratios are removed as they were accumulated in between of two cleaning cycles. The remaining 8106 measured ratios are shown in Fig. 8.13, upper left. On the upper right, the cyclotron frequency scatter is shown as a function of

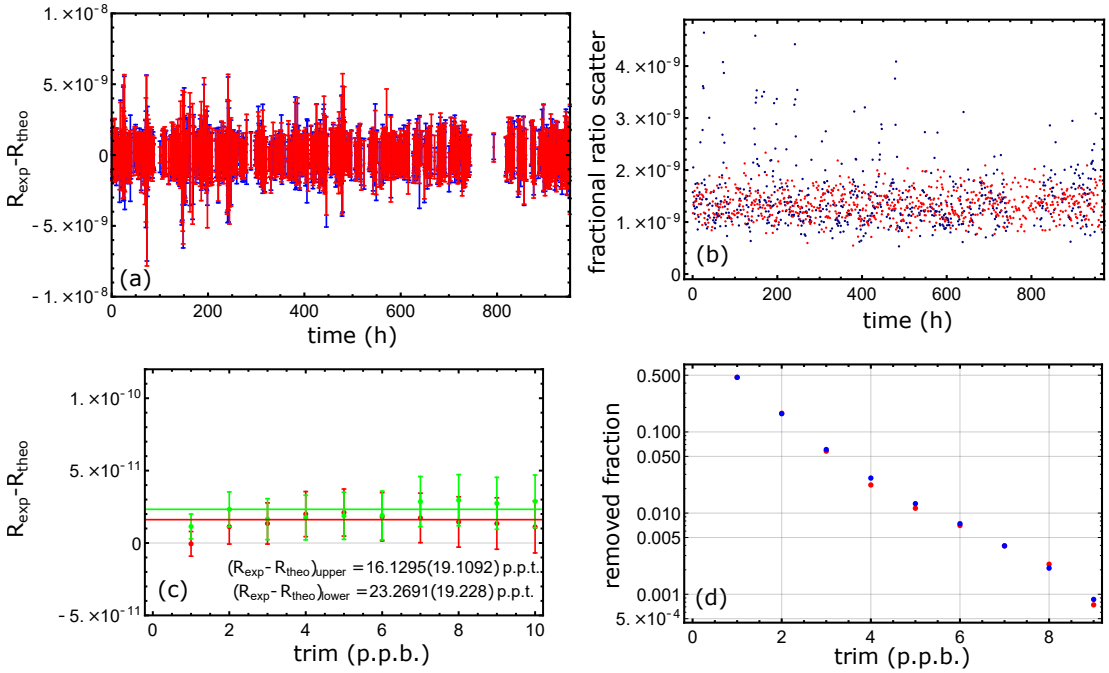

Figure 8.13.: Cyclotron frequency ratio as a function of cleaning threshold. Upper row left: Overview about the measured ratios during the entire campaign. Right: Measured ratio scatter (blue) and Monte-Carlo simulated (red). Ratio as a function of cleaning threshold for the data which were cleaned with an axial threshold filter. Lower row left: Cyclotron frequency as a function of the trim applied to the data. Right: Fraction of removed data as a function of the trim cut.

time. To this end, for each data point a 1 h sub-sequence of measured frequency ratios is considered and Kolmogorov-Smirnow and Pearson-χ^2 tests are applied in order to test whether the sub-sets are distributed according to normal distributions. From these tests, we obtain the local frequency ratio scatter values σ and p-values to check the consistency with statistical normality. The uncorrected median baseline scatter of these data is at 1.31 p.p.b. In red, the results of a Monte-Carlo simulation based on a distribution with comparable median base-line scatter is shown. This comparison clearly indicates the temporal stability variation of the experiment. Later in this section, it will the discussed how to handle this temporal stability scaling in the final data analysis. As an example, the lower two plots show the scaling of the naively determined cyclotron frequency ratio as a function of a trim cut. The plot on the left shows the upper (red) and the lower (green) ratio as a function of the trim cut. The behavior of all filters which are involved

in the data cutting procedure are studied in this way, and the final frequency ratio is investigated as a function of filtering parameters.

8.9.1. Weighted frequency ratio evaluation

The temporal stability variation of the measured data results in the measured data being distributed according to a convolution of local sub-distributions. Based on several statistical tests, the null-hypothesis that the data are distributed according to a single normal distribution is rejected with p-values < 0.001. This is mainly caused by outliers and temporal stability convolutions which contribute a standardized distribution-Kurtosis Kurt ≈ 6, while the skewness of the data is consistent with 0 within the uncertainties of standardized statistical tests.

In Fig. 8.14, the number of points accepted as a function of the chosen cut threshold

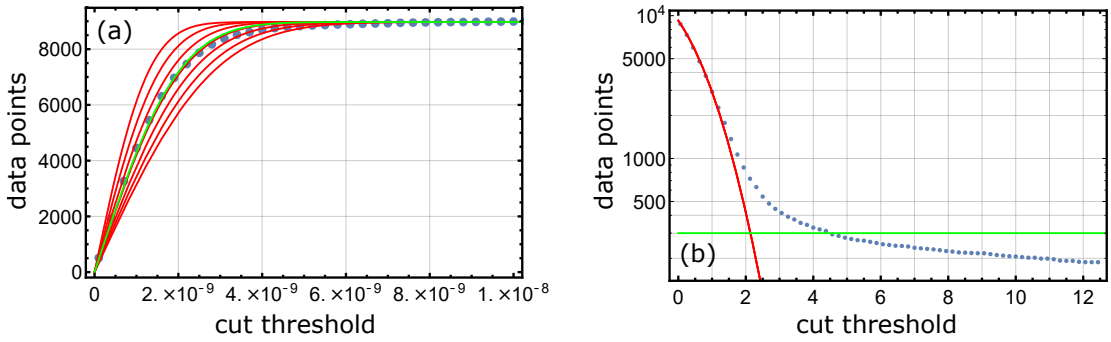

Figure 8.14.: Statistical data distribution. Left: The blue dots represent the amount of data points in the center of the measured ratio distribution as a function of the cut threshold applied to the distribution. The red solid lines represent the calculated scaling for different parameters σ of the parent distribution, the green line represents a fit to the data that gives a background center distribution with a width of 1.56(1) p.p.b. The right plot shows the data of the measured distribution that are above a certain cut threshold. Up to a cut threshold of about $2\,\sigma$ (green line), the data are consistent with the statistical modes (red line). However, above the $2\,\sigma$-threshold denoted by the green, the amount of outliers is inconsistent with the assumption of a Gaussian white distribution.

is depicted. In Fig. 8.14 (a), measured data are denoted by blue points, the red curves show the expected results from different parent-distributions, and the green line fits the data and yields an uncorrected distribution width of $\sigma = 1.56(1)$ p.p.b. In Fig. 8.14 (b), the number of points rejected as a function of the trim filter width are shown, with the red solid line depicted the expected scaling from a normal distribution with the median

standard deviation of the grouped sub distributions.

In order to account for the time-dependent background scatter, the sequence of measured frequency ratios is grouped into sub-blocks of length N_0. To each of the sub-blocks, a Pearson-χ^2 test is applied in order to compare the sub-block data structure to the null-hypothesis of normally distributed data. From the sub-blocks, local means, standard deviations and p-values are obtained. From these data, the weighted mean is computed, and the stability of the result as a function of N_0, trim threshold, hypothesis test p-value and local background fluctuations is investigated. Two examples for this are illustrated in Fig. 8.15, where the final frequency ratio is shown as for different values of N_0 between 1 h and 4 h. For $2\,\mathrm{h} \leq N_0 \leq 3.5\,\mathrm{h}$, the overall weighted mean is stable. The observed small fluctuations with N_0 are in this range consistent with results from Monte-Carlo-simulations, which are based on measured frequency scatter from the fit routine and the magnetic diffusion model described in Sec. 8.8.

In addition to the cyclotron frequencies, the differential Allan deviation is also evaluated for other relevant trap parameters such as for instance the resonator level. For $N_0 > 3.5\,\mathrm{h}$, a slow drift is observed in some of these differential Allan deviations. This might for instance indicate that assuming a single underlying magnetic field sub-distribution for data samples of such length is not appropriate, or changed behavior in other relevant trap parameters. To quote a final result, we use the mean of the ratio data evaluated with $2\,\mathrm{h} \leq N_0 \leq 3.5\,\mathrm{h}$. Fig. 8.15 (b) shows the final ratio as a function of the fluctuation cut, where data sub-blocks with high background scatter are disregarded.

Unlike for data samples that consist of data subsets with equal weights, there is no

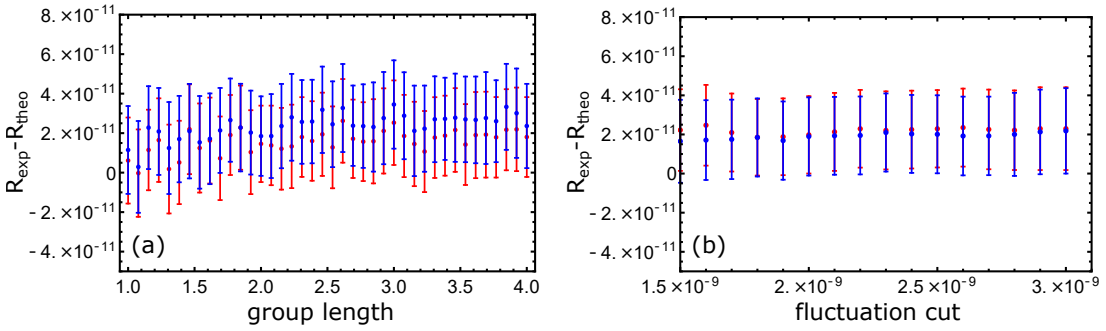

Figure 8.15.: Cyclotron frequency ratio as a function of sub-set sample length and fluctuation cut. Left: Frequency ratio as a function of group length N_0. Right: Ratio as a function of fluctuation cut.

widely accepted treatment for obtaining the standard error of a weighted mean on data subsets with varying uncertainties. We apply a statistical bootstrapping scheme from which we obtain an empirical distribution of the mean and robust estimate of the related standard error. For details we refer to [162]. The statistical measured antiproton-to-hydride cyclotron frequency ratio is

$$R_{\mathrm{exp,stat}} = 1.001\,089\,218\,775(20), \tag{8.25}$$

The statistical uncertainty is by 3.25 times more precise than the statistical uncertainty of the previously reported measurement [39], thanks to the apparatus improvements that were partly developed and implemented within this thesis (Sec. 3.2).
In order to benchmark the data evaluation approach we compare both particles to themselves by cutting the individual particle sequences $\nu_{c,\mathrm{H}^-,k}$ and $\nu_{c,\bar{p},k}$ to subsequences $\nu_{c,\mathrm{H}^-,2k-1}$ and $\nu_{c,\mathrm{H}^-,2k}$ as well as $\nu_{c,\bar{p},2k}$ and $\nu_{c,\bar{p},2k-1}$. We apply the same analysis as above to the odd sequences to reconstruct the even sequences. For the hydride to hydride comparisons,

$$R_{\mathrm{exp,stat,H^-}} - 1 = -0.000\,000\,000\,002\,8(29\,3) \tag{8.26}$$

is obtained, while the antiproton to antiproton comparison yields

$$R_{\mathrm{exp,stat},\bar{p}} - 1 = -0.000\,000\,000\,015\,2(34\,5). \tag{8.27}$$

The combined data-set supports the data evaluation approach with a fractional uncertainty of 22.6 p.p.t., its resolution being slightly less precise compared to the 20 p.p.t. yielded for the antiproton-to-hydride comparison, which is accounted to stronger pronounced magnetic field drifts in the interleaved identical particles data-treatment.

8.10. Polynomial frequency ratio evaluation

The data evaluation approach by linear interpolation outlined in Sec. 8.9 enables to study systematic effects flexibly, to simply discriminate experiment stability fluctuations and to perform high resolution oscillation studies. In this section, the evaluation by polynomial interpolation is introduced, which is inspired by early work of the trap group at MIT [163, 164]. The frequency ratio R is obtained by the following algorithm:

- We fit a polynomial $p(t)$ of order q to a data set of length N_0.
- We overlap the data sets $\nu_{c,\bar{p},k}$ and $\nu_{c,\mathrm{H}^-,k}$ with a free multiplicative estimator R, fit to the resulting overlapped data-set the polynomial $p(t)$ and evaluate the log-Likelihood function $\log L(\{\nu_{c,\bar{p},k}, \nu_{c,\mathrm{H}^-,k}\}, R)$.
- To estimate the frequency ratio uncertainty, we calculate the Fisher information [165] $I(R) = \mathrm{d}^2 \log L(\{\nu_{c,\bar{p},k}, \nu_{c,\mathrm{H}^-,k}\}, R)/\mathrm{d}R^2$ and define the uncertainty of R based on the Cramer-Rao lower bound [166],

$$\mathrm{var}(R) = -\frac{1}{\mathrm{d}^2 \log L(\{\nu_{c,\bar{p},k}, \nu_{c,\mathrm{H}^-,k}\}, R)/\mathrm{d}R^2}. \tag{8.28}$$

The polynomial order q is a-priori a free parameter that needs to be characterized. If q is chosen too small, the polynomial fit might not reproduce all drifts and non-linear features present in the data, which usually leads to high reduced χ^2 values. If q is chosen too large, the least squares fitting routine tries to fit noisy features in the data. A lot of work has been done by others to study the question of ideal polynomial order in context of analyzing data of trap experiments [164], in BASE we use F-tests, cost functions, and Akaike-information [167] to define the polynomial order. For the 2019 sideband data, a polynomial order of $N_0/q > 6$ usually leads to a reduced $\chi^2 \approx 1$ for sub-datasets of a length below 4 h. For higher q, "overfitting" may artificially reduce the error bar, the scaling of uncertainty with fitting order is weak. This behavior is visualized in Fig. 8.16. On the left, an antiproton and a hydride cyclotron frequency data set are corrected for the offset and plotted together (blue points). The shown data were recorded during about 2.5 hours. The red line denotes a polynomial fit of third order and the blue a fit of fifth order. The plot on the right shows the corresponding cost function as a function of polynomial order. The cost function is given by the quadratic sum of the fit residuals divided by q. The q-range which leads to stable results ($q > 4$) is rather robust, with the fit residuals and the obtained ratio result being stable. For $q > N_0/3$, we start to see indications of "overfitting", which is why such high polynomial orders are not considered in this data analysis.

In Figure 8.17 left, the results of the naive linear interpolation (red points) and those of an optimized polynomial fit evaluation (blue) are shown for a sub-ratio data set. This analysis is based on the work of other collaboration members at BASE, and will be fully described in a dedicated publication soon. For 90 % of the dataset, the linear and

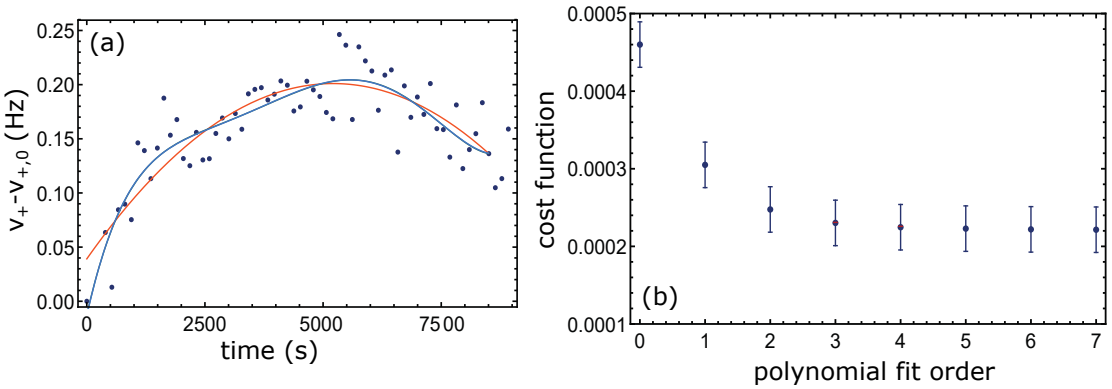

Figure 8.16.: Polynomial fitting and cost function. Left: Measured cyclotron frequency sets of the antiproton and the hydride ion (blue scatter points). Both frequency sets are plotted on top of each other for illustrative purposes. Every frequency at odd position is a hydride frequency, every frequency at even position is an antiproton frequency. The sample length is $N_0 = 64$, which correspond to a time sequence of 2.5 h. The red line indicates a third order fit, the blue line is the result of a fifth order fit. Right: Cost function (fit residuals divided by number of degrees of freedom) as a function of polynomial order for the data shown on the left. The cost function is stable above $p = 4$.

the polynomial results are consistent within about 10 % of the quoted error bars. The plot on the right hand side shows the result of the polynomial fitting approach as a function of the linear spline treatment. From evaluating the entire dataset by means of the polynomial fit approach and by treating the resulting frequency ratios with the weighted data approach outlined in the section above, we obtain

$$R_{\mathrm{exp,stat}} = 1.001\,089\,218\,772(19), \tag{8.29}$$

which is within 3 p.p.t. consistent with the linear spline evaluation frequency ratio presented in the last section. Also here, the uncertainty is obtained from a bootstrap analysis.

8.11. Systematic uncertainties and corrections

In the following sections, all relevant aspects of the systematic uncertainties and corrections are described. There are three main types of systematic shifts and uncertainties:

1. Trap shifts: Trap related shifts and uncertainties that arise from systematic shifts

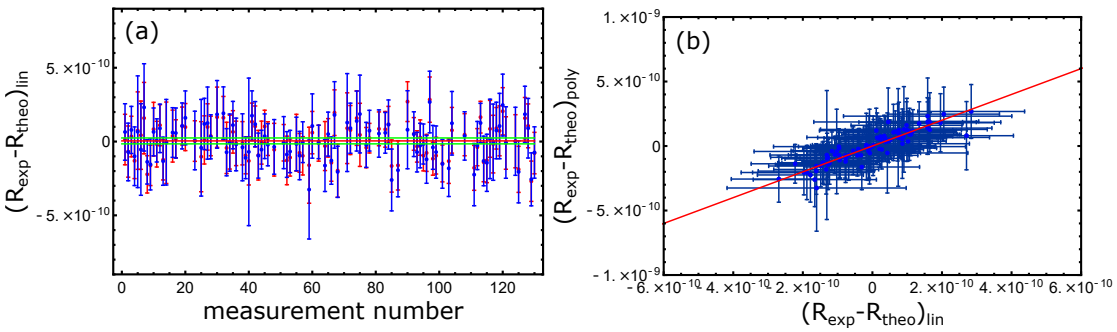

Figure 8.17.: Comparing the linear and polynomial evaluation approach. Left: Selection of a frequency ratio sequences, red data points are from the linear fitting approach, blue data from the polynomial fitting approach. The plot on the right shows the polynomial ratio as a function of the linear ratio, the red line indicates f(x)=x.

of the measured frequencies due to trap imperfections such as the slightly inhomogeneous magnetic field and higher order terms in the electric trapping potential. Any other shifts that lead to deviations of the assumptions of the Penning trap as a homogeneous magnetic field and an ideal quadrupolar potential is as well attributed to the category, such as for example shifts due to the interaction of the particle with its image charge and the resonant detection system, as well as relativistic frequency shifts.

2. Spectrum shifts: Shifts and uncertainties that are related to the applied frequency measurement process. Such shifts could arise from local and global spectrum asymmetries, which might be slightly different at the two different measurement frequencies ν_{z,H^-} and $\nu_{z,\bar{p}}$.
3. Sequence shifts: Shifts that arise from the measurement sequence itself, such as for example asymmetric voltage drifts, or shifts of the trapping potential related to varactor detuning and parasitic leakage currents.

The statistical uncertainty which has been achieved by the shuttling measurements is 20 parts in a trillion, which corresponds to an uncertainty of about 600 μHz. It is therefore necessary to study the related systematic effects at that level of absolute frequency resolution.

Any systematic shift $\Delta\nu_{c,k}$ in the determination of a cyclotron frequency $\nu_{c,k}$ is related

to a systematic shift in the cyclotron frequency ratio by

$$\begin{aligned} R_0 + \Delta R = \frac{\nu_{c,1} + \Delta\nu_{c,1}}{\nu_{c,2} + \Delta\nu_{c,2}} = R_0 \left(1 + \frac{\Delta\nu_{c,1}}{\nu_{c,1}} - \frac{\Delta\nu_{c,2}}{\nu_{c,2}}\right) \\ \Rightarrow \Delta R = R_0 \left(\frac{\Delta\nu_{c,1}}{\nu_{c,1}} - \frac{\Delta\nu_{c,2}}{\nu_{c,2}}\right). \end{aligned} \tag{8.30}$$

The invariance theorem $\nu_c^2 = \nu_+^2 + \nu_z^2 + \nu_-^2$ [69] is used to determine the free cyclotron frequency ν_c. Shifts in ν_c are therefore given by

$$\nu_c + \Delta\nu_c = \nu_c \left(1 + \frac{\nu_+}{\nu_c^2}\Delta\nu_+ + \frac{\nu_z}{\nu_c^2}\Delta\nu_z + \frac{\nu_-}{\nu_c^2}\Delta\nu_-\right). \tag{8.31}$$

For the experimental conditions of the BASE experiment, the following estimation applies:

$$\Delta\nu_c = \left(\frac{\nu_+}{\nu_c}\Delta\nu_+ + \frac{\nu_z}{\nu_c}\Delta\nu_z + \frac{\nu_-}{\nu_c}\Delta\nu_-\right) \approx \left(\Delta\nu_+ + \frac{1}{46}\Delta\nu_z + \frac{1}{4300}\Delta\nu_-\right). \tag{8.32}$$

The determination of the modified cyclotron frequency ν_+ dominates systematic shifts and uncertainties. Shifts and uncertainties in the axial frequency are suppressed by a factor of ≈ 46, while those in the determination of the magnetron frequency are negligibly small. In sideband measurements, the modified cyclotron frequency is determined by

$$\nu_+ = \nu_{\mathrm{rf}} + \nu_l + \nu_r - \nu_z. \tag{8.33}$$

Consequently, any systematic shift in one of those four frequencies will directly lead to a shift in the determined cyclotron frequency ratio. We distinguish here spectrum shifts $\Delta\nu_S$, which account to all frequencies measured via axial FFT spectra, and the trap shifts $\Delta\nu_T$, which are intrinsic in the involved cyclotron, axial, and dynamical coupling frequencies. The experimentally determined cyclotron frequency from sideband measurements therefore denotes

$$\nu_{+,\mathrm{exp}} = \nu_{+,0} + \Delta\nu_{+,T} = \nu_{\mathrm{rf}} + \nu_l + \nu_r - (\nu_z + \Delta\nu_{z,T} + \Delta\nu_{z,S}), \tag{8.34}$$

the uncertainties due to $\Delta\nu_T$ and $\Delta\nu_S$ will be discussed in the further text below.

8.11.1. Trap Shifts - axial temperature / axial temperature variation / temperature similarity

We may rewrite the cyclotron frequency ratio to

$$\Delta R = R_0 \left(\frac{\Delta\nu_{c,1}}{\nu_{c,1}} - \frac{\Delta\nu_{c,2}}{\nu_{c,2}} \right) = R_0 \frac{\Delta\nu_{c,1}}{\nu_{c,1}} \left(1 - \frac{\Delta\nu_{c,2}}{\Delta\nu_{c,1}} \frac{\nu_{c,1}}{\nu_{c,2}} \right) \approx R_0 \frac{\Delta\nu_{c,1}}{\nu_{c,1}} \left(1 - R_0 \right). \quad (8.35)$$

In the last approximation, $\Delta\nu_{c,1}/\Delta\nu_{c,2} \approx 1$ was used. It can be seen that certain trap shifts are suppressed by almost three orders of magnitude in antiproton-to-proton charge-to-mass ratio comparisons ($|1 - R_0| \approx 1/1000$). This is only true if the two particle energies are identical. As all frequency measurements in the sideband scheme rely on the particle being in thermal equilibrium with the axial detection circuit, it is especially important to investigate the detector temperature for both working points. At BASE, the axial detector temperature slowly changes over time, as depicted in Fig. 8.18. Left, the axial detector signal-to-noise ratio is shown, while the corresponding differential Allan deviation of the detector SNR over time is shown on the right. The detector SNR

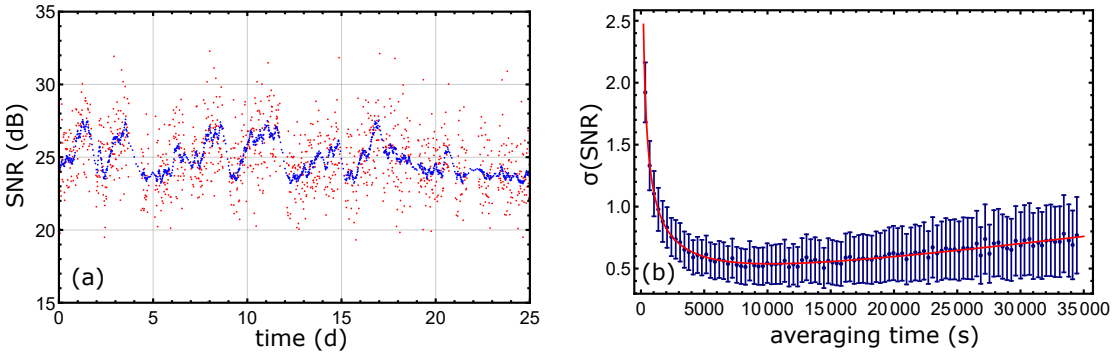

Figure 8.18.: Temporal stability of the detector SNR. Left: Detector signal-to-noise ratio as a function of time. The data set covers a time range of 25 days of continuously sampled data. Right: Differential Allan deviation of the data shown on the left, the signal-to-noise ratio of the detector can be considered stable for a period of about three hours, for longer averaging it exhibits a slow drift.

and the top-noise level of the axial resonator are related to the detector temperature T_z, with

$$\mathrm{SNR} = 10 \log_{10} \left(8\pi k_B T_z \nu_{\mathrm{res}} Q L \frac{\kappa^2}{e_n^2} - 1 \right). \quad (8.36)$$

κ describes the coupling factor of the amplifier to the resonator [76] and e_n the amplifier equivalent input noise. The temperature can be estimated by means of tuning ratio scans (Sec. 7.1.1), measurements of cyclotron frequency as a function of axial feedback strength (Sec. 7.2.5), or cyclotron excitation scatter measurements (Sec. 7.2.1). For the negative feedback applied during the sideband campaign 2019, an antiproton median baseline temperature of 5.23(34) K has been measured. A dominant systematic shift between both cyclotron frequencies is induced if the axial temperatures of both particles differ (see also Sec. 7.1.1). To investigate the temperature difference, we consider the difference dS in top-noise levels of the different detector working points $\nu_{\mathrm{res,H^-}}$ and $\nu_{\mathrm{res},\bar{p}}$. The amplifier gain difference is experimentally constrained to $\mathrm{d}G_{\mathrm{res,H^-},\bar{p}} < 0.0002\,\mathrm{dB}$ and assumed to be constant here, $\mathrm{d}G_{\mathrm{res,H^-},\bar{p}} = G_{\mathrm{res,H^-}} - G_{\mathrm{res},\bar{p}} = 0$. dS is then given by:

$$\begin{aligned}\mathrm{dS} = \mathrm{S}_{\mathrm{H^-}} - \mathrm{S}_{\bar{p}} &\approx 10\log_{10}\left(\frac{T_{z,\mathrm{H^-}}}{T_{z,\bar{p}}}\frac{\nu_{\mathrm{res,H^-}}}{\nu_{\mathrm{res},\bar{p}}}\frac{Q_{\mathrm{H^-}}}{Q_{\bar{p}}}\frac{(\kappa_{\mathrm{H^-}}/e_{n,\mathrm{H^-}})^2}{(\kappa_{\bar{p}}/e_{n,\bar{p}})^2}\right)\\ &\approx 10\log_{10}\left(\frac{T_{z,\mathrm{H^-}}}{T_{z,\bar{p}}}\frac{\nu_{\mathrm{res,H^-}}}{\nu_{\mathrm{res},\bar{p}}}\frac{Q_{\mathrm{H^-}}}{Q_{\bar{p}}}\right).\end{aligned} \tag{8.37}$$

Here, the approximation $(\kappa_{\mathrm{H^-}}/e_{n,\mathrm{H^-}})^2/(\kappa_{\bar{p}}/e_{n,\bar{p}})^2 \approx 1$ is used since the coupling factors κ are given from the geometrical tap ratio of the detector-inductance, and the equivalent amplifier input noise e_n is considered to be constant in the frequency tuning range of $\Delta\nu \approx 348.5\,\mathrm{Hz}$. Apart from the axial temperature fraction $T_{z,\mathrm{H^-}}/T_{z,\bar{p}}$, all other parameters are directly accessible from the experiment sequence, which enables us to determine the differential deviation $T_{z,\mathrm{H^-}}/T_{z,\bar{p}} - 1$. An example of the measured dS is shown in Fig. 8.19. On the left, the measured data are plotted in blue and the red points denote the 2.5 h moving median filter. The solid red line indicates the median of the full data set, while the green line shows the signal level difference expected from measurements of the effective parallel resistances of the detector, $R_{p,\bar{p}}$ and $R_{p,\mathrm{H^-}}$. On the right, the relation between temperature difference and signal level difference is shown. The gray lines in both plots in Fig. 8.19 indicate dS values corresponding to temperature differences in steps of 0.5 K. In addition to comparing the signal level difference of hydride and antiproton resonator spectra, we also compare the noise levels of single dip spectra and double dip spectra. The comparison of axial and sideband spectra show a systematic difference of $(T_{\mathrm{SB}} - T_z)_{\bar{p}} = 50.3(3.3)\,\mathrm{mK}$ and $(T_{\mathrm{SB}} - T_z)_{\mathrm{H^-}} = 50.2(3.3)\,\mathrm{mK}$.
The two axial temperatures of the particles were also compared explicitly by perform-

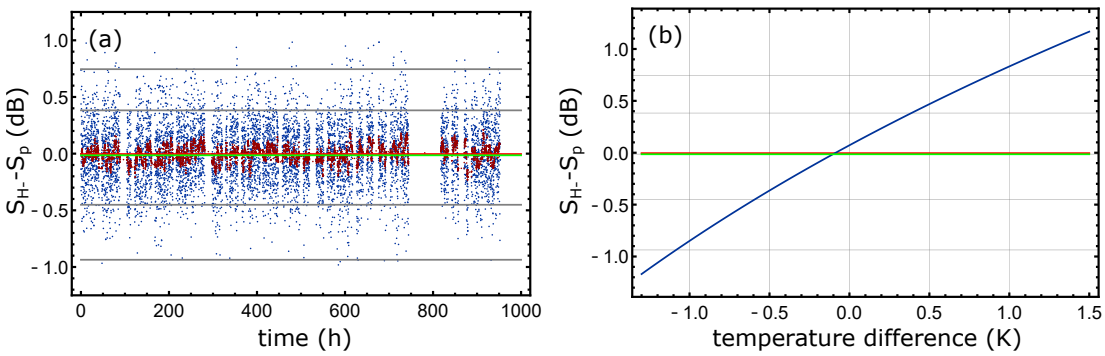

Figure 8.19.: Investigation of detector signal difference. Left: Detector signal level difference as a function of time. The scatter points indicate the measured results, the dark red data is a median filter applied to the data which averages over moving sequences with a length of 2.5 h, the red solid line is the measured median difference of the entire sequence, the green line indicates the expected signal level difference based on measurements of the resonator resistances $R_{p,\bar{p}}$ and R_{p,H^-}. The gray solid lines indicate expected signal level differences, each step corresponds to a temperature difference of 0.5 K. Right: Signal level difference as a function of temperature difference. Blue represents the signal level model, red and green indicate the same values as the plot on the left.

ing interleaved tuning ratio scans (see also Sec. 7.1.1), and by comparing the excitation scatter (see also Sec. 7.2.1) at the two different axial resonator working points $\nu_{\mathrm{res},\mathrm{H}^-}$ and $\nu_{\mathrm{res},\bar{p}}$. From tuning ratio scans, the difference in axial temperature is constrained to be around 160(220) mK, while from excitation scatter measurements both particle temperatures look similar at a level $\Delta T/T = 0.049$. The implications of these temperature differences will be discussed below.

8.11.2. Trap shifts - magnetic field

In this section, frequency shifts arising the from magnetic field gradient B_1 and the quadratic magnetic field inhomogeneity B_2 are considered. In axial direction, the magnetic field in the center of the precision trap is given by

$$B_z(z) = B_0 + B_1 z + B_2 z^2. \tag{8.38}$$

Here B_1 is the magnetic gradient coefficient $B_1 = 1.57(2)\,\mathrm{mT/m}$, which has been determined by shifting the particle along the trap axis and measuring the cyclotron frequency as a function of particle position (Sec. 7.1.4), B_2 is the magnetic bottle coefficient

$B_2 = -89.4(6)\,\mathrm{mT/m^2}$ that has been measured using the peak method, as described in Sec. 7.2.3.

Magnetic gradient shift

The effect of the magnetic field gradient B_1 in axial direction onto the measured cyclotron frequency has already been discussed in the context of the trap optimization in Sec. 7.1.4. B_1 induces a shift of equilibrium position of the axial oscillation due to an interaction with the angular moment resulting from the cyclotron oscillation $I_+(\nu_+, E_+)$. As a result, the cyclotron frequencies ν_{+,H^-} and $\nu_{+,\bar{p}}$ are measured at slightly different positions in the magnetic field. The related cyclotron frequency shift is given by

$$\frac{\Delta\nu_c}{\nu_c} = -\frac{1}{4\pi^2 m \nu_z^2}\left(\frac{B_1}{B_0}\right)^2 k_B \frac{\nu_+}{\nu_z} T_z. \tag{8.39}$$

With the parameters of our precision trap, the axial temperature similarity that was determined above, and $T_+ = (\nu_+/\nu_z)T_z$, this leads for both particles to absolute individual cyclotron frequency shifts of $(\Delta\nu_c/\nu_c) = -7.5(3) \times 10^{-14}$, which translates to a systematic frequency ratio shift of $(\Delta R/R) = -4.0 \times 10^{-17}$ and an uncertainty of 5.78×10^{-15}.

Magnetic bottle shift

The frequency shifts due to a magnetic bottle are summarized in the perturbation matrix from Sec. 2.2.1,

$$\begin{aligned}\begin{pmatrix} \frac{\Delta\nu_+}{\nu_+} \\ \frac{\Delta\nu_z}{\nu_z} \\ \frac{\Delta\nu_-}{\nu_-} \\ \frac{\Delta\nu_L}{\nu_L} \end{pmatrix} &= \frac{1}{4\pi^2 m_0 \nu_z^2}\frac{B_2}{B_0}\begin{pmatrix} -\left(\frac{\nu_z}{\nu_+}\right)^2 & 1 & -2 \\ 1 & 0 & 1 \\ 2 & -1 & 2 \\ -\left(\frac{\nu_z}{\nu_+}\right)^2 & 1 & -2 \end{pmatrix} \cdot \begin{pmatrix} E_+ \\ E_z \\ E_- \end{pmatrix} \\ &= \frac{1}{4\pi^2 m_0 \nu_z^2}\frac{B_2}{B_0}\begin{pmatrix} -\left(\frac{\nu_z}{\nu_+}\right)^2 & 1 & -2 \\ 1 & 0 & 1 \\ 2 & -1 & 2 \\ -\left(\frac{\nu_z}{\nu_+}\right)^2 & 1 & -2 \end{pmatrix} \cdot \begin{pmatrix} \frac{\nu_+}{\nu_z} k_B T_z \\ k_B T_z \\ \frac{\nu_-}{\nu_z} k_B T_z \end{pmatrix},\end{aligned} \tag{8.40}$$

where in the last equation the relations for sideband-cooled particles, $T_+ = (\nu_+/\nu_z)T_z$ and $T_- = (\nu_-/\nu_z)T_z$, were inserted. The dominant shift of the modified cyclotron frequency is imposed by the oscillation of the weakly bound axial mode over the magnetic inhomogeneity, which leads to a shift since $\langle z(t)^2 \rangle \neq 0$. With $B_2 = -89.4(6)\,\mathrm{mT/m^2}$, the shift of the cyclotron frequency obtained from the matrix is

$$\frac{\Delta\nu_c}{\nu_c} = \frac{\nu_+}{\nu_c^2}\Delta\nu_+ + \frac{\nu_z}{\nu_c^2}\Delta\nu_z \approx \frac{1}{4\pi^2 m\nu_z^2}\frac{B_2}{B_0}k_B T_z = -23.4(2)\,\frac{\mathrm{p.p.t.}}{\mathrm{K}}, \tag{8.41}$$

and has a magnitude which is of dominant concern. With the limits from explicit temperature difference measurements $\Delta T \approx 160(220)\,\mathrm{mK}$, and the temperature differences between sideband and axial spectra of $50.3(3.3)\,\mathrm{mK}$ and $50.2(3.3)\,\mathrm{mK}$, we extract $\Delta R/R = 3.75 \times 10^{-12}$ with an uncertainty of 5.16 p.p.t., which is the dominant trap related uncertainty imposed on the measurement.

8.11.3. Trap Shifts - Electrostatic Potential

As discussed in Sec. 2.2, the electrostatic potential of the trap can be expressed as a series expansion

$$\phi(z) = V_r \sum_k C_k z^k, \tag{8.42}$$

where odd coefficients are negligibly small. While the C_2 coefficient is related to the harmonic trap potential, C_4 and C_6 are the dominant higher-order coefficients to the series expansion. These can ideally be simultaneously tuned to 0 in the compensated trap design [71]. The octupolar correction matrix reads

$$\begin{pmatrix} \frac{\Delta\nu_+}{\nu_+} \\ \frac{\Delta\nu_z}{\nu_z} \\ \frac{\Delta\nu_-}{\nu_-} \\ \frac{\Delta\nu_L}{\nu_L} \end{pmatrix} = 3\frac{C_4}{C_2^2}\frac{1}{qV_r} \begin{pmatrix} \frac{1}{4}\left(\frac{\nu_z}{\nu_+}\right)^4 & -\frac{1}{2}\left(\frac{\nu_z}{\nu_+}\right)^2 & \left(\frac{\nu_z}{\nu_+}\right)^2 \\ -\frac{1}{2}\left(\frac{\nu_z}{\nu_+}\right)^2 & \frac{1}{4} & -1 \\ -\left(\frac{\nu_z}{\nu_+}\right)^2 & 1 & -1 \\ 0 & 0 & 0 \end{pmatrix} \cdot \begin{pmatrix} E_+ \\ E_z \\ E_- \end{pmatrix} \tag{8.43}$$

The axial frequency shift due to C_4 is given by

$$\frac{\Delta\nu_z}{\nu_z} = \frac{3}{4}\frac{C_4}{C_2^2}\frac{k_B T_z}{qV_r} = 33.93\,\frac{\mathrm{mHz}}{\mathrm{mUnit} \times \mathrm{K}}. \tag{8.44}$$

Using tuning ratio scans (Sec. 7.1.1), we routinely optimize the tuning ratio to the $< 10^{-5}$-level, which corresponds to an axial frequency shift of $< \Delta\nu_z = 339\mu\text{Hz/K}$ and to a related systematic uncertainty in the cyclotron frequency ratio of $\sigma(\Delta R/R)_{C_4} = 0.76\times10^{-12}$. For the C_6 coefficient, a tuning ratio compensation offset of $\Delta\text{TR}(C_4 = 0) - \Delta\text{TR}(C_6 = 0) = 3.5(1.5)\,\text{mUnits}$ has been determined based on magnetron burst scans. This compensation mismatch induces an additional ratio uncertainty $\sigma(\Delta R/R)_{C_6} = 1.4 \times 10^{-16}$.

8.11.4. Trap shifts - relativistic shift

The effects of special relativity are mainly due to the relativistic mass $m(v) = m_0/\sqrt{1-(v/c)^2}$, which leads to a correction matrix

$$\begin{pmatrix} \frac{\Delta\nu_+}{\nu_+} \\ \frac{\Delta\nu_z}{\nu_z} \\ \frac{\Delta\nu_-}{\nu_-} \\ \frac{\Delta\nu_L}{\nu_L} \end{pmatrix} = -\frac{1}{m_0c^2} \begin{pmatrix} 1 & \frac{1}{2} & \left(\frac{\nu_z}{\nu_+}\right)^2 \\ \frac{1}{2} & \frac{3}{8} & \frac{1}{4}\left(\frac{\nu_z}{\nu_+}\right)^2 \\ -\left(\frac{\nu_z}{\nu_+}\right)^2 & -\frac{1}{4}\left(\frac{\nu_z}{\nu_+}\right)^2 & -\frac{1}{4}\left(\frac{\nu_z}{\nu_+}\right)^4 \\ \frac{2}{9} & \frac{1}{2} & \left(\frac{\nu_z}{\nu_+}\right)^2 \end{pmatrix} \cdot \begin{pmatrix} E_+ \\ E_z \\ E_- \end{pmatrix}. \tag{8.45}$$

For protons and hydride ions, the only relevant frequency shift due to special relativity in the sideband scheme is the shift of the modified cyclotron frequency, which leads to ratio shift $\Delta R/R = 4.25\,\text{p.p.t./K} \times \Delta T_z$. With $\Delta T_z = 160(220)\,\text{mK}$, we yield $\Delta R/R = 0.7(9)\,\text{p.p.t.}$

8.11.5. Trap shifts - magnetron approximation and trap angle

The invariance theorem [69], which is used for determining the cyclotron frequency holds also in presence of an elliptic deformation of the trapping potential $\propto \epsilon(x^2 - y^2)$ and a misalignment angle θ of the magnetic field axis to the axis of the trapping field. At BASE, the magnetron frequency is usually not explicitly measured, but instead estimated by $\nu_- \approx \tilde{\nu}_- = \nu_z^2/(2\nu_+)$. This approach is chosen since slight inaccuracies in the magnetron frequency determination are strongly suppressed due to the frequency hierarchy at BASE ($\nu_+ \gg \nu_z \gg \nu_-$), and the sampling rate can be increased. Consequently, the trap shifts due to ϵ and θ that would cancel out in the free cyclotron frequency if all eigenfrequencies were measured cannot be neglected. The resulting shift in the

cyclotron frequency determination can be calculated explicitly. For $\epsilon \ll 1$ and $\theta \ll 1$, the dominant contribution that shifts the cyclotron frequency is

$$\frac{\Delta\nu_c}{\nu_c} = \frac{9}{16}\left(\frac{\nu_z}{\nu_+}\right)^4\left(\theta^2 - \frac{2}{9}\epsilon^2\right) = \frac{1}{4}\left(\frac{\nu_z}{\nu_+}\right)^4\left[\left(\frac{\nu_-}{\tilde{\nu}_-}\right)^2 - 1\right]. \tag{8.46}$$

This effect is precisely calculated by performing interleaved sideband measurements on the magnetron and the cyclotron sideband, and comparing $\tilde{\nu}_- = \nu_z^2/(2\nu_+)$ and the explicitly measured ν_- (see also Sec. 7.1.5). We obtain $\nu_- = 6916.661(4)$ Hz and $\tilde{\nu}_- = 6918.1945(9)$ Hz, corresponding to $(\theta^2 - 2\epsilon^2/9) = -1.97(3)\times 10^{-4}$, which indicates that the ellipticity slightly dominates over the trap angle misalignment. The resulting shift in the cyclotron frequency ratio is $\Delta R/R = 5.25(1)\times 10^{-14}$, which is three orders of magnitude below the statistical uncertainty of the measurement campaign.

8.11.6. Trap shifts - image charge shift

The particle oscillation induces an image charge in the trap electrodes that leads to an additional radially pulling electric field, which modifies the modified cyclotron frequency [168]. For cylindrical traps, the related potential problem can be solved explicitly by treating the trap as an infinitely long grounded, conductive, cylindrical tube of radius ρ_0 [169, 72]. The resulting cyclotron frequency shift is given by

$$\frac{\Delta\nu_c}{\nu_c} = -\frac{m}{4\pi\epsilon_0\rho_0^3 B_0^2}. \tag{8.47}$$

With the BASE magnetic field of $B_0 = 1.944\,846$ T and the trap radius $\rho_0 = 4.5$ mm, the image charge shifts for the proton and the H^- ion are at -43.61 p.p.t. and -43.67 p.p.t., respectively, and the resulting frequency ratio shift is given by $\Delta R = 0.0475(6)$ p.p.t. The uncertainty in ΔR is related to the $10\,\mu$m manufacturing tolerances of the trap electrodes.

8.11.7. Trap shift - damping shift and resonator pulling

The particle's axial motions is weakly coupled to the axial detection resonator and is thereby damped, which leads to a modification of the axial frequency. While the real part of the detection impedance causes a marginal shift, the interaction between the imaginary part of the detection impedance and the particle can cause considerable axial

frequency shifts, when the particle and the resonator are slightly detuned [170]. The complex impedance causes an image current that is in phase with the motion of the ion. This image current produces a dynamical pseudo-potential that shifts the axial frequency. This shift is compensated in the BASE fitting routine.

8.11.8. Sequence/Spectrum Shifts - Axial Frequency Comparisons

The measured axial frequencies of the two particles are used for characterizing sequence and spectrum shifts. From other source [71], R is known to a level of 90 p.p.t. This measurement is based on another measurement method and therefore allows us testing the consistency of the axial frequency measurement system to a level of 30 μHz, which corresponds to an equivalent frequency ratio resolution of 1 p.p.t.
We therefore compare axial frequencies of different shuttling measurements with the antiproton stored in T_4 and the hydride ion stored in T_6 as well as with interchanged particle configuration, and obtain the axial frequency differences $\Delta_{4,6} = \nu_{\bar{p},T_4} - \nu_{\mathrm{H}^-,T_6}$ and $\Delta_{6,4} = \nu_{\mathrm{H}^-,T_4} - \nu_{\bar{p},T_6}$. This enables us to disentangle spectrum offsets $\Delta_{z,S}$ and voltage drifts $\Delta_{z,D}$. Since the frequency ratio determination is only sensitive to differences between measured frequencies rather than to absolute offsets, we assign without loss of generality the drift offset to electrode T_6 and the spectrum offset to the antiproton spectrum. With

$$\Delta_{4,6} = \Delta_{z,S} - \Delta_{z,D} \text{ and } \Delta_{6,4} = -\Delta_{z,S} - \Delta_{z,D}, \tag{8.48}$$

we obtain the offsets as

$$\Delta_{4,6} + \Delta_{6,4} = -2\Delta_{z,D} \text{ and } \Delta_{4,6} - \Delta_{6,4} = 2\Delta_{z,S}. \tag{8.49}$$

From the measured data that are considered here, we extract a T_4 to T_6 drift offset of $\Delta_{z,D} = -5.03(5.12)$ p.p.t., and a spectrum offset of $\Delta_{z,S} = 28.16(11.04)$ p.p.t. ($\approx 835\,\mu$Hz). During the measurement sequence, the trap voltage was measured independently, and in addition, the axial frequency prior to the sideband measurement is compared with the axial frequency during the sideband measurement (by $\nu_z = (\nu_l + \nu_r)$). From these two measurements, the presence of additional drifts during the acquisition of the double dip spectrum is rejected. The systematic frequency offset between the two axial frequencies of $\Delta_{z,S} = 835\,\mu$Hz, and how to correct for the effect, has yet

to be understood and is investigated in the following sections. It is noted that trivial shifts such as FFT heterodyning offsets or systematic offsets imposed by the 10 MHz Rb standard (SR-FS725) with a specified frequency stability of $\Delta\nu/\nu < 2 \times 10^{-12}$, aging of $\Delta\nu/\nu < 50 \times 10^{-12}$ per month, and a temperature response of 30 p.p.t./K can be constrained to $\Delta R/R = -2.76(85)$ p.p.t.

8.11.9. Interaction of Varactor Tuning and B_1

A varactor diode (a voltage variable capacitor) is used in order to tune the detector resonance frequency between the two working points $\nu_{\mathrm{res,H^-}}$ and $\nu_{\mathrm{res},\bar{p}}$ (see Fig. 8.5). The varactor is connected via a coupling capacitor to the P_3 pick-up electrode of the precision trap, to which the detector is connected as well. P_3 and P_5 are the correction electrodes, which individually produce a potential gradient over the trap, but together facilitate a homogeneous trap potential (Sec. 2.2). A leakage current over the coupling capacitor of the varactor would lead to a voltage offset on P_3 that would shift the particle in the residual magnetic gradient B_1 and impose a shift of the measured cyclotron frequency ratio. The observed frequency shift of $\Delta_{z,S} = 835\,\mu$Hz would be consistent with a parasitic voltage offset of $250\,\mu$V on the correction electrode. With the axial position shift of $604\,\mu$m/mV on the correction electrode and the $B_1 = 0.00157(2)\,\mathrm{T/m^2}$ (Sec. 7.1.4), this would produce a frequency ratio shift $(\Delta R/R) \approx 100$ p.p.t. We therefore measure the voltage on the P_3 electrode using a precision voltmeter while changing the biasing voltage of the axial varactor. From those measurements, we can constrain the offset voltage on P_3 due to the varactor biasing to $< 2\,\mu$V and any varactor related frequency ratio shift to $< 1 \times 10^{-13}$, which is about a factor of 100 below the statistical precision reached in the experiment.

8.11.10. Lineshape and fit residuals

In order to understand the inconsistency in $\Delta\nu_{z,S}$ discussed in Sec. 8.11.8, a re-evaluation of the measured data was carried out. Here, a non-white component in the fit residuals of the axial and sideband spectrum fits was discovered. This leads to a shift of the measured axial frequency, depending on the relative position of the particle with respect to the resonator center, which has yet to be understood. In order to constrain how these additional shifts $\Delta\nu_P$ affect the measured cyclotron frequency ratio, fit residuals of all involved measured frequencies need to be considered and the transfer function $f(\nu_k)$ is

evaluated, with k denoting the measurement index. $f(\nu_k)$ is given by

$$\begin{aligned} f(\nu_k) = &(\Delta\nu_{l,\bar{p},P}(\nu_{\mathrm{res},\bar{p}}) + \Delta\nu_{r,\bar{p},P}(\nu_{\mathrm{res},\bar{p}}) - \Delta\nu_{z,\bar{p},P}(\nu_{z,\bar{p}})) \\ &- (\Delta\nu_{l,\mathrm{H}^-}, P(\nu_{\mathrm{res},\mathrm{H}^-}) + \Delta\nu_{r,\mathrm{H}^-,P}(\nu_{\mathrm{res},\mathrm{H}^-}) - \Delta\nu_{z,\mathrm{H}^-,P}(\nu_{z,\mathrm{H}^-})), \end{aligned} \tag{8.50}$$

where $\Delta\nu_{(l,r,z),\bar{p},P}(\nu_{\mathrm{res},\bar{p}})$ are the pulling shifts for the antiproton and $\Delta\nu_{(l,r,z),\mathrm{H}^-,P}(\nu_{\mathrm{res},\mathrm{H}^-})$ for the hydride ion. $f(\nu_k)$ is shown in Fig. 8.20 as a function of the hydride to antiproton resonator difference. The blue scatter point are function values $f(\nu_k)$ extracted from the data, the red line is a polynomial fit $p_P(\nu_{\mathrm{res},\mathrm{H}^-} - \nu_{\mathrm{res},\bar{p}})$. The vertical green line at $-348.5\,\mathrm{Hz}$ indicates the resonant condition, the vertical black line the integral detuning over the experiment. The horizontal line represents the integral of the scaling function over all available data points. By applying the same evaluation solely to ν_{z,H^-} and $\nu_{z,\bar{p}}$

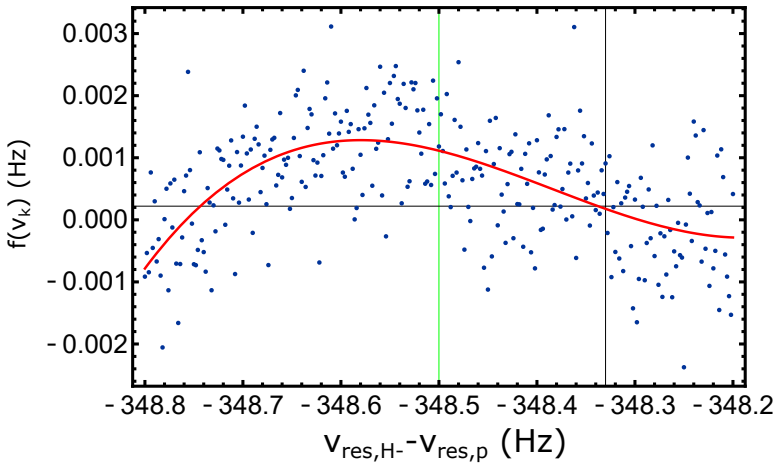

Figure 8.20.: Effect of resonator pulling in the charge-to-mass ratio. The scaling function $f(\nu_k)$ as defined in Eq. 8.50 is plotted as a function of the particle-to-resonator. The fit residuals contribute the dominant systematic uncertainty to the error budget.

data, the integral over the data set reproduces the observed axial frequency shift $\nu_{z,S}$, which is however compensated in the integral over the data set and all involved frequencies. Additional work is required to understand this inconsistency, at the moment the fitting algorithm is critically refined[1]. Although not understood in all aspects at the-

[1]This thesis was handed in on November 30th, 2020. Until submission of a corresponding manuscript by the BASE collaboration, substantial improvements in the quantitative understanding of this effect have been made, which will be described in the manuscript.

sis submission, a correction of the effect is possible based on integrating the data over the scaling function $p_P(\nu_{\mathrm{res},\mathrm{H}^-} - \nu_{\mathrm{res},\bar{p}})$. This imposes an additional systematic uncertainty that is defined by the fit residuals of $p_P(\nu_{\mathrm{res},\mathrm{H}^-} - \nu_{\mathrm{res},\bar{p}})$, the related ratio shift is $\Delta R/R = 7.41\,\mathrm{p.p.t.}$ with an uncertainty of $\Delta\nu_{LS} = 26.94\,\mathrm{p.p.t.}$, which is the dominant systematic uncertainty of the measurement.

8.11.11. Summary of considered effects

In the chapters above, we have presented a measurement of the antiproton-to-hydride charge-to-mass ratio and discussed the systematic contributions that have been investigated so far, all shifts are summarized in the table shown in Tab. 8.2. While trap intrinsic systematic shifts are well under control and cancel out in the frequency ratio, the dominant uncertainty of the trap intrinsic shift is due to the interaction of the axial mode of the particles with the residual magnetic bottle of $B_2 = -0.0894(6)\,\mathrm{T/m^2}$. The dominant current systematic uncertainty arises from a line shape correction which has yet to be understood, but which has been characterized phenomenologically (Sec. 8.11.10). The imposed uncertainty is at a level of 26.94 p.p.t., which is accounted to the error budget. In addition, frequency shifts imposed by varactor tuning were constrained to $< 2\,\mu\mathrm{V}$ and B_1 related systematic shifts of the frequency ratio were constrained to $\Delta R/R < 10^{-13}$. Considering the statistical antiproton-to-hydride charge-to-mass ratio that is extracted from the polynomial fitting approach, this leads to the preliminary value

$$R_{\mathrm{exp}} = 1.001\,089\,218\,768(19)_{\mathrm{stat}}(28)_{\mathrm{sys}}. \tag{8.51}$$

Thanks to the improvements developed by the BASE team, and within the work described in this thesis, the statistical uncertainty of the measurement improves that of the previous measurement by a factor of 3. The result shows a total measurement uncertainty of 34 p.p.t. and improves the previous value [39] by about a factor of two.

Effect	Frequency Ratio Shift (p.p.t.)	Uncertainty (p.p.t.)
$R_{\text{exp, stat}}$	1.001 089 218 772	19
B_1	0	0
B_2	4	5
C_4	0	1
C_6	0	0
Image Charge	0	0
Relativistic	1	1
Trap Angle	0	0
T4/T6 - Drift Offset	-5	5
Clock Offset	-3	1
Lineshape	7	27
B_1-Drift Offset	0	0
Varactor Offset	0	0
Systematic shift	4	28
$R_{\text{exp, corrected}}$	1.001 089 218 768	34

Table 8.2.: Summary of considered systematic shifts. The dominant trap uncertainty comes from the interaction of the particle's axial mode with the magnetic bottle of the trap. The dominant systematic contribution of the measurement campaign comes from line shape uncertainties that were phenomenologically characterized. Quantities other than the frequency ratio are expressed in terms of p.p.t.

8.12. From the hydride charge-to-mass ratio to the proton charge-to-mass ratio

This chapter describes a measurement of the proton-to-antiproton charge-to-mass ratio. However, so far only comparisons of the antiproton with the negatively charged hydrogen ion, the hydride ion H^-, have been discussed. To use hydride as a proxy for the proton has been firstly reported by Gabrielse and collaborators in 1999 [152]. The cyclotron frequency of the proton can be calculated from the hydride cyclotron frequency based on quantum electrodynamics with a precision of $0.02 \times \sqrt{2}$ p.p.t. Comparing protons and antiprotons directly would require to invert the potential depending on the ion species, which would lead to systematic trap shifts for instance due to parasitic potential patches on the trap electrodes that would displace the ions alongside the residual magnetic field gradient B_1. The resulting effects would be orders of magnitude larger compared to the precision of the proton-to-hydride conversion (see also [153, 151]).
The hydride ion mass is related to the proton mass by

$$m_{\mathrm{H}^-} = m_p \left(1 + 2\frac{m_e}{m_p} - \frac{B_e}{m_p} - \frac{A_e}{m_p} + \frac{\alpha_{\mathrm{pol,H}^-} B_0^2}{m_p}\right), \tag{8.52}$$

where m_e/m_p is the electron-to-proton mass ratio, B_e/m_p is the binding energy of the electron in hydrogen, A_e/m_p is the affinity energy of the second electron in the electron singlet and $\alpha_{\mathrm{pol,H}^-}$ the polarizability of the hydride ion.
The leading contribution is due to the two additional electrons bound to the system. The electron-to-proton mass ratio is of fundamental interest in physics and has therefore been measured by many different groups. A weighted mean from Penning trap measurements [159, 171], vibrational spectroscopy [172] and HD^+ rotational spectroscopy [173] yields

$$2\frac{m_e}{m_p} = 0.001\,089\,234\,042\,99(2), \tag{8.53}$$

its uncertainty being two orders of magnitude below the statistical uncertainty reached in our measurement.
For the binding energy of the electron in hydrogen B_e/m_p, we rely on the most recent updates of the NIST atomic spectra database [174]. The value is derived from precision hydrogen spectroscopy results [175] and bound state QED calculations [176] that

contribute to the mass to the hydrogen ion

$$-\frac{B_e}{m_p} = -0.000\,000\,014\,493\,06. \tag{8.54}$$

The uncertainty of B_e/m_p is on the 10^{-20}-level, which contributes negligibly to the m_{H^-}/m_p uncertainty.
To our knowledge, the best value for the electron affinity energy relies on Doppler-free threshold photodetachment spectroscopy using counter-propagating laser beams performed by Lykke and Lineberger [177]. They derive an affinity energy of $A_e = -0.754\,195(19)\,\mathrm{eV}$ that contributes to the H^--mass

$$-\frac{A_e}{m_p} = -0.000\,000\,000\,803\,81(2). \tag{8.55}$$

In addition to these static shifts, in a Penning trap a dynamical polarizability shift [178] adds up, which was first discovered by the Pritchard group at MIT in context of $\mathrm{N}_2^+/\mathrm{CO}^+$ mass comparisons and tests of special relativity [179]. The H^--ion oscillates in the magnetic field of the trap with velocity $\vec{v}$ pendicular to the magnetic field. In the particle's rest frame, this looks like a motional electric field $\vec{E} = \vec{v} \times \vec{B}$, which induces a dynamical dipole moment $\vec{d} = \alpha_{\mathrm{pol,H}^-}\vec{E}$. The orientation of the induced dipole adiabatically follows the motional electric field. This gives rise to a net additional Lorentzforce, which can be accounted to a dynamical mass which reduces the cyclotron frequency of the polarizable ion as

$$\frac{\Delta\nu_c}{\nu_c} = -\alpha_{\mathrm{pol,H}^-}\frac{B^2}{m_p}. \tag{8.56}$$

With the dipole polarizability $\alpha_{\mathrm{H}^-} = 0.34 \times 10^{-38}\,\mathrm{Cm}^2/\mathrm{V}$ [180, 178, 181] and the BASE magnetic field of $B_0 = 1.944\,846\,\mathrm{T}$, this amounts to an antiproton-to-H^- cyclotron frequency ratio shift of

$$\alpha_{\mathrm{H}^-}\frac{B^2}{m_p} = 7.689(18)\,\mathrm{p.p.t.} \tag{8.57}$$

Taking all the corrections together, the proton-to-hydride cyclotron frequency ratio is given as

$$R_{p,\mathrm{H}^-} = 1.001\,089\,218\,753\,80(3). \tag{8.58}$$

The antiproton-to-hydride cyclotron frequency ratio determined in this chapter is

$$R_{\bar{p},\mathrm{H}^-,\mathrm{exp}} = 1.001\,089\,218\,768(34). \tag{8.59}$$

Our experimental result $R_{\bar{p},\mathrm{H}^-,\mathrm{exp}}$ on the antiproton-to-hydride charge-to-mass ratio is in agreement with the proton-to-hydride charge-to-mass ratio $R_{\bar{p},\mathrm{H}^-,\mathrm{exp}}$ and thus supports CPT invariance at two-fold improved precision compared to the previous result [39].

8.13. Summary and discussion

The result presented here is part of a long term study that investigates the proton-to-antiproton charge-to-mass ratio, with the goal to provide a final frequency ratio with improved resolution and based on different measurement methods. A complementary part of the study, which contains additional sideband measurements and a peak-based measurement method, will be presented of the PhD thesis work of James Brydges-Harrington [52]. The currently assigned systematic uncertainty is due the physics of an observed and phenomenologically characterized axial frequency shift that has yet to be understood (Sec. 8.11.10). The related analysis of spectrum residuals that is required to further understand the effect is currently under investigation. Once all aspect of the observed shift are under control, the shift can be corrected with the potential to reduce the uncertainty from the currently dominant shift to its uncertainty, which has the potential to provide a measurement with an uncertainty of 24 p.p.t.

Compared to earlier work, in the presented measurement campaign the principal limits of the sideband method were reached, which corresponds to a stability improvement of the apparatus by a factor of three. This is directly reflected in the three-fold improved statistical uncertainty achieved within this measurement.

At the currently quoted uncertainty, and given that the result is consistent with CPT invariance, our measurement constrains the coefficient R_{H^-} of the Standard Model extension, which discusses possible CPT violating effects in the context of quantum elec-

trodynamics [41], to a level of $R_{\mathrm{H}^-} < 4.29 \times 10^{-27}$ GeV. This constitutes one of the most stringent direct tests of CPT-invariance in the baryon sector. This improves the previous best result [39] by about a factor of two, and constitutes one of the most stringent direct tests of CPT-invariance in the baryon sector.

Very recently [182], an additional non-minimal extension of the SME, discussing CPT and Lorentz violating operators of mass dimensions up to six, was applied to Penning-trap experiments comparing charge-to-mass ratios between particles and antiparticles. This extension is represented by an effective Lagrangian

$$L_{\mathrm{SME}} = L_0 + \frac{1}{2}\bar{\psi}Q\psi + \mathrm{h.c.} \tag{8.60}$$

where L_0 is the Dirac Largange-density, and h.c. denotes the hermitian conjugate. The operator Q is a general Poincare invariant 4×4 operator that contains Lorentz and CPT violation, which can be expanded in the basis of 16 Dirac matrices that contain a total of 81 interaction coefficients in the sun-centered standard frame [41]. So far 68 of those coefficients have been constrained based on measurements carried out by the TRAP and the BASE collaborations. The result presented here further improves the constraints on 15 of these coefficients, which are summarized in Tab. 8.3.

The result can as well be used to set limits on the weak equivalence principle, as first proposed by Hughes and Holzscheiter [183]. Here we interpret antiprotons and protons (H^-) in Penning traps as antimatter/matter clocks and assume that CPT invariance holds. In absence of any gravitational potential U the cyclotron frequencies $\nu_{c,p}$ and $\nu_{c,\bar{p}}$ of the particles are identical by definition. In presence of a gravitational anomaly α_g for antiprotons, which acts as $\alpha_g U$ on the particle, the antimatter/matter-clocks would experience different gravitational redshifts once moved to the surface of the earth. This would induce a modification of the cyclotron frequency ratio,

$$\frac{\nu_{c,\bar{p}}}{\nu_{c,p}} = \frac{(q/m)_{\bar{p}}}{(q/m)_p}\left(1 + \frac{3U}{c^2}(\alpha_g - 1)\right). \tag{8.61}$$

The choice of the appropriate gravitational reference potential U to set constraints on α_g has been controversially discussed [184]. Following the approach of Hughes [183] and using U of the local galactic supercluster, our measurement constraints

$$(\alpha_g - 1) < 4.2 \times 10^{-7}. \tag{8.62}$$

Coefficient	Previous Limit	Improved Limit
$\tilde{c}_e^{ZZ}$	$< 2.1 \times 10^{-14}$	$< 1.0 \times 10^{-14}$
$\tilde{b}_e^{X(XZ)}$	$< 1.2 \times 10^{-10}$ GeV^{-1}	$< 5.9 \times 10^{-11}$ GeV^{-1}
$\tilde{b}_e^{Y(YZ)}$	$< 1.2 \times 10^{-10}$ GeV^{-1}	$< 5.9 \times 10^{-11}$ GeV^{-1}
$\tilde{b}_e^{ZZZ}$	$< 1.2 \times 10^{-10}$ GeV^{-1}	$< 5.9 \times 10^{-11}$ GeV^{-1}
$\tilde{b'}_e^{X}$	$< 1.1 \times 10^{-16}$ GeV	$< 5.4 \times 10^{-17}$ GeV^{-1}
$\tilde{c}_p^{ZZ}, \tilde{c^*}_p^{ZZ}$	$< 7.9 \times 10^{-11}$	$< 3.9 \times 10^{-11}$
$\tilde{b}_p^{X(XZ)}, \tilde{b^*}_p^{X(XZ)}$	$< 2.4 \times 10^{-10}$ GeV^{-1}	$< 1.2 \times 10^{-10}$ GeV^{-1}
$\tilde{b}_p^{Y(YZ)}, \tilde{b^*}_p^{Y(YZ)}$	$< 2.4 \times 10^{-10}$ GeV^{-1}	$< 1.2 \times 10^{-10}$ GeV^{-1}
$\tilde{b}_p^{ZZZ}, \tilde{b^*}_p^{ZZZ}$	$< 2.4 \times 10^{-10}$ GeV^{-1}	$< 1.2 \times 10^{-10}$ GeV^{-1}
$\tilde{b'}_p^{ZZZ}, \tilde{b'^*}_p^{ZZZ}$	$< 7.2 \times 10^{-10}$ GeV	$< 3.5 \times 10^{-10}$ GeV

Table 8.3.: Summary of previous limits on non-minimal coefficients of the SME (second column) and limits improved by the measurement presented here. The treatment here is based on [182]. The previous best limits are all based on the experimental results presented in [39].

This limit is by four orders of magnitude more stringent than experimental goals of experiments like AEgIS [185], ALPHA-g [186] and GBAR [187], which plan to test the weak equivalence principle based on dropping antihydrogen in the gravitational field of the earth. Note however, that those experiments will lead to entirely model-independent results that are free of assumptions on the very nature of gravity.
Strictly speaking, the interpretation following [183] does also not exclude a local compensation of the simultaneous violation of the weak equivalence principle and CPT invariance exactly on the trajectory of the earth on its orbit around the sun. To the author's knowledge, no clear physical reason is known why the terrestrial inertial system would constitute such a distinguished reference frame.

9 | Phase sensitive measurements

Phase sensitive measurement methods have enabled several of the most precise measurements performed in Penning traps, such as the cyclotron frequency ratio between CO^+ and N_2^+ with a fractional precision of 400 p.p.t. in 1989 [55], which was the first application of phase sensitive methods in a Penning trap. The measurement of the mass ratio between $^{16}N^{2+}$ and $^{13}C_2H_2{}^+$ with a fractional precision of only 7 p.p.t. in 2003 [188] stands as the most precise Penning trap mass measurement since many years. Using the newly developed PnA technique [56], the most precise measurement of the proton mass with a fractional precision of 32 p.p.t. was conducted in 2017. The recent measurement of the HD^+ mass with a fractional uncertainty of 14 p.p.t. in 2020 [171] yielded also the proton mass with an uncertainty of 17 p.p.t. and the deuteron mass with an uncertainty of 8 p.p.t. and provided crucial input for resolving inconsistencies in mass measurements of light ions.

Due to the CERN long shutdown 2 (LS2), which took place in 2019 and 2020, no antiproton experiments were possible during the phase methods run. Instead, the focus of this run was to investigate phase sensitive methods for frequency measurements. The experiment was assembled on June 20th 2019, the first trapped particles in the precision trap were observed on June 27th, with the end of the run envisioned for Christmas 2019. In about six months, we characterized classical Rabi oscillations in our trap and implemented the "pulse and probe" scheme ("PnP") [55, 54] and "pulse and amplify" scheme ("PnA") [56] for phase sensitive detection of the cyclotron motion. During the time of this experimental campaign, the Antiproton Decelerator was not being operated, and no antiproton measurements were carried out at the neighboring collaborations. As a result, the magnetic field noise in the experiment surroundings was exceptionally low compared to the usual conditions during AD beam times. This allowed us to operate the experiment with a quenched self shielding coil system that otherwise increases the

cyclotron frequency scatter when active (compare Sec. 7.2.3). Enabled by the technical improvements outlined in Sec. 3.2, we reached a cyclotron frequency scatter of about 280(20) p.p.t.
This chapter is structured as follows: In Sec. 9.1, the trap parameters important for the application of phase methods are discussed, Sec. 9.2 reviews the principles of mode coupling in a Penning trap, and the experimental setup is outlined in Sec. 9.3. In Sec. 9.4, classical Rabi oscillations are shortly discussed, while in Sec. 9.5, the concept of frequency measurements by means of phase unwrapping is introduced. The limitations of phase measurements in the BASE apparatus are in investigated in Sec. 9.6, where the principal phase scatter is investigated, and in Sec. 9.7, where the phase scatter as a function of evolution time is discussed. Finally, Sec. 9.8 presents the experimental results on the frequency stability and resolution measured by means of phase methods.

9.1. Trap optimization

Phase sensitive measurement methods rely, in a nutshell, on exciting the cyclotron motion and subsequently imprinting the cyclotron phase onto the axial motion via radiofrequency pulses. The axial motion gets excited during the coupling process. After coupling, the phase of the excited axial motion is read out, which yields the initial cyclotron phase. The particle oscillation frequencies are affected by the trap inhomogeneity parameters such as the parameter C_4, C_6 and B_2 that induce energy-dependent frequency shifts. In order to optimize phase methods and to understand their limitations, it is of crucial importance to carefully characterize and tune these parameters. Some of these parameters are highly affected by small variations in the trap stack setup (for instance, if the order of the sapphire spacer rings is changed), while others depend on the position of trap inside the magnet, which slightly varies from run to run. In addition, parasitic voltage patches can build up on the trap electrodes surfaces, which also change during antiproton loading. As a result, the above listed trap parameters have to be carefully characterized for each experimental run separately. A more complete overview about Penning trap optimization is provided in Chap. 7, which is why this section will focus on aspects that are especially important for phase methods.

9.1.1. Tuning ratio scans

To determine the ideal tuning ratio $\mathrm{TR}_{\mathrm{opt}}$ at which the C_4 coefficient vanishes, the axial dip SNR is measured for different tuning ratios. One such tuning ratio scan is shown in Fig. 9.1. As described in detail in Sec. 7.1.1, it is possible to determine $\mathrm{TR}_{\mathrm{opt}}$ by fitting these data. We recall Eq. 2.16 and write $C_4 = D_4 \times \mathrm{TR} + E_4$, with $D_4 = 1.28(4) \times 10^9\,1/\mathrm{m}^4$ given by potential theory. Considering all tuning ratio scans conducted during the phase methods campaign, an ideal tuning ratio $\mathrm{TR}_{\mathrm{opt}} = 0.875\,105(10)$ is obtained for the trap configuration, where the shuttling electrodes T4 and T6 are set to 0 Volts. When

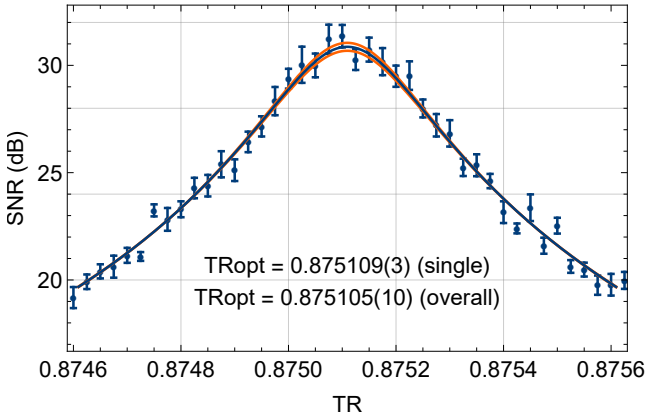

Figure 9.1.: Tuning ratio scan taken during the phase run with the park electrode voltages $V_{\mathrm{T6}} = V_{\mathrm{T4}} = 0\,\mathrm{V}$. Results of an individual tuning ratio scan, the fitted SNR as a function of the tuning ratio is shown. From performing least-squares fit relying on the model introduced in Sec. 7.1.1, an optimal tuning ratio $\mathrm{TR}_{\mathrm{opt}} = 0.875\,109(3)$ is obtained. When considering all tuning ratio scans that have been conducted throughout the phase methods run, an overall value of $\mathrm{TR}_{\mathrm{opt}} = 0.875\,105(10)$ is obtained for the non-shuttling configuration, and $\mathrm{TR}_{\mathrm{opt}} = 0.875\,949(10)$ for the shuttling configuration ($V_{\mathrm{T6}} = V_{\mathrm{T4}} = -13.5\,\mathrm{V}$).

shuttling measurements are performed, these electrodes are set to -13.5 Volts, which is referred to as "shuttling configuration". For the shuttling configuration, an ideal tuning ratio of $\mathrm{TR}_{\mathrm{opt}} = 0.875\,949(10)$ is measured, when the results of all TR scans taken over the phase run are combined together. This shift of $\mathrm{TR}_{\mathrm{opt}}$ for the shuttling configuration is in good agreement with trap theory. By inserting these values into Eq. 2.16, the respective C_4 values for each tuning ratio can be determined.

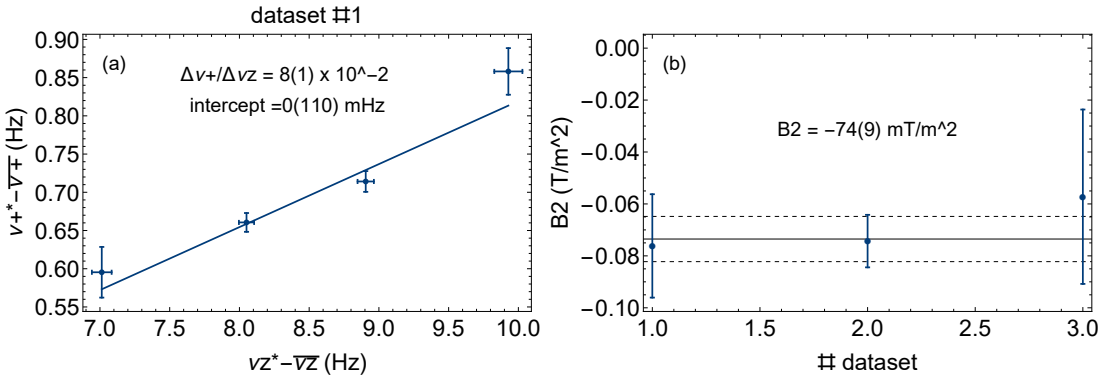

Figure 9.2.: Summary of B_2 measurements during the phase run, following the principle laid out in Sec. 7.2.3. Left: Explicit measurement of the slope $\Delta\nu_+/\Delta\nu_z$. Both frequency shifts depend linearly on the cyclotron energy, the slope is related to the trap parameters C_4 and B_2 and to the well-known effect of special relativity. Right: Inserting the C_4 values that are known from the tuning ratio scan determination in Sec. 9.1.1, absolute values for B_2 are extracted. The weighted mean of the three individual measurements yields $B_2 = -74(9)\,\mathrm{mT/m^2}$.

9.1.2. B_2 determination

The residual magnetic field inhomogeneity B_2 is determined by measuring the cyclotron frequency at different energies as also outlined in Sec. 7.2.3. The cyclotron frequency in thermal equilibrium with the detection system ($E_+/k_B = T_z \times \sqrt{\nu_+/\nu_z}$) is measured by means of the sideband method as described in Sec. 2.5 [54]. The cyclotron frequency ν_+^* when the cyclotron motion is excited ($E_+/k_B \gg T_z \times \sqrt{\nu_+/\nu_z}$) is measured by means of the peak method [152], as discussed in Sec. 7.2. After each peak measurement, the cyclotron mode is first cooled back to thermal equilibrium and afterwards measured again by means of sideband methods. Fig. 9.2 (a) shows a plot of the cyclotron frequency shift $\Delta\nu+$ compared to the axial frequency shift $\Delta\nu_z$, where different values of $\Delta\nu_z$ corresponding to different excitation energies E_+. A linear scaling of the frequency shifts $\Delta\nu_{z,+}$ as a function of cyclotron energy is observed. Its slope is given by:

$$\frac{\Delta\nu_+/\nu_+}{\Delta\nu_z/\nu_z} = \frac{\left(-\frac{1}{mc^2} + \frac{3}{4}\frac{1}{qV_r}\frac{C_4}{C_2^2}\left(\frac{\nu_z}{\nu_+}\right)^4 - \frac{1}{m(2\pi\nu_+)^2}\frac{B_2}{B_0}\right)E_+}{\left(-\frac{1}{2mc^2} - \frac{3}{2}\frac{1}{qV_r}\frac{C_4}{C_2^2}\left(\frac{\nu_z}{\nu_+}\right)^2 + \frac{1}{m(2\pi\nu_z)^2}\frac{B_2}{B_0}\right)E_+}. \tag{9.1}$$

This expression allows us to determine B_2 from the slope $\Delta\nu_+/\Delta\nu_z$ for given values of C_4, as discussed in Sec. 7.2.3 and Eq. 7.44 in greater detail. Three measurements

of B_2 are plotted in Fig. 9.2 (b). The respective slopes vary by more than a factor of 2 between these measurements, but the measured B_2 values are consistent and give a weighted mean value of $B_2 = -74(9)\,\mathrm{mT/m^2}$ over the phase run. Compared to the B_2 determined in other runs, our value of B_2 shows a comparably large uncertainty, which is partially due to the low Q-factor of the cyclotron detector in this run (Q $\approx$ 50).

9.1.3. Energy calibration

When B_2 and C_4 are known, the cyclotron energy can be calibrated by considering the axial frequency shifts $\Delta\nu_z$,

$$\frac{\Delta\nu_z}{\nu_z} = \left(-\frac{1}{2mc^2} - \frac{3}{2}\frac{1}{qV_r}\frac{C_4}{C_2^2}\left(\frac{\nu_z}{\nu_+}\right)^2 + \frac{1}{m\left(2\pi\nu_z\right)^2}\frac{B_2}{B_0}\right)E_+. \tag{9.2}$$

To this end, the particle's cyclotron frequency is excited by applying a radio frequency pulse close to the cyclotron frequency, $\omega_{\mathrm{rf}} \approx \omega_+$. The axial frequency ν_z^* at excited cyclotron motion is measured, afterwards the particle is sideband cooled back to $T_+ = T_z \times \omega_+/\omega_z$, and a reference spectrum is taken, $\Delta\nu_z = \overline{\nu_{z,\mathrm{ref}}} - \nu_z^*$. Considering the dynamics of a driven harmonic oscillator (Section 7.2.1), the cyclotron radius ρ_+ increases linearly with excitation time t_{exc}, which is why cyclotron energy E_+ and axial frequency shift $\Delta\nu_z$ increase quadratically with t_{exc}, $\Delta\nu_z \propto t_{\mathrm{exc}}^2$ and $E_+ \propto t_{\mathrm{exc}}^2$. This is shown in Fig. 9.3 (a), where the axial frequency shift is plotted against the number of burst cycles for two different tuning ratios. The excitation time t_{exc} can be expressed in terms of the number of burst cycles N_{brst} included in the drive, $t_{\mathrm{exc}} = N_{\mathrm{brst}} \times 1/\nu_+$:

$$\Delta\nu_z = A \times N_{\mathrm{brst}}^2. \tag{9.3}$$

The values of A are determined by fitting a quadratic curve to axial frequency shifts as shown in Fig. 9.3 (a), where also measured values of A are listed. Equation 9.2 is then rewritten to:

$$E_+(B_2, C_4, N_{\mathrm{brst}}) = \frac{A \times N_{\mathrm{brst}}^2}{\nu_z} \times \left(-\frac{1}{2mc^2} - \frac{3}{2}\frac{1}{qV_r}\frac{C_4}{C_2^2}\left(\frac{\omega_z}{\omega_+}\right)^2 + \frac{1}{m\omega_z^2}\frac{B_2}{B_0}\right)^{-1}. \tag{9.4}$$

While the axial shift scaling A depends on C_4 and thus on the tuning ratio, the energy scaling agrees for different tuning ratios (see Fig. 9.3 (b)), which confirms our model.

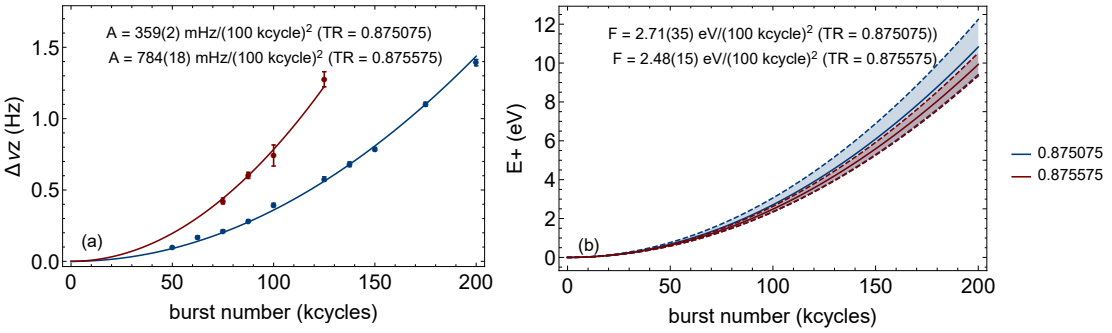

Figure 9.3.: Calibration of axial frequency shift $\Delta\nu_z$ (left) and cyclotron energy E_+ (right) as a function of excitation time t_{exc} expressed in terms of the number of burst cycles N_{brst} used to excite the particle's cyclotron motion, $t_{\mathrm{exc}} = N_{\mathrm{brst}} \times 1/\nu_+$. While the axial frequency shifts $\Delta\nu_z$ depend on the tuning ratio, the energy shifts for both tuning ratios TR are in good agreement with each other.

We rewrite the cyclotron energy,

$$E_+ = F \times N_{\mathrm{brst}}^2, \tag{9.5}$$

with the newly introduced coefficient F. From Fig. 9.3 (b), we obtain a scaling of $2.52(14)\,\mathrm{eV}/\left(100\,\mathrm{kcycles}\right)^2$ as weighted mean at a drive power of -25 dBm, which corresponds to

$$F = 0.25(1)\,\mathrm{meV/kcycles}^2. \tag{9.6}$$

Normalized to the drive power P, the corresponding coefficient $F_V = F/P$ is given by

$$F_V = 80(4)\,\mathrm{meV}/\left(\mathrm{kcycles}^2 \times \mathrm{mW}\right). \tag{9.7}$$

9.1.4. B_2 determination by considering axial frequency shifts at different tuning ratios

Instead of using C_4, B_2 and A to determine F, as done in the previous section, we can recognize that F should be independent of C_4, B_2 and A and use the measured values of C_4 and F to determine B_2. To this end, we recall that the axial shift $\Delta\nu_z$ is given by

$$\Delta\nu_z(C_4, B_2, F, N_{\mathrm{brst}}) = \nu_z \left(-\frac{1}{2mc^2} - \frac{3}{2}\frac{1}{qV_r}\frac{C_4}{C_2^2}\left(\frac{\omega_z}{\omega_+}\right)^2 + \frac{1}{m\omega_z^2}\frac{B_2}{B_0} \right) F \times N_{\mathrm{brst}}^2. \tag{9.8}$$

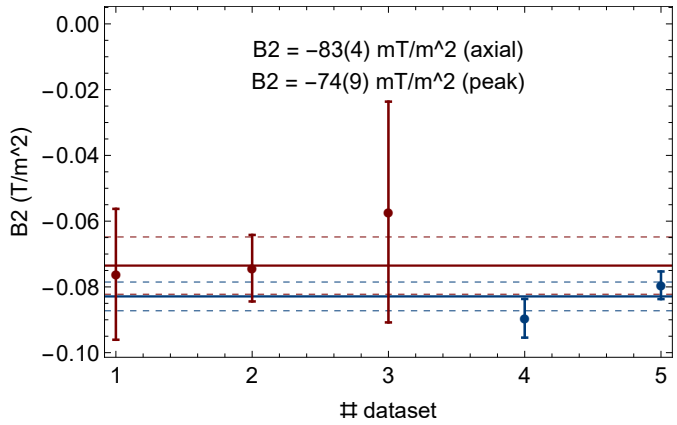

Figure 9.4.: Comparing the peak and the axial method for measuring B_2. The blue points correspond to the two axial B_2 measurements we conducted, with the weighted mean denoted by the blue grid lines. The red grid lines show the B_2 value derived by means of the peak method, which is depicted for comparison. In both cases, the solid line indicates the weighted mean value and the dashed lines the uncertainty. Both values agree with each other within their respective uncertainties. The numbers assigned to the datasets do not indicate a temporal order.

Using Eq. 9.3, we obtain

$$A(C_4, B_2) \times N_{\mathrm{brst}}^2 = \nu_z \left(-\frac{1}{2mc^2} - \frac{3}{2}\frac{1}{qV_r}\frac{C_4}{C_2^2}\left(\frac{\omega_z}{\omega_+}\right)^2 + \frac{1}{m\omega_z^2}\frac{B_2}{B_0} \right) F \times N_{\mathrm{brst}}^2, \tag{9.9}$$

which brings us to

$$F = A(C_4, B_2) \times \left(-\frac{1}{2mc^2} - \frac{3}{2}\frac{1}{qV_r}\frac{C_4}{C_2^2}\left(\frac{\omega_z}{\omega_+}\right)^2 + \frac{1}{m\omega_z^2}\frac{B_2}{B_0} \right)^{-1} 1/\nu_z. \tag{9.10}$$

We now assume that F is insensitive to C_4 and B_2,

$$\frac{\mathrm{d}F}{\mathrm{d}C_4} = \frac{\mathrm{d}F}{\mathrm{d}B_2} = 0. \tag{9.11}$$

This is equivalent to assuming that the particle is excited to the same energy for identical excitation times t_{exc} at different tuning ratios, which is suggested by Fig. 9.3. With measured values for $A_i = A(C_{4,i}, B_2)$ recorded at two different values $C_{4,1}, C_{4,2}$, we write

$$F(C_{4,1}, B_2) \stackrel{!}{=} F(C_{4,1}, B_2) \Leftrightarrow A_1 \times (...)^{-1} \stackrel{!}{=} A_2 \times (...)^{-1} \tag{9.12}$$

This equation is transformed into an explicit expression for B_2,

$$B_2 = 2B_0\pi^2\nu_z^2\left(\frac{1}{c^2} + \frac{3\left(C_{4,2}A_1 - C_{4,1}A_2\right)m\nu_z^2}{C_2^2(A_1 - A_2)qV_r\nu_+^2}\right). \tag{9.13}$$

We obtain $B_2 = -83(4)\,\mathrm{mT/m^2}$ as a weighted mean from two distinct energy calibration measurements at different tuning ratios, both individual values are depicted in Fig. 9.4. This result is in agreement with the result determined in Sec. 9.1.2 using the peak method, $B_2 = -74(9)\,\mathrm{mT/m^2}$. Combining both results yields a weighted mean of $B_2 = -82(4)\,\mathrm{mT/m^2}$. As this novel method was only discovered after the run was completed, no set of dedicated measurements has been performed to check the limits of this method. However, it should be easily possible to reach a precision of a few percent or even better, especially when curves are recorded for more than two tuning ratios. A big advantage of this method compared to the peak method commonly used in our experiment is that this method is insensitive to magnetic field fluctuations, unlike methods that rely on direct cyclotron frequency measurements for determining B_2. The method also allows to obtain high resolution B_2 data in traps where no cyclotron detector is connected.

9.1.5. Magnetron burst measurements

The concept of magnetron burst measurements, where the magnetron mode is excited with distinct energies and for different tuning ratios and axial frequency shifts $\Delta\nu_z$ are subsequently analyzed, has been introduced in Sec. 7.1.3 in detail. Only the calculations on the higher order coefficients C_6 and C_8 will be recapitulated in this section, while the considerations on C_4 are subject of Sec. 7.1.3.

The results of a magnetron burst measurement performed during the phase methods run for the non-shuttling configuration (voltage of 0 Volts applied to the T4- and T6-electrode) are depicted in Fig. 9.5 (a). The trap parameters C_6 and C_8 cause axial frequency shifts proportional to ρ_-^4 and ρ_-^6, as specified in the perturbation matrix discussed in Sec. 2.2.1:

$$\begin{aligned} C_6 &= \frac{16}{15}\frac{\Delta\nu_z}{\nu_z} \times C_2 \times \frac{1}{3\rho_-^4}, \\ C_8 &= -\frac{32}{35}\frac{\Delta\nu_z}{\nu_z} \times C_2 \times \frac{1}{4\rho_-^6}. \end{aligned} \tag{9.14}$$

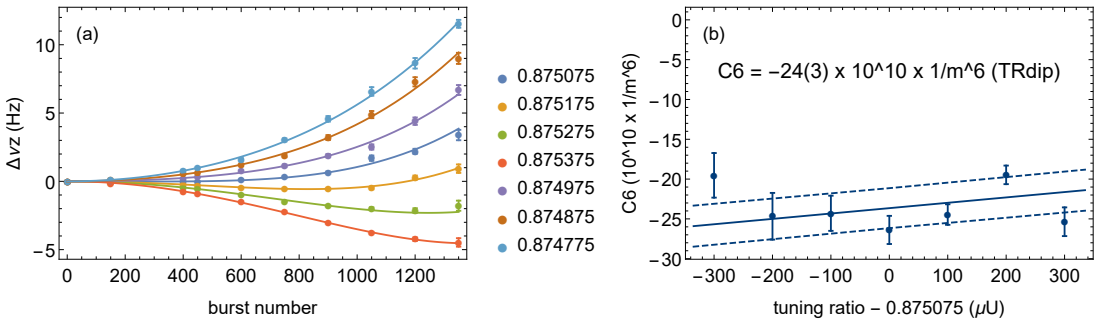

Figure 9.5.: Magnetron burst measurement conducted during the phase run. Left: Axial frequency shifts as a function magnetron burst number for various tuning ratios denoted in the legend. The depicted frequency shifts were already corrected for the effect of $C_8 = 4.0{\times}10^{17}\,1/\mathrm{m}^8$. Right: Determined C_6 coefficients based on the $\propto \rho_-^4$-scaling of the axial frequency shifts depicted in (a). The solid line represents a linear fit to the data inserting the D_6 value known from potential theory, $D_6 = \mathrm{d}C_6/(\mathrm{dTR}) = 6.7(2) \times 10^{13} \times 1/\mathrm{m}^6$. The dashed lines denote the fit uncertainties. $C_6 = -24(3) \times 10^{10}\,1/\mathrm{m}^6$ is obtained for the tuning ratio $\mathrm{TR}_{\mathrm{dip}} = 0.875\,075$, at which the dip measurements during the phase methods run were usually conducted.

The magnetron radius ρ_- is computed from Eq. 7.12, $\rho_- = \alpha \times N \times \sqrt{P}$ with the burst number N, the burst power P and the geometrical parameter α. α is derived from the quadratic scaling in $\Delta\nu_z$ that is related to the C_4 coefficient. By recording the quadratic scaling of $\Delta\nu_z$ as a function of the tuning ratio TR and recalling $C_4 = D_4 \times \mathrm{TR} + E_4$ (Eq. 2.16), $\alpha = 83.9(4)\,\mu\mathrm{m}/\left(\mathrm{cycle} \times \sqrt{\mathrm{mW}}\right)$ is determined as discussed in Eq. 7.14. $C_8 = 4.0 \times 10^{17}\,1/\mathrm{m}^8$ is a robust parameter that barely changes from experimental campaign to experimental campaign, which is why we correct the measured axial frequency shifts for the effect of C_8. Subsequently, we fit the axial frequency shifts with quartic polynomials (Fig. 9.5 (a)) and obtain individual C_6 values for each tuning ratio, as shown in Fig. 9.5 (b). We then fit the C_6 values as a function of the tuning ratio with the linear scaling expected from trap theory. For the dip tuning ratio $\mathrm{TR}_{\mathrm{dip}} = 0.875\,075$,

$$C_6 = -24(3) \times 10^{10}\,1/\mathrm{m}^6 \Leftrightarrow \Delta\nu_z(E_z) = 6.8(7)\,\mathrm{mHz/meV}^2 \tag{9.15}$$

is obtained. The scaling of C_6 as a function of the tuning ratio TR is given by

$$C_6 = D_6 \times (\mathrm{TR} - \mathrm{TR}_{\mathrm{dip}})\,, \tag{9.16}$$

with $D_6 = 6.7(2) \times 10^{13} \times 1/\mathrm{m}^6$.

9.1.6. Summary of trap parameters during the phase methods run

The most relevant trap parameters for the phase methods run are summarized in Tab. 9.1.

coefficient	size	$\Delta\nu_z(E_z)$
$\mathrm{TR}_{\mathrm{opt}}$	0.875 105(10)	-
$\mathrm{TR}_{\mathrm{dip}}$	0.875 075	-
$\mathrm{TR}_{\mathrm{phase}}$	0.875 575	-
B_2	-82(4) $\mathrm{mT/m^2}$	-
$C_4(\mathrm{TR}_{\mathrm{dip}})$	$38(13) \times 10^3\,1/\mathrm{m}^4$	-75(25) mHz/eV
$C_4(\mathrm{TR}_{\mathrm{phase}})$	$-603(22) \times 10^3\,1/\mathrm{m}^4$	1.17(4) Hz/eV
$C_6(\mathrm{TR}_{\mathrm{dip}})$	$-24(3) \times 10^{10}\,1/\mathrm{m}^6$	$6.8(7)\,\mathrm{mHz/eV^2}$
$C_6(\mathrm{TR}_{\mathrm{phase}})$	$-20(3) \times 10^{10}\,1/\mathrm{m}^6$	$5.8(7)\,\mathrm{mHz/eV^2}$
$C_8(\mathrm{TR}_{\mathrm{dip}})$	$40 \times 10^{16}\,1/\mathrm{m}^8$	$160\,\mathrm{mHz/eV^3}$
$C_8(\mathrm{TR}_{\mathrm{phase}})$	$40 \times 10^{16}\,1/\mathrm{m}^8$	$160\,\mathrm{mHz/eV^3}$

Table 9.1.: Trap parameters measured during the phase run. $\mathrm{TR}_{\mathrm{dip}}$ denotes the tuning ratio at which the dip measurements were performed, $\mathrm{TR}_{\mathrm{phase}}$ denotes the tuning ratio where most phase measurements were conducted. All values are specified for the non-shuttling configuration, which means that the T4- and T6-electrode are set to a voltage of 0 V.

9.2. Mode coupling in a Penning trap

In order to perform phase sensitive measurements of the cyclotron frequency, the cyclotron mode is firstly resonantly excited by a pulse with a well defined phase. The particle is then left to orbit in the cyclotron mode for a certain evolution time t_{evo}, so that its cyclotron phase ϕ_c as a function of time is given by $\phi_c(t) = \phi_{c,0} + \omega_+ \times t_{\mathrm{evo}}$, where $\phi_{c,0}$ is the initial cyclotron phase. By measuring the cyclotron phase, the cyclotron frequency can be inferred. The cyclotron phase is not measured directly, but instead the cyclotron and axial modes are coupled using an appropriate rf pulse, and the cyclotron phase ϕ_c is determined from the axial phase measured after coupling. We now describe theoretically how this pulse achieves a coherent phase transfer.

We start by presenting the description of mode coupling in a Penning trap provided in [54], and expand it in order to allow coupling with the upper sideband as well (the

so-called "pulse and amplify" scheme from [56]). Axial and radial modes are coupled by adding a quadrupolar radio frequency pulse with frequency ω_{rf} and electric field $\vec{E}_{\mathrm{rf}}(t)$ to the normal trapping potential, with $|\vec{E}_{\mathrm{rf}}(t)|$ being small compared to the trapping potential:

$$\vec{E}_{\mathrm{rf}}(t) = \mathrm{Re}\left(\mathcal{E}_{\mathrm{rf}} \exp\left(i\omega_{\mathrm{rf}} t\right)\right)\left(x\vec{e}_z + z\vec{e}_x\right). \tag{9.17}$$

Following the derivation in [54], we treat the cyclotron motion as a one dimensional harmonic oscillator in x. The equations of motion in the rotating wave approximation are given by

$$\begin{aligned} \ddot{x} + \omega_+^2 x &= \frac{q}{m}\mathrm{Re}\left(\mathcal{E}_{\mathrm{rf}} \exp\left(i\omega_{\mathrm{rf}} t\right)\right) z \\ \ddot{z} + \omega_z^2 z &= \frac{q}{m}\mathrm{Re}\left(\mathcal{E}_{\mathrm{rf}} \exp\left(i\omega_{\mathrm{rf}} t\right)\right) x. \end{aligned} \tag{9.18}$$

The guessed solutions are:

$$\begin{aligned} x &= \mathrm{Re}\left(\frac{C(t)}{\sqrt{\pi m \omega_+}} \exp\left(i\omega_+ t\right)\right) \\ z &= \mathrm{Re}\left(\frac{Z(t)}{\sqrt{\pi m \omega_z}} \exp\left(i\omega_{\mathrm{z}} t\right)\right). \end{aligned} \tag{9.19}$$

This decoupling ansatz is appropriate if the dynamics in $C(t)$ and $Z(t)$ are slow compared to ω_+ and ω_z, which is the case in our measurements. We define the parameter V in units of frequency:

$$V = \frac{iq\mathcal{E}_{\mathrm{rf}}}{2m\sqrt{\omega_z \omega_+}}. \tag{9.20}$$

The equations of motion yield a mode coupling when the irradiated radio frequency is close to the sum or the difference frequency between cyclotron and axial, $\omega_{\mathrm{rf}} = \omega_+ \mp \omega_z + \delta$, with the detuning δ being small. The lower sideband is used in the "pulse and phase" (PnP) scheme developed at MIT and published in 1990 [54], the upper sideband is used for the "pulse and amplify" scheme (PnA), which was developed at University of Mainz and published in 2011 [56]. We will first discuss the PnP scheme.

9.2.1. Mode coupling on the lower sideband

In the "pulse and phase" (PnP) scheme, the lower sideband $\omega_{\mathrm{rf}} = \omega_+ - \omega_z$ is used in order to couple the cyclotron and the axial motion. The equations of motion in Eq. 9.18 are

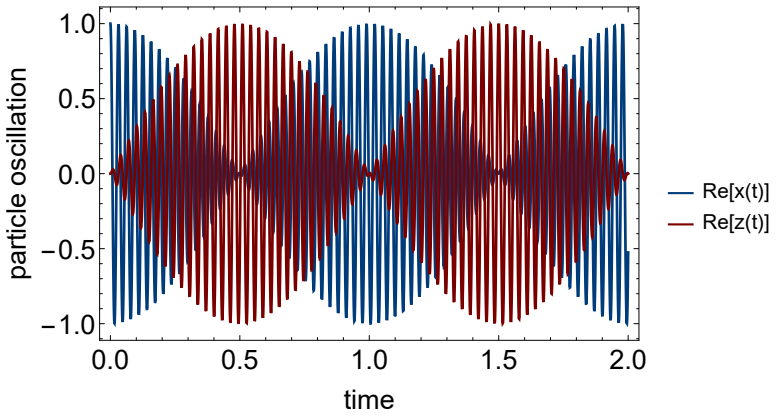

Figure 9.6.: Schematic mode transfer when coupling on the lower sideband $\omega_{\mathrm{rf}} = \omega_+ - \omega_z$ is applied. Oscillation frequencies and amplitudes do not reflect the actual parameters in the BASE experiment.

simplified by neglecting the second derivative of $C(t)$ and $Z(t)$ (adiabatic approximation since the dynamics in $C(t), Z(t)$ is slow compared to the oscillators) and considering only secular terms (rotating wave approximation). We then obtain

$$\dot{C}(t) = -\frac{V}{2}\exp\left(i\delta t\right) Z(t) \qquad \dot{Z}(t) = \frac{V^*}{2} C(t)\exp\left(-i\delta t\right). \tag{9.21}$$

The general solution to Eq. 9.21 for the initial conditions $C(0) = C_0\exp(i\phi_C)$ and $Z(0) = Z_0\exp(i\phi_Z)$ with Z_0 and C_0 being real is given by

$$\begin{aligned} C(t) &= \frac{e^{-it(\Omega'-\delta)/2}\left(C_0 e^{i\phi_C}\left(\Omega' + e^{it\Omega'}\Omega' + \delta - e^{it\Omega'}\delta\right) - Z_0 e^{i\phi_Z}\left(-1 + e^{it\Omega'}\right)\Omega\right)}{2\Omega'} \\ Z(t) &= \frac{e^{-it(\Omega'+\delta)/2}\left(Z_0 e^{i\phi_Z}\left(\Omega' + e^{it\Omega'}\Omega' + e^{it\Omega'}\delta - \delta\right) - C_0 e^{i\phi_C}\left(-1 + e^{it\Omega'}\right)\Omega\right)}{2\Omega'}, \end{aligned} \tag{9.22}$$

with the Rabi frequency $\Omega' = \sqrt{\Omega^2 + \delta^2}$, and the coupling field $|V| = \Omega$ and Ω being real and the resonant Rabi frequency. For resonant drives ($\delta = 0$), the equations above

simplify to

$$\begin{aligned} C(t) &= \frac{1}{2}e^{-i\Omega t/2}\left(C_0 e^{i\phi_C}\left(1+e^{i\Omega t}\right) - Z_0 e^{i\phi_Z}\left(e^{i\Omega t}-1\right)\right) \\ &= C_0 e^{i\phi_C}\cos\left(\Omega t/2\right) - iZ_0 e^{i\phi_Z}\sin\left(\Omega t/2\right) \\ Z(t) &= \frac{1}{2}e^{-i\Omega t/2}\left(Z_0 e^{i\phi_Z}\left(1+e^{i\Omega t}\right) - C_0 e^{i\phi_C}\left(e^{i\Omega t}-1\right)\right) \\ &= Z_0 e^{i\phi_Z}\cos\left(\Omega t/2\right) - iC_0 e^{i\phi_C}\sin\left(\Omega t/2\right). \end{aligned} \tag{9.23}$$

From this relation, the continuous transfer of amplitudes and phase between both modes during coupling can be seen, as also schematically depicted in Fig. 9.6. If a coupling time $t = \pi/\Omega$ is chosen (the "π-pulse condition"), a complete phase transfer is observed,

$$Z(\pi/\Omega) = -iC_0 e^{i\phi_C} \qquad C(\pi/\Omega) = -iZ_0 e^{i\phi_Z} \tag{9.24}$$

Note that the axial term $Z(\pi/\Omega)$ only depends on the initial cyclotron phase ϕ_C and the initial cyclotron term C_0, but not on the initial axial phase ϕ_Z and the initial axial term Z_0, and vice versa for the cyclotron term $C(\pi/\Omega)$.
In this context it is important to note that $Z(t)$ and $C(t)$ are not the respective oscillation amplitudes, but related to the oscillation amplitudes by a factor $\sqrt{\omega_+/\omega_z}$, which is seen by inserting the definitions of $C(t)$ and $Z(t)$ from Eq. 9.19 into Eq. 9.23. The corresponding equations of motion are

$$\begin{aligned} z(t) &= \left(x_0\sqrt{\frac{\omega_+}{\omega_z}}\sin\left(\Omega t/2\right)\sin(\phi_c+\omega_z t) + z_0\cos\left(\Omega t/2\right)\cos(\phi_z+\omega_z t)\right), \\ x(t) &= \left(x_0\cos\left(\Omega t/2\right)\cos\left(\phi_C+\omega_+ t\right) + z_0\sqrt{\frac{\omega_z}{\omega_+}}\sin\left(\Omega t/2\right)\sin\left(\phi_z+\omega_+ t\right)\right). \end{aligned} \tag{9.25}$$

We shall now assume that the coupling drive is turned on from $t = 0$ to $t = t_1 = \pi/\Omega$, and is turned off afterwards. We then obtain

$$\begin{aligned} z(t) &= x_0\sqrt{\frac{\omega_+}{\omega_z}} \times \sin\left(\phi_C+\omega_z t\right), \\ x(t) &= z_0\sqrt{\frac{\omega_z}{\omega_+}} \times \sin\left(\phi_Z+\omega_+ t\right), \end{aligned} \tag{9.26}$$

which describes how the action-exchanging coupling pulse maps the cyclotron and axial phases onto the final amplitudes.

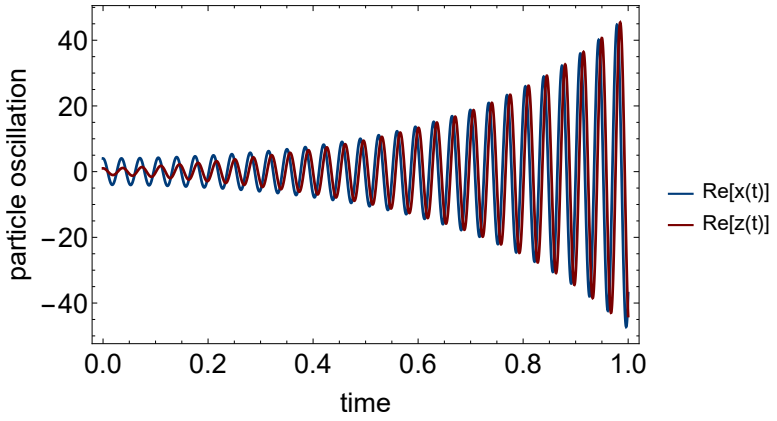

Figure 9.7.: Schematic of the mode coupling on the upper sideband. Oscillation frequencies and amplitudes do not reflect the actual parameters in the BASE experiment.

9.2.2. Mode coupling on the upper sideband

In the "pulse and amplify" (PnA) scheme, the upper sideband $\omega_{\mathrm{rf}} = \omega_+ + \omega_z + \delta$ is used for coupling the cyclotron and the axial motion. The equations of motion in Eq. 9.18 are again simplified by neglecting the second derivative of $C(t)$ and $Z(t)$ and considering only secular terms. We obtain

$$\dot{Z}(t) = -\frac{V}{2}\exp\left(i\delta t\right)C^*(t) \qquad \dot{C^*}(t) = -\frac{V^*}{2}\exp\left(-i\delta t\right)Z(t). \tag{9.27}$$

The solution of these equations for the initial conditions $Z(0) = Z_0\exp(i\phi_Z)$ and $C(0) = C_0\exp(i\phi_C)$, where Z_0, and C_0 are real, is given by

$$\begin{aligned} Z(t) &= \exp(i\phi_Z)Z_0\cosh\left(\Omega t/2\right) - iC_0\exp\left(-i\phi_C\right)\sinh\left(\Omega t/2\right), \\ C(t) &= \exp(i\phi_C)C_0\cosh\left(\Omega t/2\right) - iZ_0\exp\left(-i\phi_Z\right)\sinh\left(\Omega t/2\right). \end{aligned} \tag{9.28}$$

Our solution for $Z(t)$ is the sum of two complex numbers, of which one depends on the initial axial amplitude and phase, and the other depends on the initial cyclotron amplitude and phase. Unlike in PnP, in PnA the terms $Z(t)$ and $C(t)$, proportional to the axial and cyclotron amplitudes respectively, increase hyperbolically with the coupling time t_{coup}, as can be seen in Fig. 9.7, where the real value of $z(t)$ and $x(t)$ are depicted.

When coupling on the lower sideband, the phase and amplitude are fully exchanged

between the cyclotron and the axial modes when performing a π-pulse.This means that for an ideal π-pulse in PnP, the final axial state does not depend on the initial axial phase and amplitude. For coupling on the upper sideband on the contrary, Eq. 9.7 shows that the initial axial phase at $t = 0$ continues to influence the final axial phase after a certain time. The relative impact of the cyclotron phase and axial phase depends on the size of C_0 relative to Z_0. For the cyclotron phase to dominate, C_0 should be significantly greater than Z_0. Consequently, the cyclotron mode has also first to be excited during the PnA scheme in order to ensure that the initial cyclotron phase ϕ_C dominates the axial phase after the sideband pulse is applied.

9.3. Experimental setup for mode coupling

All phase measurements at the BASE experiment are performed in the precision trap, which is introduced in Sec. 4 in more detail. The phase-methods specific setup for mode coupling is depicted in Fig. 9.8. Separate frequency generators (Keysight 33522B), labelled FG1 and FG2 in Fig. 9.8, are used for cyclotron excitation and mode coupling. The upper sideband ($\omega_{\mathrm{rf}} = \omega_+ + \omega_z$) is used for the PnA scheme, while the lower sideband is used for recording so-called "classical Rabi oscillations" (Sec. 9.4) and for applying the PnP scheme. Another generator of the same kind is used to mix the particle signal down to $\nu_{\mathrm{sig}} = \nu_z - \nu_{\mathrm{SSB}} = 10\,\mathrm{kHz}$ by means of single-sideband down conversion using an SSB downconverter from Stahl electronics (FDC-2A). The generators are constantly turned on, with their outputs connected to fast high-insulation switches (ZASWA2-50DR-FT+ from Mini-circuits). These solid-state switches have a suppression of more than 100 dB in the relevant frequency range, a short switching time of about 20 ns and a rise/fall time of about 4 ns according to specifications [189]. They are triggered from a multichannel-delay generator (DG645 from Stanford research). The switches on both generators are connected to a radio-frequency combiner (Minicircuits ZFRSC-42-S+) via a Minicircuits ZFHP-0R23-S+ high pass filter. By default, the switches send the output of the generators to ground, except during the excitation pulse and coupling pules (duration of several of ms), when they send it to the split ring electrode of the precision trap. The signal of the axial particle motion is read out by means of a highly sensitive image current based detector [76], consisting of a superconducting resonator and a low-noise cryogenic amplifier. It is processed by a clocked FFT analyzer (Stanford Research SR1). The frequency generators, SR1 Audio analyser and DG645 are phase locked to a rubidium

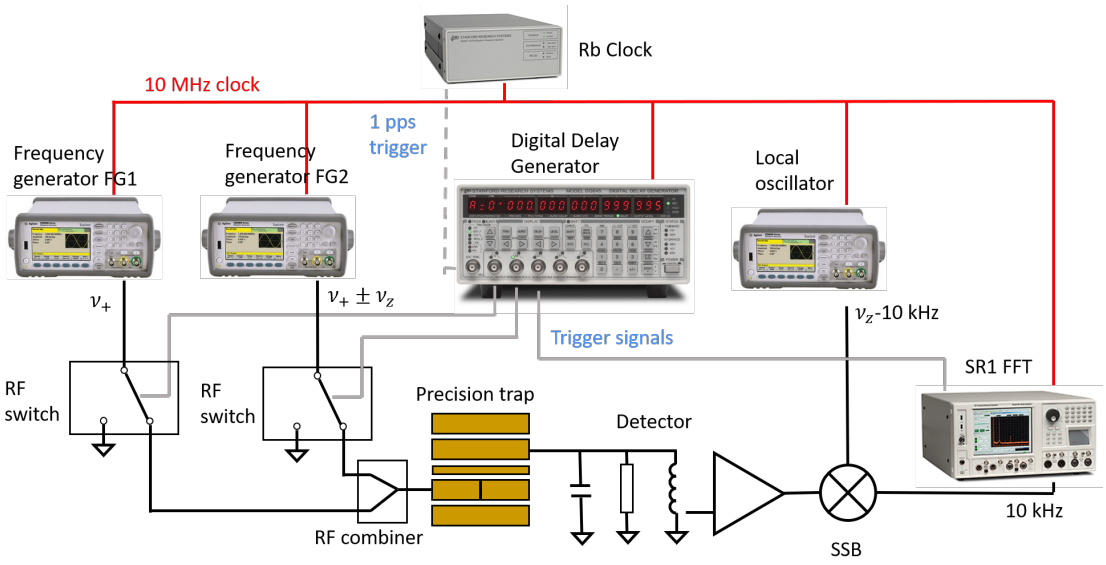

Figure 9.8.: Phase methods setup. The particle is located in the five-pole Penning trap (golden). The axial detection system consisting of a superconducting LC-circuit [76] and a cryogenic ultralow-noise amplifier is connected to a correction electrode. A signal from the particle's axial motion is picked up by the resonator and amplified by the subsequent amplifiers at 4 K and at room temperature (not depicted). Using single-sideband downconversion, the signal is mixed to $\nu_z - \nu_{\mathrm{SSB}} = 10\,\mathrm{kHz}$ and read out with a Stanford Research SR1 audio analyzer. The FG1 frequency generator is used to excite the cyclotron motion of the trapped particle, the FG2 generator applies subsequently a coupling pulse at $\omega_{\mathrm{rf}} = \omega_+ \pm \omega_z$. The excitation and the coupling pulse are applied via fast high-insulation TTL switches (ZASW from Mini-circuits) connected to an RF combiner. The switches are controlled by a delay generator (DG645 from Stanford Research). The FFT analyzer, the delay generator, and all frequency generators are synchronised to a 10 MHz rubidium clock.

atomic clock (Stanford Research FS725) and the DG645 is triggered using the 1 pulse-per-second output of the rubidium clock. To guarantee that the phase of each generator is the same for each measurement, the generators are set to output integer frequencies.

9.4. Classical Rabi oscillations

When coupling the cyclotron and the axial motion by irradiating the lower sideband, $\omega_{\mathrm{rf}} = \omega_+ - \omega_z$, the initial energies and phases are continuously exchanged as long as both modes are coupled. This behavior was schematically depicted in Fig. 9.6 and derived in Eq. 9.22 - Eq. 9.26. In analogy to the atomic two-level system, these oscillations are

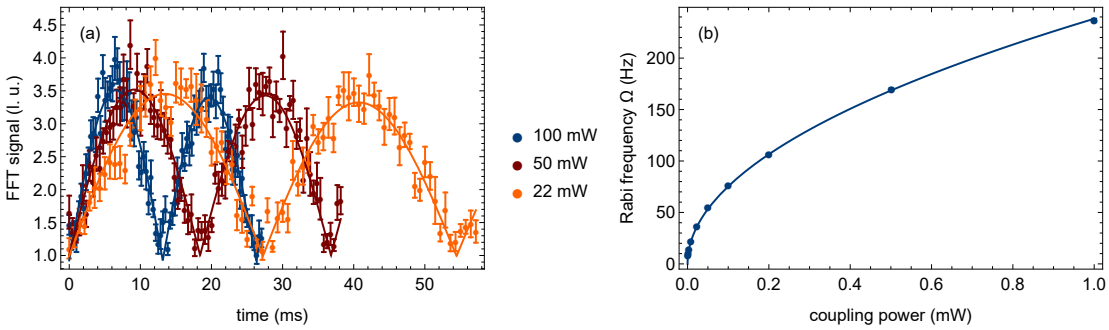

Figure 9.9.: Classical Rabi oscillations at different coupling powers. On the left, three curves of Rabi oscillations are shown, the different Rabi frequencies Ω result from the different coupling strengths. Right: According to Eq. 9.30, a scaling of the Rabi frequency with the coupling power $\sqrt{P_{\mathrm{rf}}}$ is observed.

referred to as "classical Rabi oscillations" in the field of Penning trap physics [70, 54, 190]. For $t = \pi/\Omega$, a full transfer of energy and phase between both modes is observed ("π-pulse"), which is used in the "PnP" scheme [54].

Before performing phase sensitive measurements, we firstly demonstrated this coupling by scanning the coupling time t and recording axial spectra in a triggered way. An axially excited particle will produce a peak signal in the axial resonator, similar to the signal used during for cyclotron peak measurements as discussed in Sec. 7.2 and depicted in Fig. 7.8. The particle signal U_p is given by

$$U_p = I_p \times R_p, \tag{9.29}$$

with the image current $I_p = q/D_z \times \dot{z}$, the effective electrode distance $D_z = 10.1\,\mathrm{mm}$, and the effective parallel resistance R_p of the detector. The axial cooling time constant $\tau_z \approx 35\,\mu\mathrm{s}$ is very small compared to the cyclotron cooling time constant $\tau_+ \approx 450\,\mathrm{s}$ in the peak run, which requires a short spectral acquisition time. For recording classical Rabi oscillations, we typically chose $t_{\mathrm{avg}} = 64\,\mathrm{ms}$, which corresponds to an FFT bin width of 15.625 Hz. For the cyclotron peaks, we usually recorded at $t_{\mathrm{avg}} = 64\,\mathrm{s}$, and an FFT span of 12.5 Hz.

In order to record a set of Rabi oscillations, we firstly excite the cyclotron motion to $E_+ = 7.6(1.1)\,\mathrm{eV}$, and subsequently record the axial spectra for varying coupling times in a triggered way. We then apply a coupling pulse of a particular power and duration, before triggering the acquisition of an axial spectrum. The results of such a measurement

are shown in Fig. 9.9 (a), where the maximum values of the axial spectra are plotted as a function of coupling time t_{coup}. Especially for weaker coupling, the damping in the axial mode is observed (when comparing the second blue maximum with the second orange maximum). The obtained curves are fitted with the product of an absolute sin-function and an exponential decay according to Eq. 9.26, from which the Rabi frequency Ω is extracted. Note that the exponential decay is not simply given by one of the cooling time constants $\tau_{z,+}$, but is reduced compared to τ_z, as only the fraction of energy stored in the axial motion is damped by τ_z. In total, the coupling pulse was irradiated at 10 different powers ranging from -30 dBm to 0 dBm, resulting in Rabi frequencies ranging from $\Omega = 8\,\mathrm{Hz}$ to $\Omega = 237\,\mathrm{Hz}$. From Eq. 9.20, the Rabi frequency Ω is given by

$$\Omega = \frac{qE_0}{2m\sqrt{\omega_+\omega_z}} = \frac{q\sqrt{P_{\mathrm{rf}}}\alpha}{2m\sqrt{\omega_+\omega_z}}, \tag{9.30}$$

with the coupling power P_{rf} and the geometrical parameter α. The expected scaling is reproduced very well in Fig. 9.9 (b).

9.5. Principle of frequency measurements using phase sensitive methods

Phase sensitive cyclotron frequency measurements rely on initializing the cyclotron phase, allowing the cyclotron phase ϕ to evolve during a variable evolution time t_{evo}, transferring ϕ then onto the axial mode and subsequently reading the cyclotron phase. The phase $\Delta\phi$ compared to a phase measured at $t_{\mathrm{evo}} = 0\,\mathrm{s}$ is given by

$$\Delta\phi = \nu \times t_{\mathrm{evo}} \times 360\,\mathrm{deg}. \tag{9.31}$$

For variable evolution times t_{evo}, the frequency difference $\Delta\nu$ is determined from the phase gradient $\mathrm{d}\Delta\phi/\mathrm{d}t_{\mathrm{evo}}$, as depicted in Fig. 9.10. This process is called "phase unwrapping" in literature. The unwrapping times have to be chosen accordingly such that the phase jumps of 360 deg can be unambiguously identified. As the coupling drive and the SSB downcoverter in the setup described in Fig. 9.8 are operated at integer frequencies, the reference frequency for the phase unwrapping is the nearest integer frequency.

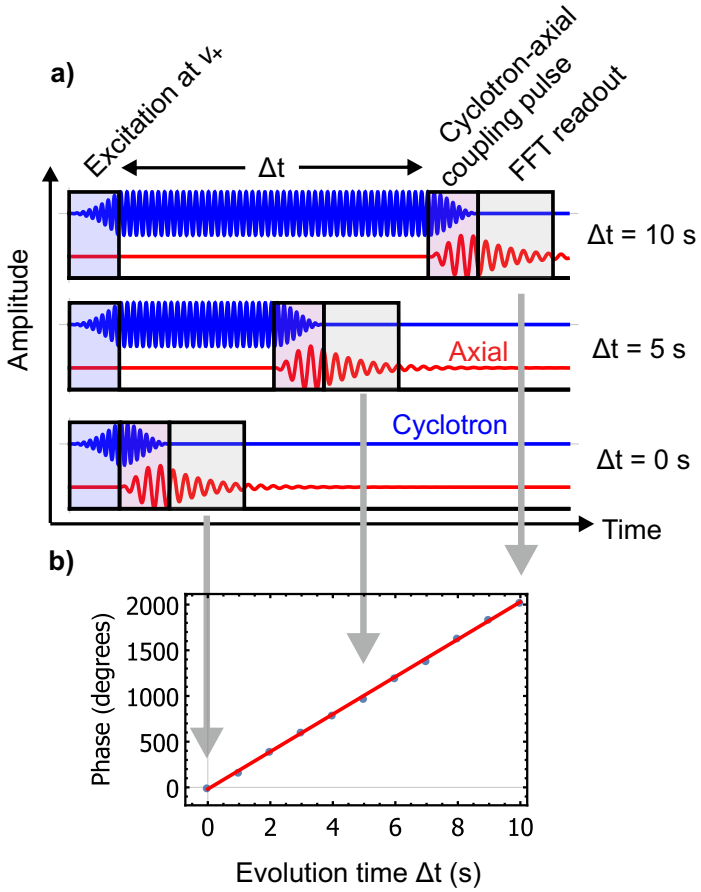

Figure 9.10.: Principle of unwrapping measurements, here depicted for coupling on the lower sideband (PnP scheme [54]). The cyclotron motion is firstly excited to a non-thermal energy E_+. During this process, the cyclotron phase is initialized. Subsequently, the phase evolves during a variable evolution time t_{evo}. Afterwards, the cyclotron phase is coupled onto the axial motion by irradiating a coupling drive at $\omega_{\mathrm{rf}} = \omega_+ - \omega_z$. During this coupling, the cyclotron mode gets de-excited, while the axial mode gets excited to a non-thermal energy $E_z = \sqrt{\omega_z/\omega_+} \times E_+$. The phase of the axial motion, which is now given by the imprinted cyclotron phase is read out. Performing this scheme several times at different evolution times allows to observe a linear scaling of $\Delta\phi$ with time as discussed in Eq. 9.31, from which the frequency difference $\Delta\nu$ compared to the integer reference frequency is given by $\mathrm{d}\Delta\phi/\mathrm{d}t_{\mathrm{evo}}$.

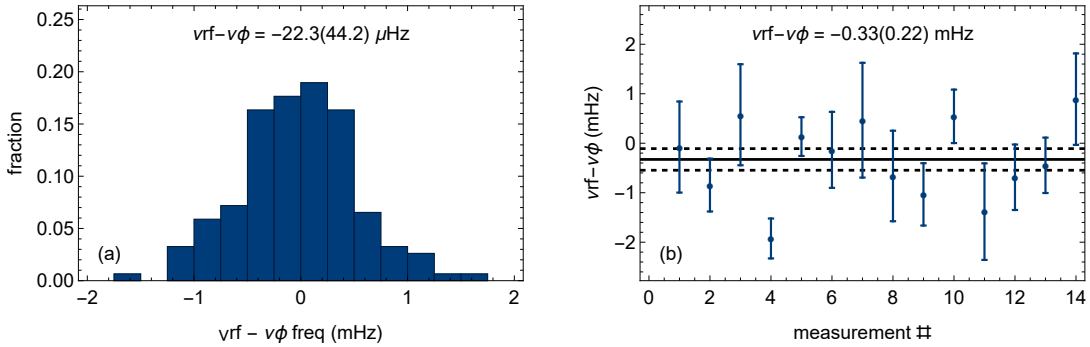

Figure 9.11.: Phase measurements with a test setup. Left: Demonstration of unwrapping with a setup consisting of a generator and an SR1 FFT analyzer. The measured frequency agrees with the generator frequency within $\nu_{\mathrm{rf}} - \nu_{\phi} = -22.3(44.2)\,\mu$Hz. For this measurement, more than 150 frequencies were measured by means of the phase method during the course of one and a half hours. Right: The measurement concept is similar to left, but the generators are set continuous wave. Now, the radio-frequency switches depicted in Fig. 9.8 are implemented into the setup. The generator frequency was kept constant throughout this measurement. The switches are opened by trigger pulses from the delay generator. We obtain $\nu_{\mathrm{rf}} - \nu_{\phi} = -0.33(22)\,$mHz, which is not significant within two standard deviations.

9.5.1. Demonstration measurements with frequency generators

In order to test the general functionality of the setup depicted in Fig. 9.8, several test measurements were conducted. Two of these measurements are shown in Fig. 9.11. In Fig. 9.11 (a), the particle's signal was simulated by means of a frequency generator burst signal at ν_{FG} that was stepped across a range of 1 Hz in steps of 10 mHz. The generator signal was irradiated at $\nu_{\mathrm{FG}} = 2.6\,$MHz with 10 million cycles, which means that the total signal length was about 3.8 s. The generator signal is mixed down by means of single-sideband downconversion resulting in $\nu_{\mathrm{sig}} = \nu_{\mathrm{FG}} - \nu_{\mathrm{SSB}} = 10\,$kHz. The FFT data acquisition is triggered after an evolution time t_{evo}. For the measurement presented here, t_{evo} ranged from 0 s to 3 s in steps of 500 ms. During each evolution cycle, the generator frequency was kept constant, and after each cycle it was stepped by 10 mHz. When comparing the generator frequency and the determined frequency from the phase unwrapping, a result of $\nu_{\mathrm{rf}} - \nu_{\phi} = -22.3(44.2)\,\mu$Hz, which confirms the general functionality of the approach at great precision.

In Fig. 9.11 (b), the switches depicted in Fig. 9.8 were implemented into the test setup, and the generator frequency output was set to continuous wave. Also, the generator frequency remained constant. $\nu_{\mathrm{rf}} - \nu_{\phi} = -0.33(22)\,$mHz was yielded as a result, with the

resolution of this 13 min long measurement being limited by statistics. The result is 1.5 sigma consistent with no offset and confirms in this way that the switches do not lead to an evolution time dependent phase shift that would affect the frequencies measured by phase unwrapping. An incorrect switch timing itself would just lead to reduced SNR, as the FFT is triggered separately, which is already investigated in Fig. 9.11 (a).

9.6. Principal phase scatter

Phase unwrapping as discussed in the section above can only be performed when the uncertainty on each measured phase (what is here referred to as "phase scatter") is sufficiently low. Two main categories of phase scatter can be assigned: Principal phase scatter, which does not scale with evolution time and is usually related to limitations of the experimental setup or the experimental procedure, and evolution-time dependent phase scatter, which is either related to magnetic field fluctuations or to frequency shifts associated with scatter in the excitation energies arising from the initial cyclotron excitation amplitude (see Eq. 7.39). This section will focus on the principal phase scatter, while the evolution-time dependent scatter will be discussed in Sec. 9.7.

9.6.1. Phase scatter as a function of SNR

When measuring the phase of signal, the principal phase uncertainty that can be achieved, is fundamentally related to the SNR, as is for instance introduced in [75]. In this section, we will review this description briefly and afterwards expand it for our purposes.
The particles motion is described by $\vec{\rho} = (x, -v/\omega)$, with the vector length ρ given by the mode energy,

$$\rho = |\vec{\rho}| = \left(2E/\left(m\omega^2\right)\right)^{1/2}. \tag{9.32}$$

The mode energy is Boltzmann distributed,

$$f(E) = 1/E_0 \exp\left(-E/E_0\right) \mathrm{d}E. \tag{9.33}$$

In polar coordinates, the vector is described by (ρ, ϕ). Inserting the energy $E = (1/2)m\omega^2\rho^2$ and defining $\sigma^2 = E_0/(m\omega^2)$, we obtain

$$f(\rho, \phi) = \frac{\rho}{2\pi\sigma^2} \exp(-\rho^2/(2\sigma^2))\mathrm{d}\rho\mathrm{d}\phi. \tag{9.34}$$

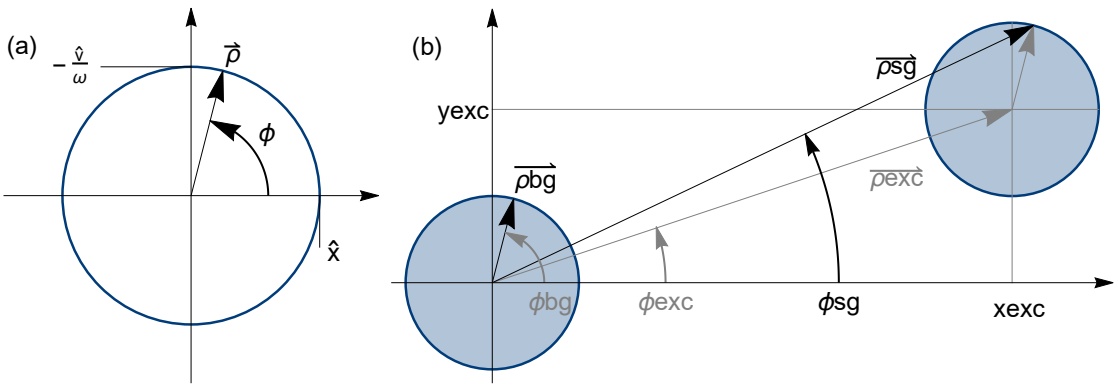

Figure 9.12.: Left: General phase space diagram. Right: Phase space diagram before and after excitation. The initial distribution ($\vec{\rho}_{\mathrm{bg}}$) is shown on the left. Its excitation is described by the excitation vector $\vec{\rho}_{\mathrm{exc}}$. The particle after excitation is described by $\vec{\rho}_{\mathrm{sg}} = \vec{\rho}_{\mathrm{bg}} + \vec{\rho}_{\mathrm{exc}}$. The SNR is given by $\langle \vec{\rho}_{\mathrm{sg}} \rangle / \langle \vec{\rho}_{\mathrm{bg}} \rangle$.

This equation shows that the initial radius ρ is distributed according to a Rayleigh distribution, while the phase ϕ is initially uniformly distributed between 0 and $2\,\pi$. In order to derive the theoretical SNR, we consider Fig. 9.12 [72, 191, 192, 75]. Before excitation, the particle is described by $\vec{\rho}_{bg}$. The excitation drive $\vec{\rho}_{exc}$ transfers the particle to $\vec{\rho}_{sg} = \vec{\rho}_{bg} + \vec{\rho}_{exc}$. The initial and final distributions are schematically illustrated by the blue circles, with the circle radius ρ_{bg} given by the initial particle energy, $\rho_{bg} = \sqrt{E_0/(2m)}$. In order to compute the SNR, Eq. 9.34 is shifted to $\vec{\rho}_{exc} = (x_{exc}, y_{exc})$,

$$f(\rho, \phi, \vec{\rho}_{exc}) = \frac{\rho}{2\pi\sigma^2} \exp\left(-\left((\rho\cos(\phi) - x_{exc})^2 + (\rho\sin(\phi) - y_{exc})^2\right)/(2\sigma^2)\right) \mathrm{d}\rho\mathrm{d}\phi. \tag{9.35}$$

The expectation value for the background radius $\langle|\vec{\rho}_{bg}|\rangle$ is given by integrating over the entire range of ρ and ϕ denoted by $\mathcal{B}$

$$\langle|\vec{\rho}_{bg}|\rangle = \int_{\mathcal{B}} \mathrm{d}A f(\rho, \phi, \vec{0})\rho = \sqrt{\frac{\pi\sigma^2}{2}}. \tag{9.36}$$

For the excited particle:

$$\langle|\vec{\rho}_{sg}|\rangle = \int_{\mathcal{B}} \mathrm{d}A f(\rho, \phi, \vec{\rho}_{exc})\rho \tag{9.37}$$

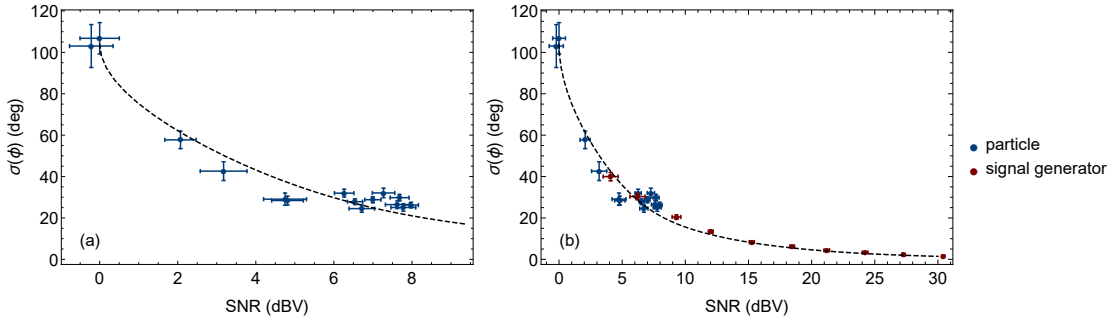

Figure 9.13.: Phase scatter as a function of SNR. Left: Particle data obtained from a measurement when the coupling pulse length T_{coup} was varied between $0 \leq T_{\mathrm{coup}} \leq 2 \times 1/\Omega$ with Rabi frequency Ω. As a result, the cyclotron energy was only partially transferred onto the axial motion, thereby leading to an weaker SNR. Right: The blue data points depict the data from (a), the red data points depict an independently conducted measurement analyzing a signal generated by a signal generator. Both data sets, the particle data and the signal generator data, agree well with the prediction (black dotted line).

The SNR in decibel is then given by

$$\mathrm{SNR}(\rho_{exc}) = 20 \log_{10} \frac{\langle |\vec{\rho}_{sg}| \rangle}{\langle |\vec{\rho}_{bg}| \rangle}. \tag{9.38}$$

The phase scatter is given by

$$\sigma_\phi(\vec{\rho}_{exc}) = \sqrt{\int_{\mathcal{B}} \mathrm{d}A f(\rho, \phi, \vec{\rho}_{exc})(\phi - \phi_{exc})^2 - \left(\int_{\mathcal{B}} \mathrm{d}A f(\rho, \phi, \vec{\rho}_{exc})(\phi - \phi_{exc}) \right)^2} \tag{9.39}$$

For an SNR approaching zero, we obtain

$$\lim_{\rho_{exc} \to 0} \sigma_\phi(\vec{\rho}_{exc}) = \frac{\pi}{\sqrt{3}} \approx 103.923\,\mathrm{deg}, \tag{9.40}$$

which is the standard deviation of a uniform distribution between 0 and 2π, $\sigma(\mathcal{U}(0,2\pi)) = \pi/\sqrt{3}$. When discussing measured phase scatter, it should be kept in mind that the maximum value for phase scatter is not given by 360 deg, but by 104 deg due to the modulo nature of the phase. The relation from Eq. 9.39 is confirmed both by particle measurements and by measurements performed in a test setup consisting of a signal generator and a Stanford Research Audio Analyzer, as shown in Fig. 9.13.

Predicting the particle signal

Equation 9.39 holds for signals where the SNR is known, for instance for test signals from a frequency generator and also for particle signals with known SNR. We will now discuss a model to predict the particle SNR and thus the particle phase scatter. To this end, we consider the cyclotron burst and Eq. 9.35 again. The cyclotron-wise excited particle with a known energy given by $(x_{\mathrm{exc}}, y_{exc})$ is described by

$$f_+ = \frac{m\omega_+^2}{\pi k_B T_+}\rho_+ \exp\left[\frac{m\omega_+^2}{k_B T_+}\left((\rho_+\cos[\phi] - x_{\mathrm{exc}})^2 + (\rho_+\sin[\phi] - y_{\mathrm{exc}})^2\right)\right] \mathrm{d}\rho_+ \mathrm{d}\phi. \quad (9.41)$$

After a perfect π-pulse, and considering the relation $\rho_+ = z\sqrt{\omega_z/\omega_+}$ (see Eq. 9.26), the resulting axial distribution is described by

$$f_z = \frac{m\omega_+^2}{\pi k_B T_+}\rho_z \times \sqrt{\omega_z/\omega_+}\times \exp\left[-\frac{m\omega_+\omega_z}{k_B T_+}\rho_z^2\left(\left(\cos[\phi] - \frac{x_{\mathrm{exc}}}{\rho_z\sqrt{\omega_z/\omega_+}}\right)^2 + \left(\sin[\phi] - \frac{y_{\mathrm{exc}}}{\rho_z\sqrt{\omega_z/\omega_+}}\right)^2\right)\right] \mathrm{d}\rho_z \mathrm{d}\phi, \quad (9.42)$$

which is rewritten to

$$f_z = A \times z \exp\left[-\frac{1}{2\sigma_1^2}\rho_z^2\left(\left(\cos[\phi] - \frac{x_{\mathrm{exc}}}{\rho_z\sqrt{\omega_z/\omega_+}}\right)^2 + \left(\sin[\phi] - \frac{y_{\mathrm{exc}}}{\rho_z\sqrt{\omega_z/\omega_+}}\right)\right)\right] \mathrm{d}\rho_z \mathrm{d}\phi, \quad (9.43)$$

with σ_1^2 given by

$$\sigma_1^2 = \frac{k_B T_+}{2m\omega_+\omega_z}. \quad (9.44)$$

During the duration of the spectrum acquisition t_{avg}, the axial mode is cooled with cooling time constant γ_z, with the axial amplitude following a $\gamma_z/2$ cooling. The excitation radius $\rho_{\mathrm{exc}} = \sqrt{x_{\mathrm{exc}}^2 + y_{\mathrm{exc}}^2}$ is then given by

$$\rho_{\mathrm{exc}} = \frac{1}{t_{\mathrm{avg}}} \times \int_0^{t_{\mathrm{avg}}} \mathrm{d}t \rho_{\mathrm{exc},0} \times \exp(-\gamma_z/2t), \quad (9.45)$$

with $\rho_{\mathrm{exc},0} = \rho_{+,0}$ being the initial cyclotron radius after excitation.

The axial frequency is shifted during the spectrum acquisition due to trap parameter

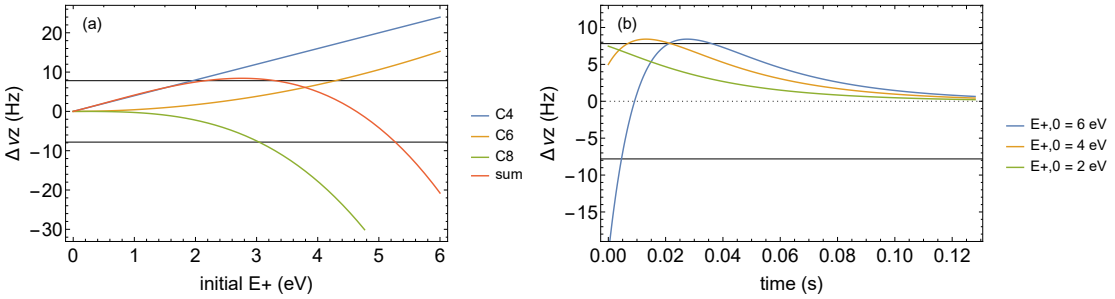

Figure 9.14.: Left plot: Axial frequency shift as a function of axial energy expressed in units of cyclotron energy prior to the coupling. Right plot: Axial frequency shift vs time, assuming feedback-free cooling of the axial mode with $\gamma_z \approx 35\,\mathrm{ms}$. The B_2, C_4, C_6 and C_8 coefficients specified in Tab. 9.1 for the phase tuning ratio $\mathrm{TR}_{\mathrm{phase}}$ are used for the calculation. The axial spectra are typically recorded at an averaging time $t_{\mathrm{avg}} = 64\,\mathrm{ms}$, which corresponds to an FFT bin width of $b = 15.625\,\mathrm{mHz}$. The FFT bin width is indicated by the two horizontal grid lines. Since the measured signal is constrained by the bin width, a modification of phase scatter as a function of tuning ratio is obtained as shown in Fig. 9.15. Note that uncertainties on the inhomogeneity parameters were not considered here, which is why this should be seen as a more qualitative investigation.

such as C_4, C_6 and C_8 specified in Tab. 9.1 and due to the non-negligible axial energy after coupling (see Sec. 2.2.1). The axial frequency shift as a function of the energy E_+ of the excited cyclotron mode prior to the coupling is depicted in Fig. 9.14 (a). Incorporating the feedback-free axial cooling time constant $\gamma_z \approx 35\,\mathrm{ms}$, the axial frequency shift as function of time is shown in Fig. 9.14 (b). The typically chosen acquisition time $t_{\mathrm{avg}} = 64\,\mathrm{ms}$ for phase measurements corresponds to an FFT bin width of $b = 15.625\,\mathrm{Hz}$, which is depicted by the grid lines in Fig. 9.14. Only the axial signal for which the axial frequency shift fulfills $|\Delta\nu_z| < b/2$ contributes to the signal acquired by the FFT. This behavior is incorporated to Eq. 9.43 by replacing ρ_z with a conditional expression that sets $\rho_z = 0$ for $|\Delta\nu_z| > b/2$.

Predicting the background signal

In addition to the excited cyclotron distribution, the resonator background U_{res} has to be considered. It is given by the Johnson noise,

$$U_{\mathrm{res}} = \sqrt{4k_B T_z R_p \Delta f}, \tag{9.46}$$

with the resonator temperature T_z, the effective parallel resistance on resonance R_p, and the bandwidth Δf defined by the inverse acquisition time, $\Delta f = 1/t_{\mathrm{avg}}$. In order to apply the framework introduced above, the idea is to assign a fictitious background rms radius ρ_J to the voltage noise distribution of the detector. We recall that the particle signal is given by (see Sec. 2.3)

$$\sqrt{\langle V_{\mathrm{part}}^2 \rangle} = \sqrt{\langle i_p \rangle^2} R_p = \sqrt{\frac{1}{2}} \frac{q}{D} \omega_z \rho_J R_p, \tag{9.47}$$

with D being the effective electrode distance. ρ_J is then obtained by equating both expressions,

$$\rho_J = \frac{\sqrt{8 k_B T_z \Delta f}}{\sqrt{R_p} q / D \omega_z} = \sqrt{\frac{8 k_B T_z \Delta f}{2\pi \delta\nu_z m \omega_z^2}}. \tag{9.48}$$

In the last step, the axial dip width $\delta\nu_z$ is inserted (Eq. 2.34). The absolute value ρ_J describing the complex Johnson noise is Rayleigh-distributed. Inserting the corresponding relation $\rho_J = \sqrt{\pi/2}\sigma_J$, we obtain

$$\sigma_J = \sqrt{\frac{2}{\pi}} \sqrt{\frac{8 k_B T_z \Delta f}{2\pi \delta\nu_z m \omega_z^2}}. \tag{9.49}$$

The noise contribution from the detector Johnson noise and finite cyclotron temperature are uncorrelated random variables. The measured signal is therefore given by quadratically summing up the particle and the resonator background. The resulting distribution is given by

$$f_z = A \times \rho_z \exp\left[-\frac{1}{2\sigma_t^2} \rho_z^2 \left(\left(\cos[\phi] - \frac{x_{\mathrm{exc}}}{\rho_z \sqrt{\omega_z/\omega_+}} \right)^2 + \left(\sin[\phi] - \frac{y_{\mathrm{exc}}}{\rho_z \sqrt{\omega_z/\omega_+}} \right) \right) \right] \mathrm{d}\rho_z \mathrm{d}\phi, \tag{9.50}$$

where σ_t is,

$$\sigma_t^2 = \sigma_1^2 + \sigma_J^2. \tag{9.51}$$

The expected SNR is given by inserting this distribution together with Eq. 9.45 into Eq. 9.38, the phase scatter is given by applying Eq. 9.39.

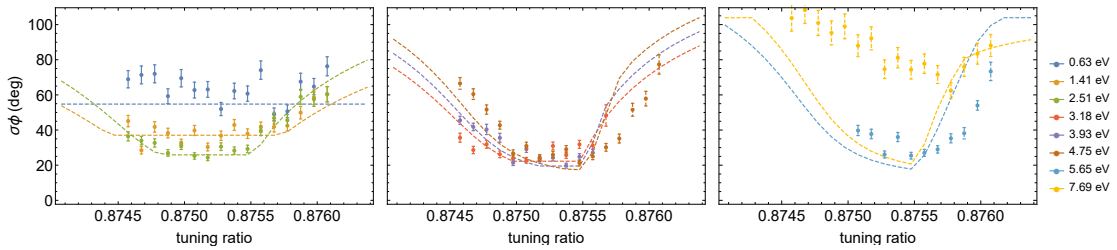

Figure 9.15.: Measured phase scatter (dots) and phase scatter prediction (dashed lines) as a function of initial cyclotron energy, assuming an axial detector temperature of $T_z \approx 20\,\mathrm{K}$ and an FFT acquisition time $t_{\mathrm{avg}} = 64\,\mathrm{ms}$ corresponding to a bin width of 15.625 Hz. The scaling with tuning ratio is related to the bin size argument described in Fig. 9.14, for B_2, C_4, C_6 and C_8 the values from Tab. 9.1 are used. The lower limit for the phase scatter is given from the particle energy and the initial cyclotron temperature, as discussed in Eq. 9.50. Note here that no trap parameter uncertainties are considered, which is why the dashed lines rather represent a rather qualitative model. For energies $E_+ > 6\,\mathrm{eV}$, the model breaks down, which indicates the occurrence of non-linear phenomena in the coupling, which are related to higher-order anharmonicities (see for instance [72]).

9.6.2. Phase scatter as a function of tuning ratio

When the energy dissipation during the phase readout (Eq. 9.45) and the signal-cutoff due to the FFT bin size (Fig. 9.14) are considered, the phase scatter scaling as a function of tuning ratio and as a function of excitation energy can be predicted from Eq. 9.50. In order to compare it to measurements, we excited the particle to energies between 0.6 eV and 7.7 eV and recorded the phase scatter as a function of the tuning ratio, the results of which are depicted in Fig. 9.15. Note here, that the scatter predictions shown by the dashed lines assume $T_z = 20\,\mathrm{K}$ and the B_2, C_4, C_6, and C_8 values specified in Tab. 9.1, but do not consider the respective trap parameter uncertainties. In this way, the scatter prediction can be inaccurate in some cases, but it reproduces the general trend very well up to energies of 5.7 eV. For the 7.7 eV data point, we see a strong deviation between prediction and measured data. This is likely related to the occurrence of non-linear phenomena, which have been for instance discussed in [72]. They have also been observed during this run for Rabi oscillations at energies of at least 7-8 eV, but are not discussed in greater detail within this thesis.

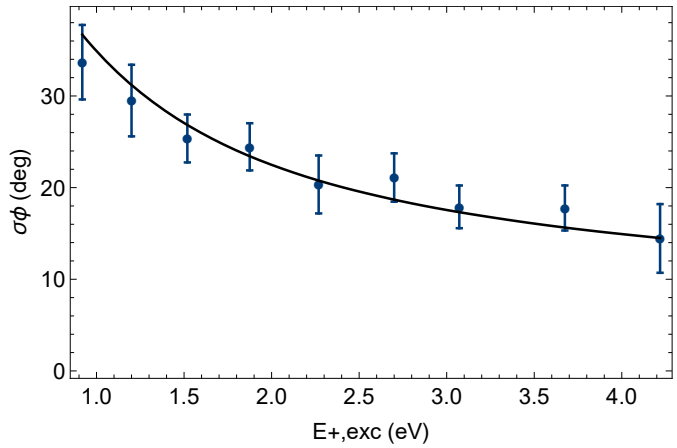

Figure 9.16.: Phase scatter as a function of excitation energy. The fit according to Eq. 9.50 has the axial temperature as only free fit parameter, and yields $T_z = 13.0(9)\,\mathrm{K}$. The model reproduces the observed scaling very well.

9.6.3. Phase scatter as a function of excitation energy

In the end of November 2019, we conducted a detailed measurement on phase unwrapping for different excitation energies. While the evolution time dependent scatter will be discussed in the next section, this data set is used here to discuss the phase scatter as a function of excitation energy. To this end, we again apply the formalism outlined in Eq. 9.50. As depicted in Fig. 9.16, the obtained scaling of the initial phase scatter σ_0 as a function of the initial excitation energy $E_{+,0}$ follows the expected behavior very well. The phase scatter was here computed from the median absolute deviation and afterwards corrected accordingly to yield the corresponding phase scatter [193]. Considering the comparably low excitation energies of only up to 4.3 eV, the signal loss due to FFT binning does not need to be incorporated (compare Fig. 9.15). The only free fit parameter when applying Eq. 9.50 is the axial temperature. Here, we yield $T_z = 13.0(9)\,\mathrm{K}$. This axial temperature is lower compared to Fig. 9.15 ($T_z \approx 20\,\mathrm{K}$), for which the data were acquired in August. This change of temperature throughout the run is not surprising as the experimental setup was optimized several times in between, which usually affects the pick-up of stray signals and thus the effective detector temperature.

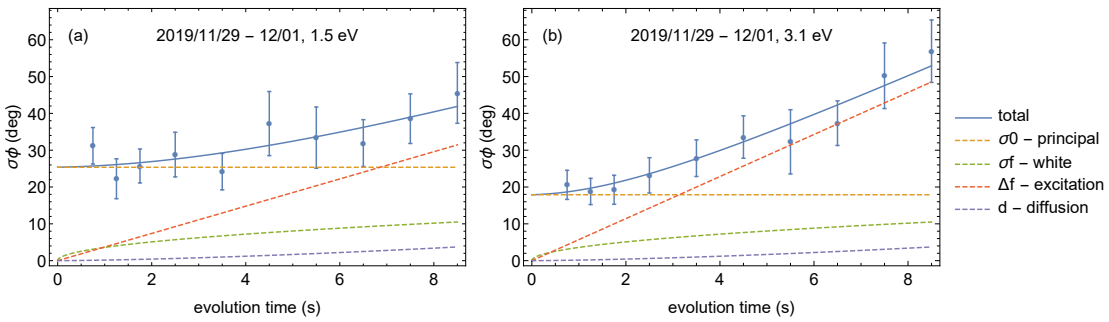

Figure 9.17.: Phase scatter as a function of evolution time for two different energies. The measured data points are depicted in blue, several contributions to the phase scatter are indicated by dotted lines, with the squared sum of the contributions depicted by the solid blue line. The underlying phase scatter model is summarized in Eq. 9.52. The phase scatter is given by the principal phase scatter σ_0 (yellow) related to the SNR and discussed in Sec. 9.6, the excitation scatter Δ_f (red) discussed in Sec. 9.7.1, and the contributions of the white magnetic field noise σ_f (green) and the magnetfic field diffusion d (purple) (Sec. 9.7.2). Comparing the left plot ($E_{\mathrm{exc}} = 1.5\,\mathrm{eV}$) and the right plot ($E_{\mathrm{exc}} = 3.1\,\mathrm{eV}$), it is observed that the principal scatter σ_0 is decreased for higher excitation energies, while the excitation scatter contribution Δ_f is increased, as expected from theory and further discussed in this section.

9.7. Phase scatter as a function of evolution time

After having discussed the principal phase scatter σ_0 in the section above, now the phase scatter as a function of evolution time shall be investigated. Throughout phase evolution, the phase scatter is affected by magnetic field fluctuations characterized by the diffusion parameter d and the white noise parameter σ_f. It is also affected by excitation scatter that leads to scatter in the energy-dependent cyclotron frequency shift and consequently to phase scatter described by Δ_f. While the magnetic parameters d and σ_f depend on external parameters, the principal phase scatter σ_0 is decreased at higher excitation energies (Eq. 7.39), while the excitation scatter contribution Δ_f is increased for higher excitation energies. The phase scatter σ_ϕ as a function of evolution time t_{evo}) is described by

$$\sigma_\phi(t_{\mathrm{evo}}) = \sqrt{\sigma_0^2 + (360\sigma_f)^2\, t_{\mathrm{evo}} + (360\Delta_f)^2\, t_{\mathrm{evo}}^2 + \left(360\sqrt{2/3 \times d}\right)^2 t_{\mathrm{evo}}^3}. \tag{9.52}$$

This behavior is visualized in Fig. 9.17, where the phase scatter scaling for two different excitation energies is shown. While the magnet noise contributions σ_f and d are energy-

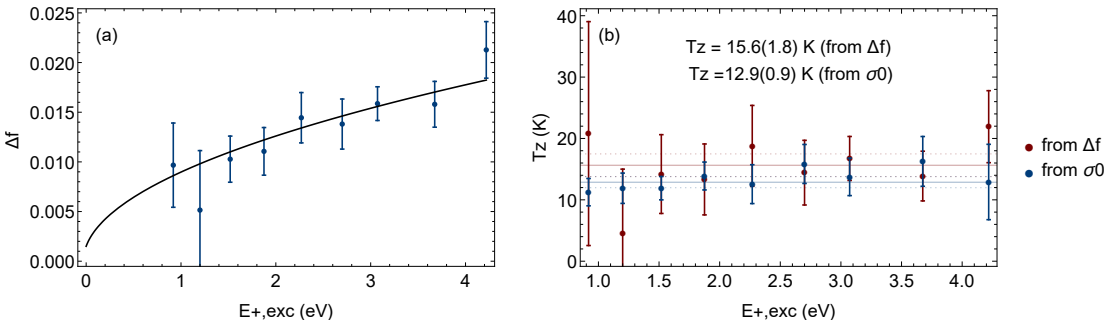

Figure 9.18.: Results from evaluating phase scatter data as a function of evolution time. On the left, the Δ_f parameters obtained from fits to the individual phase scatters as a function of evolution time (compare Fig. 9.17) are depicted for several excitation energies. The data follow the behavior predicted in Eq. 9.54, a least-squares fit yields $T_z = 14.4(1.7)\,\mathrm{K}$. Right: It is also possible to examine each individual phase scatter versus evolution time plot and extract individual axial temperatures for each data set. In red, the extracted temperatures from Δ_f following Eq. 9.54 are shown, in blue the temperatures determined from σ_0 following Eq. 9.50 are given. The weighted mean yields $T_z = 15.6(1.8)\,\mathrm{K}$ (Δ_f) and $T_z = 12.9(0.9)\,\mathrm{K}$ (σ_0), both values being in agreement with the fit results from (a) and Fig. 9.16.

independent, the principal scatter σ_0 is reduced for higher excitation energies, but the excitation scatter contribution Δ_f is increased. In this section, the time-dependent scatter contributions d, σ_f and Δ_f are characterized and discussed.

9.7.1. Excitation scatter

In order to discuss the effect of cyclotron excitation scatter, we first recall Eq. 7.39, which describes the increase of energy scatter as a function of excitation energy:

$$\sigma(E_+) = \sqrt{2E_{\mathrm{th}}E_{\mathrm{exc}}} \times \sqrt{1 + \frac{1}{2}\frac{E_{\mathrm{th}}}{E_{\mathrm{exc}}}}, \tag{9.53}$$

with excitation energy E_{exc} and the initial energy E_{th}, given by $E_{\mathrm{th}} = \nu_+/\nu_z \times k_B T_z$ when the particle is sideband cooled prior to the excitation pulse. Hence, we may write

$$\Delta_f = \frac{\mathrm{d}\Delta\nu_+}{\mathrm{d}E_+} \times \Delta_f = \frac{\mathrm{d}\Delta\nu_+}{\mathrm{d}E_+} \times \sqrt{2k_B T_z \times \nu_+/\nu_z \times E_{\mathrm{exc}}} \tag{9.54}$$

The cyclotron frequency shift $\Delta\nu_+$ as a function of cyclotron energy E_+ is given by (see

Eq. 7.41 and Tab. 7.1)

$$\frac{\mathrm{d}\Delta\nu_+}{\mathrm{d}E_+} = -27(4)\,\mathrm{mHz/eV}. \tag{9.55}$$

The Δ_f scaling is obtained by analyzing the unwrapping measurements partly depicted in Fig. 9.17, which shows the phase scatter as a function of evolution time for two distinct excitation energies. From least-squares fits to these data, the excitation scatter component Δ_f for each excitation energy is obtained, as shown in Fig. 9.18 (a). These data resemble the model from Eq. 9.54 nicely. The only fit parameter in Fig. 9.18 (a) is the axial temperature, for which a value of $T_z = 14.4(1.7)\,\mathrm{K}$ is obtained, which is similar to the value $T_z = 13.0(9)\,\mathrm{K}$ determined from the σ_0 values in Fig. 9.16. In addition, we may compute axial temperature values from the individual value of σ_0 and Δ_f for each excitation energy, as shown in Fig. 9.18 (b). Here, we yield similar temperatures compared to the fits, $T_z = 12.9(0.9)\,\mathrm{K}$ from considering σ_0 and $T_z = 15.6(1.8)\,\mathrm{K}$ from considering Δ_f.

9.7.2. Magnetic field contribution

The magnetic field stability enters in two ways into $\sigma_\phi(t_{\mathrm{evo}})$. As discussed above, magnetic field fluctuations (white noise) are described by the parameter σ_f. The long term magnetic diffusion is described by d. In order to measure the white magnetic field noise, we placed two fluxgate sensors (FLC3-70 from Stefan Mayer Instruments) in the experiment surroundings, one of which is enclosed in a mu-metal housing with an approximate magnetic shielding factor of about 100 in order to calibrate the sensor noise. The measured magnetic field of both sensors is Fourier transformed, and expressed in equivalent cyclotron frequency shifts. By quadratically subtracting the sensor noise from the measured noise, the real magnet noise is determined, as shown in Fig. 9.19 (a). We observe a mostly stable magnetic field noise for frequencies above 100 mHz, which is the behavior expected from white noise. The mean across this frequency range is therefore used to estimate the white magnetic noise density at the frequency of 1 Hz:

$$\Delta_f = 10\,\mathrm{mHz}/\sqrt{\mathrm{Hz}}, \text{ which corresponds to } 0.68\,\mathrm{nT}/\sqrt{\mathrm{Hz}}. \tag{9.56}$$

Looking at Fig. 9.17, the contribution of the magnetic field diffusion d is the least pronounced contribution among the four main contributions in σ_ϕ, which is why extracting d from direct scatter fits would only yield very imprecise values. On the other hand,

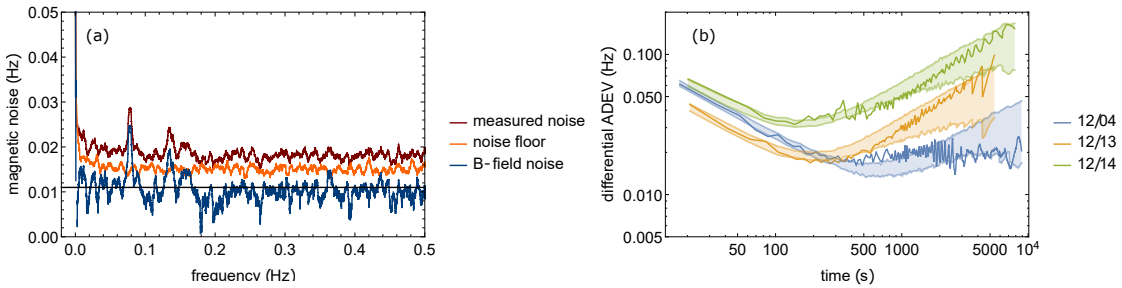

Figure 9.19.: Magnetic field diffusion and white magnetic field noise. Left: White magnetic field noise determination. The magnetic field noise in the experiment environment is measured by a dedicated fluxgate sensor, the Fourier transforms of the measured data are plotted in red. Another sensor is located in a magnetically shielded mu-metal box in order to calibrate the sensor noise (orange). The quadratic difference yields the magnetic noise (blue). The magnetic noise data do not show a scaling with frequency for the frequency range above 100 mHz, indicating the predominantly white nature of the magnetic noise. Right: Differential Allan deviation of the cyclotron frequency computed for three different dates (solid lines). Every individual phase measurement is interpreted as an individual frequency measurement. The pale data show simulated Allan deviations for the diffusion constant fitted to the measured data, with the upper and lower line indicating the 1-sigma confidence interval.

the contribution of d is still large enough such that a wrongly assigned value of d would affect the fitted contribution of the Δ_f coefficient in an unfavorable way. Therefore, d is determining choosing an approach similar to the heating rate evaluation by investigating the differential Allan deviation (see Sec. 5.3). To this end, we calculate the cyclotron frequency from each phase individually, by globally averaging the phase after 0 s evolution time (this is stable throughout the entire measurement) and computing the phase gradient for each of the measured phases[1]. We then fit a phenomenological model to the obtained differential Allan deviation as shown in Fig. 9.19 (b),

$$\sigma_{\nu_+} = \sqrt{a/t + d_{\mathrm{fit}} \times t}, \tag{9.57}$$

with the parameter a describing the decrease in the differential Allan deviation due to averaging, and d_{fit} being the contribution due to magnetic field diffusion. The parameter d_{fit} is closely related to the magnetic diffusion constant d, but d typically varies on the order of 10 % to 20 %. This is likely related to the fact that the measured phases are

[1]Note that this differential Allan deviation is higher compared to the differential Allan deviation yielded when all unwrapped phase points from one unwrapping cycle are combined into one determined frequency and the differential Allan deviation is computed subsequently.

not taken at even time increments and that the dead time between two phase measurements is not considered when calculating the differential Allan deviation. In order to derive the relation between d and d_{fit}, Monte-Carlo simulations are conducted using the specific evolution times employed in the measurement and for different test values of d. Out of the relation between inputted and yielded d, the relation between d and d_{fit} is yielded. The uncertainty of d is then again extracted from performing Monte-Carlo simulations. Looking at Fig. 9.19 (b), it is observed that the magnetic diffusion constant can vary by factors $\sqrt{d_1/d_2} > 4$ between different dates. When performing long unwrapping sequences as in Fig. 9.20, where 18 different evolution times were probed at an unwrapping cycle length of about 320 s, the diffusion constant d turned out to be one of the dominantly limiting parameters for the achievable frequency scatter.

9.7.3. PnA vs PnP phase scatter as a function of evolution time

After the PnP scheme [54] had been successfully demonstrated and main aspects had been characterized during the months of October and November 2019, we decided to investigate the PnA scheme [56] during the last three weeks left in December before the experiment had to be warmed up. In the PnA scheme, the upper sideband is used for mode coupling as described in Sec. 9.2.2. As the PnA scheme needs the same periphery as the PnP scheme, the main challenge consisted in finding optimal experimental settings or at least settings that enabled a reasonable application of this method. As little time was available during the commissioning phase, only a few results on applying the PnA scheme can be discussed here, but a detailed and thorough characterization remains to be the focus of further experimental campaigns.

In Fig. 9.20, the results of a comparison of phase scatters obtained with PnA and PnP is shown. To this end, blocks of 12 unwrapping cycles with either method were performed in an interleaved way, thereby securing identical conditions in the magnetic field diffusion and the magnetic field scatter. 18 different evolution times up to $t_{\mathrm{evo}} = 15\,\mathrm{s}$ were probed, leading to an unwrapping cycle length of 320 s and demonstrating phase coherence for evolution times of up to $t_{\mathrm{evo}} = 15\,\mathrm{s}$. The PnP data were acquired without the application of axial feedback, while for PnA very strong axial feedback resulting in a dip width $\delta\nu_z = 400\,\mathrm{mHz}$ was applied (feedback-free dip width $\delta\nu_z = 4.1\,\mathrm{Hz}$). For the PnP data, we obtained an axial temperature of $T_z = 18(3)\,\mathrm{K}$ by considering the principal scatter σ_0, and $T_z = 15(5)\,\mathrm{K}$ by examining the energy scatter related parameter

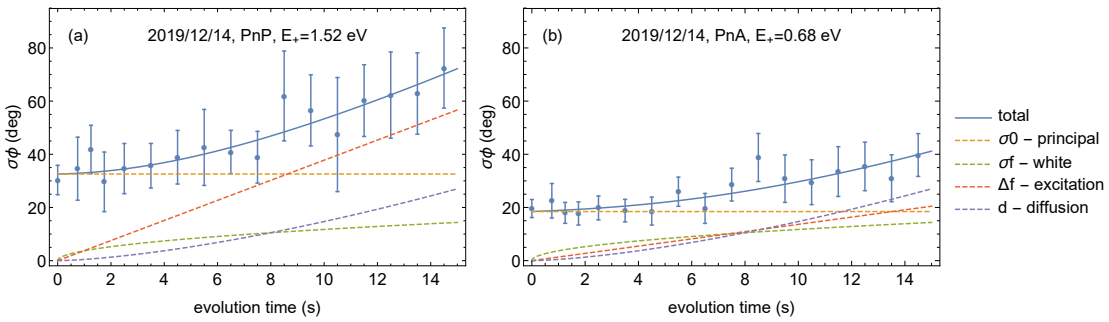

Figure 9.20.: Phase scatter as a function of evolution time obtained with the PnP scheme at an excitation energy of $E_{\mathrm{exc}} = 1.52\,\mathrm{eV}$ (left) and with the PnA scheme for an excitation energy of $E_{\mathrm{exc}} = 0.68\,\mathrm{eV}$ (right). Compared to the PnP scheme, the contribution due to excitation scatter Δ_f and the principal scatter σ_0 are significantly lower.

Δ_f. For the PnA data, $T_z = 4.5(3.8)\,\mathrm{K}$ is obtained from evaluating Δ_f, while a temperature based on σ_0 cannot be provided at this stage as the required model is still under development. Please note that the temperature ratio does not fully reflect the ratio of the two corresponding dip widths, which would be naively expected from theory (see Eq. 2.38). This is in line with observation from previous runs, where the application of very strong negative axial feedback led to additional axial temperature as noise from the feedback loop was coupled onto the resonator. While the PnP data were acquired with an excitation energy of $E_{\mathrm{exc}} = 1.52\,\mathrm{eV}$, the PnA data were acquired with $E_{\mathrm{exc}} = 0.68\,\mathrm{eV}$. Consequently, the excitation scatter contribution Δ_f to the PnA data is much smaller compared to the PnP. Due to the advantages of the PnA method, the principal scatter σ_0 of the PnA method is significantly lower compared to the PnP method despite of the higher PnP energy, which indicates the potential to perform even better measurements with PnA compared to PnP.

During the presented measurement, the cyclotron frequency was alternatingly measured twelve times by both methods. As a figure of merit for the frequency scatter we consider the standard deviation $\sigma(\Delta_{\mathrm{int}})$ between a measured frequency and the frequency interpolated from the two neighboring frequencies:

$$\sigma(\Delta_{\mathrm{int}}) = \sigma(\nu_{+,i} - \mathrm{Int}(\nu_{+,i-1}, \nu_{+,i+1})) \text{ for even } i, \tag{9.58}$$

with Int denoting the interpolated cyclotron frequency. By dedicated Monte-Carlo simulations, it can be shown that this value is by about 15 % underestimated due to corre-

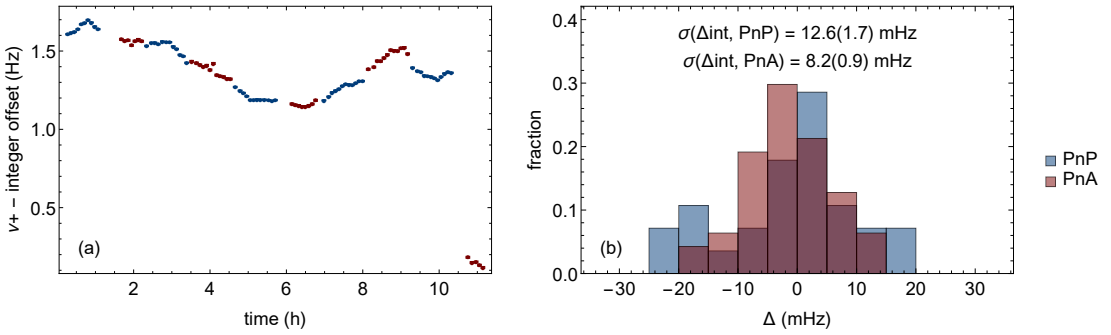

Figure 9.21.: Left: Cyclotron frequencies measured with the PnP scheme at an excitation energy of $E_{\mathrm{exc}} = 1.52\,\mathrm{eV}$ and with the PnA scheme for an excitation energy of $E_{\mathrm{exc}} = 0.68\,\mathrm{eV}$. Right: Interpolated Grubbs filtered frequency scatter obtained for both methods. The measurement depicted here is the same as depicted in Fig. 9.20.

lations related to the interpolation. For all given uncertainties and standard deviations on Δ_{int}, this 15 % is applied throughout this thesis unless otherwise stated.

We obtain Grubbs filtered values of $\sigma(\Delta\nu_+)_{\mathrm{int,PnP}} = 430(60)\,\mathrm{p.p.t.}$ and $\sigma(\Delta\nu_+)_{\mathrm{int,PnA}} = 280(30)\,\mathrm{p.p.t}$, as shown in Fig. 9.21. From the phase scatter shown in Fig. 9.20, a fundamental frequency uncertainty $\sigma_{\nu_+,\phi}$ can be calculated from

$$\sigma_{\nu_+,\phi} = \frac{\sigma_\phi}{360\,\mathrm{deg}} \times \frac{1}{t_{\mathrm{evo}}}. \tag{9.59}$$

From the weighted mean of all 17 individually unwrapped frequencies, $\sigma(\nu_+,\phi)_{\mathrm{PnP}} = 152\,\mathrm{p.p.t.}$ and $\sigma(\nu_+,\phi)_{\mathrm{PnA}} = 85\,\mathrm{p.p.t.}$ are yielded, which would correspond to $\sigma(\Delta\nu_+)_{\mathrm{int,PnP}} = 183\,\mathrm{p.p.t.}$ and $\sigma(\Delta\nu_+)_{\mathrm{int,PnA}} = 102\,\mathrm{p.p.t.}$ Note that $\sigma_{\nu_+,\phi}$ does not consider that the magnetic field changes during the unwrapping cycle due to diffusion, but only the changes due to the magnetic diffusion on the time scale of each individual unwrapping time. Consequently, $\sigma_{\nu_+,\phi}$ should be interpreted as the frequency scatter predicted for the magnetic diffusion being negligible on the time scale of an unwrapping cycle.

In order to predict the frequency uncertainty σ_{ν_+}, the magnetic diffusion that happens during the time t_{cyc} of one unwrapping cycle has to be considered as well. This contribution σ_d due to the diffusion constant d is estimated by

$$\sigma_d = e \times \sqrt{d \times t_{\mathrm{cyc}}}, \tag{9.60}$$

with the dimensionless parameter e accounting for dead time in the measurement sequence. e is determined from performing dedicated Monte-Carlo simulations to be $e \approx 0.85$. The frequency uncertainty is then given by the quadratic sum of the diffusion and the phase scatter contribution,

$$\sigma_{\nu_+} = \sqrt{\sigma^2_{\nu_+,\phi} + \sigma^2_d}. \tag{9.61}$$

Considering the measured values of $\sigma(\Delta\nu_+)_{\mathrm{int,PnA}} = 280(30)$ p.p.t and $\sigma(\Delta\nu_+)_{\mathrm{int,PnP}} = 430(60)$ p.p.t., a diffusion effect of $\sigma_d = 390(60)$ p.p.t. from the PnP data and $\sigma_d = 260(30)$ p.p.t. from the PnA data would be expected. The small discrepancy between both values might be explained by assuming that the diffusion constant fluctuates over time, and taking into account the comparably low number of measured frequencies in this data set, as seen in Fig. 9.21. In this measurement and also in most of the other phase unwrapping measurements conducted during the run with long evolution times, the diffusion effect leads to significantly larger frequency scatter values than the individual phase scatters, and thus represents the largest impediment to better phase measurements.

9.8. Frequency measurements by phase sensitive methods - experimental results

After having discussed the principle of phase unwrapping measurements and discussing how the measured frequency is limited by the phase scatter, this section will now focus on the resolution of frequency measurements by means of phase methods. Even though the experimental campaign focusing on the implementation of new measurements techniques was a pure technical run, and no physics measurements could be performed during this run, the results on frequency measurements by phase methods indicate the frequency resolution that can be achieved with the current experimental apparatus. This section will compare the phase methods stability with the frequency stability obtained by means of sideband method, which was so far the method of choice at the BASE collaboration. Subsequently, the frequency scatter with active and quenched self shielding coils will be compared. Afterwards, the best stability of the cyclotron frequency ratio measured at the BASE apparatus so far will be presented. This section concludes by discussing the frequency stability achieved in the BASE-CERN apparatus since the start in 2014 until now.

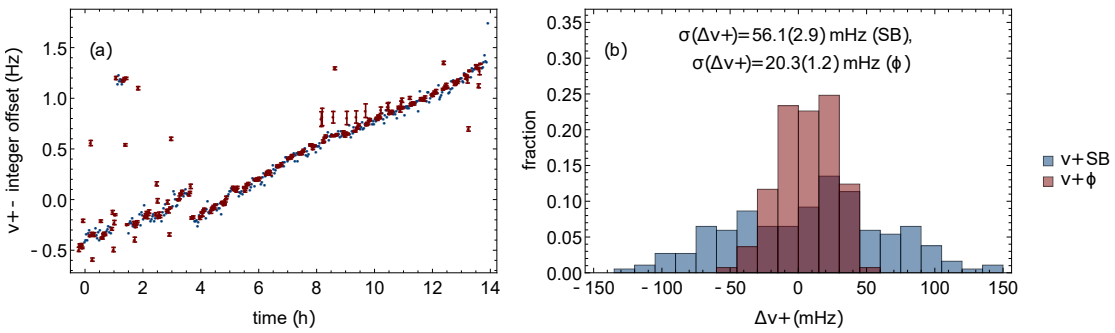

Figure 9.22.: Comparison between the PnP (red) and the sideband method (blue). LLeft: Measured cyclotron frequencies. Right: Grubbs filtered frequency scatter. The frequency scatter obtained with the phase method is a factor of 2.8(2) lower compared to the sideband method. The SSCs were quenched during these measurements.

9.8.1. Direct comparison between PnP and sideband measurements

After the phase methods were commissioned and frequency unwrapping measurements had been demonstrated, one of the first measurement ideas was to compare the PnP and the sideband method. To this end, we measured the cyclotron frequency in blocks of six frequencies sequentially by both methods. For PnP, we used an excitation energy of $E_{\mathrm{exc}} = 2.0(1)\,\mathrm{eV}$. The evolution times ranged from $t_{\mathrm{evo}} = 0.5\,\mathrm{s}$ to $t_{\mathrm{evo}} = 9\,\mathrm{s}$, with a total cycle length of $t_{\mathrm{cyc}} = 105\,\mathrm{s}$, thereby taking a similar amount of time as cyclotron frequency measurement by means of the sideband measurement, which consists of recording an axial dip and double dip on the axial spectrum, with a total duration of typically $t_{\mathrm{SB}} = 110\,\mathrm{s}$. The results of this measurement are depicted in Fig. 9.22, with (a) showing the measured frequencies, and (b) the frequency scatter $\sigma(\Delta\nu_+) = \sigma(\nu_{+,i+1} - \nu_{+,i})$. The frequency scatter of the PnP measured is a factor of 2.8(2) lower, which already is a substantial improvement. This improvement is explained by recalling that the sideband method is limited by the axial frequency stability, while the PnP methods yields a direct way for determining ν_+. The measurement was performed with all self-shielding coils [85] quenched. Note that the frequency resolution with the sideband method increases with $\propto 1/\sqrt{t_{\mathrm{avg}}}$, while the frequency resolution of the phase method increases with $\propto 1/t_{\mathrm{evo}}$ (compare Eq. 9.31), which is why the PnP method will perform even better compared to the sideband method when longer cycle times are investigated (as will be done in Sec. 9.8.3). It should also be noted that the cyclotron frequency is shifted by about $\Delta\nu_+ = 52\,\mathrm{mHz}$ for the PnP data due to the effects of special relativity, C_4 and

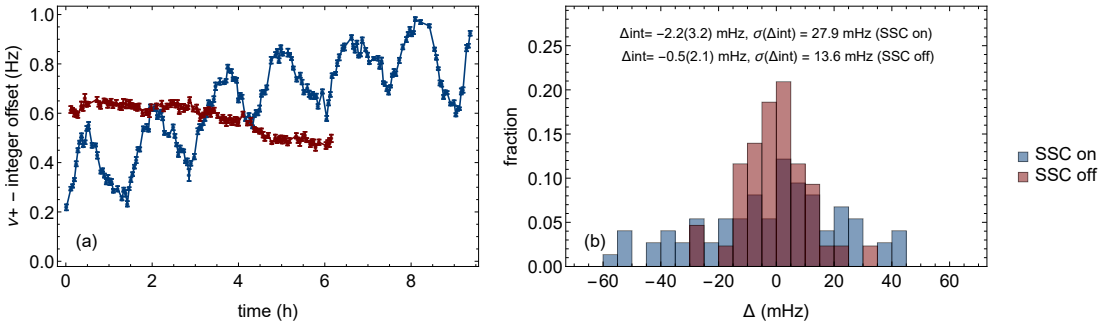

Figure 9.23.: Comparing frequency scatter as a function of the SSC status. Left: Cyclotron frequency measurements performed with the PnP methods at unwrapping times of up to $t_{evo} = 9\,\mathrm{s}$, a cycle length of $t_{\mathrm{cyc}} = 148\,\mathrm{s}$, and an energy of $E_{\mathrm{exc}} = 1.5(2)\,\mathrm{eV}$ for the SSC system being active (blue) and $E_{\mathrm{exc}} = 0.7(1)\,\mathrm{eV}$ for quenched SSCs (red). Right: Grubbs filtered results on the interpolated ratio $\sigma(\Delta\nu_+)_{\mathrm{int}}$ for both measurement types.

B_2. These frequency shifts will not be discussed here, but this section focuses exclusively on the frequency resolution. When performing a cyclotron frequency ratio measurement however, it will be very important to carefully characterize such effects. Before investigating longer evolution times, the effect of the self-shielding coil system, which impact on the achievable frequency resolution as outlined in Sec. 7.2.3, shall be investigated further.

9.8.2. SSC ON/OFF comparison

In context of the peak method measurement, it was observed that the cyclotron frequency stability was strongly influenced by the status of the self shielding coil system [85] (see Sec. 7.2.3). This behavior was quantitatively investigated with phase methods by performing frequency measurements with two protons, were the cyclotron frequencies of both particles were measured in an interleaved way, simulating the shuttling measurements known in context of the charge-to-mass ratio measurements on the antiproton [39]. On 2019/12/09, we conducted a PnP measurement with active coils, an excitation energy of $E_{\mathrm{exc}} = 1.5(2)\,\mathrm{eV}$ and evolution times of up to $t_{\mathrm{evo}} = 9$, but with more unwrapping points compared to the measurements described in Sec. 9.8.1, resulting in a cycle time of $t_{\mathrm{cyc}} = 148\,\mathrm{s}$. A PnA measured with an excitation energy of $E_{\mathrm{exc}} = 0.7(1)\,\mathrm{eV}$ and otherwise identical settings was repeated two days later for quenched SSCs. The results of both measurements are depicted in Fig. 9.23, with the

measured frequencies shown in (a). The interpolated frequency difference Δ_{int} as introduced in Eq. 9.58 is used as a measure for the obtained frequency resolution in Fig. 9.23 (b). While the first points of differential Allan deviations $\sigma_{\nu_+,\mathrm{SSC\ active}} = 40.8(2)\,\mathrm{mHz}$ and $\sigma_{\nu_+,\mathrm{SSC\ off}} = 15.3(1)\,\mathrm{mHz}$ vary by a factor of 2.7, the standard deviations of the interpolated frequencies, $\sigma((\Delta\nu_+)_{\mathrm{int,\ SSC\ active}}) = 26.1\,\mathrm{mHz}$ and $(\Delta\nu_+)_{\mathrm{int,\ SSC\ off}} = 11.8\,\mathrm{mHz}$, differ by about a factor of two. This is likely due to that long-term effects such as the periodic patterns caused by the active SSCs are slightly suppressed when computing the interpolated frequency difference $\Delta(\nu_+)_{\mathrm{int}}$. While the PnA method yields generally slightly lower frequency scatters compared to the PnP method (Sec. 9.7.3), this effect can be safely neglected at overall scatter values of around 1.3 p.p.b. for the frequency measurements conducted at active SSCs.
It is important to note here that every high resolution measurement performed during the phase methods run has been performed with quenched SSCs. However, cyclotron frequency measurements with quenched SSCs are only possible in magnetically quiet conditions, when the Antiproton Decelerator and the ELENA apparatus are not being operated, and the time-dependent stray magnetic field generated by other collaborations is negligible.

9.8.3. Most stable unwrapping measurement

In this section we will discuss the phase unwrapping measurement that yielded the lowest frequency scatter obtained during the phase methods run, which was of order $\sigma(\Delta\nu_+) = 280(20)\,\mathrm{p.p.t.}$ The results of this 10 hour long night measurement are depicted in Fig. 9.24. The PnP scheme was used for this measurement, with an excitation energy of $E_{\mathrm{exc}} = 1.5(2)\,\mathrm{eV}$, a maximum evolution time of $t_{\mathrm{evo}} = 15\,\mathrm{s}$, in total 18 different unwrapping times, and an unwrapping cycle length of $t_{\mathrm{cyc}} = 250\,\mathrm{s}$. In addition, particle transport has to be considered and waiting periods of a few seconds had been implemented after each measurement. In total, two unwrapping cycles are separated by about 265 s. As sideband frequency measurements and magnetron coolings were performed every twelve and every six cycles, the overall sampling rate during this measurement is lower than the inverse cycle length $1/t_{\mathrm{cyc}}$. In order to simulate a cyclotron frequency ratio measurement, the measurement was conducted using two protons, of which one is trapped in a parking electrode, and the other is located in the precision trap. After each unwrapping cycle, the parked ion was shuttled into the precision trap, and the

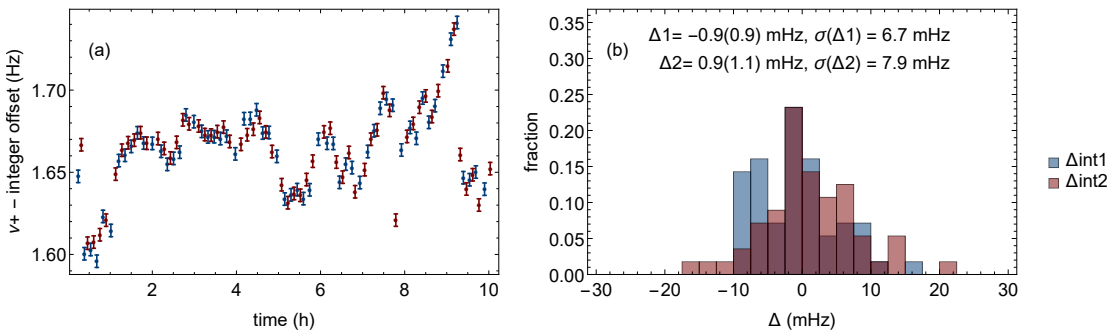

Figure 9.24.: Phase unwrapping measurement that yielded the highest cyclotron frequency resolution. Left: Measured cyclotron frequencies. The cyclotron frequency of two separate protons (denoted by red and blue dots respectively) was measured alternatingly, the ions were exchanged by adiabatic shuttling as for instance described in [39]. The frequency scatter $\sigma(\Delta\nu_+) = \sigma(\nu_{+,i+1} - \nu_{+,i})$ is given by $\sigma(\Delta\nu_+) = 280(20)$ p.p.t. A peak-to-peak stability of the cyclotron frequency of 150 mHz during the course of one night is unprecedented at BASE. This exceptionally good stability is reflected in the low corresponding diffusion constant depicted in Fig. 9.19 (b) (blue data). Right: Grubbs filtered results on the interpolated frequency difference. The obtained values correspond to a ratio scatter of 230 p.p.t. and 270 p.p.t. respectively.

previous measurement ion was transported into the other parking electrode (as done in [39]). Like in the previous section, the interpolated frequency difference Δ_{int} is used a measure for the obtained frequency resolution. After a total measurement time of 10 hours, we obtain $\Delta_{\text{int}} = -0.9(9)$ mHz and $\Delta_{\text{int}} = 0.9(1.1)$ mHz depending on which ion is considered to be the first or the second. Here, the 15 % correction in the uncertainty of Δ_{int} have already been applied as discussed in the previous section. The frequency scatter for this dataset is $\sigma(\Delta\nu_+) = 280(20)$ p.p.t. With the demonstrated resolution on Δ_{int}, a cyclotron frequency ratio measurement with a resolution of 20 p.p.t. would be achieved within around 24 hours of measurement time.

Future improvements of the presented unwrapping schemes

The measurement presented in Fig. 9.24 was set up following a conservative unwrapping scheme incorporating evolution times separated by only one second in order to make sure that the phase unwrapping would function under all circumstances, meaning that every phase jump of 360 degrees could be identified from the measured phases, as outlined in Fig. 9.10. This approach leads to comparably long unwrapping cycles times t_{cyc}. As has been discussed in Sec. 9.7.2 and Sec. 9.7.3, the achieved frequency scatter largely

depends on the magnetic diffusion constant, which can vary by more than a factor of 10 between two days. The scatter contribution scales $\propto \sqrt{d \times t_{\mathrm{cyc}}}$ (see Eq. 9.60). One way of counteracting this effect would be to introduce alternative unwrapping sequences with fewer points, leading to a shorter frequency cycle duration t_{cyc} and accordingly to a lower diffusion contribution to the measured frequency scatter.
During the PnP measurements described in this thesis, no axial feedback was applied during the sideband cooling of the cyclotron mode prior to the excitation. Implementing axial feedback here in the future will reduce the excitation scatter contribution Δ_f significantly.
Judging from the PnA phase scatter in Fig. 9.20, it should also be possible to measure at longer evolution times, which is favorable as the frequency scatter σ_{ν_+} increases with $1/t_{\mathrm{evo}}$ assuming identical phase scatter. For $t_{\mathrm{evo}} = 20\,\mathrm{s}$, we would obtain a phase scatter of $\sigma_\phi = 55\,\mathrm{deg}$, a phase scatter at which frequency unwrapping is still reasonably well possible. In order to improve upon the already excellent frequency scatter presented in Fig. 9.24, both avenues well be pursued in the future, for which the time was lacking at the end of this experimental campaign.

9.8.4. Resolution

The BASE experiment at CERN was approved in 2013 by CERN's research board. BASE conducted its first measurement campaign on the antiproton-to-proton charge to mass ratio already in 2014, with an unprecedented fractional precision of 69 p.p.t. reached by employing the sideband method [39]. The corresponding frequency scatter $\sigma(\Delta\nu_+)$ was of order 5.5 p.p.b. Afterwards, the experimental setup was partially reconstructed, and a custom-made superconducting magnet with high stability was implemented. During the sideband campaign in 2017, a significant scaling of the frequency scatter with the helium level in the cryostats was observed, with a maximum scatter of $\sigma(\Delta\nu_+) = 3.5\,\mathrm{p.p.b.}$ for full cryostats and a minimum frequency scatter of $\sigma(\Delta\nu_+) = 2.2\,\mathrm{p.p.b.}$ for low helium levels (see Fig. 3.2). In 2018, the apparatus was carefully revised, to which the author contributed by designing a new cryogenic support structure, introducing new heat shields on the 77 K stage, rearranging the electronic filter boards at the 77 K stage, as described in Sec. 3.2, and by implementing a frame around the experiment, which partly decoupled the experiment temperature from the ambient temperature and thereby enabled a much higher long-term frequency stability (see Sec. 3.2.2). As a result, no cyclotron

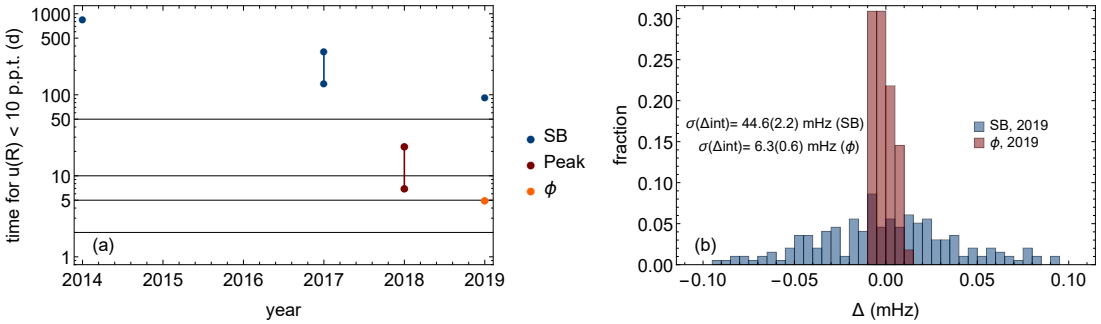

Figure 9.25.: Left: Measurement time in days required to reach a frequency ratio resolution of 10 p.p.t. for simulated ratio measurements based on the frequency stabilities summarized in Tab. 9.2. For the 2017 sideband run, a range of measurement time is given, as the cyclotron frequency scatter was varying between 3.5 p.p.b. and 2.2 p.p.b. depending on the filling level, as discussed in Sec. 3.2. Similarly, for the 2018 peak run, a range for scatter values between 500 p.p.t. (best measured values for quenched self shielding coils) and 900 p.p.t. (median scatter during the peak measurement campaign with active SSCs) is given. Right: Comparing the cyclotron frequency scatter measured during the sideband run in 2019 (blue data) and the phase run (red data). So, far the sideband method was the method of choice and enabled q/m measurements on the antiproton with a fractional precision of 25 p.p.t. (see Chap. 8). The ratio scatter obtained by phase methods is a factor of around 7 lower compared to the sideband method. Note that the sideband cycle time was $t_{\mathrm{cyc}} = 120\,\mathrm{s}$ and the phase cycle time was $t_{\mathrm{cyc}} = 265\,\mathrm{s}$. Thus, the fair improvement factor is $\sigma_{\mathrm{SB}}/\sigma_{\phi} \times \sqrt{t_{\mathrm{cyc,SB}}/t_{\mathrm{cyc},\phi}} = 5$.

frequency scatter scaling as a function of cryoliquid level could be observed any more, and the sideband scatter could be improved down to $\sigma(\Delta\nu_+) = 1.8\,\mathrm{p.p.b.}$ in 2019 for ideal conditions.

The sideband measurements are indirect cyclotron frequency measurements, which are fundamentally limited by the measurement resolution of the axial frequency as well as by the voltage source stability and by the magnetic field stability. Direct cyclotron frequency measurements are to first order only limited by the magnetic field stability. The first dedicated direct measurements in the BASE experiment were performed by means of the peak method in the 2018/2019 measurement campaign. Here, the best observed frequency scatters were on the order of 500 p.p.t., when all self shielding coils were quenched. For active SSCs, we observe much higher scatter values that could range from 800 p.p.t. to even more than 2 p.p.b. (see Fig. 7.14). During the phase run, we finally achieved a frequency scatter of about 280(20) p.p.t. at a shot-to-shot sampling rate of $1/(265\,\mathrm{s})$.

In order to quantify the improvements in experiment stability and attainable frequency

year	method	t_{meas}	$\sigma(\nu_+)$	$u(R)/\sqrt{t}$	$u(R)/\sqrt{t}$	$u(R)(1\,\mathrm{d})$
2014	sideband	120 s	5.5 p.p.b.	1.45 p.p.b./$\sqrt{\mathrm{h}}$	43 mHz/$\sqrt{\mathrm{h}}$	296 p.p.t.
2017	SB (max)	120 s	3.5 p.p.b.	920 p.p.t./$\sqrt{\mathrm{h}}$	27 mHz/$\sqrt{\mathrm{h}}$	187 p.p.t.
2017	SB (min)	120 s	2.2 p.p.b.	580 p.p.t./$\sqrt{\mathrm{h}}$	17 mHz/$\sqrt{\mathrm{h}}$	118 p.p.t.
2018	PK (med)	120 s	900 p.p.t.	240 p.p.t./$\sqrt{\mathrm{h}}$	7.1 mHz/$\sqrt{\mathrm{h}}$	49 p.p.t.
2018	PK (min)	120 s	500 p.p.t.	130 p.p.t./$\sqrt{\mathrm{h}}$	3.9 mHz/$\sqrt{\mathrm{h}}$	27 p.p.t.
2019	sideband	120 s	1.8 p.p.b.	470 p.p.t./$\sqrt{\mathrm{h}}$	14.0 mHz/$\sqrt{\mathrm{h}}$	97 p.p.t.
2019	phase	265 s	280 p.p.t.	110 p.p.t./$\sqrt{\mathrm{h}}$	3.2 mHz/$\sqrt{\mathrm{h}}$	22 p.p.t.

Table 9.2.: Simulated antiproton-to-proton charge-to-mass ratio resolution for the frequency stability demonstrated in different experimental campaigns. The frequency scatter values $\sigma(\Delta\nu_+)$ measured during the respective runs were taken as the basis for the simulation. $u(R)$ denotes the corresponding ratio uncertainty as a function of measurement time. The most right column is the ratio resolution after 1 day of measurement. For the 2017 sideband run (abbreviated with SB), the cyclotron frequency scatter was heavily dependent on the filling level ranged from 3.5 p.p.b. to 2.2 p.p.b.. For the 2019 sideband data, the 1.8 p.p.b. scatter did not show any dependency on the filling level as the experimental support was entirely redesigned as described in Sec. 3.2.1. The scatter of the 2018 peak run (abbreviated with PK) was strongly affected by ambient field fluctuations and the SSC status. For quenched SSCs and a calm ambient field, we observed scatters of 500 p.p.t. in the best cases. During measurement campaigns, the median shot-to-shot scatter during measurement blocks of 1 h was around 900 p.p.t. (see discussion in Sec. 7.2.3), the SSCs were active during these measurements. The frequency scatter of 280(20) p.p.t. quoted for the phase method is described in Sec. 9.8.3. It was achieved for a magnetically calm hall and quenched SSCs. The corresponding frequency stability constitutes a stability improvement of a factor of around 13 in scatter compared to the start of BASE in 2014.

resolution, we simulated frequency ratio measurements based on the respective frequency scatter values. The results of these simulations are depicted in Fig. 9.25, where the required measurement time in order to reach a ratio resolution of 10 p.p.t. is specified, and in Tab. 9.2, where the ratio resolution as a function of measurement time is given.
Note that for all of the simulated measurement schemes, occasional dead times, for instance for particle cleaning or magnetron cooling, have not been considered in the simulation for simplicity, only the pure measurement time and the transport time are taken into account. For the phase methods, the axial frequency measurement can be measured less frequently than the cyclotron frequency, but it needs to be measured occasionally, which is also not considered in this simulation. In the peak and the sideband scheme, the axial frequency is essentially needed for the cyclotron frequency determination, which is why its measurement time is considered in the quoted cycle times. Also note that the

shot-to-shot scatter of 500 p.p.t. for the peak method and 280 p.p.t. for the phase method could only be achieved in a magnetically calm hall and with quenched self shielding coils. With the current apparatus, the measurement performance is significantly worse during times when the SSCs have to be activated, for instance during the AD beam time. It should also be stated here that a number of systematic investigations have to be carried out before the phase methods could be used for performing a high-resolution measurement on the antiproton-to-proton charge-to-mass ratio. However, with the measurement resolution demonstrated in Sec. 9.8.3, a cyclotron frequency ratio measurement with a fractional resolution of at least 10 p.p.t. is feasible with a measurement time of only a few days.

10 | Summary and outlook

10.1. Summary

The claim of this thesis is to "Challenge the Standard Model by high precision comparisons of the fundamental properties of protons and antiprotons". To this end, the work of this thesis contributed to improving the BASE apparatus at CERN, characterizing the measurement apparatus and understanding relevant trap systematics. New measurement techniques were implemented, and a new measurement of one fundamental property of the antiproton was performed. The results of this thesis are summarized in the following bullet points:

- Improved the long-term stability and the shot-to-shot stability below the sideband limit by substantial apparatus revisions. The dominant source of frequency scatter given by pressure-fluctuation induced vibrations on the cryogenic stage was addressed by re-designing the cryogenic support structure, improving the heat shield structure on the 77 K stage and reducing the radiation heat load onto the 4 K stage from 685 mW to 285 mW (open beam port on the 77 K stage), and down to 155 mW (closed beam port). Prior to the upgrades, the experiment scatter was given by 3.5 p.p.b. - 1.8 p.p.b. depending on the cryoliquid level. Now, for the sideband method, the scatter is continuously limited on the 1.8 p.p.b. level (Chap. 3). The technical upgrades were proposed and supervised by Stefan Ulmer.
- Re-analyzed the data from the magnetic moment measurement campaign in 2015/ 2016, and published the first dedicated heating rate measurement in a cryogenic ion trap, which shows orders of magnitude lower scaled field noise compared to other ion traps [51] (Chap. 5).
- Carefully characterized and optimized the BASE Penning trap by means of axial

dip methods and cyclotron peak methods. The characterization by means of axial dip methods has been developed and discussed for instance in [72]. Some aspects of the peak method optimization such as the explicit measurement of D_4 (Sec. 7.2.4), the explicit measurement of the $B_2 \times T_z$-scaling implemented by the variation of axial feedback and peak methods (Sec. 7.2.5) are to the authors knowledge conceptually new and have been developed within this thesis in collaboration between Stefan Ulmer and the author. Also, a novel method for measuring the B_2 coefficient without cyclotron frequency measurements has been proposed and demonstrated by the author (Sec. 9.1.4). The Penning trap optimizations are mainly presented in Chap. 7.

- With the improved apparatus, the BASE collaboration conducted a sideband campaign on the antiproton-to-proton charge-to-mass ratio q/m by means of the sideband method in 2019 with a statistical resolution of 20 p.p.t and a precision of about 35 p.p.t., when statistics and systematics are considered. Together with several other experimental campaigns that are discussed in [52] and [53], these data will lead to a significantly improved antiproton-to-proton charge-to-mass ratio comparison. A publication is under preparation (Chap. 8).
- The implementation of phase sensitive methods for measuring the cyclotron frequency by means of the "Pulse and Probe" (PnP) scheme [54] and the "Pulse and Amplify" (PnA) scheme [56]. For a measurement time of 265 s, we achieved shot-to-shot scatters of around 280(20) p.p.t., which is a scatter improvement by a factor of about five compared to the sideband scatter measured in 2019. With the experiment stability here, an improved charge-to-mass ratio measurement with a fractional uncertainty of 10 p.p.t. becomes feasible, assuming a good understanding of the related measurement systematics, which has to be developed within the group. The improvement in frequency was only possible thanks to apparatus upgrades described in Sec. 3.2. The work on phase methods has been carried out in joined collaborative efforts of Jack Devlin and the author (Chap. 9).

10.2. Outlook

The future strategy of BASE has been laid out in 2019, when the BASE midterm proposal was submitted [42]. The improvements made in apparatus stability and the imple-

mentation of phase sensitive methods offer a lot of potential for dedicated measurement campaigns on the antiproton fundamental properties after the end of LS2, when antiprotons will be supplied again to the BASE apparatus. As a magnetic moment measurement is the likely candidate for the next high-precision measurement, the discussion in this section will mainly focus on this quantity. In the 2016 measurement of the antiproton magnetic moment [28], a fractional uncertainty of 1.5 p.p.b. was achieved, which improved upon the previous best measurement from BASE [38] by about a factor of 300. This measurement was the first antiproton magnetic moment measurement performed in a multi-ion trap scheme. In the "triple trap method", which was purposely developed for this measurement campaign [28], the Larmor frequency and the cyclotron frequency are measured by two different particles. This removes the necessity to cool the cyclotron mode to subthermal cyclotron energies after each measurement of the cyclotron frequency. These sub-thermal energies are needed in order to reduce the cyclotron heating rate (Eq. 5.12) and to resolve individual spin transitions. Compared to a double-trap scheme [91, 37, 29], additional systematic effects have to be considered since the axial temperature of the Larmor particle might differ from the axial temperature of the cyclotron particle during the respective measurements, which induced a systematic uncertainty of order 1 p.p.b. [47]. In the double trap method, both radio-frequency pulses can be irradiated at the same time to the identical particle. The cyclotron frequency scatter during the 2016 measurement campaign was around 4 p.p.b. With the 280 p.p.t. that were achieved within this work, a considerably improved magnetic moment would become possible.

10.2.1. ELENA interface

Prior to discussing the measurement precision achievable in antiproton campaigns after the long shutdown 2 (LS2), it is stressed that the implementation of the ELENA upgrade to the AD [161] requires a re-design of the antiproton catching setup. ELENA will further slow down the antiprotons ejected from the AD at 5.3 MeV to energies of 100 keV. One essential component of the current BASE degrader setup is a stainless steel vacuum window with 25 μm thickness, which is vacuum tight but transparent for antiprotons at 5.3 MeV. The corresponding aluminum window for antiprotons at 100 keV would have a thickness of 1.4 μm and would not be vacuum-tight at the given diameter of 9 mm for a pressure difference of $\Delta P = 1$ atm. This pressure difference necessarily occurs during

pre-pumping of the trap can prior to the experiment assembly. A careful and intricate re-design of the degrader section was performed by Barbara Latacz. The main design idea for the new degrader is to support the vacuum window with a metal disk at which in total seven holes with each 1 mm diameter are drilled. Thereby, the vacuum window with a diameter of 9 mm is effectively divided into seven small vacuum windows. While this improves the vacuum tightness dramatically, the total area of all vacuum windows is reduced by about 90 % compared to the previous vacuum window. This reduction is overcompensated due to the much higher trapping efficiency at lower injection energies. Under these conditions, a mylar foil with around 2 μm thickness that features 80 nm aluminum coatings on both sides is at the same time vacuum-tight and transparent for antiprotons at 100 keV. Careful tests for the leak-rate of the designed structure with overpressure of about 1 bar at room temperature and under cryogenic conditions have been performed and show excellent agreement with the design goals.

10.2.2. Cooling trap

A long desired upgrade to the BASE apparatus is the implementation of a dedicated cooling trap (CT) for ultra efficient cooling of the cyclotron mode [43], which has not been operated so far. The cooling trap will serve for fast cyclotron cooling and thereby enable much reduced preparation times for the application of the double trap technique. In order to enable fast cooling of the cyclotron motion, the trap features an inner diameter of 3.6 mm, like the analysis trap. The CT will be equipped with a dedicated cyclotron detector featuring a cooling time constant $\tau_+ = 10\,\mathrm{s}$. The CT is equipped with a magnetic bottle $B_2 = 16\,\mathrm{kT/m^2}$ for determining the cyclotron energy during after each mode thermalization cycle [90]. The cooling trap will be implemented as part of the PhD project of Markus Fleck [194]. Once implemented, the cooling trap will reduce the average preparation time for reaching sufficiently low subthermal energies from about 15 h to about 2 h. This assumes that 70 cooling cycles are needed on average for particle preparation, which is a typical number of thermalization cycles given the typical electric-field noise amplitudes and detector temperatures at BASE. A fast method for preparing particles at very low cyclotron energies would also be of great use for the application of phase sensitive methods (Sec. 9.7.1).

10.2.3. Minimized residual B_2 by redesigned transport section and in-situ shim coil

Another substantial and very promising upgrade will be the implementation of a dedicated in-situ B_2 shimming coil, that is designed to entirely suppress the residual B_2 in the precision trap. This implementation will be realized in a new-designed multi-layer SSC setup, incorporating as well a dedicated B_1-shimming coil and three self-shielding coils. In the 2016 measurement, a $B_{2,\mathrm{res}} = 2.7(3)\,\mathrm{mT/m^2}$ was measured [47], where the distance between analysis trap and precision trap was 49 mm. In the new setup, the transport electrode section between the precision trap and the analysis trap has been redesigned yielding a distance of 74 mm between both traps and reduces the residual $B_{2,\mathrm{res}}$ by about a factor of about 8 according to simulations. The experiment will strongly profit from a reduced residual $B_{2,\mathrm{res}}$, as $B_{2,\mathrm{res}}$ induces undesired cyclotron frequency shifts that scale with the axial energy. This would especially hamper the implementation of phase sensitive methods. This work is also of great interest for charge-to-mass ratio measurements, as it will allow to measure the cyclotron frequency ratio as a function of the B_2 coefficient, which opens up great opportunities for the investigation of systematic uncertainties. The work described in this section is part of the PhD project of Stefan Erlewein [195].

10.2.4. Seven-pole trap

Another upgrade envisioned for the future is the implementation of a seven-pole Penning trap. While in the five-pole design (Sec. 2.2), one set of correction electrodes is used, in the seven-pole design a second pair of correction electrodes is introduced. While the five-pole trap in orthogonal and compensated design [71] allows in principle to tune the C_4 and the C_6 parameter simultaneously to zero, in a seven-pole Penning trap also the C_8 and C_10 parameters could be tuned to zero thanks to the additional degree of freedom in the trap potential configuration. A better control of higher-order trap coefficients would be beneficial for the application of phase methods, as potentially higher particle energies and thus better SNRs could be realized (compare Sec. 9.6.2 and Sec. 9.6.3). A seven-pole trap has been demonstrated in the SMILETRAP experiment [196], and in the LIONTRAP experiment for the proton mass-measurement in 2017 [159].

10.2.5. Transportable antiproton trap

Despite the continuous efforts in apparatus stabilization, a particle accelerator will never be an ideal place for conducting high-precision radio-frequency spectroscopy experiments on charged particles in Penning traps. Our experiment stability is affected by ambient magnetic ramps and kicks, high voltage ramps, strong radio-frequency noise and strong temperature fluctuations. BASE is counteracting these effects for instance by implementing a multi-layer self shielding coil system with a high shielding factor of $S = 225(15)$ [85] and by introducing a multi-layer passive temperature shielding. In order to perform antiproton measurements under the best ambient conditions possible, the BASE-STEP project (Symmetry Tests in Experiments with Portable antiprotons) lead by Christian Smorra is developing a transportable trap for antiprotons [42]. Recently, BASE-STEP was awarded with an ERC starting grant. Once ready, BASE will be able to conduct high-precision measurements on antimatter in a dedicated high-precision laboratory, which will temperature stabilized and far away from stray magnetic fields and radio-frequency noise.

10.2.6. Future precision goals

Considering the apparatus improvements outlined in Chap. 3 and the demonstrated sideband frequency scatter of 1.8 p.p.b., a magnetic moment measurement with a fractional uncertainty of at least 200 p.p.t. should be possible with the current apparatus. This would be a slightly better precision compared to the 300 p.p.t. achieved in the BASE sister experiment in Mainz in 2017, where the double trap method was employed for the proton magnetic moment measurement [29, 75]. In this measurement, the cyclotron frequency was measured by means of sideband methods, and no cooling trap was implemented into the setup.

On longer time scales, after successful implementation of the cooling trap, of a B_2 shim coil in the precision trap, and the implementation of phase methods, another improvement of the fractional resolutions seems feasible according to the author's estimation.

For the charge-to-mass ratio, the achieved cyclotron frequency shot-to-shot stability of order 280(20) p.p.t. (Sec. 9.8.3) for a measurement time of $t_{\mathrm{cyc}} = 265\,\mathrm{s}$ has already briefly been discussed in Sec. 9.8.4. Assuming a magnetically calm hall, and assuming that systematic effects of phase methods will be understood well enough, a charge-to-mass ratio comparison between the proton and the antiproton with a fractional precision of 10 p.p.t.

or better seems feasible with the experimental developments outlined in this thesis. It shall be stressed here that shot-to-shot cyclotron frequency scatter values of a few hundred p.p.t. were only achieved during magnetically calm conditions, while the cyclotron frequency scatter was usually of order 900 p.p.t. and higher when the SSCs were active. Under such conditions, an improvement in the charge-to-mass ratio would require an extended amount of measurement time, but an improvement of the magnetic moment to the 200 p.p.t.-level should be feasible even under such conditions. Currently, the BASE magnet is operated at $B_0 \approx 2\,\mathrm{T}$, but can be tuned up to $B_0 \approx 5\,\mathrm{T}$, which yields the potential to increase the measurement precision again by a factor of 2.5.

Acknowledgments

Stefan Ulmer, im Februar 2014 durfte ich zuächst als Bachelorand für einige Monate Teil von BASE werden. Aus diesen Monaten sind nun insgesamt sieben Jahre geworden, in denen ich unglaublich viel von Dir lernen durfte. Ich danke Dir für die umfassende und intensive Betreuung bei der experimentellen Arbeit und beim Schreiben dieser Doktorarbeit, Deinen Einsatz und Hingabe, Dein Vertrauen in meine Stärken, und dafür, dass Du mir wortwörtlich jederzeit mit Rat und Tat zur Seite gestanden bist. In diesen Jahren hast Du mich gefördert, mich inspiriert, und mir ein physikalisches Zuhause gegeben, wo ich mich wohlfühlen konnte. Ich denke gerne zurück an abendliche Diskussionen im CERN R1, an sommerliche Grillabende und winterliches Raclette. Es war mir eine große Ehre und eine große Freude, bei BASE zu arbeiten und Teil dieser phantastischen Kollaboration sein zu dürfen! Ich wünsche Dir und dem Experiment alles erdenklich Gute und bin sehr gespannt, welche großartigen Fortschritte und Messungen am Experiment in Zukunft erreicht werden.

Christian Ospelkaus, Dir danke ich sehr herzlich für die umfassende Betreuung meiner Doktorarbeit von Hannover aus, für die Unterstützung meiner Arbeit und dafür, dass Du immer ein offenes Ohr hattest. Auch wenn wir uns aufgrund der räumlichen Entfernung leider nur sehr selten gesehen haben, so war es doch jedes mal eine große Freude, Dich zu treffen, mit Dir über Physik zu sprechen, Neues aus Deinem großen Wissens- und Erfahrungsschatz zu lernen, oder gemeinsam im Wallis unterwegs zu sein. Ich wünsche Dir viel Erfolg bei allen Projekten und im Quantum Valley, und bin sehr darauf gespannt, wann es die ersten großen Quatencomputer made in Niedersachsen gibt!

Fritz Riehle, Ihnen danke ich sehr herzlich für die Zweitbetreuung meiner Promotion, für die vetrauensvolle Kommunikation, für die Treffen an der PTB inklusive der schönen Touren durch die PTB. Ebenso danke ich Ihnen besonders für das detaillierte Korrekturlesen meiner Doktorarbeit und die vielen Anmerkungen dazu!

Klemens Hammerer, Ihnen danke ich für die Übernahme des Prüfungsvorsitzes meiner Disputation.
Herzlich möchte ich mich bei *Frau Faber*, *Frau Ludwig* und *Frau Ohlendorf* für die administrative Unterstützung aus dem IQO, der PTB und der QUEST-LFS bedanken!
Many thanks as well to *Megumi Morita* from RIKEN/Japan for all the administrative support and help!

I would like to express my grateful thanks to all BASE team members for being such a wonderful team, for all the help and support that I have received during the past seven years, and for all the joy we had together! It was a pleasure to be part of such a great collaboration and team!
Thanks a lot to *Mustafa Bersirli*, *Pascal Blessing*, *James Brydges-Harrington*, *Jack Devlin*, *Stefan Erlewein*, *Markus Fleck*, *Takashi Higuchi*, *Kurt Franke*, *Barbara Latacz*, *Jonathan Morgner*, *Andreas Mooser*, *Hiroki Nagahama*, *Motoki Sato*, *Georg Schneider*, *Stefan Sellner*, *Christian Smorra*, *Toya Tanaka*, *Jan Warncke*, *Elise Wursten*.

Thanks a lot also to my colleagues from BASE-Hannover, *Amado Bautista-Salvador*, *Juanma Cornejo*, *Julia-Aileen Fenske*, *Teresa Meiners*, *Johannes Mielke*, *Malte Niemann* and *Anna-Greta Paschke*, and to my colleagues from BASE-Mainz, *Matthew Bohmann*, *Christian Will*, *Markus Wiesinger*, for working on the same project and for having great discussions whenever we had the chance to meet at conferences and seminars!

I would like to especially thank my colleagues
James Brydges-Harrington, for spending endless hours together in the zone, for fighting with a broken transfer line during Helium filling in the night, for doing many measurements together with me when I started in the zone, for having endless conversations about virtually any topic and for educating me on British humor!
Jack Devlin, for your willingness to assist in any way, for the great collaboration on the implementation of phase methods, for sharing lots of excellent Mathematica notebooks with me, and for your dedicated proofreading of my thesis, especially the phase methods chapter!
Christian Smorra, for teaching me many things in the zone and in the lab, for providing guidance and feedback, for not taking my excuses seriously when I was trying to escape

our running exercise, and for having wonderful runs in the vineyards around CERN!
Elise Wursten and *Barbara Latacz* for not only bringing a flowery and lively touch to our office, but also contributing so thoroughly through your comments and emails/chats!
My office mates, *Pascal Blessing*, *Jonathan Morgner*, and *Hiroki Nagahama* for bearing with me, the chaos on my desk and my favour for freezing office ventilation!

I would also like to acknowledge support and thank RIKEN/Ulmer Fundamental Symmetries Lab, Physikalisch-Technische Bundesanstalt, University of Hannover/Institute for Quantum Optics for funding, enabling and supporting my work! Also many thanks to CERN for being a place that allows to do such amazing research, and enabling cooperation across borders!

Ebenso danke ich der Konrad-Adenauer-Stiftung/dem BMBF und der Graduiertenakademie der Leibniz Universität Hannover für die Förderung meiner Promotion.

Ich danke auch meiner Familie, meiner Mutter *Marina* und meinem Vater *Eckhard*, der den Abschluß meiner Promotion gerne noch miterlebt hätte, meiner Schwester *Elisabeth*, und ebenso *Alicas* Mutter *Isabella* und *Alicas* Großeltern *Anneliese* und *Waldemar*, von Herzen für die Begleitung meiner Doktorarbeit mit großer Anteilnahme, die Unterstützung fernab von physikalischen Fragestellungen, die ebenso zum Erfolg dieser Arbeit beigetragen haben. Schön, dass es Euch gibt und Ihr immer zu mir steht!
Liebe *Alica*, das schönste Resultat dieser Doktorarbeit ist, dass ich Dich in Genf kennenlernen durfte! Danke, dass wir unser Leben miteinander teilen und danke, dass Du mich von Zeit zu Zeit daran erinnerst, dass “time is measured not by clocks but in moments”.

Appendices

A | On the use of the words “precision” and “accuracy” throughout this thesis

Sometimes a distinction between the terms “precision” and “accuracy” is made in physics, with “precision” denoting the statistical resolution of a measurement, and with “accuracy” denoting the knowledge about systematic shifts. In the context of comparisons of matter/antimatter conjugates, a precise but inaccurate measurement would not reveal meaningful information for testing the CPT invariance. Therefore, the term precision in this thesis denotes the uncertainty of a measurement after correction for known systematic effects. The precision/the overall measurement uncertainty is then given jointly from the statistical resolution and the systematic uncertainty. This is in line with the conventions used in all BASE measurements published so far [37, 38, 28, 29].

B | Frequency shifts due to anharmonicity coefficients - perturbation matrices

$$\mathcal{M}_{C8} = \frac{35}{32}\frac{C_8}{C_2^4}\left(\frac{1}{qV_r}\right)^3 \times$$
$$\begin{pmatrix} \Omega^8 & -4\Omega^2 & 32\Omega^2 & -12\Omega^6 & 24\Omega^6 & 18\Omega^4 & 72\Omega^2 & 72\Omega^4 & -144\Omega^2 & -144\Omega^4 \\ -4\Omega^6 & 1 & -32 & 18\Omega^4 & -72\Omega^4 & -12\Omega^2 & -24 & -144\Omega^2 & 72 & 144\Omega^2 \\ 4\Omega^8 & -4\Omega^2 & 8\Omega^2 & -36\Omega^6 & 36\Omega^6 & 36\Omega^4 & 36\Omega^2 & 48\Omega^4 & -48\Omega^2 & -144\Omega^4 \\ 0 & 0 & 0 & 0 & 0 & 0 & 0 & 0 & 0 & 0 \end{pmatrix} \tag{B.1}$$

The shift due to C_8 is given by

$$\begin{pmatrix} \Delta\omega_+/\omega_+ \\ \Delta\omega_z/\omega_z \\ \Delta\omega_-/\omega_- \\ \Delta\omega_L/\omega_L \end{pmatrix} = \mathcal{M}_{C8}\times \tag{B.2}$$
$$\begin{pmatrix} E_+^3 & E_z^3 & E_-^3 & E_+^2E_z & E_+^2E_- & E_+E_z^2 & E_z^2E_- & E_+E_-^2 & E_zE_-^2 & E_+E_zE_- \end{pmatrix}^\intercal .$$

The shift matrices for C_4, C_6, C_8 and B_2 can also be specified in terms of the oscillations amplitudes [68, 74]:

$$\begin{pmatrix} \Delta\omega_+/\omega_+ \\ \Delta\omega_z/\omega_z \\ \Delta\omega_-/\omega_- \\ \Delta\omega_L/\omega_L \end{pmatrix} = (\mathcal{M}_{C4} + \mathcal{M}_{B2}) \begin{pmatrix} \rho_+^2 \\ z^2 \\ \rho_-^2 \end{pmatrix} + \mathcal{M}_{C6} \begin{pmatrix} \rho_+^4 \\ z^4 \\ \rho_-^4 \\ \rho_+^2 z^2 \\ \rho_+^2 \rho_-^2 \\ z^2 \rho_-^2 \end{pmatrix} + ... \tag{B.3}$$

The matrices are given by

$$\begin{aligned} \mathcal{M}_{C4} &= \frac{3}{4}\frac{C_4}{C_2} \begin{pmatrix} \Omega^2 & -2\Omega^2 & 2\Omega^2 \\ -2 & 1 & -2 \\ -4 & 4 & -2 \\ 0 & 0 & 0 \end{pmatrix} \qquad \mathcal{M}_{B2} = \frac{1}{2}\frac{B_2}{B_0} \begin{pmatrix} -1 & 1 & -1 \\ 1/\Omega^2 & 0 & 1/2 \\ 1 & -1 & 1 \\ \Omega^2/2 & 1 & -1 \end{pmatrix} \\ \mathcal{M}_{C6} &= \frac{15}{16}\frac{C_6}{C_2} \begin{pmatrix} -\Omega^2 & -3\Omega^2 & -3\Omega^2 & 6\Omega^2 & -6\Omega^2 & 12\Omega^2 \\ 3 & 1 & 3 & -6 & 12 & -6 \\ 6 & 6 & 2 & -24 & 12 & -12 \\ 0 & 0 & 0 & 0 & 0 & 0 \end{pmatrix}, \end{aligned} \tag{B.4}$$

with $\Omega = \omega_z/\omega_+$.

$$\begin{aligned} \mathcal{M}_{C8} &= \frac{35}{32}\frac{C_8}{C_2}\times \\ &\begin{pmatrix} \Omega^2 & -4\Omega^2 & 4\Omega^2 & -12\Omega^2 & 12\Omega^2 & 18\Omega^2 & 36\Omega^2 & 18\Omega^2 & -36\Omega^2 & -72\Omega^2 \\ -4 & 1 & -4 & 18 & -36 & -12 & -12 & -36 & 18 & 72 \\ 8 & -8 & 2 & -72 & 36 & 72 & 36 & 24 & -24 & -144 \\ 0 & 0 & 0 & 0 & 0 & 0 & 0 & 0 & 0 & 0 \end{pmatrix} \end{aligned} \tag{B.5}$$

The shifts due to C_8 are given by

$$\begin{pmatrix} \Delta\omega_+/\omega_+ \\ \Delta\omega_z/\omega_z \\ \Delta\omega_-/\omega_- \\ \Delta\omega_L/\omega_L \end{pmatrix} = \mathcal{M}_{C8}\times \\ \begin{pmatrix} \rho_+^6 & z^6 & \rho_-^6 & \rho_+^4 z^2 & \rho_+^4\rho_-^2 & \rho_+^2 z^4 & z^4\rho_-^2 & \rho_+^2\rho_-^4 & z^2\rho_-^4 & \rho_+^2 z^2\rho_-^2 \end{pmatrix}^{\mathsf{T}} \tag{B.6}$$

C | Full derivation of noise driven quantum transition by perturbation theory

Eq. 5.8 is derived using perturbation theory in the interaction picture [123, 124]. The Hamiltonian is described as

$$\hat{H} = \hat{H}_0 + \hat{V}(t), \tag{C.1}$$

where $\hat{H}_0$ is the time independent Penning trap Hamiltonian, the time-dependent perturbing potential $\langle \hat{V}(t) \rangle$ is small compared to $\langle \hat{H}_0 \rangle$ and $\langle \hat{V}(t) \rangle = 0$ for $t \leq t_0$. In the interaction picture, the Schrödinger equation is given by

$$i\hbar \frac{\partial}{\partial t} |\psi^0, t\rangle = \hat{H}_0 |\psi^0, t\rangle . \tag{C.2}$$

When the perturbation interacts with the system, the new state $|\psi, t\rangle$ is described by

$$i\hbar \frac{\partial}{\partial t} |\psi, t\rangle = \left[\hat{H}_0 + \hat{V}(t)\right] |\psi, t\rangle . \tag{C.3}$$

In the interaction picture, the states $|\psi, t\rangle_I$ are given by

$$|\psi, t\rangle_I = e^{i\hat{H}_0 t/\hbar} |\psi, t\rangle \tag{C.4}$$

One obtains the Schrödinger equation in the interaction picture by

$$i\hbar \frac{\partial}{\partial t} |\psi, t\rangle_I = -\hat{H}_0 |\psi, t\rangle_I + e^{i\hat{H}_0 t/\hbar} \left[\hat{H}_0 + \hat{V}(t)\right] |\psi, t\rangle \tag{C.5}$$

which is equivalent to

$$i\hbar\frac{\partial}{\partial t}\left|\psi,t\right\rangle_I = \hat{V}_I(t)\left|\psi,t\right\rangle_I, \tag{C.6}$$

the perturbation operator in the interaction picture $\hat{V}_I(t)$ is given by

$$\hat{V}_I(t) = e^{i\hat{H}_0 t/\hbar}\hat{V}(t)e^{-i\hat{H}_0 t/\hbar}. \tag{C.7}$$

The state results in

$$\left|\psi,t\right\rangle_I = \left|\psi,t_0\right\rangle_I + \frac{1}{i\hbar}\int_{t_0}^{t} dt'\hat{V}_I(t')\left|\psi,t'\right\rangle \tag{C.8}$$

which can be expanded to the so called Neumann-series

$$\begin{aligned}\left|\psi,t\right\rangle_I = \left|\psi,t_0\right\rangle_I &+ \frac{1}{i\hbar}\int_{t_0}^{t} dt'\hat{V}_I(t')\left|\psi,t_0\right\rangle_I \\ &+ \frac{1}{(i\hbar)^2}\int_{t}^{t_0} dt'\int_{t_0}^{t'} dt''\hat{V}_I(t')\hat{V}_I(t'')\left|\psi,t_0\right\rangle_I + ...\end{aligned} \tag{C.9}$$

Now first order transitions will be described. The initial state is $\left|\psi,t\right\rangle = \exp(-iH_0t/\hbar)\left|i\right\rangle = \left|i\right\rangle_I$. The evolution is given by

$$\left|\psi,t\right\rangle = \left|i\right\rangle + \frac{1}{i\hbar}\int_{t_0}^{t} dt'\hat{V}_I(t')\left|i\right\rangle. \tag{C.10}$$

the transition amplitude $\left|i\right\rangle \rightarrow \left|f\right\rangle$ follows directly

$$\left\langle f|\psi,t\right\rangle = \delta_{f,i} + \frac{1}{i\hbar}\int_{t_0}^{t} dt' e^{i(E_i-E_f)t'/\hbar}\left\langle f\right|\hat{V}(t')\left|i\right\rangle. \tag{C.11}$$

The transition probability $p_{i\rightarrow f}$ is given by the square of the absolute value of the rate:

$$p_{i\rightarrow f} = \left|\left\langle f|\psi,t\right\rangle\right|^2 = \frac{1}{\hbar^2}\left|\int_{t_0}^{t} dt' e^{i(E_f-E_i)t'/\hbar}\left\langle f\right|\hat{V}(t')\left|i\right\rangle\right|^2 \tag{C.12}$$

the perturbation operator $\hat{V}$ is expanded in a Taylor series as electric field noise might be present in terms of zero-th order field noise, gradient field noise, and higher order field noise,

$$\hat{V}(t,x) = q\left(E_0(t,x)\hat{x} + E_1(t,x)\hat{x}^2 + \mathcal{O}\left(\hat{x}^3\right)\right), \tag{C.13}$$

with particle charge q and position operator $\hat{x}$. In a harmonic oscillator the position operator can be rewritten in terms of ladder operators $\hat{a}$ and $\hat{a}^\dagger$,

$$\hat{x} = \sqrt{\frac{\hbar}{2m\omega}} \left(\hat{a} + \hat{a}^\dagger\right). \tag{C.14}$$

The annihilation operator $\hat{a}$ subtracts one oscillation quantum, the creation operator $\hat{a}^\dagger$ adds one.

$$\hat{a} \left|n\right\rangle = \sqrt{n} \left|n-1\right\rangle \tag{C.15}$$

$$\hat{a}^\dagger \left|n\right\rangle = \sqrt{n+1} \left|n\right\rangle \tag{C.16}$$

The transition matrix elements $\langle f| \hat{V} \left|i\right\rangle$ follows as:

$$\langle f| \hat{V}(t) \left|i\right\rangle = qE_{j-1}(t) \left(\frac{\hbar}{2m\omega}\right)^{j/2} \sqrt{f + \frac{1}{2} + \frac{j}{2}}, \qquad j = f - i. \tag{C.17}$$

Here only perturbation operator terms of order j are considered, since transitions of order $j+2n$ are strongly suppressed. The first order transition rate $\Gamma_{i\to i\pm1}$ is calculated:

$$\begin{aligned} \Gamma_{i\to i\pm} &= \frac{1}{T} \left|\langle i \pm 1|\psi, t\rangle\right|^2 \\ &= \frac{1}{T} \left| \frac{1}{i\hbar} \int_0^T dt' \left\langle i \pm 1\right| qE_0(t', x)\hat{x} \left|f \pm 1\right\rangle e^{i\omega_m t'} \right|^2. \end{aligned} \tag{C.18}$$

The averaging time T is short compared to the time scale over which the level population changes, but it is large compared to the correlation time of the electric field noise E_i. Therefore it is justified to treat the transition matrix elements as constants, and to extend T to $+\infty$ [125], which brings us to Eq. 5.8:

$$\begin{aligned} \Gamma_{i\to i\pm1} &= \frac{q^2}{\hbar^2} \left|\left\langle i \pm 1\right| \hat{x} \left|i\right\rangle\right|^2 \cdot \frac{1}{T} \left| \int_0^T dt' E_0(t', x) e^{i\omega_m t'} \right|^2 \\ &= \frac{q^2}{\hbar^2} \left|\left\langle i \pm 1\right| \hat{x} \left|i\right\rangle\right|^2 \cdot \lim_{T\to\infty} \frac{1}{T} \left| \int_0^T dt' E_0(t', x) e^{i\omega_m t'} \right|^2 \\ &= \frac{q^2}{2\hbar m\omega} \left(i + \frac{1}{2} \pm \frac{1}{2}\right) \int_0^\infty dt' e^{i\omega_m t'} \left\langle E_0(t) E_0(t+t')\right\rangle, \end{aligned} \tag{C.19}$$

with ω_m denoting the frequency of the considered mode m.

Bibliography

[1] F. Abe and others, on behalf of the CDF Collaboration. Observation of Top Quark Production in $\bar{p}p$ Collisions with the Collider Detector at Fermilab. *Physical Review Letters*, 74(14):2626–2631, April 1995.

[2] S. Abachi and others, on behalf of the D0 Collaboration. Search for High Mass Top Quark Production in $\bar{p}p$ Collisions at $\sqrt{s} = 1.8\,\text{TeV}$. *Physical Review Letters*, 74(13):2422–2426, March 1995.

[3] G. Aad and others, on behalf of the ATLAS collaboration. Observation of a new particle in the search for the Standard Model Higgs boson with the ATLAS detector at the LHC. *Physics Letters B*, 716(1):1–29, September 2012.

[4] S. Chatrchyan and others, on behalf of the CMS collaboration. Observation of a new boson at a mass of 125 GeV with the CMS experiment at the LHC. *Physics Letters B*, 716(1):30–61, September 2012.

[5] Paul Adrien Maurice Dirac and Ralph Howard Fowler. A theory of electrons and protons. *Proceedings of the Royal Society of London. Series A, Containing Papers of a Mathematical and Physical Character*, 126(801):360–365, January 1930. Publisher: Royal Society.

[6] Paul Adrien Maurice Dirac and Ralph Howard Fowler. The quantum theory of the electron. *Proceedings of the Royal Society of London. Series A, Containing Papers of a Mathematical and Physical Character*, 117(778):610–624, February 1928. Publisher: Royal Society.

[7] Carl D. Anderson. The Positive Electron. *Physical Review*, 43(6):491–494, March 1933. Publisher: American Physical Society.

[8] E. Stückelberg. La signification du temps propre en mécanique ondulatoire. *Helv. Phys. Acta*, 14:322–323, 1941.

[9] R. P. Feynman. Space-Time Approach to Non-Relativistic Quantum Mechanics. *Reviews of Modern Physics*, 20(2):367–387, April 1948. Publisher: American Physical Society.

[10] Julian Schwinger. The Theory of Quantized Fields. I. *Physical Review*, 82(6):914–927, June 1951. Publisher: American Physical Society.

[11] G. Lüders. On the equivalence of invariance under time reversal and under particle-antiparticle conjugation for relativistic field theories, 1954. Institution: CERN-PRE-54-7 Pages: 1-17 Volume: 28.

[12] Wolfgang Pauli. *Niels Bohr and the development of physics: essays dedicated to Niels Bohr on the occasion of his seventieth birthday.* Pergamon Press, London, 1955.

[13] P. a. R. Ade and others, on behalf of the Planck collaboration. Planck 2015 results - XIII. Cosmological parameters. *Astronomy & Astrophysics*, 594:A13, October 2016. Publisher: EDP Sciences.

[14] F. Capozzi, E. Lisi, A. Marrone, D. Montanino, and A. Palazzo. Neutrino masses and mixings: Status of known and unknown 3ν parameters. *Nuclear Physics B*, 908:218–234, July 2016.

[15] Michael Dine and Alexander Kusenko. Origin of the matter-antimatter asymmetry. *Reviews of Modern Physics*, 76(1):1–30, December 2003.

[16] A. D. Sakharov. Violation of CP Invariance, C asymmetry, and baryon asymmetry of the universe. *JETP Lett.*, 5:24–27, 1967.

[17] J. H. Christenson, J. W. Cronin, V. L. Fitch, and R. Turlay. Evidence for the 2π Decay of the K_0^2 Meson. *Physical Review Letters*, 13(4):138–140, July 1964.

[18] B. Aubert and others, on behalf of the BABAR Collaboration. Observation of CP Violation in the B^0 Meson System. *Physical Review Letters*, 87(9):091801, August 2001. Publisher: American Physical Society.

[19] R. Aaij and others, on behalf of the LHCb Collaboration. First Observation of CP Violation in the Decays of B_s^0 Mesons. *Physical Review Letters*, 110(22):221601, May 2013. Publisher: American Physical Society.

[20] R. Aaij and others, on behalf of the LHCb Collaboration. Observation of CP Violation in Charm Decays. *Physical Review Letters*, 122(21):211803, May 2019. Publisher: American Physical Society.

[21] R. H. Cyburt, B. D. Fields, and K. A. Olive. Primordial nucleosynthesis in light of WMAP. *Physics Letters B*, 567(3–4):227–234, 2003.

[22] Particle Data Group. Review of Particle Physics. *Physical Review D*, 98(3):030001, August 2018. Publisher: American Physical Society.

[23] F. R. Klinkhamer and N. S. Manton. A saddle-point solution in the Weinberg-Salam theory. *Physical Review D*, 30(10):2212–2220, November 1984. Publisher: American Physical Society.

[24] O. Bertolami, Don Colladay, V. Alan Kostelecký, and R. Potting. CPT violation and baryogenesis. *Physics Letters B*, 395(3):178–183, March 1997.

[25] B. Schwingenheuer, R. A. Briere, A. R. Barker, E. Cheu, L. K. Gibbons, D. A. Harris, G. Makoff, K. S. McFarland, A. Roodman, Y. W. Wah, B. Winstein, R. Winston, E. C. Swallow, G. J. Bock, R. Coleman, M. Crisler, J. Enagonio, R. Ford, Y. B. Hsiung, D. A. Jensen, E. Ramberg, R. Tschirhart, T. Yamanaka, E. M. Collins, G. D. Gollin, P. Gu, P. Haas, W. P. Hogan, S. K. Kim, J. N. Matthews, S. S. Myung, S. Schnetzer, S. V. Somalwar, G. B. Thomson, and Y. Zou. CPT Tests in the Neutral Kaon System. *Physical Review Letters*, 74(22):4376–4379, May 1995. Publisher: American Physical Society.

[26] Robert S. Van Dyck, Paul B. Schwinberg, and Hans G. Dehmelt. New high-precision comparison of electron and positron g factors. *Physical Review Letters*, 59(1):26–29, July 1987.

[27] H. Dehmelt, R. Mittleman, R. S. Van Dyck, and P. Schwinberg. Past Electron-Positron g-2 Experiments Yielded Sharpest Bound on CPT Violation for Point Particles. *Physical Review Letters*, 83(23), 1999.

[28] C. Smorra, S. Sellner, M. J. Borchert, J. A. Harrington, T. Higuchi, H. Nagahama, T. Tanaka, A. Mooser, G. Schneider, M. Bohman, K. Blaum, Y. Matsuda, C. Ospelkaus, W. Quint, J. Walz, Y. Yamazaki, and S. Ulmer. A parts-per-billion measurement of the antiproton magnetic moment. *Nature*, 550(7676):371–374, October 2017.

[29] Georg Schneider, Andreas Mooser, Matthew Bohman, Natalie Schön, James Harrington, Takashi Higuchi, Hiroki Nagahama, Stefan Sellner, Christian Smorra, Klaus Blaum, Yasuyuki Matsuda, Wolfgang Quint, Jochen Walz, and Stefan Ulmer. Double-trap measurement of the proton magnetic moment at 0.3 parts per billion precision. *Science*, 358(6366):1081–1084, November 2017.

[30] G. W. Bennett and others, on behalf of the Muon g-2 Collaboration. Final report of the E821 muon anomalous magnetic moment measurement at BNL. *Physical Review D*, 73(7):072003, April 2006.

[31] G. W. Bennett and others, on behalf of the Muon g-2 Collaboration. Search for Lorentz and CPT Violation Effects in Muon Spin Precession. *Physical Review Letters*, 100(9):091602, March 2008. Publisher: American Physical Society.

[32] M. Hori and J. Walz. Physics at CERN's Antiproton Decelerator. *Progress in Particle and Nuclear Physics*, 72:206–253, September 2013.

[33] G. Gabrielse, X. Fei, K. Helmerson, S. L. Rolston, R. Tjoelker, T. A. Trainor, H. Kalinowsky, J. Haas, and W. Kells. First Capture of Antiprotons in a Penning Trap: A Kiloelectronvolt Source. *Physical Review Letters*, 57(20):2504–2507, November 1986. Publisher: American Physical Society.

[34] C. Amole and others, on behalf of the ALPHA collaboration. An experimental limit on the charge of antihydrogen. *Nature Communications*, 5(1):3955, June 2014. Number: 1 Publisher: Nature Publishing Group.

[35] M. Ahmadi and others, on behalf of the ALPHA collaboration. Observation of the hyperfine spectrum of antihydrogen. *Nature*, 548(7665):66–69, August 2017. Number: 7665 Publisher: Nature Publishing Group.

[36] M. Ahmadi and others, on behalf of the ALPHA collaboration. Characterization of the 1S-2S transition in antihydrogen. *Nature*, 557(7703):71–75, May 2018. Number: 7703 Publisher: Nature Publishing Group.

[37] A. Mooser, S. Ulmer, K. Blaum, K. Franke, H. Kracke, C. Leiteritz, W. Quint, C. C. Rodegheri, C. Smorra, and J. Walz. Direct high-precision measurement of the magnetic moment of the proton. *Nature*, 509(7502):596–599, May 2014.

[38] H. Nagahama, C. Smorra, S. Sellner, J. Harrington, T. Higuchi, M. J. Borchert, T. Tanaka, M. Besirli, A. Mooser, G. Schneider, K. Blaum, Y. Matsuda, C. Ospelkaus, W. Quint, J. Walz, Y. Yamazaki, and S. Ulmer. Sixfold improved single particle measurement of the magnetic moment of the antiproton. *Nature Communications*, 8:14084, January 2017.

[39] S. Ulmer, C. Smorra, A. Mooser, K. Franke, H. Nagahama, G. Schneider, T. Higuchi, S. Van Gorp, K. Blaum, Y. Matsuda, W. Quint, J. Walz, and Y. Yamazaki. High-precision comparison of the antiproton-to-proton charge-to-mass ratio. *Nature*, 524(7564):196–199, August 2015.

[40] J. DiSciacca and others, on behalf of the ATRAP collaboration. One-Particle Measurement of the Antiproton Magnetic Moment. *Physical Review Letters*, 110(13):130801, 2013.

[41] V. Alan Kostelecký and Neil Russell. Data tables for Lorentz and CPT violation. *Reviews of Modern Physics*, 83(1):11–31, March 2011. Publisher: American Physical Society.

[42] S. Ulmer, J. Walz, K. Blaum, M. Borchert, C. Ospelkaus, J. Harrington, C. Smorra, Y. Matsuda, W. Quint, M. Fleck, E. Wursten, Y. Yamazaki, M. Wiesinger, M. Bohman, J. Devlin, and S. Erlewein. Future Program of the BASE Experiment at the Antiproton Decelerator of CERN, November 2019. Number: CERN-SPSC-2019-047, https://cds.cern.ch/record/2702758?

[43] C. Smorra, K. Blaum, L. Bojtar, M. Borchert, K.A. Franke, T. Higuchi, N. Leefer, H. Nagahama, Y. Matsuda, A. Mooser, M. Niemann, C. Ospelkaus, W. Quint, G. Schneider, S. Sellner, T. Tanaka, S. Van Gorp, J. Walz, Y. Yamazaki, and S. Ulmer. BASE – The Baryon Antibaryon Symmetry Experiment. *The European Physical Journal Special Topics*, 224(16):1–54, November 2015.

[44] Matthias Borchert. *Detektor für ein (Anti-)Proton in einer Penningfalle*. Bachelor's thesis, Leibniz Universität Hannover, Hannover, 2014.

[45] M. Niemann, T. Meiners, J. Mielke, M. J. Borchert, J. M. Cornejo, S. Ulmer, and C. Ospelkaus. Cryogenic $^{9}Be^{+}$ Penning trap for precision measurements with (anti-)protons. *Measurement Science and Technology*, 31(3):035003, December 2019.

[46] Matthias Borchert. *Developments for the high precision measurement of the antiproton magnetic moment*. Master's thesis, Leibniz Universität Hannover, Hannover, 2017.

[47] C. Smorra, A. Mooser, M. Besirli, M. Bohman, M. J. Borchert, J. Harrington, T. Higuchi, H. Nagahama, G. L. Schneider, S. Sellner, T. Tanaka, K. Blaum, Y. Matsuda, C. Ospelkaus, W. Quint, J. Walz, Y. Yamazaki, and S. Ulmer. Observation of individual spin quantum transitions of a single antiproton. *Physics Letters B*, 769:1–6, June 2017.

[48] S. Sellner, M. Besirli, M. Bohman, M. J. Borchert, J. Harrington, T. Higuchi, A. Mooser, H. Nagahama, G. Schneider, C. Smorra, T. Tanaka, K. Blaum, Y. Matsuda, C. Ospelkaus, W. Quint, J. Walz, Y. Yamazaki, and S. Ulmer. Improved

limit on the directly measured antiproton lifetime. *New Journal of Physics*, 19(8):083023, August 2017.

[49] C. Smorra, A. Mooser, K. Franke, H. Nagahama, G. Schneider, T. Higuchi, S. V. Gorp, K. Blaum, Y. Matsuda, W. Quint, J. Walz, Y. Yamazaki, and S. Ulmer. A reservoir trap for antiprotons. *International Journal of Mass Spectrometry*, 389:10–13, October 2015.

[50] C. Smorra, Y. V. Stadnik, P. E. Blessing, M. Bohman, M. J. Borchert, J. A. Devlin, S. Erlewein, J. A. Harrington, T. Higuchi, A. Mooser, G. Schneider, M. Wiesinger, E. Wursten, K. Blaum, Y. Matsuda, C. Ospelkaus, W. Quint, J. Walz, Y. Yamazaki, D. Budker, and S. Ulmer. Direct limits on the interaction of antiprotons with axion-like dark matter. *Nature*, 575(7782):310–314, November 2019.

[51] M. J. Borchert, P. E. Blessing, J. A. Devlin, J. A. Harrington, T. Higuchi, J. Morgner, C. Smorra, E. Wursten, M. Bohman, M. Wiesinger, A. Mooser, K. Blaum, Y. Matsuda, C. Ospelkaus, W. Quint, J. Walz, Y. Yamazaki, and S. Ulmer. Measurement of ultralow heating rates of a single antiproton in a cryogenic penning trap. *Physical Review Letters*, 122(4):043201, January 2019.

[52] James Brydges-Harrington. *High-Precision Measurement of the Antiproton charge-to-mass ratio, to be submitted.* PhD Thesis, Ruprecht-Karls-Universität Heidelberg, Heidelberg, 2020.

[53] Takashi Higuchi. *Development for an improved comparison of proton-to-antiproton charge-to-mass ratio.* Phd thesis, Graduate School of Arts and Sciences, The University of Tokyo, Tokyo, 2018.

[54] Eric A. Cornell, Robert M. Weisskoff, Kevin R. Boyce, and David E. Pritchard. Mode coupling in a Penning trap: Pi pulses and a classical avoided crossing. *Physical Review A*, 41(1):312–315, January 1990.

[55] Eric A. Cornell, Robert M. Weisskoff, Kevin R. Boyce, Robert W. Flanagan, Gregory P. Lafyatis, and David E. Pritchard. Single-ion cyclotron resonance measurement of M(CO+)/M(N2+). *Physical Review Letters*, 63(16):1674–1677, 1989.

[56] Sven Sturm, Anke Wagner, Birgit Schabinger, and Klaus Blaum. Phase-Sensitive Cyclotron Frequency Measurements at Ultralow Energies. *Physical Review Letters*, 107(14):143003, September 2011.

[57] D. J. Wineland and H. G. Dehmelt. Principles of the stored ion calorimeter. *Journal of Applied Physics*, 46(919), 1975.

[58] J. I. Cirac and P. Zoller. Quantum Computations with Cold Trapped Ions. *Physical Review Letters*, 74(20):4091, 1995.

[59] K. Wright, K. M. Beck, S. Debnath, J. M. Amini, Y. Nam, N. Grzesiak, J.-S. Chen, N. C. Pisenti, M. Chmielewski, C. Collins, K. M. Hudek, J. Mizrahi, J. D. Wong-Campos, S. Allen, J. Apisdorf, P. Solomon, M. Williams, A. M. Ducore, A. Blinov, S. M. Kreikemeier, V. Chaplin, M. Keesan, C. Monroe, and J. Kim. Benchmarking an 11-qubit quantum computer. *Nature Communications*, 10(1):5464, November 2019. Publisher: Nature Publishing Group.

[60] Thomas Monz, Daniel Nigg, Esteban A. Martinez, Matthias F. Brandl, Philipp Schindler, Richard Rines, Shannon X. Wang, Isaac L. Chuang, and Rainer Blatt. Realization of a scalable Shor algorithm. *Science*, 351(6277):1068–1070, March 2016.

[61] D. Hanneke, S. Fogwell, and G. Gabrielse. New Measurement of the Electron Magnetic Moment and the Fine Structure Constant. *Physical Review Letters*, 100(12):120801, March 2008.

[62] M. Amoretti and others, on behalf of the ATHENA collaboration. Production and detection of cold antihydrogen atoms. *Nature*, 419(6906):456–459, October 2002. Number: 6906 Publisher: Nature Publishing Group.

[63] Samuel Earnshaw. On the nature of the molecular forces which regulate the constitution of the luminiferous ether. *Trans. Camb. Phil. Soc*, 7:97–112, 1842.

[64] Wolfgang Paul and Helmut Steinwedel. Ein neues Massenspektrometer ohne Magnetfeld. *Zeitschrift für Naturforschung A*, 8(7):448–450, 1953.

[65] F. M. Penning. Die Glimmentladung bei niedrigem druck zwischen koaxialen Zylindern in einem axialen Magnetfeld. *Physica*, 3(9):873–894, November 1936.

[66] J. R. Pierce. Theory and Design of Electron Beams. In *Theory and Design of Electron Beams*. Van Nostrand Company, 1949.

[67] M. Kretzschmar. Particle motion in a Penning trap. *European Journal of Physics*, 12(5):240–246, September 1991. Publisher: IOP Publishing.

[68] Fouad G. Major, Viorica N. Gheorghe, and Günther Werth. *Charged particle traps: physics and techniques of charged particle field confinement*, volume 37. Springer Science & Business Media, 2006.

[69] Lowell S. Brown and Gerald Gabrielse. Precision spectroscopy of a charged particle in an imperfect Penning trap. *Physical Review A*, 25(4):2423–2425, April 1982.

[70] Lowell S. Brown and Gerald Gabrielse. Geonium theory: Physics of a single electron or ion in a penning trap. *Reviews of Modern Physics*, 58(1):233–311, January 1986.

[71] G. Gabrielse, L. Haarsma, and S. L. Rolston. Open-endcap Penning traps for high precision experiments. *International Journal of Mass Spectrometry and Ion Processes*, 88(2):319–332, April 1989.

[72] Stefan Ulmer. *First Observation of Spin Flips with a Single Proton Stored in a Cryogenic Penning Trap*. PhD thesis, Universität Heidelberg, Heidelberg, 2011. http://www.ub.uni-heidelberg.de/archiv/12306/.

[73] F. C. Moon. *Chaotic Vibrations*. John Wiley & Sons Ltd., New York, 1987.

[74] Jochen Ketter, Tommi Eronen, Martin Höcker, Sebastian Streubel, and Klaus Blaum. First-order perturbative calculation of the frequency-shifts caused by static cylindrically-symmetric electric and magnetic imperfections of a Penning trap. *International Journal of Mass Spectrometry*, 358:1–16, January 2014.

[75] Georg Schneider. *300 ppt Measurement of the Proton g-Factor*. PhD thesis, Johannes Gutenberg-Universität, Mainz, December 2017. https://inspirehep.net/literature/1770271.

[76] H. Nagahama, G. Schneider, A. Mooser, C. Smorra, S. Sellner, J. Harrington, T. Higuchi, M. Borchert, T. Tanaka, M. Besirli, K. Blaum, Y. Matsuda, C. Ospelkaus, W. Quint, J. Walz, Y. Yamazaki, and S. Ulmer. Highly sensitive superconducting circuits at ~700 kHz with tunable quality factors for image-current detection of single trapped antiprotons. *Review of Scientific Instruments*, 87(11):113305, November 2016.

[77] Hans Dehmelt, Warren Nagourney, and Jon Sandberg. Self-excited mono-ion oscillator. *Proceedings of the National Academy of Sciences of the United States of America*, 83(16):5761–5763, August 1986.

[78] B. D'Urso, B. Odom, and G. Gabrielse. Feedback Cooling of a One-Electron Oscillator. *Physical Review Letters*, 90(4):043001, January 2003.

[79] H. Dehmelt and P. Ekstrom. Proposed g-2 experiment on stored single electron or positron. *Bull. Am. Phys. Soc.*, 18:727, 1973.

[80] S. Ulmer, C. C. Rodegheri, K. Blaum, H. Kracke, A. Mooser, W. Quint, and J. Walz. Observation of spin flips with a single trapped proton. *Physical Review Letters*, 106(25):253001, June 2011.

[81] J. DiSciacca and G. Gabrielse. Direct Measurement of the Proton Magnetic Moment. *Physical Review Letters*, 108(15):153001, April 2012.

[82] C. C. Rodegheri, K. Blaum, H. Kracke, S. Kreim, A. Mooser, W. Quint, S. Ulmer, and J. Walz. An experiment for the direct determination of the g-factor of a single proton in a Penning trap. *New Journal of Physics*, 14(6):063011, June 2012.

[83] Lowell S Brown. Geonium lineshape. *Annals of Physics*, 159(1):62–98, January 1985.

[84] Hiroki Nagahama. *High-Precision Measurements of the Fundamental Properties of the Antiproton*. PhD Thesis, Graduate School of Arts and Sciences, The University of Tokyo, Tokyo, 2016.

[85] Jack A. Devlin, Elise Wursten, James A. Harrington, Takashi Higuchi, Pascal E. Blessing, Matthias J. Borchert, Stefan Erlewein, Jannek J. Hansen, Jonathan Morgner, Matthew A. Bohman, Andreas H. Mooser, Christian Smorra, Markus Wiesinger, Klaus Blaum, Yasuyuki Matsuda, Christian Ospelkaus, Wolfgang Quint, Jochen Walz, Yasunori Yamazaki, and Stefan Ulmer. Superconducting Solenoid System with Adjustable Shielding Factor for Precision Measurements of the Properties of the Antiproton. *Physical Review Applied*, 12(4):044012, October 2019.

[86] G. Gabrielse, X. Fei, L. A. Orozco, R. L. Tjoelker, J. Haas, H. Kalinowsky, T. A. Trainor, and W. Kells. Cooling and slowing of trapped antiprotons below 100 meV. *Physical Review Letters*, 63(13):1360–1363, September 1989.

[87] X. Fei, R. Davisson, and G. Gabrielse. High-voltage switching for in-flight capture of keV antiprotons in a Penning trap. *Review of Scientific Instruments*, 58(11):2197–2199, November 1987. Publisher: American Institute of Physics.

[88] S. Ulmer, K. Blaum, H. Kracke, A. Mooser, W. Quint, C. C. Rodegheri, and J. Walz. A cryogenic detection system at 28.9 MHz for the non-destructive observation of a single proton at low particle energy. *Nuclear Instruments and Methods in Physics Research Section A: Accelerators, Spectrometers, Detectors and Associated Equipment*, 705:55–60, 2013.

[89] A. Mooser, H. Kracke, K. Blaum, S. A. Bräuninger, K. Franke, C. Leiteritz,

W. Quint, C. C. Rodegheri, S. Ulmer, and J. Walz. Resolution of single spin flips of a single proton. *Physical Review Letters*, 110(14):140405, April 2013.

[90] S. Djekic, J. Alonso, H.-J. Kluge, W. Quint, S. Stahl, T. Valenzuela, J. Verdú, M. Vogel, and G. Werth. Temperature measurement of a single ion in a Penning trap. *The European Physical Journal D - Atomic, Molecular, Optical and Plasma Physics*, 31(3):451–457, December 2004.

[91] H. Häffner, T. Beier, Djekić S., N. Hermanspahn, H.-J. Kluge, W. Quint, S. Stahl, J. Verdú, T. Valenzuela, and G. Werth. Double Penning trap technique for precise g factor determinations in highly charged ions. *The European Physical Journal D - Atomic, Molecular, Optical and Plasma Physics*, 22(2):163–182, February 2003.

[92] A. Mooser, S. Bräuninger, K. Franke, H. Kracke, C. Leiteritz, C.C. Rodegheri, H. Nagahama, G. Schneider, C. Smorra, K. Blaum, Y. Matsuda, W. Quint, J. Walz, Y. Yamazaki, and S. Ulmer. Demonstration of the double Penning Trap technique with a single proton. *Physics Letters B*, 723(1–3):78–81, June 2013.

[93] D. Colladay and V. Alan Kostelecký. Lorentz-violating extension of the standard model. *Physical Review D*, 58(11):116002, October 1998.

[94] Robert Bluhm, V. Alan Kostelecký, and Neil Russell. CPT and Lorentz tests in Penning traps. *Physical Review D*, 57(7):3932–3943, April 1998.

[95] Yunhua Ding and V. Alan Kostelecký. Lorentz-violating spinor electrodynamics and Penning traps. *Physical Review D*, 94(5):056008, September 2016.

[96] M. Ahmadi and others, on behalf of the ALPHA collaboration. Observation of the 1s-2s transition in trapped antihydrogen. *Nature*, 541(7638):506–510, January 2017.

[97] E. Widmann, C. Amsler, S. Arguedas Cuendis, H. Breuker, M. Diermaier, P. Duprè, C. Evans, M. Fleck, A. Gligorova, H. Higaki, Y. Kanai, B. Kolbinger, N. Kuroda, M. Leali, A. M. M. Leite, V. Mäckel, C. Malbrunot, V. Mascagna, O. Massiczek, Y. Matsuda, D. J. Murtagh, Y. Nagata, A. Nanda, D. Phan, C. Sauerzopf, M. C. Simon, M. Tajima, H. Spitzer, M. Strube, S. Ulmer, L. Venturelli, M. Wiesinger, Y. Yamazaki, and J. Zmeskal. Hyperfine spectroscopy of hydrogen and antihydrogen in ASACUSA. *Hyperfine Interactions*, 240(1):5, December 2018.

[98] Arnaldo J. Vargas. Overview of the Phenomenology of Lorentz and CPT Viola-

tion in Atomic Systems. *Symmetry*, 11(12):1433, December 2019. Number: 12 Publisher: Multidisciplinary Digital Publishing Institute.

[99] R. K. Mittleman, I. I. Ioannou, H. G. Dehmelt, and Neil Russell. Bound on CPT and Lorentz Symmetry with a Trapped Electron. *Physical Review Letters*, 83(11):2116–2119, September 1999. Publisher: American Physical Society.

[100] Particle Data Group et al. Review of Particle Physics. *Physical Review D*, 86(1):010001, July 2012. Publisher: American Physical Society.

[101] Steven Weinberg. A New Light Boson? *Physical Review Letters*, 40(4):223–226, January 1978. Publisher: American Physical Society.

[102] F. Wilczek. Problem of Strong p and t Invariance in the Presence of Instantons. *Physical Review Letters*, 40(5):279–282, January 1978. Publisher: American Physical Society.

[103] Peter W. Graham, Igor G. Irastorza, Steven K. Lamoreaux, Axel Lindner, and Karl A. van Bibber. Experimental Searches for the Axion and Axion-Like Particles. *Annual Review of Nuclear and Particle Science*, 65(1):485–514, October 2015. Publisher: Annual Reviews.

[104] Y. V. Stadnik and V. V. Flambaum. Searches for New Particles Including Dark Matter with Atomic, Molecular and Optical Systems. *arXiv:1806.03115 [hep-ph, physics:physics]*, June 2018. arXiv: 1806.03115.

[105] O. W. Greenberg. CPT Violation Implies Violation of Lorentz Invariance. *Physical Review Letters*, 89(23):231602, November 2002.

[106] David J. E. Marsh. Axion cosmology. *Physics Reports*, 643:1–79, July 2016.

[107] C. Abel and others, on behalf of the nEDM project. Search for Axionlike Dark Matter through Nuclear Spin Precession in Electric and Magnetic Fields. *Physical Review X*, 7(4):041034, November 2017. Publisher: American Physical Society.

[108] Y. V. Stadnik and V. V. Flambaum. Axion-induced effects in atoms, molecules, and nuclei: Parity nonconservation, anapole moments, electric dipole moments, and spin-gravity and spin-axion momentum couplings. *Physical Review D*, 89(4):043522, February 2014. Publisher: American Physical Society.

[109] C. Smorra, Y. V. Stadnik, P. E. Blessing, M. Bohman, M. J. Borchert, J. A. Devlin, S. Erlewein, J. A. Harrington, T. Higuchi, A. Mooser, G. Schneider, M. Wiesinger, E. Wursten, K. Blaum, Y. Matsuda, C. Ospelkaus, W. Quint, J. Walz, Y. Ya-

mazaki, D. Budker, and S. Ulmer. Supplementary Information to direct limits on the interaction of antiprotons with axion-like dark matter. *Nature*, 575(7782), 2019.

[110] S. S. Wilks. The Large-Sample Distribution of the Likelihood Ratio for Testing Composite Hypotheses. *Annals of Mathematical Statistics*, 9(1):60–62, March 1938. Publisher: Institute of Mathematical Statistics.

[111] Teng Wu, John W. Blanchard, Gary P. Centers, Nataniel L. Figueroa, Antoine Garcon, Peter W. Graham, Derek F. Jackson Kimball, Surjeet Rajendran, Yevgeny V. Stadnik, Alexander O. Sushkov, Arne Wickenbrock, and Dmitry Budker. Search for Axionlike Dark Matter with a Liquid-State Nuclear Spin Comagnetometer. *Physical Review Letters*, 122(19):191302, May 2019. Publisher: American Physical Society.

[112] Georg G. Raffelt. Astrophysical Axion Bounds. In Markus Kuster, Georg Raffelt, and Berta Beltrán, editors, *Axions: Theory, Cosmology, and Experimental Searches*, Lecture Notes in Physics, pages 51–71. Springer, Berlin, Heidelberg, 2008.

[113] Q. A. Turchette, Kielpinski, B. E. King, D. Leibfried, D. M. Meekhof, C. J. Myatt, M. A. Rowe, C. A. Sackett, C. S. Wood, W. M. Itano, C. Monroe, and D. J. Wineland. Heating of trapped ions from the quantum ground state. *Physical Review A*, 61(6):063418, May 2000.

[114] M. Brownnutt, M. Kumph, P. Rabl, and R. Blatt. Ion-trap measurements of electric-field noise near surfaces. *Reviews of Modern Physics*, 87(4):1419–1482, December 2015.

[115] C. Monroe, D. M. Meekhof, B. E. King, S. R. Jefferts, W. M. Itano, D. J. Wineland, and P. Gould. Resolved-sideband Raman cooling of a bound atom to the 3D zero-point energy. *Physical Review Letters*, 75(22):4011–4014, 1995.

[116] L. Deslauriers, S. Olmschenk, D. Stick, W. K. Hensinger, J. Sterk, and C. Monroe. Scaling and Suppression of Anomalous Heating in Ion Traps. *Physical Review Letters*, 97(10):103007, 2006.

[117] D. A. Hite, K. S. McKay, S. Kotler, D. Leibfried, D. J. Wineland, and D. P. Pappas. Measurements of trapped-ion heating rates with exchangeable surfaces in close proximity. *MRS Advances*, 2(41):2189–2197, January 2017.

[118] Ivan A. Boldin, Alexander Kraft, and Christof Wunderlich. Measuring anomalous

heating in a planar ion trap with variable ion-surface separation. *Physical Review Letters*, 120(2), January 2018. arXiv: 1708.03147.

[119] J. A. Sedlacek, A. Greene, J. Stuart, R. McConnell, C. D. Bruzewicz, J. M. Sage, and J. Chiaverini. Distance scaling of electric-field noise in a surface-electrode ion trap. *Physical Review A*, 97(2):020302, February 2018.

[120] Da An, Clemens Matthiesen, Erik Urban, and Hartmut Häffner. Distance scaling and polarization of electric-field noise in a surface ion trap. *Physical Review A*, 100(6):063405, December 2019. Publisher: American Physical Society.

[121] J.F. Goodwin, G. Stutter, R.C. Thompson, and D.M. Segal. Resolved-sideband laser cooling in a penning trap. *Physical Review Letters*, 116(14):143002, April 2016.

[122] Michael Niedermayr, Kirill Lakhmanskiy, Muir Kumph, Stefan Partel, Jonannes Edlinger, Michael Brownnutt, and Rainer Blatt. Cryogenic surface ion trap based on intrinsic silicon. *New Journal of Physics*, 16(11):113068, 2014.

[123] Georg Schneider. *Development of a Penning trap system for the high precision measurement of the antiproton's magnetic moment.* Master's thesis, Johannes Gutenberg-Universität Mainz, Mainz, March 2014.

[124] F. Schwabel. Quantenmechanik (QM I): Eine Einführung. *7. ed., Springer*, 2007.

[125] T. A. Savard, K. M. O'Hara, and J. E. Thomas. Laser-noise-induced heating in far-off resonance optical traps. *Physical Review A*, 56(R1095(R)), 1997.

[126] D.W. Allan. Statistics of atomic frequency standards. *Proceedings of the IEEE*, 54(2), 1966.

[127] Stefan Ulmer. Mode-coupling, avoided crossing, double dip measurements, action exchanging pulses, and non-linear dynamics. *BASE internal document*, to be published, 2020.

[128] C. Henkel, S. Pötting, and M. Wilkens. Loss and heating of particles in small and noisy traps. *Applied Physics B*, 69(5):379–387, December 1999.

[129] R. A. Matula. Electrical resistivity of copper, gold, palladium, and silver. *Journal of Physical and Chemical Reference Data*, 8(4):1147–1298, October 1979. Publisher: American Institute of Physics.

[130] J. Chiaverini and J. M. Sage. Insensitivity of the rate of ion motional heating

to trap-electrode material over a large temperature range. *Physical Review A*, 89(1):012318, January 2014.

[131] D.J. Wineland, C.R. Monroe, W.M. Itano, D. Leibfried, B.E. King, and D.M. Meekhof. Experimental issues in coherent quantum-state manipulation of trapped atomic ions. *J. Res. NIST*, 103(3):259, 1998.

[132] L. D. Landau and E. M. Lifshitz. *Quantum Mechanics: Non-Relativistic Theory*. Elsevier, December 1981. Google-Books-ID: SvdoN3k8EysC.

[133] J. M. Schulman and J. I. Musher. Hydrogen-atom polarizability as a hartree-fock pertubation expansion: A geometric approximation to atomic polarizabilities. *The Journal of Chemical Physics*, 49(11):4845–4848, December 1968. Publisher: American Institute of Physics.

[134] M. A. Thomas and J. W. Humberston. The polarizability of helium. *Journal of Physics B: Atomic and Molecular Physics*, 5(11):L229–L232, November 1972. Publisher: IOP Publishing.

[135] Iratxe Landa, Amaia Arrinda, Igor Fernandez, and Pablo Angueira. Indoor Radio Noise Long-Term Measurements in Medium Wave Band in Buildings of City Areas in the North of Spain. *IEEE Antennas and Wireless Propagation Letters*, 10:17–20, 2011. Conference Name: IEEE Antennas and Wireless Propagation Letters.

[136] Jaroslaw Labaziewicz, Yufei Ge, Paul Antohi, David Leibrandt, Kenneth R. Brown, and Isaac L. Chuang. Suppression of Heating Rates in Cryogenic Surface-Electrode Ion Traps. *Physical Review Letters*, 100(1):013001, January 2008.

[137] Jaroslaw Labaziewicz, Yufei Ge, David R. Leibrandt, Shannon X. Wang, Ruth Shewmon, and Isaac L. Chuang. Temperature Dependence of Electric Field Noise above Gold Surfaces. *Physical Review Letters*, 101(18):180602, October 2008.

[138] Shannon X. Wang, Yufei Ge, Jaroslaw Labaziewicz, Eric Dauler, Karl Berggren, and Isaac L. Chuang. Superconducting microfabricated ion traps. *Applied Physics Letters*, 97(24):244102, 2010.

[139] C. D. Bruzewicz, J. M. Sage, and J. Chiaverini. Measurement of ion motional heating rates over a range of trap frequencies and temperatures. *Physical Review A*, 91(4), April 2015.

[140] Brian C. Sawyer, Joseph W. Britton, and John J. Bollinger. Spin dephasing as a probe of mode temperature, motional state distributions, and heating rates in a

two-dimensional ion crystal. *Physical Review A*, 89(3):033408, March 2014. Publisher: American Physical Society.

[141] G. Stutter, P. Hrmo, V. Jarlaud, M. K. Joshi, J. F. Goodwin, and R. C. Thompson. Sideband cooling of small ion Coulomb crystals in a Penning trap. *Journal of Modern Optics*, 65(5-6):549–559, March 2018.

[142] The SNO+ Collaboration and M. et al. Anderson. Search for invisible modes of nucleon decay in water with the SNO+ detector. *Physical Review D*, 99(3):032008, February 2019. Publisher: American Physical Society.

[143] Stephen H. Geer and Dallas C. Kennedy. A New Limit on the Antiproton Lifetime. *The Astrophysical Journal*, 532(1):648, March 2000. Publisher: IOP Publishing.

[144] S. Geer and others, on behalf of the APEX collaboration. New Limit on *CPT* Violation. *Physical Review Letters*, 84(4):590–593, January 2000. Publisher: American Physical Society.

[145] S. Geer and others, on behalf of the APEX collaboration. Erratum: New Limit on *CPT* Violation [Phys. Rev. Lett. 84, 590 (2000)]. *Physical Review Letters*, 85(16):3546–3546, October 2000. Publisher: American Physical Society.

[146] K. S. Babu, Jogesh C. Pati, and Frank Wilczek. Suggested new modes in supersymmetric proton decay. *Physics Letters B*, 423(3):337–347, March 1998.

[147] Xiang Fei. *Trapping Low Energy Antiprotons in an Ion Trap*. PhD thesis, Harvard University, Cambridge, 1990.

[148] Gary King. *Unifying political methodology: The likelihood theory of statistical inference*. University of Michigan Press, 1998.

[149] G. Gabrielse, X. Fei, L. A. Orozco, R. L. Tjoelker, J. Haas, H. Kalinowsky, T. A. Trainor, and W. Kells. Thousandfold improvement in the measured antiproton mass. *Physical Review Letters*, 65(11):1317–1320, September 1990.

[150] Andreas Mooser. *Der g-Faktor des Protons*. PhD thesis, Johannes Gutenberg-Universität Mainz, December 2013. https://inspirehep.net/files/e309bfad506d75ce4d6dc34cdc74ea5c.

[151] G. Gabrielse, D. Phillips, W. Quint, H. Kalinowsky, G. Rouleau, and W. Jhe. Special Relativity and the Single Antiproton: Fortyfold Improved Comparison of p- and p Charge-to-Mass Ratios. *Physical Review Letters*, 74(18):3544–3547, May 1995.

[152] G. Gabrielse, A. Khabbaz, D. S. Hall, C. Heimann, H. Kalinowsky, and W. Jhe. Precision Mass Spectroscopy of the Antiproton and Proton Using Simultaneously Trapped Particles. *Physical Review Letters*, 82(16):3198–3201, April 1999.

[153] G. Gabrielse. Antiproton mass measurements. *International Journal of Mass Spectrometry*, 251(2):273–280, April 2006.

[154] Frank E. Grubbs. Sample criteria for testing outlying observations. *Annals of Mathematical Statistics*, 21:27–58, 1950.

[155] Norman R. Draper and Harry Smith. Fitting a Straight Line by Least Squares. In *Applied Regression Analysis*. John Wiley & Sons, Ltd, 2014.

[156] Jennifer A. Hutcheon, Arnaud Chiolero, and James A. Hanley. Random measurement error and regression dilution bias. *BMJ*, 340, June 2010. Publisher: British Medical Journal Publishing Group Section: Research Methods & Reporting.

[157] G. Gabrielse and J. Tan. Self-shielding superconducting solenoid systems. *Journal of Applied Physics*, 63(5143), 1988.

[158] Toya Tanaka. *Development of tunable single particle detection system for an improved measurement of proton-to-antiproton charge-to-mass ratio.* Master's thesis, Graduate School of Arts and Sciences, The University of Tokyo, Tokyo, 2017.

[159] F. Heiße, F. Köhler-Langes, S. Rau, J. Hou, S. Junck, A. Kracke, A. Mooser, W. Quint, S. Ulmer, G. Werth, K. Blaum, and S. Sturm. High-Precision Measurement of the Proton's Atomic Mass. *Physical Review Letters*, 119(3):033001, July 2017.

[160] Mustafa Besirli. *Development of single sideband down converters for precise measurements of the axial frequency of a single trapped antiproton.* Bachelor's thesis, Sabanca University Istanbul, Istanbul, 2016.

[161] W. Oelert. The ELENA Project at CERN. *Acta Physica Polonica B*, 46:181, 2015.

[162] Donald F. Gatz and Luther Smith. The standard error of a weighted mean concentration-I. Bootstrapping vs other methods. *Atmospheric Environment*, 29(11):1185–1193, June 1995.

[163] Eric Allin Cornell. *Mass spectroscopy using single ion cyclotron resonance.* Thesis, Massachusetts Institute of Technology, 1990. Accepted: 2007-07-17T19:26:33Z.

[164] Vasant Natarajan. *Penning trap mass spectroscopy at 0.1 ppb.* Thesis, Massachusetts Institute of Technology, 1993. Accepted: 2005-09-26T18:02:01Z.

[165] Lucien Le Cam. *Asymptotic Methods in Statistical Decision Theory*. Springer Series in Statistics. Springer-Verlag, New York, 1986.

[166] C. Radhakrishna Rao. Information and the Accuracy Attainable in the Estimation of Statistical Parameters. In Samuel Kotz and Norman L. Johnson, editors, *Breakthroughs in Statistics: Foundations and Basic Theory*, Springer Series in Statistics, pages 235–247. Springer, New York, NY, 1992.

[167] Hirotogu Akaike. Information Theory and an Extension of the Maximum Likelihood Principle. In Emanuel Parzen, Kunio Tanabe, and Genshiro Kitagawa, editors, *Selected Papers of Hirotugu Akaike*, Springer Series in Statistics, pages 199–213. Springer, New York, NY, 1998.

[168] J. V. Porto. Series solution for the image charge fields in arbitrary cylindrically symmetric Penning traps. *Physical Review A*, 64(2):023403, June 2001. Publisher: American Physical Society.

[169] Hartmut Häffner. *Präzisionsmessung des magnetischen Moments des Elektrons in wasserstoffähnlichem Kohlenstoff*. PhD thesis, Johannes Gutenberg-Universität Mainz, 2000.

[170] Robert Mark Weisskoff. *Detecting single, trapped ions*. Thesis, Massachusetts Institute of Technology, 1988. Accepted: 2012-01-12T18:32:01Z.

[171] Sascha Rau, Fabian Heiße, Florian Köhler-Langes, Sangeetha Sasidharan, Raphael Haas, Dennis Renisch, Christoph E. Düllmann, Wolfgang Quint, Sven Sturm, and Klaus Blaum. Penning trap mass measurements of the deuteron and the HD + molecular ion. *Nature*, 585(7823):43–47, September 2020. Number: 7823 Publisher: Nature Publishing Group.

[172] Sayan Patra, M. Germann, J.-Ph Karr, M. Haidar, L. Hilico, V. I. Korobov, F. M. J. Cozijn, K. S. E. Eikema, W. Ubachs, and J. C. J. Koelemeij. Proton-electron mass ratio from laser spectroscopy of HD+ at the part-per-trillion level. *Science*, 369(6508):1238–1241, September 2020. Publisher: American Association for the Advancement of Science Section: Report.

[173] I. V. Kortunov, S. Alighanbari, M. G. Hansen, G. S. Giri, V. I. Korobov, and S. Schiller. Proton-electron mass ratio by high-resolution optical spectroscopy of ion ensembles in the resolved-carrier regime. *Nature Physics*, 17(5):569–573, May 2021.

[174] A. Kramida, Y. Ralchenko, J. Reader, and NIST ASD Team. NIST Atomic Spectra

Database (ver. 5.8),[Online]. *Physical Review A*, October 2020. Available https://physics.nist.gov/asd [2020, November 26].

[175] Christian G. Parthey, Arthur Matveev, Janis Alnis, Birgitta Bernhardt, Axel Beyer, Ronald Holzwarth, Aliaksei Maistrou, Randolf Pohl, Katharina Predehl, Thomas Udem, Tobias Wilken, Nikolai Kolachevsky, Michel Abgrall, Daniele Rovera, Christophe Salomon, Philippe Laurent, and Theodor W. Hänsch. Improved Measurement of the 1s-2s Transition Frequency. *Physical Review Letters*, 107(20):203001, November 2011. Publisher: American Physical Society.

[176] Ulrich D. Jentschura, Svetlana Kotochigova, Eric-Olivier Le Bigot, Peter J. Mohr, and Barry N. Taylor. Precise Calculation of Transition Frequencies of Hydrogen and Deuterium Based on a Least-Squares Analysis. *Physical Review Letters*, 95(16):163003, October 2005. Publisher: American Physical Society.

[177] K. R. Lykke, K. K. Murray, and W. C. Lineberger. Threshold photodetachment of H^-. *Physical Review A*, 43(11):6104–6107, June 1991. Publisher: American Physical Society.

[178] James K. Thompson, Simon Rainville, and David E. Pritchard. Cyclotron frequency shifts arising from polarization forces. *Nature*, 430(6995):58–61, July 2004. Number: 6995 Publisher: Nature Publishing Group.

[179] Simon Rainville, James K. Thompson, Edmund G. Myers, John M. Brown, Maynard S. Dewey, Ernest G. Kessler Jr, Richard D. Deslattes, Hans G. Börner, Michael Jentschel, Paolo Mutti, and David E. Pritchard. A direct test of $e = mc^2$. *Nature*, 438(7071):1096–1097, December 2005.

[180] A. K. Bhatia and R. J. Drachman. Polarizability of helium and the negative hydrogen ion. *Journal of Physics B: Atomic, Molecular and Optical Physics*, 27(7):1299–1305, April 1994. Publisher: IOP Publishing.

[181] B. K. Sahoo. Determination of the dipole polarizability of the alkali-metal negative ions. *Physical Review A*, 102(2):022820, August 2020. Publisher: American Physical Society.

[182] Yunhua Ding and Mohammad Farhan Rawnak. Lorentz and cpt tests with charge-to-mass ratio comparisons in Penning traps. *Physical Review D*, 102(5):056009, September 2020. Publisher: American Physical Society.

[183] Richard J. Hughes and Michael H. Holzscheiter. Constraints on the gravitational properties of antiprotons and positrons from cyclotron-frequency measurements.

Physical Review Letters, 66(7):854–857, February 1991. Publisher: American Physical Society.

[184] Michael Martin Nieto and T. Goldman. The arguments against "antigravity" and the gravitational acceleration of antimatter. *Physics Reports*, 205(5):221–281, July 1991.

[185] A. Kellerbauer and others, on behalf of the AEgIS collaboration. Proposed antimatter gravity measurement with an antihydrogen beam. *Nuclear Instruments and Methods in Physics Research Section B: Beam Interactions with Materials and Atoms*, 266(3):351–356, February 2008.

[186] W. A. Bertsche. Prospects for comparison of matter and antimatter gravitation with ALPHA-g. *Philosophical Transactions of the Royal Society A: Mathematical, Physical and Engineering Sciences*, 376(2116):20170265, March 2018. Publisher: Royal Society.

[187] P. Pérez and others, on behalf of the GBAR collaboration. The GBAR antimatter gravity experiment. *Hyperfine Interactions*, 233(1):21–27, August 2015.

[188] Simon Rainville, James K. Thompson, and David E. Pritchard. An Ion Balance for Ultra-High-Precision Atomic Mass Measurements. *Science*, 303(5656):334–338, January 2004.

[189] Mini-Circuits. Reflective spdt rf switch zasw-2-50dra+. https://www.minicircuits.com/pdfs/ZASW-2-50DRA+.pdf. [Online; accessed 02-November-2020].

[190] Martin Kretzschmar. A quantum mechanical model of Rabi oscillations between two interacting harmonic oscillator modes and the interconversion of modes in a Penning trap. *AIP Conference Proceedings*, 457(1):242–251, 1999.

[191] Sven Sturm. *The g-factor of the electron bound in $^{28}Si^{13+}$: The most stringent test of bound-state quantum electrodynamics.* PhD Thesis, Johannes Gutenberg-Universität, Mainz, 2012.

[192] Florian Köhler. *Bound-Electron g-Factor Measurements for the Determination of the Electron Mass and Isotope Shifts in Highly Charged Ions.* PhD Thesis, Ruprecht-Karls-Universität Heidelberg, Heidelberg, 2015. Library Catalog: archiv.ub.uni-heidelberg.de.

[193] David Ruppert and David S. Matteson. *Statistics and Data Analysis for Financial*

Engineering: with R examples. Springer Texts in Statistics. Springer-Verlag, New York, 2 edition, 2015.

[194] Markus Fleck. *To be submitted*. PhD Thesis, Graduate School of Arts and Sciences, The University of Tokyo, Tokyo, 2021.

[195] Stefan Erlewein. *To be submitted*. PhD Thesis, Ruprecht-Karls-Universität Heidelberg, Heidelberg, 2021.

[196] I. Bergström, C. Carlberg, T. Fritioff, G. Douysset, J. Schönfelder, and R. Schuch. SMILETRAP-A Penning trap facility for precision mass measurements using highly charged ions. *Nuclear Instruments and Methods in Physics Research Section A: Accelerators, Spectrometers, Detectors and Associated Equipment*, 487(3):618–651, July 2002.